Photoelectron Circular Dichroism of Anionic Chiral Metal Complexes and Deprotonated Molecules

vorgelegt von
M.Sc.
Jenny Triptow
ORCID:0000-0002-4048-3348

an der Fakultät II - Mathematik und Naturwissenschaften
der Technischen Universität Berlin
zur Erlangung des akademischen Grades

Doktor*in der Naturwissenschaften
- Dr. rer. nat. -

genehmigte Dissertation

Promotionsausschuss:

Vorsitzender: Prof. Dr. Mario Dähne
Gutachter: Prof. Dr. Otto Dopfer
Gutachter: Prof. Dr. Melanie Schnell

Tag der wissenschaftlichen Aussprache: 20.11.2023

Berlin 2024

Contents

List of Abbreviations

3HTHF	3-hydroxytetrahydrofuran
ADE	adiabatic detachment energy
AIM	(Bader's quantum theory of) atom-in-molecule
Ala	alaninol
Ala-H	deprotonated alaninol
aug-cc-pVTZ	augmented correlation-consistent polarized valence triple zeta (basisset)
B3LYP-D3	Becke-3-parameters-Lee-Yang-Parr (hybrid functional) with Grimme's 3. variant of dispersion correction
DFT	density functional theory
FC	Franck-Condon
Fen	fenchone
FWHM	full width at half maximum
HOMO	highest occupied molecular orbital
Ind-H	deprotonated 1-indanol
IUPAC	International Union of Pure and Applied Chemistry
LCP	left circular polarized
LIN	linear polarized
MCP	multichannel plate
Men	menthone
MS	mass spectrum/spectra
NBO	natural bond orbitals
PAD	photoelectron angular distribution
PECD	photoelectron circular dichroism
PES	photoelectron spectrum/spectra
PEM	photoelastic modulator

POP	polar onion peeling
QWP	quarter waveplate
RCP	right circular polarized
SE	standard error
ToF-MS	time of flight mass spectrometer
VDE	vertical detachment energy
VMI	velocity map imaging
ZPE	zero-point energy

"If we knew what it was we were doing,
it would not be called research, would it?"
–Albert Einstein

Abstract

Photoelectron circular dichroism (PECD) emerges as an asymmetry in the spatial distribution (regarding the light direction) of electrons detached from chiral molecules with left or right circular polarized light. In the past two decades PECD spectroscopy has manifested as a potential method for enantiomeric discrimination, with a chiral sensitivity that can surpass conventional methods, such as absorption circular dichroism.

Conventionally, photoemitted electrons from neutral chiral molecules are studied, which can lead to PECD values of up to 20% [1]. Here, a modified version of PECD is implemented where photodetached electrons from chiral anions are considered. It can be called PECD in photodetachment or anion PECD.

This approach simplifies the experiment since photodetachment requires in general less energy than ionization. Therefore, single photoelectron emission is achievable using common table-top lasers. Furthermore, mass selection before photodetachment is possible such that electrons can clearly be assigned to a species of specific mass. Apart from experimental advantages, the impact of short-range interactions (e.g. dipole moment, scattering potential) between molecule and electron on the PECD will be revealed since no cation but a neutral core is left behind after electron removal. Hence, this eliminates the need for considering long-range Coulombic interactions. Furthermore, the idea of a photodetached electron as a plane wave is challenged.

At the start of this work, no experimental or theoretical work had reported on anion PECD. This effect in anions was even doubted to exist since photodetached electrons are usually considered to be plane waves, which cannot carry an asymmetry. Only a few years ago, the first successful experiments and calculations on anion PECD were published [2–4].

The here investigated chiral anions are either chiral gold complexes, consisting of a neutral chiral molecule (fenchone, menthone, 3-hydroxytetrahydrofuran or alaninol) and an atomic gold anion, or deprotonated chiral molecules (alaninol, 1-indanol), which are (in most cases) deprotonated at the hydroxyl group. These chiral systems are mass-selected and subsequently photodetached by a tunable laser with either linear or circular polarized light. Using velocity map imaging (VMI) photoelectron spectroscopy, the kinetic energy of the detached electron and its spatial distribution are recorded, providing insight into the energy-resolved PECD.

Unfortunately, gold complexes do not reveal any PECD but photoelectron spectra measured with linear polarized light combined with density functional theory calculations yield intriguing results toward nonconventional hydrogen bonding. The photoelectron spectra show that the hydrogen bonds are strong enough for an interaction between gold and the chiral molecule. However, it does not lead to a measurable PECD effect.

Anion PECD is successfully measured for the deprotonated molecules from which the deprotonated 1-indanol shows a particularly clear PECD. The strongest PECD is found for detachment from HOMO-2 with around 11%, which is comparable to PECD values of neutral molecules. Considering this asymmetry strength and the kinetic energy range the PECD asymmetry is recorded, this work emphasizes the importance of short-range interactions.

Zusammenfassung

Photoelektronen-Zirkulardichroismus (im Folgenden mit PECD abgekürzt nach der englischen Bezeichnung) zeigt sich als Asymmetrie in der räumlichen Verteilung von Elektronen bezüglich der Ausbreitungsrichtung des Lichts, welche von ihrem chiralen Molekül durch links oder rechts zirkular polarisiertes Licht getrennt wurden. In den letzten beiden Jahrzehnten hat sich PECD Spektroskopie als potentielle Methode zur Enantiomerenunterscheidung behauptet und kann wegen der höheren chiralen Sensitivität etablierte Methoden wie den Absorptions-Zirkulardichroismus übertreffen.

Konventionell werden Elektronen aus photoionisierten chiralen neutralen Molekülen untersucht. Dies kann zu PECD Werten von bis zu 20% führen [1]. Hier wird eine modifizierte Version des konventionellen PECD umgesetzt, welche die Untersuchung chiraler Anionen zum Ziel hat. Diese Methode kann entweder PECD im Photodetachment oder Anionen PECD genannt werden.

Dieser Ansatz vereinfacht das Experiment dahingehend, dass Photodetachment im Allgemeinen weniger Energie benötigt als Ionisation. Folglich werden Einphotonenprozesse mit kommerziell erhältlichen Tischlasern ermöglicht. Weiterhin können Anionen zuvor nach der Masse selektiert und dadurch eine bessere Zuordnung erreicht werden. Neben den Vorteilen im experimentellen Aufbau können auch der Einfluss von kurzreichweitigen Wechselwirkungen (z.B. durch Dipolmoment und Streupotentialen) zwischen Elektron und Molekül auf das PECD Signal untersucht werden, da kein Kation sondern ein neutrales Molekül nach dem Photodetachment zurückgelassen wird. Folglich können langreichweitige Coulombwechselwirkungen vernachlässigt werden. Außerdem wird die Idee, das abgelöste Elektron als ebene Welle zu betrachten in Frage gestellt.

Zunächst waren weder experimentelle noch theoretische Arbeiten mit dieser Methode veröffentlicht worden. Es wurde sogar angezweifelt, ob Anionen-PECD überhaupt detektierbar sei, da Photoelektronen aus Anionen üblicherweise als ebene Welle betrachtet werden und daher keine Asymmetrie übermitteln können. Erst kürzlich zeigten experimentelle und theoretische Arbeiten einen Anion-PECD [2–4].

Bei den hier untersuchten chiralen Anionen handelt es sich entweder um chirale Goldkomplexe, welche aus einem neutralen chiralen Molekül (Fenchon, Menthon, 3-Hydroxytetrahydrofuran oder Alaninol) und einem Goldanion bestehen, oder um ein deprotoniertes Molekül (Alaninol, 1-Indanol), was (meist) an der Hydroxyl-Gruppe deprotoniert wird. Diese chiralen Systeme werden massenselektiert und anschließend mittels eines durchstimmbaren Laser mit linearem oder zirkular polarisierten Licht photodetached. Ein velocity-map-imaging (VMI) Spektrometer ermöglicht die Messung der kinetischen Energie und räumlichen Verteilung der abgelösten Elektronen, welches schlussendlich die Messung eines energieaufgelösten PECDs ermöglicht.

Leider war es nicht möglich, einen PECD für die Goldkomplexe zu messen. Dafür konnten aber Photoelektronenspektren (gemessen mit linear polarisierten Licht) und density-functional-theory (DFT)-Rechnungen interessante Ergebnise bezüglich unüblicher Wasserstoffbrückenbindungen hervorbringen. Die Spektren zeigen, dass diese Bindungen stark genug sind für eine Wechselwirkung zwischen Gold und chiralem Molekül, aber zu keinem messbaren PECD Effekt führen.

Ein Anionen-PECD wurde hingegen erfolgreich bestimmt für deprotonierte Moleküle, insbesondere deprotoniertes 1-Indanol zeigt einen deutlichen PECD. Der stärkste PECD wurde für Detachment aus dem HOMO-2 mit etwa 11% gemessen und ist in der Stärke vergleichbar mit PECD-Werten von neutralen Molekülen. Wenn diese Signalstärke und der Bereich der verwendeten kinetischen Energien, bei dem der PECD nachgewiesen wurde, betrachtet werden, fällt auf, dass kurzreichweitige Wechselwirkungen in der Tat eine wichtige Rolle spielen.

Eidesstattliche Erklärung: Hiermit versichere ich, dass ich die vorliegende Arbeit selbstständig verfasst und keine anderen als die angegebenen Quellen und Hilfsmittel benutzt habe. Alle Ausführungen, die anderen veröffentlichten oder nicht veröffentlichten Schriften wörtlich oder sinngemäß entnommen wurden, habe ich kenntlich gemacht.

Die Arbeit hat in gleicher oder ähnlicher Fassung noch keiner anderen Prüfungsbehörde vorgelegen.

Statutory Declaration: I declare that I have authored this thesis independently, that I have not used other than the declared sources/resources and that I have explicitly marked all material which has been quoted either literally or by content from the used sources.

This paper was not previously presented to another examination board and has not been published.

Ort, Datum/Place, Date	Jenny Triptow

1. Introduction

1.1. Chirality

Importance of Chirality in Daily Life

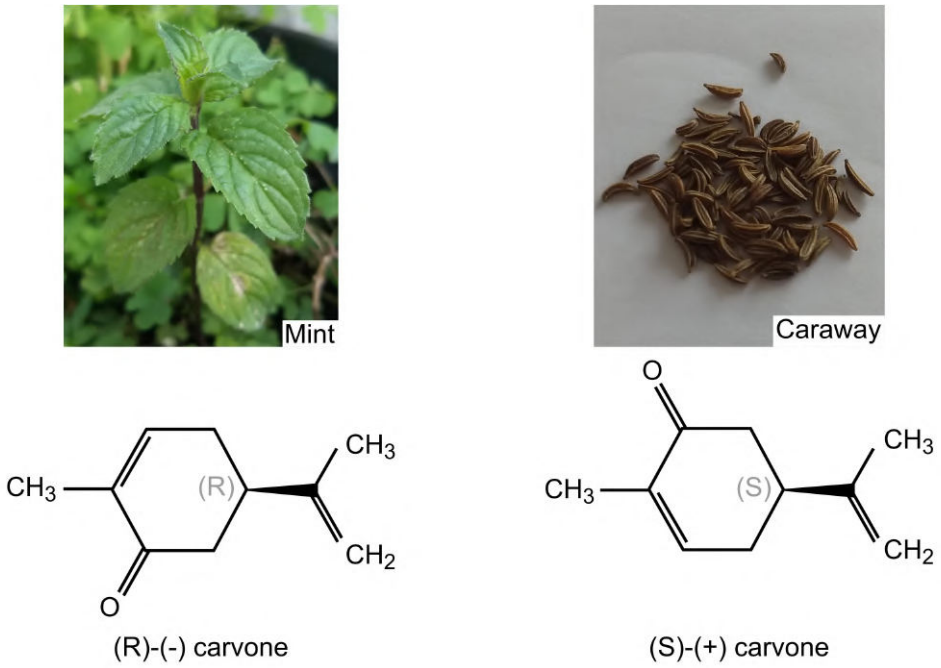

Fig. 1.1.1.: Carvone is a chiral molecule where the (R)-enantiomer can be found in mint and the (S)-enantiomer is found in caraway. Despite the similar molecular structure, these enantiomers lead to smell and taste that are quite different.

A familiar and famous beginner example of a chiral system is a pair of hands where left and right hand can be seen as enantiomers of each other. Hence it is referred to as "handedness" in the english language, which is the translation from the greek word "chirality". Although enantiomers are just mirror images of each other the effect in e.g. biological systems can be quite different, even noxious.

On a benign scale, molecules like carvone exist in two different enantiomers, which can be found in mint or caraway, respectively (figure 1.1.1). Regardless of the alike structure both enantiomers lead to a different taste and smell, due to the different interactions between the respective enantiomers and the taste/smell receptors. Unfortunately, there are more harmful examples like methamphetamine or thalidomide. In the case of

methamphetamine, the (R)-enantiomer (R from rectus, latin for right) is used in nasal decongestant while the (S)-enantiomer (S from sinister, latin for left) is an addictive stimulant, also known as crystal meth. Thalidomide, the active substance in Contergan, was meant to be a sleep and sedatives medication but deformities of newborns were connected with this medication in the 1960s. The malefactor is the (S)-enantiomer, which was not properly separated from the sedative (R)-enantiomer.

Some Methods for Chiral Recognition

The methamphetamine and thalidomide examples show that the discrimination and separation of enantiomers is of utter importance in medicine. Unfortunately, such separation is not easy since both enantiomers are "mirror-twins" of each other and hence share almost the exact same properties like melting point, mass and dipole moment. A lot of different methods for chiral recognition have been developed over time. They all share the same general feature: to determine the type of enantiomer a chiral probe has to be used. Going back to the example of the hand, the type of hand of person A can be determined by a hand of person B (chiral probe) via a handshake (the experiment). As always, person B offers the right hand for a greeting. If person A answers with a right hand the handshake is successful and if A presents the left hand the handshake fails.

Some methods for chiral recognition are mentioned here: While Pasteur had to use a simple microscope for chiral discrimination to separate the enantiomers of tartaric acid crystals by hand [5] todays scientists can choose from a variety of chiral separation and discrimination methods. Chemical techniques use diastereomer formation, which is applied in chiral chromatography [6] and mass spectroscopy [7]. Conventional chiroptical methods for chiral discrimination include polarimetry [8], Raman optical activity [9] and circular dichroism [10]. However, the chiral response is strongly dependent on interaction with the magnetic dipole moment, which leads in general to weak signals. Thus only highly concentrated samples in solution are applicable for these techniques.

Meanwhile, a new class of chiroptical methods has emerged, which are solely dependent on interactions with the electrical dipole moment of the chiral molecule and consequently lead to a much bigger chiral response. Such techniques make chiral recognition in the gas phase feasible. These methods include microwave three-wave mixing [11, 12], Coulomb explosion imaging [13, 14] and photoelectron circular dichroism (PECD) techniques [15].

1.2. PECD in the Ionization of Neutral Molecules

In angle resolved photoelectron spectroscopy, the intensity in single photon ionization can be described as

$$I_p = 1 + b_{1,\mathrm{p}} P_1(\cos(\Theta_p)) + b_{2,\mathrm{p}} P_2(\cos(\Theta_p)) \tag{1.2.1}$$

with p being the light polarization and P being Legendre polynominals. Θ_p is the angle between the departing electron and the symmetry axis (for the PECD effect this coincides with the propagation direction of light).

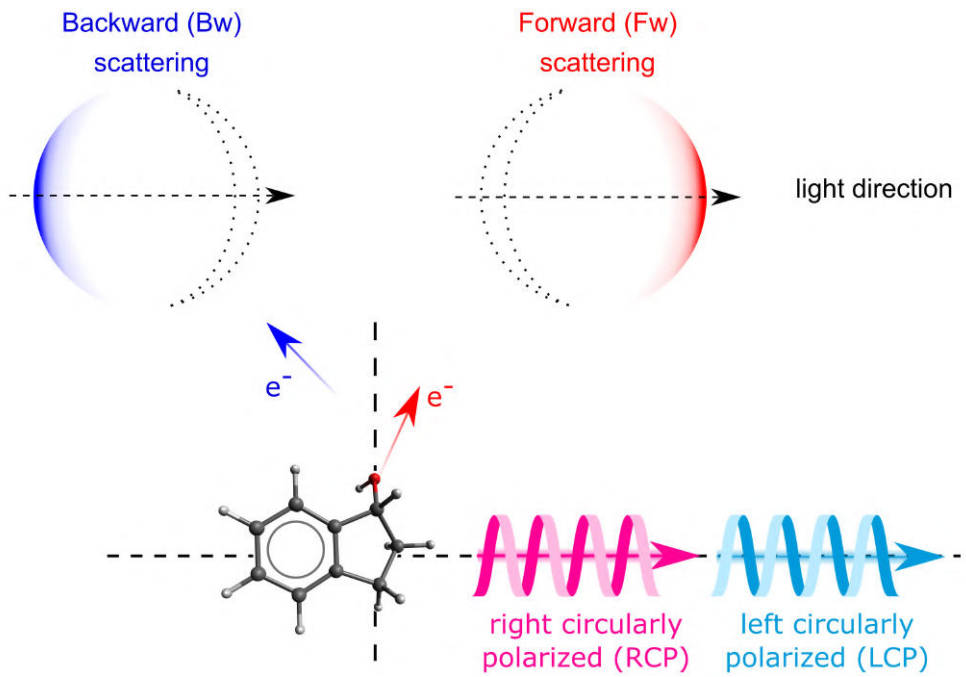

Fig. 1.2.1.: PECD principle. A chiral molecule ((R)-(-)-1-indanol) is ionized by circular polarized light. The electron is traveling either in for- or backward direction regarding the light direction and depending on the type of circularly polarized light and the used enantiomer.

For an achiral system or linear polarized light, the $b_{1,\mathrm{p}}$ term vanishes and the anisotropy parameter $b_{2,\mathrm{p}}$ (also known as β) is used to describe the intensity distribution for molecules and atoms. Ritchie showed 1976 [16] that for the special case of chiral molecules being photoionized by circularly polarized light, the $b_{1,\mathrm{p}}$ term of equation 1.2.1 does not vanish and that an asymmetry, described by the dichroism parameter $b_{1,\mathrm{p}}$, contributes to the intensity distribution. $b_{1,\mathrm{p}}$ describes an asymmetry in the forward-backward emission of emitted electrons regarding the propagation direction of the ionizing light (figure 1.2.1) and changes sign if either the enantiomer or the circular polarized light is changed (figure 1.2.2). Also, a clear dependency on the kinetic energy of the emitted electron exists. This asymmetry is now known as the PECD effect and is conventionally performed in the photoionization of neutral chiral molecules. In the following it is referred to as neutral PECD or conventional PECD.

The PECD asymmetry is a pure electrical dipole effect and does not depend on weak magnetic components, like it is the case with circular dichroism in absorption (CD). The chiral sensitivity of the PECD effect is therefore expected to be superior to CD. The first experimental confirmation was found in 2001 for the single photon ionization of 3-bromocamphor with a strength in asymmetry of 3-4% and hence confirms the superiority over CD, which typically has an effect on the order of 10^{-4} - 10^{-5}[17].

An analogous asymmetry can be found in the photoelectron angular distribution of achiral molecules like CO and N_2 or even in an atom like He [18, 19]. Such experiments require either alignment of the achiral molecules or double photoionization, like in the

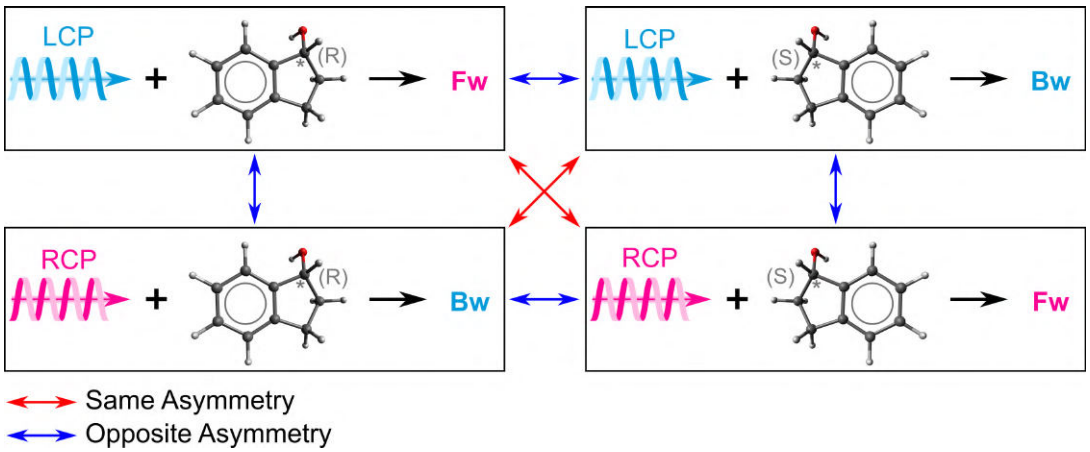

Fig. 1.2.2.: PECD asymmetry dependencies. The electron flies either in forward (Fw) or backward (Bw) direction, which defines the sign of the PECD asymmetry. The PECD asymmetry reverses sign if either the other enantiomer or the other light polarization is taken.

case of He, to show Circular Dichroism in Angular Distribution (CDAD). Neither double photoionization nor alignment of the molecules is needed in the case for chiral molecules for CDAD (or PECD). However, alignment can have an enhancing effect on the PECD asymmetry [20]. All PECD experiments presented here are performed on unoriented molecules and still provide a significant PECD effect.

Further experiments show that the PECD effect is quite stable under changes in the oscillator strength or electronic character of resonances in a multiphoton scheme. PECD asymmetries occur always for a chiral molecule, that is, the ionization regime (tunneling ionization regime, single or multiphoton) does not decide if a PECD is measured or not: the PECD effect is a universal or general effect [21–23]. The PECD effect is of pure quantum origin and can be depicted as the scattering of outgoing photoelectrons or partial waves at the remaining chiral cation [15, 20, 21, 23].

The picture of an electron probing the molecule by scattering is supported by the observation that PECD asymmetries are strongest for slow electrons and vanish completely for too fast electrons, meaning electrons with a kinetic energy of more than about 10 or 20 eV [15, 23–25]. Such electrons barely have any time to probe the chiral environment and hence will not show a PECD effect.

Structural and Vibrational Sensitivity

An outstanding feature of the PECD asymmetry is the sensitivity to the structure (isomerism, conformerism) and to even small structural changes (atomic and functional group substitution), which neither the cross section for photoionization nor the anisotropy parameter β in the case of ionization can deliver in such an extent [26]: In the case of methyloxirane, the substitution from H to F in the CH_3 group at the chiral center results in huge changes in the PECD signal of the highest occupied molecular orbital (HOMO) at low electron kinetic energies (below 3 eV) while β stays quite un-

changed [15, 27]. Even if the substitution occurs not at a chiral center, like in the case of camphor and 3-bromocamphor where an H is exchanged with Br, the PECD asymmetry shows clear differences [23]. However, the substitution for an heavy element like Br does not necessarily show an enhanced PECD effect [23].

Besides substitution, exchanging and moving groups within the molecule (isomerism) leads to different PECD asymmetries: The isomerism of isopropanolamine and alaninol can be described as the exchange of the NH_2 and the OH group. Fenchone and camphor differ from each other by moving two methyl groups to another spot in the molecule. While in the first example, the structural change happens at the chiral center, the moving of methyl groups in fenchone/camphor occurs not at a chiral center and not at the O-localized HOMO. Nevertheless, both examples show quite different PECD signals for the isomers, confirming again that PECD asymmetries are sensitive to structural changes even if the chiral center is not involved [28–31].

Even if no groups are moved or being substituted and only the orientation of groups is changed in the molecule, the PECD effect is not alike as shown for isopropanolamine and alaninol [30, 31]. Another example is the rotation of the methyl group in methyloxirane, which has shown to have a considerable influence on the PECD signal [15].

Due to the strong structural sensitivity, the amount of conformers and isomers has to be controlled in PECD experiments by either using cooled molecules or molecules with a low conformational space like fenchone [32]. If they are not accounted for, only a PECD signal averaged over all conformers is measured. This could lead to a weakened overall recorded PECD signal if the PECD signals of individual conformers compensate each other, like in the case of alanine [15, 33].

Besides structural differences, which are of static nature, dynamic processes like population in different vibrational levels can have noticeable influence on the PECD signal as well. Responsible for this dependence is the "breakdown of the FC [Franck-Condon] approximation" [34]: This approximation is based on the Born-Oppenheimer approximation and it is assumed that electron-nuclear dynamics are completely decoupled, meaning that the transition matrix elements, which govern the probability of an electronic transition are independent on the nuclear structure. Hence features of the electron continuum should be independent from the vibrations of the cation and, except for shape resonances, the PECD effect (and the β parameter) should not be sensitive to vibrational modes [15, 34]. Surprisingly, one of the first vibrationally resolved PECD experiments from Garcia *et al.* [34] could find a clear dependence of PECD signals on vibrational levels. The PECD signal can even change signs for adjacent vibrational modes. Neither the Franck-Condon approximation nor simple kinetic energy effects could explain this effect [15].

Similar to conformeric dependence, a PECD signal averaged over the vibrational levels is measured if the molecule is vibrationally excited or the spectrum is not vibrationally resolved. Especially for multiphoton experiments the vibrational excitation is important since it can involve (specific) intermediate vibronic states.

Influence of Ionized Molecular Orbital

The localization of the orbital the electron is coming from does not seem to determine the strength of a PECD signal: While orbitals of molecules like 3-bromocamphor can show a strong PECD effect for delocalized lone pairs and a weak PECD effect for localized lone pairs (localized at bromine) [17] other molecules like fenchone or camphor can also give strong PECD signals for localized lone pairs [29]. This seems counter-intuitive since an electron in a delocalized orbital should "feel" more of the molecular structure. However, there seems to be no simple correlation between the localization of orbitals and the strength of the PECD signal [23].

Furthermore, the PECD asymmetry has been observed in detachment from both core and valence orbitals. Most intriguing are the core orbitals since they are of s character (symmetric) and hence should not contribute to an asymmetry. Consequently, PECD asymmetries at core levels indicate that the PECD effect is a final state effect [1, 20, 23, 24, 31]. On the other hand, PECD asymmetries are also dependent on the initial state as seen from PECD effects arising in valence level ionization [23, 29, 31, 33].

Some PECD Methods

PECD measurements can be performed with hemispherical analyzers like it is done in the first PECD experiments and this method is still in use today [17, 35–37]. In hemispherical analyzers chiral probes can be used in gas [17, 35], liquid phase (e.g. fenchone) [37] and aqueous solution [36]. The liquid state is the "natural" state of many chiral substances under environmental conditions and reflect conditions of biological systems better than e.g. the gas phase. However, the hemispherical analyzer is restricted in the angles it can cover. Mostly, the magic angle (around 54.7°) is used to avoid anisotropy affecting the measured intensities. In contrast to the hemispherical analyzers, a VMI spectrometer can not handle the liquid phase well (so far) [36]. On the other hand, the combination of PECD experiments and velocity map imaging (VMI) spectroscopy not only provides nice VMI-images but also allows to record the PECD signal over all angles [15]. The experiments here are performed in gas phase and the combination of PECD experiment and VMI spectroscopy is preferred to obtain the full-angle PECD signals.

Since conventional PECD experiments are focused on the ionization of neutrals, either synchrotron facilities or complex ionization schemes like multiphoton ionization have to be employed. Synchrotron radiation can ionize the neutral molecules via single photons and avoids the complex multiphoton processes but a special facility and beam time are needed to perform the experiments. Such experiments include coincidence techniques where photoelectrons and ions are detected coincidentally, like the photoelectron-photoion coincidence (PEPICO) experiments [15, 38].

Multiphoton processes on the other hand can be studied in the home laboratory with fs- or ns lasers [21, 39, 40]. Experiments using the multiphoton technique involve intermediate states, which influences the PECD signal since the strength in asymmetry can change depending on the involved states. Theoretically, if certain intermediate

states are carefully selected, a PECD signal of 68% could be possible, but this needs good quantum control of the system and has so far not been shown experimentally [41]. Resonantly enhanced multiphoton ionization (REMPI) is one example for multiphoton experiments. REMPI is molecule selective since the initial resonant photoabsorption has to match a specific transition energy of the molecule. However, this scheme can be quite complicated and the role of intermediate states in the PECD effect are not immediately clear [21, 39]. Further multiphoton experiments involve coincidence techniques, which enables mass selective experiments [29, 42, 43] and even asymmetry measurements on electrons and ions (PICD) [44]. It is important to mention that all ion detection and hence the mass selections happens after ionization of the neutral molecules.

Further PECD experiments concentrate on enantiomeric excess measurements, which can be facilitated by measuring forward and backward emitted electrons at the same time [45] or by utilizing elliptical polarized light [46]. Also, clustering shows a noticeable influence on the PECD signal like it is demonstrated for glycidol clusters [47].

PECD experiments with anions is a relatively new method, which emerged in the recent years and involves mass selection before photodetachment, a relatively simple laser system and a single photon process [2, 3, 48]. The ideas, challenges and advantages of this experiment are described in more detail in section 1.3 but on a fundamental perspective, it will be able to reveal the influence of short range interactions between electron and molecule in contrast to long range interactions.

Summary

Conventional PECD on neutrals is an important technique to probe structures of chiral molecules and to determine the enantiomer at hand. Many studies tried to reveal the nature of the PECD effect by investigating its properties, which can be summarized as:

1. Universal effect: every chiral molecule should show a PECD asymmetry. The PECD effect can be understand as scattering of the emitted electron in the potential of the chiral molecule. The ionization regime does not determine if a PECD asymmetry exists or not.

2. Depends on the kinetic energy. Slow electrons (around $E_{\mathrm{kin}} < 10$ eV) are needed to measure a PECD signal since the chiral molecule has to be probed.

3. Sensitive to the structure of the whole molecule (involvement of chiral center not necessary)

4. Sensitive to vibrational level

5. Localization of electron does not correlate with PECD strength

6. Initial and final state effect (valence and core level)

7. Alignment not necessary but would enhance effect

8. No clear dependence on heavy elements like Br

Considering the measurement of any PECD effect, the universality of the PECD asymmetry gives a lot of freedom for theoretical and experimental designs. Experimental setups can e.g. include single- or multiphoton setups and (apart from chirality) there are no (strict) restrictions on molecular properties (in context of the PECD effect). A PECD signal should always appear if the molecule is chiral and the electrons are slow enough. The details about e.g. strength and kinetic energy dependency will be determined by the experimental method and choice of molecule.

The high sensitivity of the PECD asymmetry on structural differences makes this effect an important tool to unambiguously identify the exact molecule at hand, if the molecule can coexist as different conformers. Especially enantiomers can be differentiated. The vibrational dependency can help to determine the internal energy of the molecule.

Unfortunately, there is a downside: A missing obvious correlation between the strength of the PECD signal and molecular properties makes it difficult to "cherry-pick" chiral molecules or systems. Even if a molecule is chosen in context of the PECD effect, the conformeric space and vibrations need to be controlled since averaged PECD signals can be weaker than individual ones. All these make conventional PECD experiments to a complex problem, which requires proper control of the experiment. The same problems could emerge for the PECD effect in photodetachment.

1.3. PECD in Photodetachment or Anion PECD

In this thesis, PECD spectroscopy is performed not on neutral molecules but on chiral anions. The main difference is the detachment of an excess electron, which leaves behind not a cation but a neutral core. The consequence is a missing long range Coulomb potential from a monopole charge (cation core), leaving only short range potentials originating from, for example, dipole interactions. Such a system would reveal the importance of short range interactions on the PECD effect.

Furthermore, anionic systems enable mass selection before photodetachment and facilitate the removal of the electron since electron affinities are in general smaller than ionization energies. This leads to the simplification of the used laser systems and processes: Complex laser systems, like synchrotron radiation sources, can be replaced with simpler ones, like nanosecond table top lasers. Furthermore, single photon processes can be used instead of multiphoton schemes.

Up until recently, PECD studies were focused on neutral chiral molecules. It was not clear if PECD asymmetries for chiral anions can be experimentally detected or even exist since photodetached electrons were described as plane waves [49], which can not carry an asymmetry. Neither experimental nor theoretical studies were available to this topic for a long time and also when this project started. However, one study from Dreiling *et al.* [50] already gave hope for a working PECD effect in photodetachment. In this study, the quasi-elastic scattering of spin-polarized electrons on neutral 3-bromocamphor lead to an asymmetry in electron transmission in the range of 10^{-4}, hence, proving that electrons can be scattered on a neutral chiral core and still pickup (detectable) chiral asymmetries. If the PECD effect on neutrals is seen as scattering process, then PECD

asymmetries could also occur in chiral anions, where the electron interacts with the remaining neutral core.

Experimental and theoretical studies for PECD asymmetries on anions emerged in the last few years. The first experimental conformation came from Krüger *et al.* who found a PECD effect for anionic (2S)-2-amino-3-(3,4-dihydroxyphenyl)propanoic acid (L-DOPA) and glutamic acid of around 4.6 and 3.6%, respectively [2]. In a subsequent study, they also found a PECD asymmetry of around 0.5% for the peptide gramicidin [3]. Unfortunately, both experimental studies do not provide any energy dependence or resolution of the PECD effect since only a split electron detector and only one photon energy (355 nm) were used to determine the difference between for- and backward emitted number of electrons. In a theoretical study from Artemyev *et al.* [4] a simple model of a chiral molecule is designed and a non-vanishing anion PECD effect is calculated.

Our studies started years before the publication of theoretical and experimental proof by Artemyev and Weitzel. The problem at this time was the choice of a good chiral molecule or chiral system, which creates a (strong) PECD effect in photodetachment. As already described for conventional PECD asymmetries, the chemical or physical rules to determine the (ideal) molecule with a good PECD signal are not yet known. In the end, several anionic systems like various gold complexes (chiral molecule + Au^-) and deprotonated molecules have been studied. Of these, only deprotonated 1-indanol showed a significant PECD effect [48].

1.4. Outline of this thesis

The main focus of this work lays in the search for a PECD effect in the two classes of chiral anions, namely gold complexes and deprotonated molecules. First, for this thesis relevant scientific background is given in chapter 2. It covers briefly basics of molecular structure, photodetachment, selection rules and angular distributions always in comparison of linear and circular polarized light. The scientific conventions for determining (R)- and (S)-enantiomers of chiral molecules and the polarization of light (left circular polarized (LCP) or right circular polarized (RCP)) complete this chapter.

Experimental and computational methods are presented in chapter 3. The experimental methods summarize the setup, an illustration of the choice of molecules and tools for analysis. Finally, density functional theory (DFT) is described and relevant energies are defined.

The following two chapters present the experimental results, analysis and discussion of the gold complexes (chapter 4) and the deprotonated chiral molecules (chapter 5). The chapters are subdivided in a similar way to not only show the results for PECD asymmetries but also present mass spectra, photoelectron spectra measured with linear polarized light and DFT calculations. Next to PECD asymmetries, the focus in the chapter for the gold complexes is also on hydrogen bonding. Parts of these chapters are already published in [51] and [48].

The last chapter summarizes this work and gives an outlook for PECD asymmetries on anions.

2. Scientific Background

2.1. Molecular Structures

Many molecules have the same molecular formula but are composed in different ways. Such molecules have different properties only due to their structure and are called isomers. Depending on how the molecules are structured they can be subdivided in further groups from which some are shown in figure 2.1.1. Here, the main focus is on the enan-

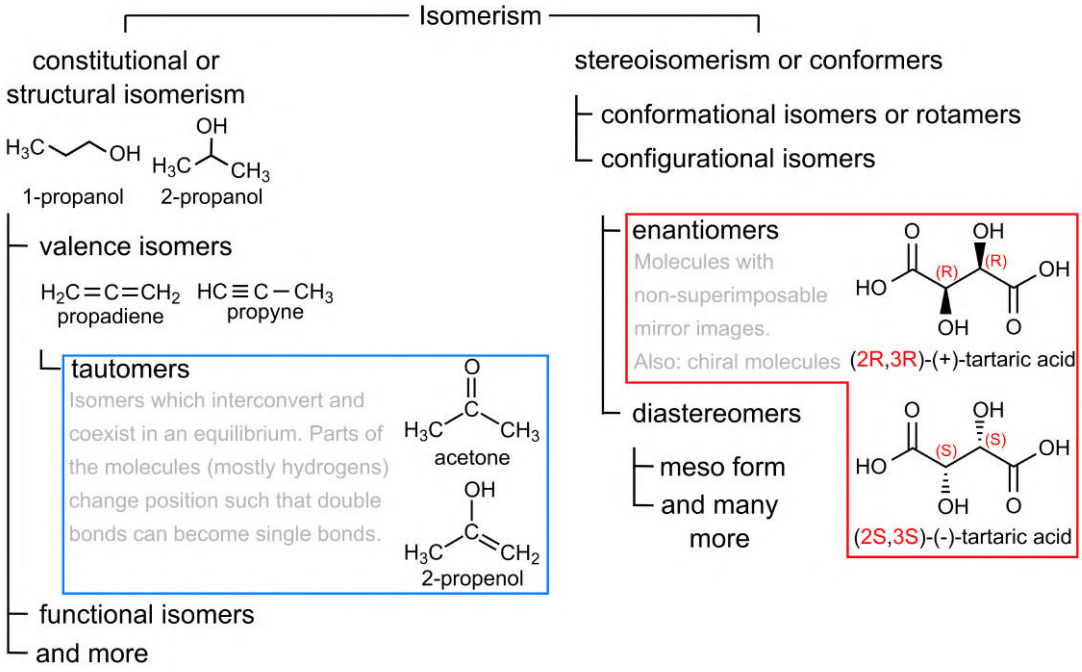

Fig. 2.1.1.: Different categories of isomers with some examples. Tautomers and enantiomers are highlighted since they are important for this work.

tiomers or chiral molecules. They belong to the stereoisomers (same connectivity but different shape) and configurational isomers (isomers, which can not be interconverted by rotating the molecule around a single bond). One famous example for a chiral molecule is tartaric acid, which shows two enantiomers (figure 2.1.1)[1].

However, other forms like tautomers are also present in the experiments. They belong to the constitutional isomers (same molecular formula but different connectivity)

[1]Tartaric acid can also be (2R,3S)-tartaric acid but it is not chiral anymore and belongs to the diastereomers.

and valence isomers (isomers, which differ in the amount and/or position of σ- and π-bonds). Acetone and 2-propenol are examples for tautomers since an hydrogen – and consequently a double bond – changes the position. In this work, tautomers become important when a chiral molecule is deprotonated.

2.2. Anion Photoelectron Spectroscopy

Photoelectron detachment refers to the extraction of the excess electron e^- from an anion M^- with photons that have an energy of at least the electron affinity (EA). If the anion is singly charged, the corresponding neutral M is probed (equation 2.2.1).

$$M^- \xrightarrow{h\nu} M + e^- \tag{2.2.1}$$

The electron's kinetic energy complies with energy conservation

$$E_{B,i} = h\nu - E_{kin,i} \tag{2.2.2}$$

with $E_{B,i}$ being the binding energy of the i-th state, the corresponding electron kinetic energy $E_{kin,i}$ and the photon energy $h\nu$.

Equation 2.2.2 is valid for isolated atomic systems. If molecules are considered, the binding energy will not only describe electronic transitions but also contributions from vibrations and rotations.

In figure 2.2.1, the photodetachment process is illustrated for a molecule: The photon with an energy of $E_{ph} = h\nu$ detaches the excess electron and forms a neutral molecule, which can be in a ground (M) or excited state (M^*). The electron probes the neutral molecule and a measurement of its energy distribution (e.g. in form of photoelectron spectrum/spectra (PES)) gives information about the (excited) states of the neutral molecule. In a PES the measured quantity is (basically) the kinetic energy. However, PES are often plotted over the electron binding energy rather than the kinetic energy since it is independent from the chosen photon energy.

Experimentally, and as indicated in figure 2.2.1, not all transitions allowed by equation 2.2.2 have the same intensity or are observable. In other words, the transition probability varies for different states. In general, this probability or intensity variations need to consider momentum conservation and symmetry principles next to the energy conservation (equation 2.2.2). This leads to quite simple selection rules, which determine if a transition is allowed or how probable the transition is. In the end, information about geometry changes between anion and neutral configuration can be gained from this.

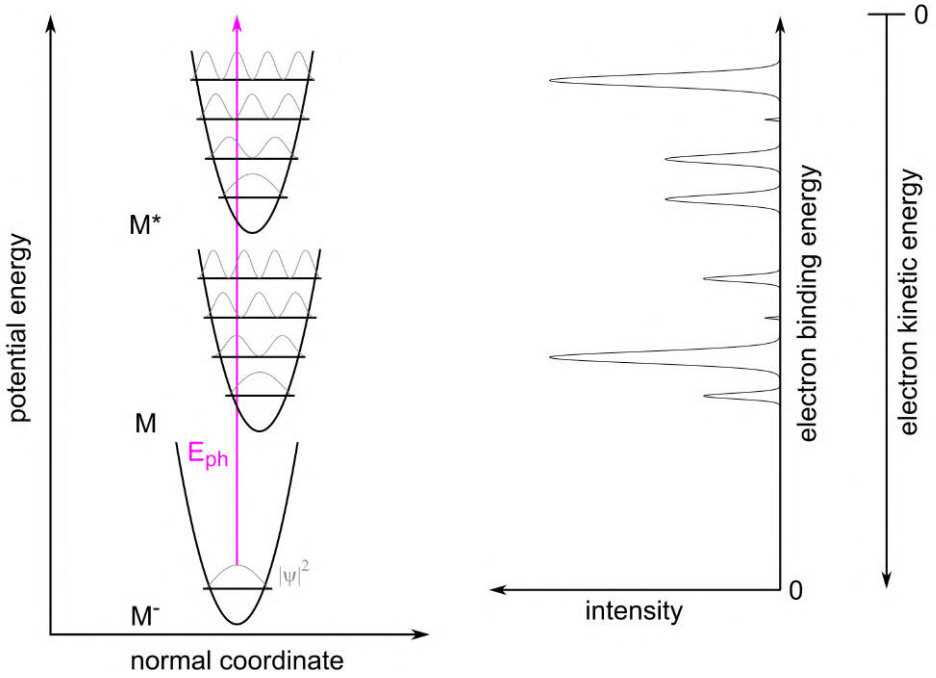

Fig. 2.2.1.: Energy diagram (left) and corresponding spectra (right) for anion photoelectron spectroscopy on a molecule. A photon with energy E_{ph} detaches an electron from the anion M^-. Thereby the electronic ground state M and excited states M^* of the neutral as well as various vibrational states (black lines) can be probed. The intensity is described by the Franck-Condon principle and determined by the overlap of the absolute squares of the wave functions. Rotational levels are not shown.

2.2.1. Selection Rules and Transition Probabilities in Photoelectron Detachment

The probability of a transition from state i to k is determined by the transition dipole moment $\mathbf{M}_{ik}$. Only for non-zero values the transition is allowed. The conditions leading to non-zero values are the selection rules for which the important steps of their derivation are given here.

The following derivation uses the dipole approximation, which is valid for light with a wavelength much larger than the dimensions of the dipole (e.g. the molecule). The transition dipole moment is defined as

$$\begin{pmatrix}(M_{ik})_x\\(M_{ik})_y\\(M_{ik})_z\end{pmatrix} = e \cdot \int \psi_i^* \begin{pmatrix}x\\y\\z\end{pmatrix} \psi_k \mathrm{d}\vec{r} \tag{2.2.3}$$

with ψ_i^* being the complex conjugated initial state wave function, ψ_k the final state wave function, e the charge of the detached electron and $\mathrm{d}\vec{r} = \mathrm{d}x\mathrm{d}y\mathrm{d}z$.

The requirement for one of the components of $\mathbf{M}_{ik}$ being non-zero is demonstrated for the hydrogen atom (H) in the following. Furthermore, the spin is neglected for now.

The resulting selection rules are of course not restricted to the H atom but can be also shown for the general case.

Usually, spherical coordinates (r,ϑ,ϕ) with a radial component r, a polar angle ϑ and an azimuth angle ϕ are used to solve problems with the hydrogen atom since it catches the symmetry of the system in a better way than e.g. the Cartesian system. If furthermore the spherical symmetry of the H atom is used the wave function can be separated in two parts: the radial function $R_{n,l}(r)$ and spherical harmonic functions $Y_l^m(\vartheta,\phi)$, which are solutions of the radial and angular part of the Schrödinger equation. n, l and m denote the principal, azimuthal and magnetic quantum number, respectively.

With $Y_l^m(\vartheta,\phi) = 1/\sqrt{2\pi}\theta_m^l \cdot \mathrm{e}^{\mathrm{i}m\phi}$ the wave function of the H atom can be written as

$$\psi_{n,l,m} = \frac{1}{\sqrt{2\pi}} R_{n,l}(r)\theta_m^l(\vartheta) \cdot \mathrm{e}^{\mathrm{i}m\phi} \tag{2.2.4}$$

with n_i, l_i and m_i being the quantum numbers for the i-th state. The quantum numbers for the k-th state are noted correspondingly.

2.2.1.1. Polarized Light

If linear polarized light with $\vec{E} = (0,0,E_0)$ is interacting with the H atom, the z component of $\mathbf{M}_{ik}$ can be written as

$$\begin{aligned}(\mathbf{M}_{ik})_z = \frac{e}{2\pi} &\int_{r=0}^{\infty} R_i R_k r^3 \mathrm{d}r \\ &\cdot \int_{\vartheta=0}^{\pi} \theta_{m_k}^{l_k}\theta_{m_i}^{l_i} \sin(\vartheta)\cos(\vartheta)\mathrm{d}\vartheta \\ &\cdot \int_{\phi=0}^{2\pi} \mathrm{e}^{\mathrm{i}(m_k-m_i)\phi}\mathrm{d}\phi\end{aligned} \tag{2.2.5}$$

with $z = r\cos(\vartheta)$.

If circular polarized light (CPL) propagates in z direction with an amplitude of $E = E_x + \mathrm{i}E_y$, the complex linear combinations of the x and y component are considered

$$\begin{aligned}(\mathbf{M}_{ik})_x \pm \mathrm{i}(\mathbf{M}_{ik})_y = \frac{1}{2\pi} &\int_{r=0}^{\infty} R_i R_k r^3 \mathrm{d}r \\ &\cdot \int_{\vartheta=0}^{\pi} \theta_{m_i}^{l_i}\theta_{m_k}^{l_k} \sin^2(\vartheta)\mathrm{d}\vartheta \\ &\cdot \int_{\phi=0}^{2\pi} \mathrm{e}^{\mathrm{i}(m_k-m_i\pm1)\phi}\mathrm{d}\phi\end{aligned} \tag{2.2.6}$$

with $x = r\sin(\vartheta)\cos(\phi)$ and $y = r\sin(\vartheta)\sin(\phi)$.

2.2.1.2. Selection Rules

Magnetic Quantum Number m In the case of linear polarized light the last factor of equation 2.2.5 is non-zero for

$$\Delta m = m_i - m_k = 0 \tag{2.2.7}$$

The selection rule for the magnetic quantum number changes for CPL with either left or right polarized light (LCP and RCP) to

$$\Delta m = m_i - m_k = \begin{cases} +1 & \text{for LCP} \\ -1 & \text{for RCP} \end{cases} \tag{2.2.8}$$

since only here the last factor of equation 2.2.6 is not zero.

The selection rules in equation 2.2.7 and 2.2.8 are a result of the conservation of the total angular momentum: Circular polarized light propagating in z direction either carries a photon momentum of $+\hbar$ for LCP or -$\hbar$ for RCP. Hence, the z component of the atom angular momentum has to change by either $+\hbar$ or -$\hbar$ after photon absorption. If linear polarized light is considered to be a superposition of LCP and RCP both photon momenta cancel each other and m remains unchanged.

Parity Selection Rule or Selection Rule for the Angular Momentum l Let's consider the transition dipole moment in Cartesian coordinates and rewrite equation 2.2.3

$$\mathbf{M}_{ik} = e \cdot \iiint_{-\infty}^{\infty} f(x,y,z)\mathrm{d}x\mathrm{d}y\mathrm{d}z \tag{2.2.9a}$$

$$\text{with } f(x,y,z) = \psi_i^* \, \vec{r} \, \psi_k \tag{2.2.9b}$$

Integrals of the form as seen in equation 2.2.9a are always zero if $f(x,y,z)$ is an uneven function of (x,y,z) (meaning $f(x,y,z) = -f(-x,-y,-z)$). To achieve an even function the product $\psi_i^* \cdot \psi_k$ must be an uneven function since $\vec{r} = (x,y,z)$ is already an uneven function.

Another word for (un)even function is parity. An uneven function corresponds to odd parity while the even function refers to even parity. Consequently, ψ_i and ψ_k must have different parity for an allowed transition.

For a wave function of the hydrogen atom the parity is $(-1)^l$. Hence, l has to change by an odd value for an allowed transition. Since a photon only carries one $\hbar$, the selection rule is

$$\Delta l = l_i - l_k = \pm 1 \tag{2.2.10}$$

This selection rule is valid for linear and circular polarized light and is connected to the conservation of angular momentum: If a photon with a momentum of $\hbar$ is absorbed, the atom angular momentum must change accordingly. For a many-electron system with weak spin-orbit coupling, this selection rule changes to $\Delta L = \pm 1$ with the total angular momentum $L = \sum_i l_i$.

The second term in the transition dipole moment in spherical coordinates (equation 2.2.5) is only non-zero if equation 2.2.10 holds.

Selection Rule for Spin For the sake of completeness, the selection rule for the spin is given. For a small spin-orbit coupling

$$\Delta S = S_i - S_k = \pm\frac{1}{2} \tag{2.2.11}$$

with the total spin $S = \sum_i s_i$ is valid. In other words, the spin multiplicity $2S + 1$ must change by ± 1. This means that the remaining neutral core must change its spin to compensate for the spin the departing electron carries away.

For heavier atoms like Au, relativistic effects result in a strong spin-orbit coupling and the selection rule changes to

$$\Delta J = J_i - J_k = \pm\frac{1}{2}, \pm\frac{3}{2} \tag{2.2.12}$$

with the total momentum $J = L + S$ (L-S coupling) or $J = \sum_i j_i$ with $j_i = l_i + s_i$ (jj-coupling). Normally, jj-coupling is used for atoms with $Z > 40$, which includes Au ($Z = 79$).

Summary The selection rules for the dipole approximation are summarized in table 2.2.1. Under these conditions the transition dipole moment does not vanish and a peak can emerge in the PES.

Table 2.2.1.: Summary of the selection rules in dipole approximation. Transitions fulfilling these conditions are considered "allowed", others forbidden.

Selection rule	comments
$\Delta l = \pm 1$	for one electron systems
$\Delta L = \pm 1$	for many electron systems with $L = \sum_i l_i$
$\Delta M = 0$	for linear polarized light
$\Delta M = \pm 1$	+1 for LCP and -1 for RCP
$\Delta S = \frac{1}{2}$	for weak spin-orbit coupling
$\Delta J = \pm\frac{1}{2}, \pm\frac{3}{2}$	for strong spin-orbit coupling

2.2.1.3. Transition Probability

The transition probability determines the intensity of a transition and can be given by the golden rule of Fermi

$$I \sim |\mathbf{M}_{ik}|^2 \cdot \rho(E_{\mathrm{B},i}) \cdot \delta(\Delta E - h\nu) \tag{2.2.13}$$

with $\rho(E_{\mathrm{B},i})$ being the density of the final states and ΔE being the energy difference between initial and final state. Basically, the delta function $\delta(\Delta E - h\nu)$ is another expression for the conservation of energy in equation 2.2.2 for photoelectron spectroscopy.

The matrix elements of the transition dipole moments defines the probability or intensity I of a transition. Transitions fulfilling the selection rules are referred to as allowed transition (in the dipole approximation) and will most probably lead to high intensities. Besides allowed transitions, transitions, which are forbidden in the dipole approximation could emerge in the spectrum but are of much lower intensity or are less probable. Such transitions could originate from e.g. magnetic dipole transitions or electric quadrupole transitions.

2.2.1.4. Franck-Condon Principle

The principle known today under the name Franck-Condon principle (or short FC principle) was first described 1926 for photoreactions by James Franck [52] and extended by Edward Condon in the same year [53]. It describes transition probabilities between different vibrational states and hence can be used for predicting the intensity of a transition. The Franck-Condon factor is given in equation 2.2.14.

$$\mathrm{FC}(\nu_i, \nu_k) = \left| \int \psi_{\mathrm{vib}}(\nu_i)\psi_{\mathrm{vib}}(\nu_k)dR \right|^2 \tag{2.2.14}$$

The principle is based on the assumption that electronic transitions happen immediately in comparison to nuclei movements (Born-Oppenheimer approximation). An vibronic transition becomes more probable/intense the more the vibrational wave functions of both contributing states overlap or in other words if the maximum of both wave functions are at (almost) the same position to the core (figure 2.2.1). In the special case of no change between the potential curves of different electronic states (meaning minima at the same core distance or according to figure 2.2.1 at the same normal coordinate) transitions with $\nu_i - \nu_k = 0$ are most probable and will give the highest intensity. If the potential curves are different other transitions will become more probable.

2.2.2. Photoelectron Angular Distribution

Apart from energy information (binding energy E_{B}) the angular distribution can be obtained by certain spectrometers like the VMI spectrometer. In this angular distribution, anisotropies can occur, which give information about the orbital from which the electron departed after photodetachment. For linear polarized light, the parameter describing the anisotropy has been described by many researchers [54–57]. However, here, the focus of the anisotropy parameter is mainly based on the work of Sanov *et al.* [58–61].

In general, the angular distribution can be described by

$$\frac{d\sigma}{d\Omega} = \frac{\sigma_{\text{tot}}}{4\pi}(1 + \sum_{n=1}^{2n} b_n P_n(\cos(\Theta))) \tag{2.2.15a}$$

$$\rightarrow I(\Theta) \sim 1 + \sum_{n=1}^{2n} b_n P_n(\cos(\Theta)) \tag{2.2.15b}$$

with P_n being the n-th Legendre polynomial, $\frac{d\sigma}{d\Omega}$ the differential cross section, σ_{tot} the total cross section and I(Θ) the corresponding signal intensity depending on the angle Θ, which is measured between the electron flight path and the symmetry axis of the system. Equation 2.2.15 is valid for non-chiral and chiral systems, which are photodetached by n-photons. For the case of linear polarized light, the symmetry axis is the polarization axis of the electrical field component. Circularly polarized light uses the direction of the light as symmetry axis [62, 63].

If only single photon detachment (n=1) is considered and p is introduced as light polarization index (p =linear polarized (LIN), p =LCP, RCP) the equation is reduced to equation 1.2.1 from chapter 1.2:

$$I_p = 1 + b_{1,\text{p}} P_1(\cos(\Theta_p)) + b_{2,\text{p}} P_2(\cos(\Theta_p)) \tag{2.2.16}$$

Considering the different polarizations, the dichroism parameter b_1 and the anisotropy parameter b_2 have the following relationship [62, 63]:

$$b_{1,\text{LIN}} = 0 \tag{2.2.17a}$$

$$b_{1,\text{LCP}} = -b_{1,\text{RCP}} \tag{2.2.17b}$$

$$b_{2,\text{LCP/RCP}} = -\frac{1}{2} b_{2,\text{LIN}} \tag{2.2.17c}$$

From now on, b_2 will be mostly written as β and either called β- or anisotropy parameter to be consistent with literature [54, 58].

2.2.2.1. Anisotropy Parameter

An equation for the anisotropy parameter β was derived by Bethe [64] and generalized by Cooper and Zare [54] for atomic or atomic-like systems that experience photodetachment with linear polarized light. By restricting the problem to low kinetic energies, Hanstrop *et al.* [57] could use the Wigner threshold law [65]

$$\sigma \sim E_{\text{kin}}^{l+1/2} \tag{2.2.18}$$

to simplify the equation for β. E_{kin} is the kinetic energy of the departing electron and l is the orbital angular momentum from which the electron originates. Technically, equation 2.2.18 applies for all l but just small l like $l = 0$ or 1 produce relevant cross sections in the threshold limit for low kinetic energies ($E_{\text{kin}} < 1$ eV).

The simplified version for β is also called β in the Cooper-Zare-Hanstrop (CZH) formulation and is given as

$$\beta_{\mathrm{CZH}}(E_{\mathrm{kin}}) = \frac{l(l-1) + (l+1)(l+2)A^2E_{\mathrm{kin}}^2 - 6l(l+1)AE_{\mathrm{kin}}\cos(\delta_{l+1} - \delta_{l-1})}{(2l+1)(l+(l+1)A^2E_{\mathrm{kin}}^2)}] \tag{2.2.19a}$$

$$AE_{\mathrm{kin}} = \frac{\chi_{\mathrm{l,l+1}}}{\chi_{\mathrm{l,l-1}}} \tag{2.2.19b}$$

with $\delta_{l+1} - \delta_{l-1}$ being the phase shift originating from the interaction of the electron with the neutral atom after photodetachment. The parameter A is a proportionality coefficient for the ratio of the radial matrix elements χ of the outgoing partial waves $l\pm1$ and has the unit of a reciprocal energy. Since A was introduced by Hanstrop *et al.* [57], it is referred to as Hanstrop parameter.

In a figurative way, the Hanstrop parameter reflects the spatial extent of the anion wave function and is sensitive to the diffusivity of the long-range tail of that wave function. It roughly correlates with the size of the atom, e.g., the Hanstrop parameter of O^- and C^- are 0.55 eV^{-1} and 0.75 eV^{-1}, respectively and correspond to the relative sizes of the anions [58]. Apart from the size of the anion the relative electron affinities give a hint of the size of the Hanstrop parameter since lower EA tend to more diffuse tails (EA of O^- is 1.46 eV and EA of C^- is 1.26 eV) [58].

In order to guarantee a positive intensity (or cross section) in equation 2.2.16 for linear polarized light, β has to be restricted between the values -1 and 2. $\beta = 2$ is achieved for the case of $l = 0$ (s-orbital). Furthermore, this is the only case where β is independent of the kinetic energy and is a constant. Negative values, especially β = -1, are determined by the strength of the interference term $-6l(l+1)AE_{\mathrm{kin}}\cos(\delta_{l+1} - \delta_{l-1})$ (equation 2.2.19a) relative to the other non-interference terms.

2.2.2.2. s-p Mixing Model from Sanov

For molecules and complexes no l can be given due to the "mixing" of orbitals. Hence, equation 2.2.19a is not valid anymore. A proper way to obtain β for molecules is to apply the s-p mixing model from Sanov [58]. As for β for atomic and atomic-like systems (2.2.19a), Sanov developed his model for the low kinetic energy regime and could define a parameter for the outgoing partial waves similar to the Hanstrop parameter from equation 2.2.19b. Being in the low kinetic energy regime, Sanov restricts the model for $l = 0$ (s-orbital) and $l = 1$ (p-orbital) since here only small l create measurable cross sections according to Wigners law 2.2.18. Furthermore Sanov uses the central-atom approximations, meaning the detachment happens predominantly at one atom. The β parameter in this model is then given as

$$\beta_{\mathrm{sp}}(E_{\mathrm{kin}}) = \frac{2(1-f)BE_{\mathrm{kin}} + 2fA^2E_{\mathrm{kin}}^2 - 4fAE_{\mathrm{kin}}\cos(\delta_2 - \delta_0)}{(1-f)BE_{\mathrm{kin}} + 2fA^2E_{\mathrm{kin}}^2 + f} \tag{2.2.20a}$$

$$AE_{\mathrm{kin}} = \frac{\chi_{1,2}}{\chi_{1,0}} \tag{2.2.20b}$$

$$BE_{\mathrm{kin}} = \frac{\chi_{0,1}}{\chi_{1,0}} \tag{2.2.20c}$$

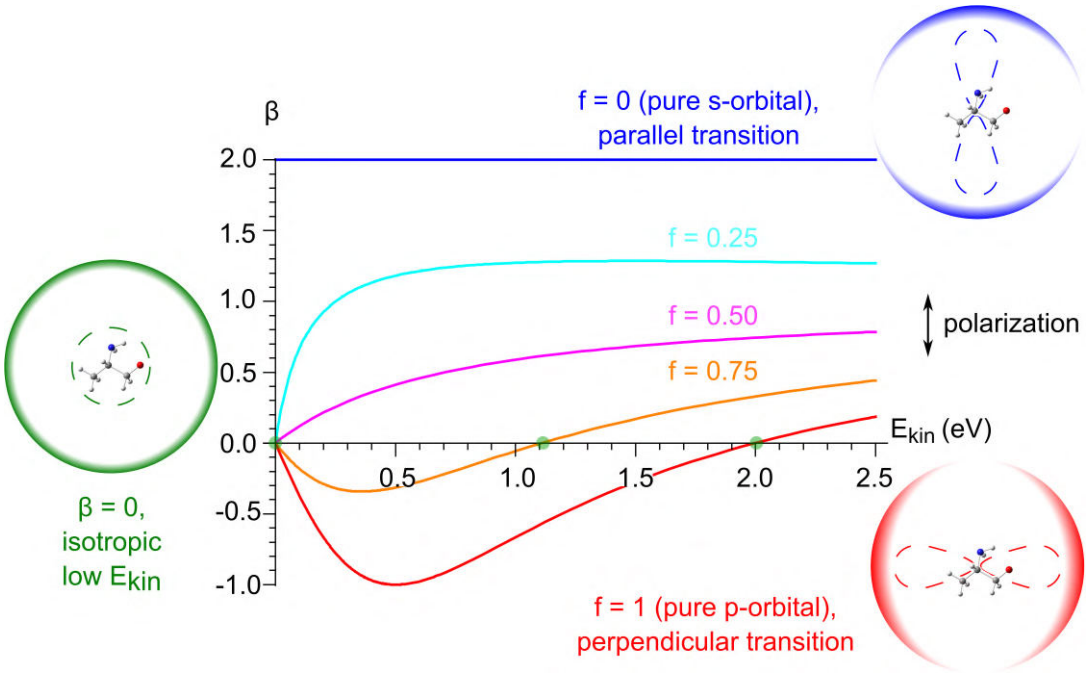

Fig. 2.2.2.: The anisotropy parameter β as a function of the kinetic energy plotted with the s-p mixing model of Sanov (equation 2.2.20a). The curves correspond to different fractional p character f. For this plot $A = 1$ and $B/A = 8/3$ are set arbitrarily. Next to the plot, the corresponding photoelectron angular distribution (PAD)s for the limits $\beta = 2$ (blue half moons) and -1 (red half moons) are shown. The special case of $\beta = 0$ creates a circular PAD (green) and is reached for tiny kinetic energies or for zero-crossings (green transparent ball). Dashed contour lines indicate the s and p partial waves of the departing electron. There are parallel (blue) and perpendicular (red) transitions regarding the light polarization (black arrow). A similar figure can be found in [58].

The parameter A describes the $p \to d$ and $p \to s$ photodetachment channels like the Hanstrop parameter. The newly introduced parameter B is used for the $s \to p$ and $p \to s$ channels. f is the fractional p character of the orbital and describes the "amount of p-orbital" in the s-p mixed molecular orbital. It ranges from 0 (pure s-orbital) to 1 (pure p-orbital) and reduces β_{sp} for $f = 0$ or 1 to β_{czh} with $l = 0$ (s-orbital) or $l = 1$ (p-orbital).

f can be gained from an orbital composition analysis. The ratio B/A depends on the participating orbitals as well as the effective nuclear charges and can be calculated to some extent if these orbitals are known [55, 59]. B, A or the nuclear charges need to be determined by fitting the experimental data to the model of Sanov.

A visualization of equation 2.2.20a is given in figure 2.2.2. The effect on the angular distribution is given next to the plot, dependent on the light polarization. These distributions can be imaged if a VMI spectrometer is used.

Since the *s*-*p* mixing model from Sanov is developed for low kinetic energies, the question of a limiting kinetic energy arises. In general, the model becomes more inaccurate for higher kinetic energies but can still be considered accurate in the range of $E_{\text{kin}} < 1$ eV according to Wigner's law. However, according to Sanov *et al.* [59][2], the model can be applied to a wider energy range of $E_{\text{kin}} < 5$ eV due to the use of ratios rather than absolute numbers. In this thesis, the used energy range is $E_{\text{kin}} < 3.4$ eV.

For photodetachment it is assumed that the electron does not interact (in a noticeable way) with the neutral atom or molecule. Hence, in both anisotropy parameter β_{CZH} and β_{sp} no phase shift between the partial waves ($\cos(\delta_2 - \delta_0) = \cos(\delta_{l+1} - \delta_{l-1}) = 1$) exists. However, for some systems, e.g., I^- [61], O^- [57] and O_2^- [66] it is appropriate to assume a small interaction ($\cos(\delta_2 - \delta_0) = 0.86 - 0.96$) to match the model better to the experimental data [58]. Such interactions could arise from many-electron correlations (between departing and remaining electrons) or via the polarizing field of the departing electron on the neutral molecule [67].

Apart from electron correlations and polarizing fields, the departing electron can interact with the dipole moment of the neutral core μ. However, instead of adjusting the phase shift parameter, the Cooper-Zare model is expanded to the case of dipole moments [61]. The β parameter is dependent on μ and still reaches the value 2 for detachment from the *s*-orbital.

Before evaluation of the β parameter, the type of molecular orbitals can be estimated by their shape and defined more precisely with an orbital composition analysis. For some molecules, like ortho-pyridinide, the shape of the molecular orbital of interest resembles an atomic *d*-orbital. For such orbitals, the *s*-*p* mixing model from Sanov is not sufficient and the model has to be expanded to *d*-orbitals [56, 68].

With the central-atom approximation, the *s*-*p* mixing model can fail for system like CS^-, which are not approximated by a central atom. These cases have to be treated differently [60]. Systems with molecules that are solvated with a heavy anion like iodine are best suited for this model since the heavy atom iodine can be used as central atom [61]. Among the systems investigated here, chiral molecules are solvated with the (heavy) anion gold. With gold acting as central atom, the central-atom approximation can be used and hence the *s*-*p* mixing model by Sanov is suited to describe this kind of systems. However, the systems solvated with iodine and gold anions need to consider the dipole moment to model the β parameter exactly. In the case of the iodine systems, the experimental data might not be perfectly fitted by the model, which does not consider the dipole moment but it gives the right form for β.

[2] This information is discussed in the supporting information of this paper

2.2.2.3. Dichroism Parameter

Next to the anisotropy parameter, a second parameter becomes important if circular polarized light and chiral molecules are used, the dichroism parameter, which describes the PECD effect. The PECD asymmetry is twice the difference in electron counts for LCP and RCP light with respect to the total amount and is given by

$$\mathrm{PECD} = 2 \cdot \frac{I_{\mathrm{LCP}} - I_{\mathrm{RCP}}}{I_{\mathrm{LCP}} + I_{\mathrm{RCP}}} \tag{2.2.21}$$

The intensity for chiral systems, which are photodetached via a single photon process is given in equation 2.2.16 and yields in combination with equation 2.2.21:

$$\mathrm{PECD} = 2 \cdot \frac{b_1 P_1(\cos(\Theta_p))}{1 + b_{2,\mathrm{p}} P_2(\cos(\Theta_p))} \tag{2.2.22}$$

in which $b_{1,\mathrm{LCP}} = -b_{1,\mathrm{RCP}}$ (equation 2.2.17b) was used. Since $b_{2,\mathrm{p}}(\beta)$ is the same for LCP and RCP (equation 2.2.17c), the subscript p will be omitted for clarity in the following.

For specific angles, this equation can be simplified. If the maximum PECD signal is of interest, the angles $\Theta = 0°$ or $180°$ (axis for light propagation) are taken and equation 2.2.22 simplifies to

$$\mathrm{PECD} = \pm \frac{2b_1}{1 + b_2} \tag{2.2.23}$$

Often, the relationship $\mathrm{PECD} \approx 2b_1$ can be found in the literature, which only considers the asymmetry giving numerator [15, 34]. While it is certainly the important part for the PECD asymmetry, it should be emphasized that the full PECD signal also depends on the anisotropy parameter.

b_2 can be avoided if the experiment is designed such that Θ is equal to the magic angle $\Theta_{\mathrm{m}} = \arctan(\sqrt{2}) \approx 54.7°$. $P_2(\cos(\Theta_{\mathrm{m}}))$ will vanish and equation 2.2.22 then simplifies to

$$\mathrm{PECD} = 2 \cdot b_1 \cos(\Theta_{\mathrm{m}}) \tag{2.2.24}$$

and is important for PECD experiments with hemispherical analyzers [37]. Equation 2.2.23 and 2.2.24 are quite simple but are only valid for specific angles. If, however, the full angular distribution is measured, the restriction to certain angles is not necessary and instead the PECD signal over the full PAD is available. Since in this thesis, a VMI spectrometer enables the measurement of the full PAD, the more general form of the PECD equation (equation 2.2.21) is used.

2.3. Enantiomers and Circular Polarized Light

2.3.1. Nomenclature of Enantiomers

Molecules are chiral if there is a mirror image molecule (enantiomers) and they are not superimposable. The enantiomers are discriminated by the labels (R) and (S) in

combination with (+) and (-) or with D and L. Here, just a summarized version of the labeling systems and how to apply them is given. A more comprehensive explanation can be found, e.g., in the Beyer/Walter textbook [69].

The (R) and (S) system gives the absolute configuration since it is based on the arrangement of different atoms or atom groups around the chiral center. The Cahn-Ingold-Prelog (CIP) rules assign each atom or atom group priorities according to their atomic numbers. With the help of the Fischer projection and molecule rotations, the (R) and (S) label are assigned according to a clockwise or anti-clockwise order of the priorities.

(+) and (-) are determined by the direction in which the plane of the polarized light is rotated. If the light travels toward the observer, a clockwise rotation is labeled as (+), in the other case as (-). It also can be labeled as d- or l- isomer.

The D- L- system determines the enantiomer relative to glyceraldehyde, which has a clearly assigned D and L enantiomer. In contrast to (R) and (S), it is a relative configuration system and not an absolute one. It is independent from the d- and l- or (+) and (-) labeling system but can be easily confused.

The recommended system by International Union of Pure and Applied Chemistry (IUPAC) is the (R) and (S) system and is exclusively used in this thesis since it gives the absolute configuration [70].

2.3.2. Light polarization

2.3.2.1. Stokes Parameter

Polarized light with two independent orthogonal components x and y propagating in z direction can be described as

$$E_{\mathrm{x}}(z,t) = E_{0\mathrm{x}}\cos(\omega t - kz + \delta_{\mathrm{x}}) \tag{2.3.25a}$$

$$E_{\mathrm{y}}(z,t) = E_{0\mathrm{y}}\cos(\omega t - kz + \delta_{\mathrm{y}}) \tag{2.3.25b}$$

with $E_{0\mathrm{x}}$ and $E_{0\mathrm{y}}$ being amplitudes, ω being the optical frequency, k being the wave number and δ being the phase constants.

If the propagator $\omega t - kz$ is eliminated, a more visual form of equation 2.3.25 is found.

$$\frac{E_{\mathrm{x}}(z,t)^2}{E_{0\mathrm{x}}^2} + \frac{E_{\mathrm{y}}(z,t)^2}{E_{0\mathrm{y}}^2} - \frac{E_{\mathrm{x}}(z,t)E_{\mathrm{y}}(z,t)}{E_{0\mathrm{x}}E_{0\mathrm{y}}}\cos(\delta) = \sin^2(\delta) \tag{2.3.26}$$

This is called the polarization ellipse and describes the polarization with its field components E. Unfortunately, the field components and consequently the polarization ellipse are not observable and need to be transformed in the observable intensity domain. The transformation requires a time average over equation 2.3.26 and leads to

$$S_0^2 = S_1^2 + S_2^2 + S_3^2 \tag{2.3.27}$$

with

$$S_0 = E_{0x}^2 + E_{y0}^2 \tag{2.3.28a}$$
$$S_1 = E_{0x}^2 - E_{y0}^2 \tag{2.3.28b}$$
$$S_2 = 2E_{0x}E_{y0}\cos(\delta) \tag{2.3.28c}$$
$$S_3 = 2E_{0x}E_{y0}\sin(\delta) \tag{2.3.28d}$$

Equations 2.3.28 define the Stokes parameters, which describe the polarization of light. They are given in terms of intensity (squared amplitudes) and are therefore measurable. The first parameter gives the total intensity while the others describe the amount of polarization for certain directions: S_1 describes the polarization in horizontal (0°) and vertical polarization (90°), S_2 is used for ±45° and S_3 is for LCP and RCP:

$$S_0 = I_x + I_y \tag{2.3.29a}$$
$$S_1 = I_x - I_y \tag{2.3.29b}$$
$$S_2 = I_{+45} - I_{-45} \tag{2.3.29c}$$
$$S_3 = I_{RCP} - I_{LCP} \tag{2.3.29d}$$

The Stokes parameter for different polarizations are summarized in table 2.3.1. If the

Table 2.3.1.: Stokes parameter describe the polarization of light.

S/polarization	no	0°	90 °	±45°	LCP	RCP
S_0	1	1	1	1	1	1
S_1	0	1	-1	0	0	0
S_2	0	0	0	±1	0	0
S_3	0	0	0	0	-1	1

Stokes parameters are known, the degree of polarization P, can be calculated

$$P = \frac{\sqrt{S_1^2 + S_2^2 + S_3^2}}{S_0}. \tag{2.3.30}$$

In other words, it describes the quality of polarization, which goes from unpolarized ($P = 0$) to fully polarized ($P = 1$).

2.3.2.2. Convention for Circular Polarized Light

Circular polarized light comes in two forms: LCP and RCP whereas the definition of left and right depends on what an observer or – in this thesis – the molecular beam "sees" coming towards them. If the polarization of light is rotating in clockwise direction, the light is called right circular polarized while a counter-clockwise rotation refers to as left circular polarized. This convention coincides with the definition given by Born and Wolf [71] and will be used throughout this thesis.

3. Experimental and Computational Methods

3.1. Chiral Anions

3.1.1. Properties for Anions and Molecules

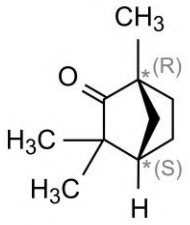

(a) (1R)-(-)-fenchone

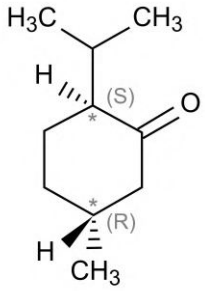

(b) (2S,5R)-(-)-menthone

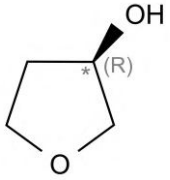

(c) (R)-(-)-3-hydroxytetrahydrofuran

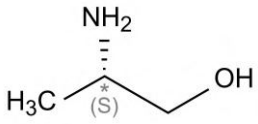

(d) (S)-(+)-alaninol

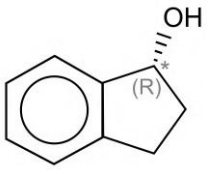

(e) (R)-(-)-1-indanol

Fig. 3.1.1.: Chiral molecules used in this project. The chiral center is highlighted with a gray * and its absolute configuration is given.

The molecules (1R)-(-)-fenchone, (2S,5R)-(-)-menthone, (R)-(-)-3-hydroxytetrahydrofuran, (S)-(+)-alaninol and (R)-(-)-1-indanol (figure 3.1.1) were chosen to build the chiral part of the anionic chiral system. (1R)-(-)-fenchone, (2S,5R)-(-)-menthone and (R)-(-)-1-indanol were obtained from Sigma Aldrich while (R)-(-)-3-hydroxytetrahydro-

furan comes from Alfa Aesar and (S)-(+)-alaninol from TCI. Additionally, (S)-(+)-1-indanol was purchased from Biosynth.

To create an anionic chiral system these molecules are either used in combination with an anionic atom to form a complex or are deprotonated. The molecules itself and the anionic systems containing these molecules need to fulfill certain criteria including properties, which are beneficial for the PECD signal, anion production and measurement.

Properties for PECD

In section 1.2, it is shown that no obvious molecular properties are known, which could lead to (strong) PECD signals. The only certain requirements seem to be that the molecules have to be chiral and the sample enantiopure.

Not strictly necessary for the PECD effect itself but still helpful is a simple conformational space. It reduces the possibility of overlapping PECD signals originating from different structural isomers that could cancel each other out like it is observed for alanine [15, 33]. Apart from PECD effects, simple conformational space can – in combination with a simple structure – help to reduce the complexity of a photoelectron spectrum, which simplifies the subsequent analysis and facilitates straightforward comparisons with DFT calculations. However, this is not a necessary condition for the chiral system since the conformational space can be restricted by adequate experimental resolution. However, the experimental setup might become more difficult if this constraint is not met.

Another helpful property is the price and commercial availability of the other enantiomer as well as the racemic mixture of the molecule. Both are needed to confirm the PECD measurements and exclude other asymmetry sources.

Assuming that properties demanded for the PECD effect on neutrals are also valid for the PECD effect on anions, the following properties can be required for the anionic chiral systems:

1. It is chiral and the sample is enantiopure
2. Chiral structure remains intact after formation of the anion
3. Ideally, simple conformational space (and simple structure)
4. Ideally, it is based on a molecule with a strong PECD signal in the neutral case
5. Price and commercial availability of both enantiomers (and racemate) of the chiral molecule the anionic chiral system is based on

The chosen molecules (figure 3.1.1) fulfill these properties. Especially, fenchone seems to be a good fit since it shows quite large PECD values of $\approx$ 8-16% in conventional PECD experiments [28, 29, 72] and is also a rigid molecule [32]. 1-indanol and 3-hydroxytetrahydrofuran are also relatively rigid molecules and can reach PECD values of around 5% [73, 74]. Similar PECD values (3 - 5%) can be found in alaninol [31], which has a relatively simple structure but can be pretty flexible [75]. Menthone belongs in

the same molecular category as fenchone and finds special interest in other asymmetry studies like circular dichroism or 3-wave-mixing [11, 76]. While the choice of the anionic chiral system is relatively unconstrained regarding the PECD effect it will be restrained more strictly by other factors like the production requirements.

Properties for Chiral Molecules

The following requirements imposed on the molecule for anion production in gas phase are:

1. Easy to bring into gas phase (high vapor pressure, low sublimation enthalpy)
2. Stable molecule (no decomposition before or during evaporation)
3. Low toxicity

Since all sources used in this project are for gas-phase experiments, the chiral substance should have relatively high vapor pressure when fluid and low sublimation enthalpy when solid (assuming ambient environment). For example, the molecules shown in figure 3.1.1a - 3.1.1d are good examples because they are liquid in the ambient environment and require just a few mbar (< 3 mbar) to evaporate at room temperature (≈ 25 °C). 1-indanol (figure 3.1.1e) is also useful despite being solid (it is a powder) in the ambient environment due to the low sublimation enthalpy; heating to around 100 °C is enough to bring a sufficient amount of it to the gas phase. In combination with the requirement of a stable molecule an acceptable amount of stable anion signal for the photodetachment process should be possible.

Finally, while requiring low toxicity neither helps with anion production nor with the size of the PECD effect, it is preferential for the sake of the experimentalist. Luckily, all presented molecules show this property.

Properties for Anions

After selecting the chiral molecules, beneficial characteristics for the corresponding anion should be chosen:

1. Stable anion (positive electron affinity)
2. Electron affinity in range for “simple” laser systems (ns pulsed laser)
3. Precursor available or easy to produce

These properties are quickly explained: Long measurements are typically necessary to get reliable statistics in a experiment with low repetition rates (here 10 Hz), which demands stable anion production over the long measurement time and stable anions over the timescale of an experimental cycle.

Another aspect is the electron affinity of the anionic chiral system. If the electron is too strongly bound, more complicated laser systems are needed for detachment, which

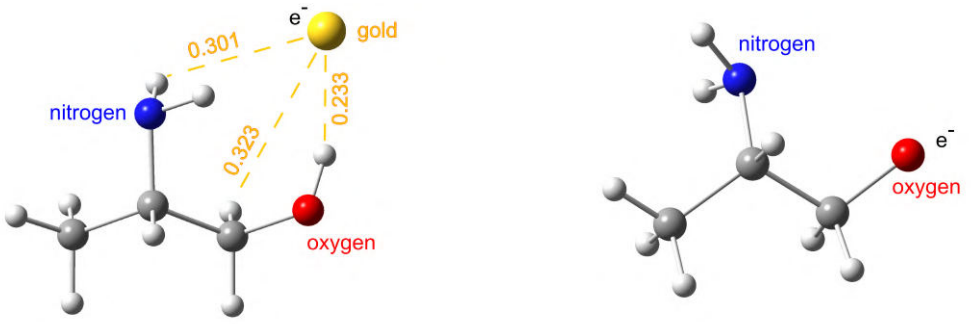

(a) (b)

Fig. 3.1.2.: Two different anionic chiral systems exemplary shown for the chiral molecule alaninol. The gold complex (left) consists of a gold anion Au^- and a chiral molecule. A second possibility to create an anion is the deprotonation of a chiral molecule (right). The (transparent) hydrogen from the hydroxy group is most likely removed. The charge will be located at the Au^- for the gold complex and at the oxygen for the deprotonated molecule. These structures are optimized with B3LYP-D3/aug-cc-pVTZ(-PP). Distances (yellow) are given in nm.

contradicts the idea of being able to work with easy laser systems in anion PECD experiments.

The last point refers to the availability of a precursor of the anionic chiral system or of precursor elements, which can be easily combined to an anionic chiral system, e.g. metal anion and chiral molecule to create a chiral metal complex. The (commercial) availability of the chiral molecule is already demanded in a previous subsection but of course this has to be valid for the precursor of the metal anion as well.

3.1.2. Creation of Anionic Chiral Systems

Many well-known chiral molecules – including the ones used in this thesis (figure 3.1.1) – have closed-shell configurations and are expected to show low electron binding energy. In table 3.1.1, the vertical detachment energy (VDE), which corresponds to the electron binding energy, is given for some of the radical anions of the molecules used here and features as expected quite low values. Consequently, the attachment of an additional electron to these systems is difficult and an alternative to produce chiral anions is favored. The used approaches are complexing atomic anions[1] with the neutral chiral molecules, consequently creating an anionic chiral complex as shown in figure 3.1.2a, as well as deprotonation of chiral molecules (figure 3.1.2b).

[1] molecular anions and clusters could be possible as well

Table 3.1.1.: Listed are the calculated vertical detachment energy (VDE) for the gold anion and the radical anions of the chiral molecules as well as the experimental electron affinity for the gold anion. Calculations are performed with B3LYP-D3 and aug-cc-pVTZ(-PP). Since the VDE estimates the (electron) binding energy, small values indicate a system with a weakly bound electron while for gold the electron is strongly bound.

system	VDE (eV)	exp (eV)
fenchone	0.249	
menthone	0.157	
3HTHF	0.335	
alaninol	0.263	
Au	2.215	2.309 [77]

Gold Complexes

The first approach – attaching an atomic anion to the neutral chiral molecule – was realized with the existing laser ablation source. Here, Au^- was chosen to provide the extra electron to create an anionic chiral Au^--molecule complex (Au^--M). This decision was made due to the following reasons:

1. Au^- is relatively heavy with m/z 197, allowing the complex to be differentiated easily from other substances in the mass spectrum.

2. Only one stable isotope of Au^- ($^{197}Au^-$) exists, making the mass spectrum easy to analyze.

3. Au^- has a closed-shell configuration $[Xe]4f^{14}5d^{10}6s^2$.
   - This makes Au^- rather inert. Hence, Au^- does not react much with other components.
   - The electron is also strongly-bound with an electron affinity of 2.309 eV [77], which is still easily accessible with ns-pulsed lasers.

4. The production of large amounts of Au^- in the existing source is effortless and if the connection between Au^- and the chosen molecule is possible, the creation of the anionic complex will be highly likely.

The calculated VDEs of table 3.1.1 show that Au has always a higher VDE than the chiral molecules. Hence, the gold anion is more stable and the additional electron is most likely localized at the gold atom. The chiral molecule can be polarized by the gold anion, which gently forms and stabilizes the complex.

In the following these cluster anions are written as Au^--M, with M being either fenchone (Fen), menthone (Men), 3-hydroxytetrahydrofuran (3HTHF) or alaninol (Ala).

Deprotonated Molecules

The second method used here is the production of a chiral molecular anion via deprotonation. Here, several properties have to be considered:

1. Easy to deprotonate, e.g., molecules with a hydroxy group.
2. Ideally, just one deprotonation site to avoid isomers. However, if several deprotonation sites can not be avoided, try to separate them (e.g. energetically).
3. No deprotonation at the chiral center

In order to find a molecule (M), which is easy to deprotonate, the enthalpy of the reaction $M^- + H^+ \rightarrow M$ in gas phase needs to be considered whereas M^- denotes the deprotonated molecule $M^- \equiv (M\text{-}H^+)^-$. In general, certain groups of molecules are easier to deprotonate than others due to their functional groups. This is exemplary shown for methyl-alcohol, -amine and -methane in table 3.1.2. Here, the molecule with the -OH group is the easiest to deprotonate while the CH_3 is less likely to be deprotonated. The molecule with $-NH_2$ lies in between. In a system like methyl alcohol or -amine the -OH and $-NH_2$ group are considered as distinctive deprotonation sites since deprotonation will happen most likely at this position. Methylmethane has no distinctive deprotonation site since all positions are more or less equiprobable.

Another group of possible molecules, which can be deprotonated are carboxylic acids (-COOH), like lactic acid. However, while deprotonation is relatively easy the photodetachment of the anion ($-COO^-$) can be rather complicated due to the high electron affinity (at least ≈5 eV for deprotonated lactic acid).

To avoid several isomers and a possible weaker averaged PECD signal, it would be ideal to have only one distinct deprotonation site meaning that molecules with, for example, two hydroxy groups like 2-propandiol, are not ideal since it is not instantly clear which hydroxy group is deprotonated. However, even with only one distinct deprotonation site deprotonations on other groups can sometimes not be avoided even if such groups are less likely to be deprotonated. 1-indanol for example has only one hydroxy group but can also be deprotonated at the -CH groups. Luckily, the differently deprotonated 1-indanols can be easily distinguished in a photoelectron spectrum due to their sufficient different binding energies [48].

Table 3.1.2.: Enthalpy $\Delta_r H^o$ for the reaction $M^- + H^+ \rightarrow M$ in gas phase. M is the respective molecule and $M^- \equiv (M\text{-}H^+)^-$ the deprotonated molecule. The values are from the "Reaction Thermochemistry Data" of NIST [78].

molecule	formula	$\Delta_r H^o$ (eV)
Methyl alcohol	CH_3OH	≈16.6
Methylamine	CH_3NH_2	≈17.4
Methylmethane (ethane)	C_2H_6	≈18.2

Of course, the chirality has to be maintained after deprotonation meaning that the most likely deprotonation site should not be the chiral center. 1-indanol and alaninol can be deprotonated at the chiral center but since the main deprotonation site is not at the chiral center, most of the created molecules are chiral.

In the case of deprotonation at the hydroxy group the excess electron will be located at the deprotonation site (oxygen). This locates the excess electron closer to the chiral center compared to the gold complex as can be seen for alaninol: The gold complex Au^--Ala has a distance between Au^- and the chiral center of around 0.4 nm while the deprotonated form has a distance of around 0.2 nm between deprotonation site and the chiral center. More importantly, the relevant electron is also no longer localized at an achiral part like Au. If the localization is too strong, the electron might mostly experience the atomic potential and not the chiral potential of the molecule, which could probably suppress the PECD effect.

In the following, deprotonated molecules are written with "-H" indicating to the removed H. The both molecules used for the experiments with deprotonation are [deprotonated alaninol (Ala-H)]$^-$ and [deprotonated 1-indanol (Ind-H)]$^-$.

3.2. Setup and Data Treatment

Overview of Experiment

Roughly, the experiment consists of an anion source, two spectrometers and a laser system. The whole experiment is operated under high vacuum and is pulsed with 10 Hz. This experiment is already partly described by Grüne, Härtelt and Yubero [68, 79, 80].

The anionic chiral systems of interest, i.e. chiral gold complexes (Au^--M) and deprotonated chiral molecules, are created with two different sources: For Au^--M, the existing laser ablation source is ideal since Au^- is easily produced in such sources. The plasma entrainment source after the design of Lineberger *et al.* [81] was implemented for the production of the deprotonated molecules since it is optimized for the deprotonation process. Both sources are described in section 3.2.1.

Identifying the anions is possible with spectrometry: A linear time of flight mass spectrometer (ToF-MS) separates substances according to their different mass-charge ratios in their flight times and hence gives a first impression of the produced substances (section 3.2.2). Furthermore, different flight times of the substances offer the possibility of synchronizing a laser to a specific flight time and selecting the corresponding substance for further spectroscopic study. Further measurements with an electron spectrometer are needed to reveal the energy levels and substantiate the identification of the substance in the ToF-MS. The spectrometer utilized in the experiments included in this thesis is an anion-PES-VMI spectrometer, which yields, energy information and information about the angular distribution (section 3.2.3). For PECD measurements, the polarization of light is essential since it requires circularly polarized light in good quality and shot-to-shot alternation to reduce the influence of long and short-term fluctuations (section 3.2.4).

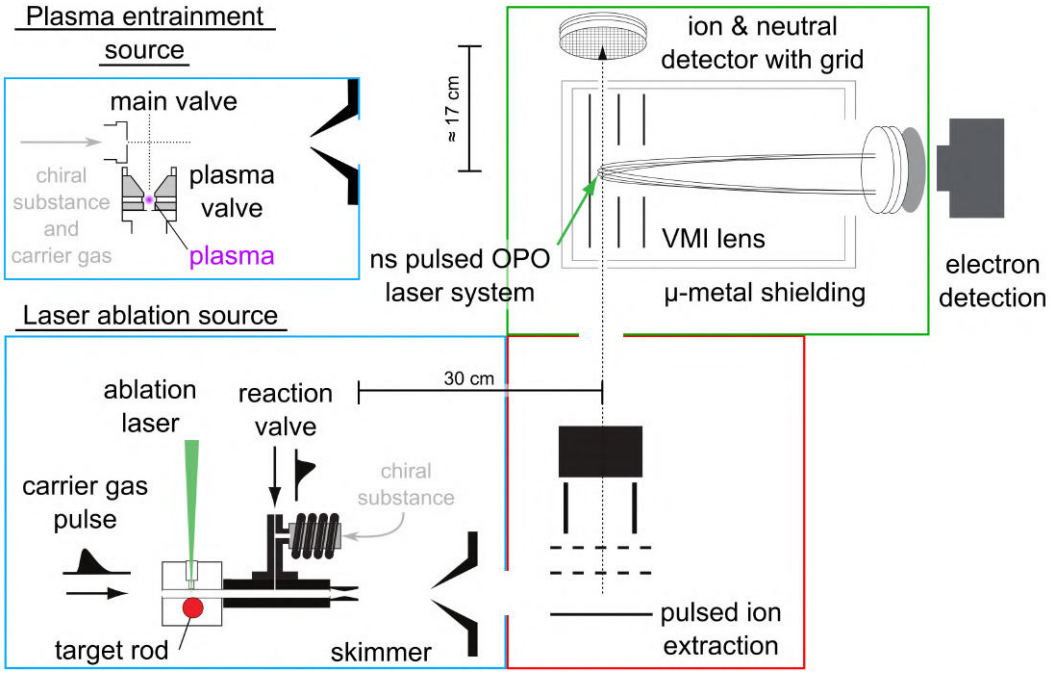

Fig. 3.2.1.: Schematic setup of the experiment. In the source chamber (blue frame), anions are created by either the laser ablation or the plasma entrainment source. After a skimmer, the anions enter the chamber with a linear ToF mass spectrometer (red frame). Here the anions are mass-selected and accelerated to the VMI chamber (green frame) where they are detected. In the VMI chamber, a ns-pulsed OPO (1.1 - 5.77 eV) that is synchronized with the mass spectrometer photodetaches electrons from the anions, which are subsequently directed to a VMI lens system and are collected by a position sensitive detector.

Hardware Setup

Each element of the experiment (source, ToF-MS, VMI spectrometer) is in a separate vacuum chamber equipped with a high-vacuum pump and can be separated from each other through gate valves. A more detailed description of the vacuum system is given elsewhere [79] and will thus be omitted for brevity. The three main vacuum chambers contain, respectively, the source for anion production, the ToF-MS for mass separation and the VMI lens system for photodetachment and PECD measurements (see figure 3.2.1). The source chamber holds a laser ablation source, which was later replaced by a plasma entrainment source to investigate other molecular systems. A skimmer with a 2 mm diameter orifice shapes the molecular beam of the source chamber and is the only opening to the next chamber, which contains a linear ToF-MS. Even with a relatively high pressure in the source chamber (10^{-4}-10^{-3} mbar) during operation, this small orifice aids in maintaining a pressure of around 10^{-6} mbar in the ToF-MS chamber (differential pumping). Here, the anions in the molecular beam are extracted by a pulsed electric field created by fast-rising, pulsed, negative, high voltages at the ToF-MS electrodes, perpendicular to the molecular beam. The anion beam enters the VMI chamber through an aperture of 5 mm in diameter, confining the anion beam and facilitating the

preservation of 10^{-7}-10^{-8} mbar of pressure even when the source is operating. A 10 Hz nanosecond Nd:YAG laser with an optical parametric oscillator (OPO) synchronized to the arrival time of the desired anion, performs photodetachment about 17 cm in front of the multichannel plate (MCP) detector of the ToF-MS (ToF-MCP detector). The photodetached electrons are extracted to the MCP detector of the VMI spectrometer (VMI-MCP detector) by pulsed high voltages on the VMI electrodes, while the neutrals continue to travel to the ToF-MCP detector.

In general, the neutrals have the same kinetic energy as the corresponding anions, which are accelerated in the ToF-MS to around 2-4 keV. Hitting the ToF-MCP detector with such energies generates a measurable neutral signal if the anion intensity is high enough[2]. A grid, placed in front of the ToF-MCP detector with a deflecting field for the anions, allows the background-free observation of the neutral signal. The signal will be at the same timing as the anion signal and can therefore be used to confirm the desired photodetachment. Most importantly, both the PADs as well as the signal of the laser produced neutrals can be measured simultaneously.

Software Setup

The experiment runs at 10 Hz and was controlled through a Software called KouDa, which was designed in the Molecular Physics (MP) Department in collaboration with the IT-Support Group (PP&B) at the FHI Berlin. KouDa allows the digital management of power supplies and triggers as well as the real-time visualization of the ToF spectrum. A 16 bit digital-to-analog converter (16+8 channel Acromac IP231) transforms the digital information to an analog signal for the power supplies, while the trigger information is processed in four interconnected digitizer cards (BU 3008 delay generators manufactured by the Electronics Workshop (E-Lab) of the FHI Berlin). The master clock was provided by the Q-Switch of the laser. This setup was used in previous projects [68] as well as for the measurements with the gold complexes. The hardware was updated to a National Instrument system in 2019. Additionally, new software based on LabVIEW called SDaq is used.

SDaq was implemented in the MP Department by Uwe Hoppe and provides a collection of units for different applications. Out of those, programs for controlling the power supplies and triggers, as well as the observation of the time-of-flight spectrum with a digital oscilloscope are utilized. Each of these programs controls a hardware module from National Instruments, which are all encased in a NI PXIe-1082 chassis and connected to the computer via the remote control module NI PXIe-8381 MXI-Express x8. A NI PXIe-6738 analog output device with a resolution of 16 bits for voltage control is used. Two NI PXI-6602 Timing I/O – each with 8 channels, 32 bit resolution and a time base of 80 MHz[3] – handle the triggers for the experiment. The conversion of the digital signal to an analog signal (DAC) takes place in a digital counter panel 6602 (E-Lab # 6186) built by the E-Lab for each of the timing I/O cards. The module NI PXIe-5160 is a

[2]Since the gain in neutral signal is low, a high anion signal is required.
[3]100 kHz and 20 MHz are available as well but are not used here

two channel, 500 MHz oscilloscope with a sample rate of 2.5 GS/s and permits real-time observation of the ToF spectrum. The oscilloscope starts recording simultaneously with the extraction voltages at the ToF-MS electrodes and stops recording after a time depending on the minimum sample rate S_{min} and minimum record length L_{min}. Here, a minimum sample rate of $2.5{\cdot}10^8$ Hz and a minimum record length of 5000 samples are used and give a recording time of $L_{\text{min}}/S_{\text{min}} = 20\mu$s. The data can be recorded in a single shot mode or in two different averaging modes. The mode "scan" averages over a specific amount of shot-to-shot measurements where each measurement has the same weight, while in the mode "EWMA" (exponentially weighted moving average) the weight of previous measurements decreases exponentially. During measurement, EWMA is used to see the most up-to-date averaged data, while mass spectra are saved after measuring in scan mode.

Since the oscilloscope only provides the flight time of anions and neutrals, a custom-made program is added to the SDaq project for mass-calibration and for converting the time-of-flight spectrum to a mass spectrum in real time. Another custom-made program to fit specific peaks of the measured spectrum with a Gaussian function provides information about the full width at half maximum (FWHM) of the mass peaks and thus the resolution of the linear ToF-MS.

With SDaq, a photoelastic modulator (PEM) from Hinds Instruments was implemented for shot-to-shot alternation of the polarization of the light for the PECD measurements. Since the operation of the PEM is determined by material properties it can not receive trigger signals but only provide trigger signals. Hence, the PEM has to be, in combination with a pulse-delay generator (Quantum Composer 9420 Series), the master clock of the experiment. More details about the functionality of the PEM and on how it is connected with the pulse-delay generator to control the experiment can be found in section 3.2.4.

3.2.1. Production of Anionic Chiral Systems

3.2.1.1. Laser Ablation Source

The production of anionic chiral complexes Au^--M is performed with an existing laser ablation source [68, 79] consisting mainly of a (gold) target, an ablation laser and a pulsed electromagnetic valve (em-valve). Here, Au^- is created in the laser ablation region of the source. The neutral chiral molecules are introduced later with a second perpendicular pulsed em-valve, i.e. reaction valve, and react with Au^- to form the chiral Au^--M.

Laser ablation sources were developed in the 1980s out of the ambition to produce and investigate metal clusters. Smalley's research group – as well as the group of Bondybey – were the first to apply this technique in experiments [82–84] and are therefore often referred to as its inventors. This technique combines two precursor methods: the laser vaporization technique for creating metal vapors and the pulsed supersonic nozzle technique for subsequent cooling. This results in various vibrationally cooled metal clusters with different charges and sizes, which provide a mass spectrum that is easy to

interpret. In comparison to previous methods (e.g. oven sources), extensive heating and subsequent cooling is avoided, which would impede the formation of big, cooled clusters. Due to these improvements, the laser ablation source – along with its numerous variations – is still frequently used in modern cluster and material sciences [85].

The design of the here used laser ablation source is based on a source that is used in another experiment for infrared spectroscopic studies of clusters and cluster complexes [86]. The source has been described before in detail [68, 79, 80]. Hence, only a short and more focused description is given here.

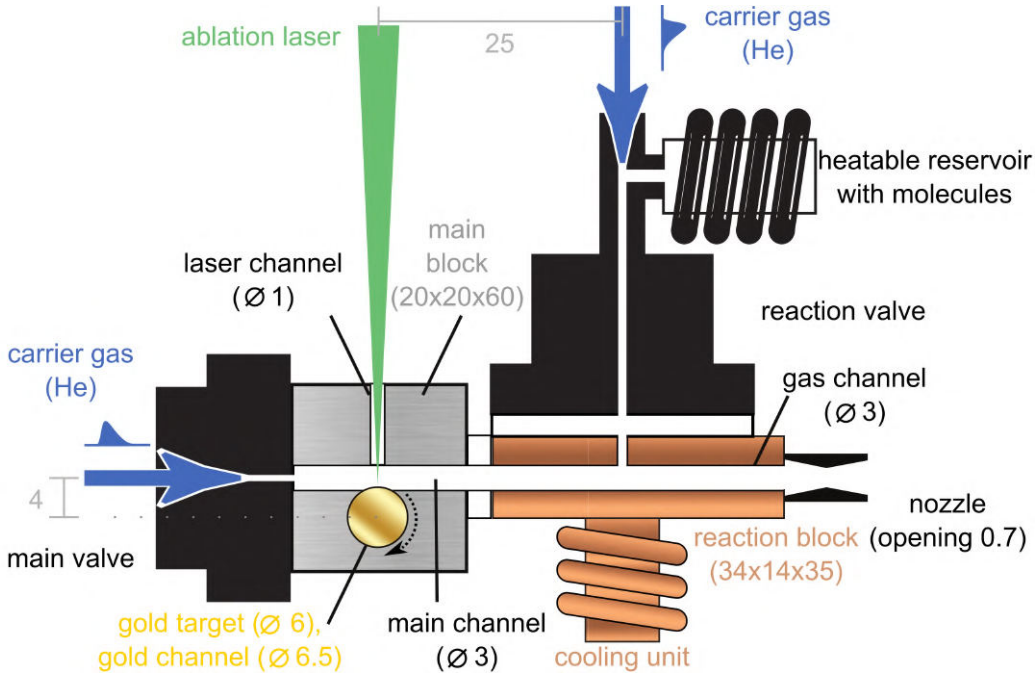

Fig. 3.2.2.: Laser ablation source with two pulsed em-valves. The main valve contains the carrier gas helium, which crosses the laser ablation zone and entrains laser-ablated material from a turning metal rod. A second valve, the reaction valve, releases another substance also seeded in helium. This substance can react with the laser-ablated material and enters the chamber through a nozzle. All dimensions are given in mm. The figure is not to scale.

Figure 3.2.2 shows dimensions and the essential parts of the laser ablation source, which are the main stainless steel block for the laser ablation process and the copper reaction block for reactions with other reactants. The copper block also gives the opportunity for temperature control with liquid nitrogen and a controllable heater.

Attached to the main block is a pulsed em-valve (General Valve, Series 9 from Parker, $\approx$ 0.8 mm orifice, 28 V, teflon poppet), the main valve, to provide carrier gas (helium). The carrier gas flows inside the main channel while passing the laser ablation region. Here, a gold rod (or target) is placed perpendicular to the main channel with a small offset to achieve contact between carrier gas and target without blocking the main channel. A ns-pulsed BRIO Nd:YAG laser (Quantel, Model: Brio/IR-SB) serves as the ablation laser. Its light passes through a third channel perpendicular to the other two while

being focused on the target with a movable convex lens with 250 mm focal length[4]. The second harmonic (532 nm) provides enough energy (1-12 mJ/pulse) to create a plasma and ablate material from the target, which is picked up by the passing carrier gas and cooled while moving in the direction of the reaction block.

While ablating material from the target, the laser induces structural changes at the surface of the rod. In order to prevent these changes from accumulating and impeding the efficiency of laser ablation, the target is turned continuously (mostly ≈ 1.8 revolutions/h for a gold target of 6 mm diameter) and simultaneously translated with a stepper motor and a specially designed target holder (for details see [68, 79]) allowing the laser to always hit a fresh surface.

The reaction block contains a second pulsed em-valve (with the same specifications as the main valve), the reaction valve, to introduce substances seeded in a carrier gas that can react with the laser ablation products. In this particular case, chiral molecules like alaninol are delivered to the laser ablation products.

Another feature of this reaction block is the temperature control between -180 °C and 100 °C resulting from a combination of liquid nitrogen flowing through a copper spiral attached to the reaction block and a controllable heater bar (not shown in figure 3.2.2). The reaction block is thermally insulated from the main block. In this experiment, the source parts were never cooled but were sometimes heated by several degrees to facilitate the vaporization of less volatile chiral substances.

Typical products from this laser ablation source are metal clusters. In this thesis a gold target was used and hence Au_n^- are mostly produced. With the introduction of the reaction valve other types of atoms or molecules can be introduced additionally to form metal cluster complexes. With the laser ablation source, the focus here is in the production of the complexes Au^--M.

The formed laser ablation products enter the source chamber through a conical converging-diverging nozzle and pass through a skimmer into the ToF chamber.

3.2.1.2. Plasma Entrainment Source

For the production of deprotonated molecules, a plasma entrainment source according to Lineberger *et al.* [81] replaces the laser ablation source (figure 3.2.3). The important components are two perpendicular em-valves from which one, the main valve, supplies the chiral molecule via a supersonic expansion and the other, the plasma valve, produces (mainly) OH^- in a pulsed dc glow discharge plasma [87, 88] from a special gas mixture. Argon is used as carrier gas and is the main component of the gas mixture. The OH^- is entrained in the expansion of the main valve to deprotonate the chiral molecule. If the entrainment happens close to the main valve, further cooling of the main expansion is achieved. Compared to the laser ablation source, this source can produce deprotonated molecular anions with higher intensity due to the increased controllability and at a lower temperature.

[4]Sometimes a good signal is achieved when the focus is not directly on the target.

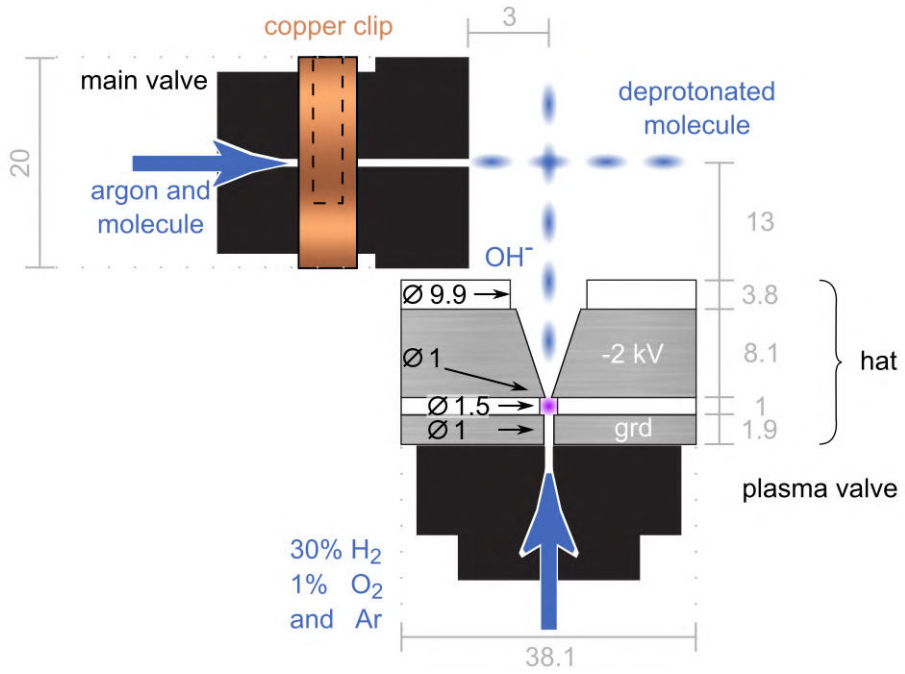

Fig. 3.2.3.: The plasma entrainment source consists of the main valve, which transports the chiral molecule and a plasma valve with a hat consisting of electrodes (gray) and macor plates (white) stacked in an alternating way. The main valve is fixed by a copper clip, which holds a heater rod (dashed lines) to heat the valve. For heat distribution a copper wire is wrapped around valve head and line (not shown). The plasma is formed between the electrodes (purple dot) and produces OH^- for the deprotonation of the molecule. The outer diameter of the hat is ∅ 38.1 mm (for comparison: the size of a general valve head is ∅ 33.8 mm). The high voltage electrode opens in a 40° cone. All dimensions are given in mm. The figure is not to scale.

Constructional Aspects

The em-valves used for this source are recycled from the former laser ablation source (General Valve, Series 9 from Parker, ≈ 0.8 mm orifice, 28 V, teflon poppet). For the sake of purity, the reaction valve, which delivered the molecules, will act as main valve and is still responsible for the supply of chiral molecules, while the former main valve will now act as plasma valve for the supply of OH^-. In contrast to the laser ablation source, the poppet in the main valve was changed from a teflon to a more robust PEEK poppet when the valve was heated for 1-indanol.

Before the valves can be used for the plasma entrainment source some adaptations need to be made. The plasma valve needs a "hat" in which the plasma can be created. The hat is shown in figure 3.2.3 and contains the electrodes (stainless steel in gray) and electrical insulators (MACOR in white) in an alternating way.

The first stainless steel plate is the ground electrode and has direct contact to the pulsed plasma valve. The following plate is a MACOR plate, which insulates the ground plate electrically from the subsequent stainless steel plate for high negative voltages (around 0.5 - 2 kV). The top plate is another MACOR plate. The dimensions of these

plates are given in figure 3.2.3. Here, an important value is the channel size of the first MACOR plate in comparison to the stainless steel electrodes: The channel is 0.5 mm wider than the channel of the electrodes such that a discharge between the stainless steel edges is (by design) facilitated.

It is crucial for optimal signal intensity and cooling to carefully select the vertical and horizontal distance between the main and the plasma valve. The horizontal distance between the orifice of the main valve and the plasma valve is set to 3 mm. If the distance were smaller, the valve body would intrude in the plasma expansion and disturb the entrainment. On the other hand, a larger distance would cause the plasma products to be introduced after the cooling process and thus heat the molecules again. The vertical distance between the MACOR surface and the orifice of the main valve is set to a value of around 13 mm. Here, a closer distance is recommended by Lineberger *et al.* since the gas beam from the plasma valves spreads in space and fewer molecules interact with the main gas beam. [81]

To comply with the vertical and horizontal distances mentioned above, the original 33.8 mm diameter of the main valve's front plate needed to be reduced. While Lineberger *et al.* [81] created their own adapted front plate, here, an original front plate from Parker is modified, instead, by decreasing its diameter to 20 mm.

Operational Aspects

Normally, a glow discharge plasma operates under low pressure conditions (10^{-3} - 100 mbar) [87, 88] with pulse length of 15 - 900 μs and several hundreds or thousands of volts. The backing pressure can be around 2 - 8 bar for a 150 μs long gas pulse. [88–92]

According to Lineberger *et al.*, voltage gradients between -500 and -2000 V applied for 40 to 140 μs are sufficient for plasma production. The plasma valve operates with around 2.8 bar for 110 - 160 μs, which is similar to the main valve, but the driving voltage is set such that the plasma valve contributes only around 10% to the total source chamber pressure. [81]

In this project, a voltage of around -2000 V for 70 to 200 μs is used. The backing pressure is around 5 bar and the pulse trigger length can be between 170 and 300 μs. However, the contribution to the total source chamber pressure remains around 10%.

Plasma

The type of plasma is a pulsed dc glow discharge plasma, which is named after the "glow" generated by excitation collisions of electrons with the neutral part of the gas (e.g. argon atoms) [88]. The color of the glow depends on the used gas mixture.

Here, the gas consists of 30% H_2, 1% O_2 and 69% Ar and is supplied by the plasma valve. This mixture is recommended by Lineberger *et al.* to achieve a significant OH^- signal [81]. The discharge itself occurs in the "hat" of the plasma valve between the ground and high negative voltage electrode. A plasma is created in this region (purple dot in figure 3.2.3) and glows in a purple-blueish color.

Possible chemical reactions happening in the plasma that lead to the creation of OH^- are

$$2H_2 + O_2 \longrightarrow 2H_2O + 6.3\ \text{eV} \tag{3.2.1a}$$
$$e^-\ (3.2\ \text{eV}) + H_2O \longrightarrow H_2 + O^- \tag{3.2.1b}$$
$$O^- + H_2 \longrightarrow OH^- + H + 0.1\ \text{eV} \tag{3.2.1c}$$
$$O^- + H_2O \longrightarrow OH^- + OH - 0.4\ \text{eV} \tag{3.2.1d}$$

Reactions 3.2.1b-3.2.1d (without the energies) are suggested by [93]. The energies given here are calculated with B3LYP-D3/aug-cc-pVTZ. The energy of reaction 3.2.1a is known to be around 5.9 eV, hence an error of 0.4 eV can be assumed for the other energies. Apart from reaction 3.2.1a water can also be created by heterogeneous processes at the wall surface [93].

In this setup it is possible to confirm the production of plasma by observing the discharge either through a window or by monitoring the discharge voltage on an oscilloscope. However, plasma formation can also be confirmed by the entrainment of electrons in the main expansion. Slow and fast electrons have to be detected.

According to reference [81], slow and fast electrons are verified indirectly by the creation of O_2^- and O^- in the ToF-MS, respectively. Slow electrons attach to molecular oxygen and produce exited anionic molecular oxygen $(O_2^-)^*$, which is subsequently cooled collisionally and thereby stabilized in the presence of the carrier gas argon (equation 3.2.2b). The attachment of slow electrons to neutral molecules like O_2 in the main expansion is possible due to the ambipolar diffusion of the plasma[5]. Hot electrons dissociate O_2 into its components and create O^- (equation 3.2.3). If the dissociation energy of O_2 is considered, hot electrons need to have an energy of at least 5.1 eV, while slow electrons have less [94].

$$O_2 + e^- \rightarrow (O_2^-)^* \tag{3.2.2a}$$
$$(O_2^-)^* + Ar \rightarrow O_2^- + Ar^* \tag{3.2.2b}$$

$$O_2 + \text{hot } e^- \rightarrow O^- + O \tag{3.2.3}$$

Equation 3.2.1b and 3.2.3 represent two possibilities for the production of O^-, which can be used as proof for successful plasma entrainment and OH^- production (equation 3.2.1c and 3.2.1d).

With successful plasma formation and entrainment, the deprotonation of a molecule from the main expansion can be conducted with OH^-. If the molecule is an alcohol, the deprotonation will preferentially occur at the hydroxy group. For alaninol and 1-indanol, this deprotonation process is shown in figures 5.2.1a and 5.2.1b in chapter 5.

In addition to deprotonated molecules and the plasma products (OH^-, O_2^-, O^-), the corresponding Ar clusters are observed by Lineberger. Here, the same products are observed and it is possible even to observe an Ar cluster with $[\text{Ind-H}]^-$.

[5] Electrons and ions move with the same diffusion rate since slow, heavy ions pull back on the electrons while the electrons pull the ions forward.

3.2.1.3. Comparison of Laser Ablation and Plasma Entrainment Source

The laser ablation source is able to produce a variety of metal containing clusters and complexes like gold anions. Via side channels placed after the laser ablation region, it is possible to incite various interactions with other molecules, like chiral molecules, which keeps the molecules often intact.

In contrast, the plasma entrainment source uses samples with comparably high vapor pressure or low sublimation enthalpy and hence is more specialized for fluids, gases and a few solid substances. Due to the presence of OH^-, this source is specialized in deprotonation and molecules with hydroxy groups are of primary interest. The deprotonation leads to modified molecules.

Apart from changing sources, the carrier gas is exchanged from helium to argon. This influences the expansion conditions and should result in superior cooling in the case of the plasma entrainment source.

Another difference is the different m/z region the mass spectra possess. Since Au is used here, the mass spectra feature normally high m/z ($m/z \geq 197$) while the plasma entrainment source in this thesis features mass spectra (MS) at lower m/z. This affects the resolution of the peaks in the mass spectrum since the ToF-MS has a resolution dependent on the mass m and the FWHM Δm ($m/\Delta m$) favoring low m.

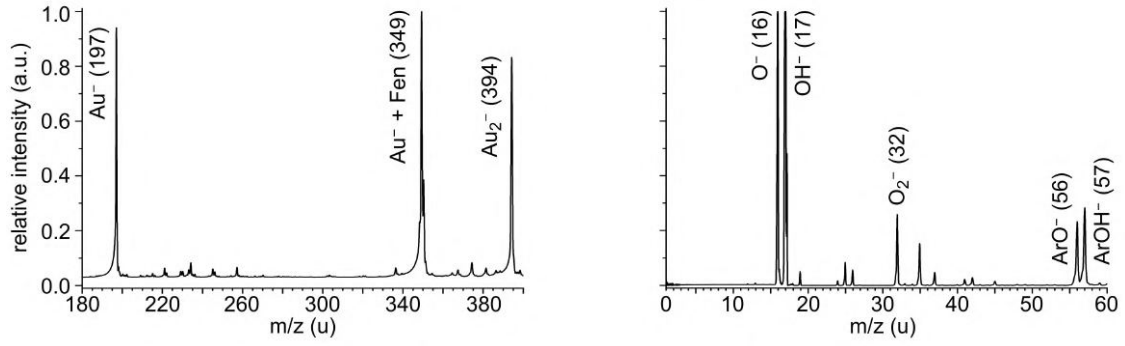

(a) **(b)**

Fig. 3.2.4.: Exemplary mass spectra (MS) for the two sources. Left: MS for laser ablation source with typical source products like Au^- and Au_2^- and Au^-Fen. Right: MS for the plasma entrainment source with the plasma products O^-, OH^- and O_2^-. For OH^- and O^- Ar complexes are observed. A more detailed analysis is given in section 4.2.

Mass spectra obtained with the laser ablation source and plasma entrainment source are compared in figure 3.2.4. They give a first impression of the capability of the sources: The mass spectra of laser ablation source working with a gold target (figure 3.2.4a) shows Au^- and Au_2^- as well as Au^--fenchone (Au^--Fen). $Au_{n>2}^-$ can also be produced with this source but are not shown here. Figure 3.2.4b is a mass spectrum from the plasma entrainment source and features predominantly the plasma products O^-, OH^- and O_2^-. For all these products respective argon clusters are possible as shown partly in figure 3.2.4b and to an larger extent later in figure 3.2.6. Carbon contaminations (e.g. m/z

24 - 26) may be the result from sputtering from stainless steel electrodes since this mass spectrum was recorded before a (chiral) molecule was introduced to the source.

Although its specialization for ablation of solids, deprotonation is also possible for the laser ablation source. Figure 3.2.5 shows next to typical laser ablation source substances (Au^- and Au-Ala^-), the anion $[Ala\text{-}H]^-$ at m/z 74 and other substances like $[Ala_n\text{-}H]^-$ and $[Ala_n\text{-}OH]^-$. The deprotonation process could be performed with OH^-, which is probably produced in the plasma of the laser ablation region. However, oxygen and hydrogen are not supplied actively, which makes the OH^- production and, hence, the deprotonation a rather erratic (side) effect. In contrast, the plasma entrainment source offers a controlled and hence more effective way for the creation of OH^- and consequently, the deprotonation process.

It should be noted that this mass spectrum is optimized for $[Ala\text{-}H]^-$ and not for the gold-alaninol complex. If the source parameters are optimized for the gold-alaninol complex, the signal would be much stronger and outperform the $[Ala\text{-}H]^-$ signal easily.

The typical products of the plasma entrainment source depend on the chosen gas mixture and are, for the here used gas mixture, the plasma products O^-, OH^- and O_2^- (figures 3.2.4b and 3.2.6). The strongest signals are O^- and OH^-, indicative of an effective OH^- production. A bond between O^-, OH^- and argon is also possible (ArO^-, $ArOH^-$) via ion-induced dipole interactions [81, 95].

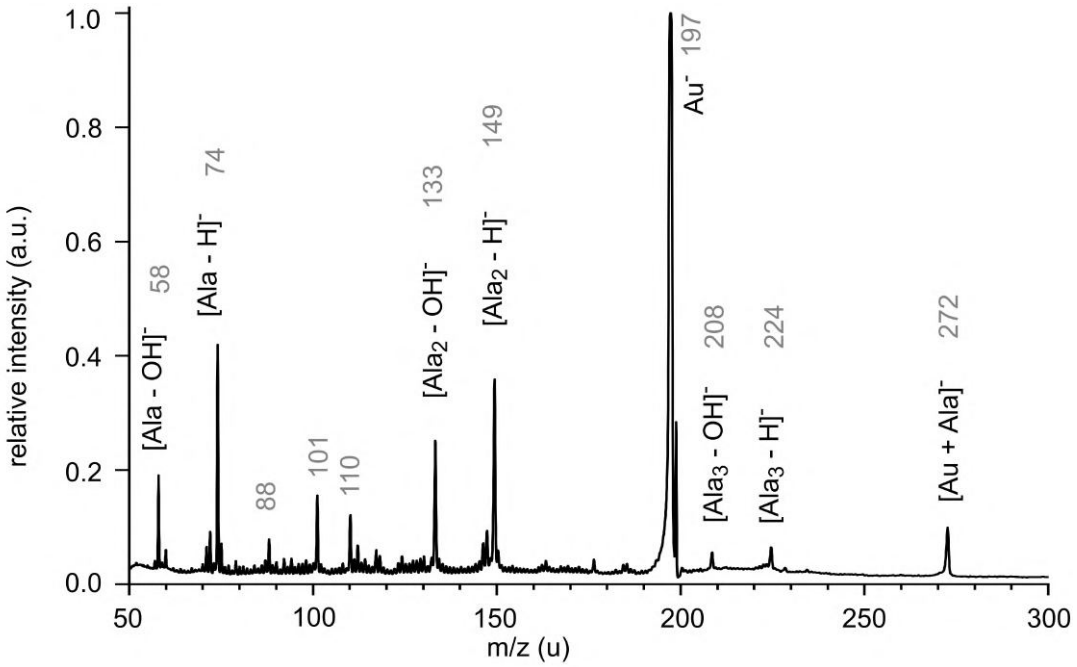

Fig. 3.2.5.: Detection of deprotonation in the laser ablation source. Next to typical laser ablation source products like Au^- (m/z 197) and Au-Ala^- (m/z 272), Ala-H (m/z 74), deprotonated clusters of alaninol ($[Ala_n\text{-}H]^-$) and clusters with a removed OH group ($[Ala_n\text{-}OH]^-$) can be found. m/z 88, 101 and 110 can not be clearly assigned to a reaction product or fragment of alaninol. They are considered to be contaminations.

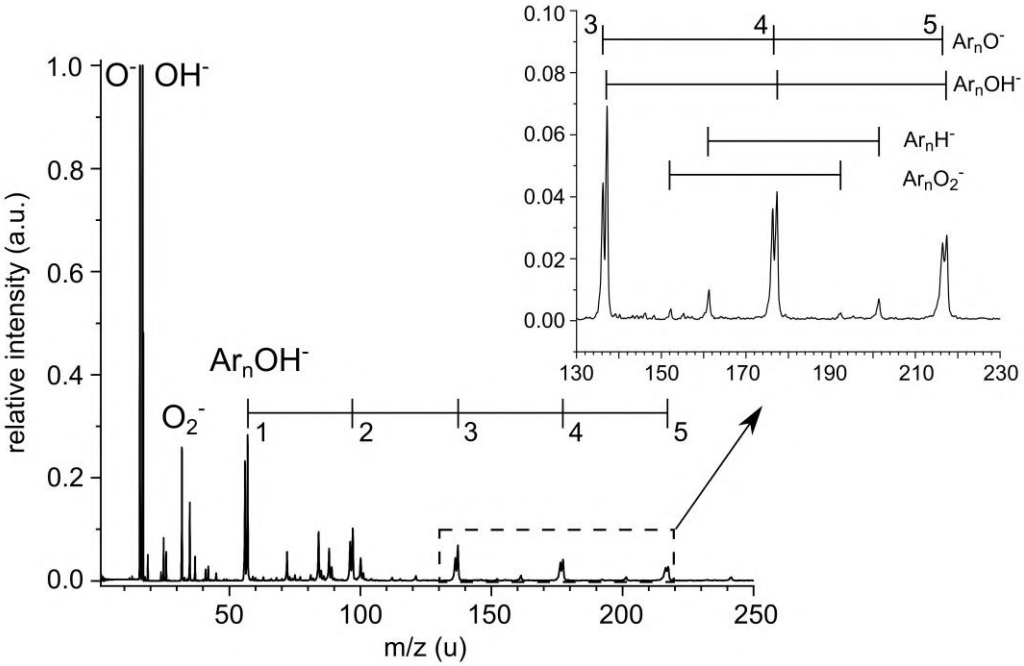

Fig. 3.2.6.: MS obtained from the plasma entrainment source. It is possible to create O^- (m/z 16), OH^- (m/z 17), O_2^- (m/z 32) as well as Ar_nOH^--clusters at m/z (n·40 + 17) (with n being the number of argon atoms) and thus reproduce the results of Lineberger *et al.* [81]. Furthermore, Ar-clusters with O^-, O_2^- or H^- are possible as well, which is not reported in [81].

However, besides the already reported species new ones are identified here as well: $Ar_nO_2^-$ and Ar_nH^- (subset of figure 3.2.6) indicating that – so far – every anion produced in this source can connect to one or several argon atoms.

Another ability of the plasma entrainment source is the production of big argon clusters. Ar_nOH^- clusters with n > 40 are reported in [81] and also measured here in figure 3.2.7. Such clusters were not observed in the laser ablation source since the expansion conditions are different and argon is known for its high likelihood to cluster in comparison to helium.

Figure 3.2.8 shows next to the typical products of the source different carbon clusters (C_2H^-,$C_2H_2^-$ and $C_2H_2O^-$). They can also be considered typical source products since they are generated in the plasma, which sputters material from the stainless steel electrodes of the plasma valve hat. However, laser ablation also creates a plasma, which can sputter carbon from the stainless steel of the main block and form various clusters with Au^- (m/z 200 - 260 in figure 3.2.4a). However, they could also be the result of impurities of the gold target.

Apart from carbon clusters, figure 3.2.8 also shows $[Ala\text{-}H]^-$ at m/z 74 verifying the deprotonation process. A relative comparison of signal strength and temperature of this signal between both sources is not possible but the signal in the plasma entrainment source is in general more stable and intense than in the laser ablation source. Fur-

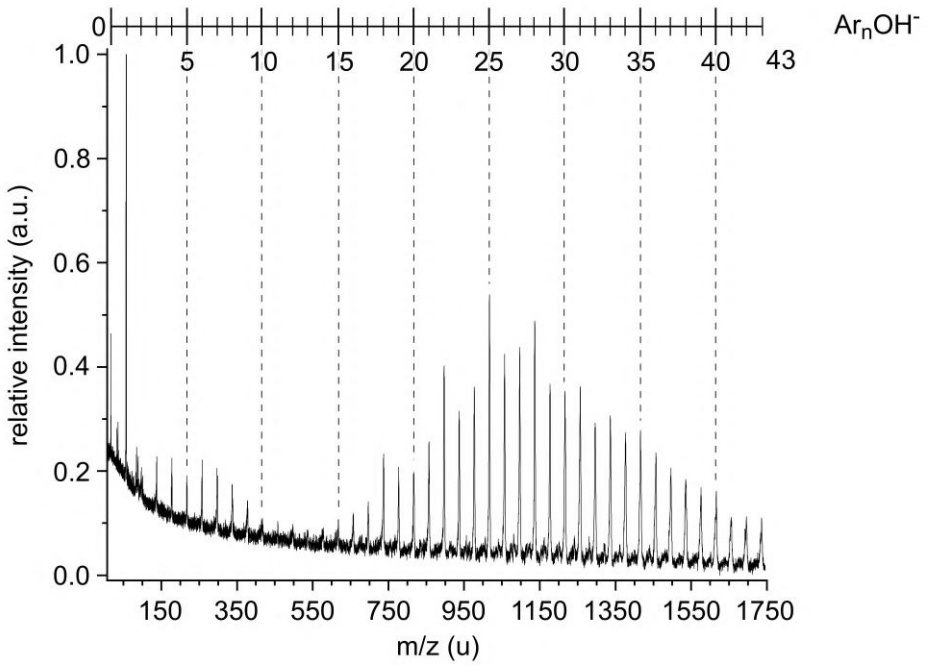

Fig. 3.2.7.: MS illustrating the production of large Ar clusters with the new plasma entrainment source. Large clusters indicate an effective cooling process of clusters.

thermore, due to the better cooling efficiency of Ar in comparison to He and due to the supersonic expansion of the plasma entrainment source, the source products will be cooler than in the laser ablation source.

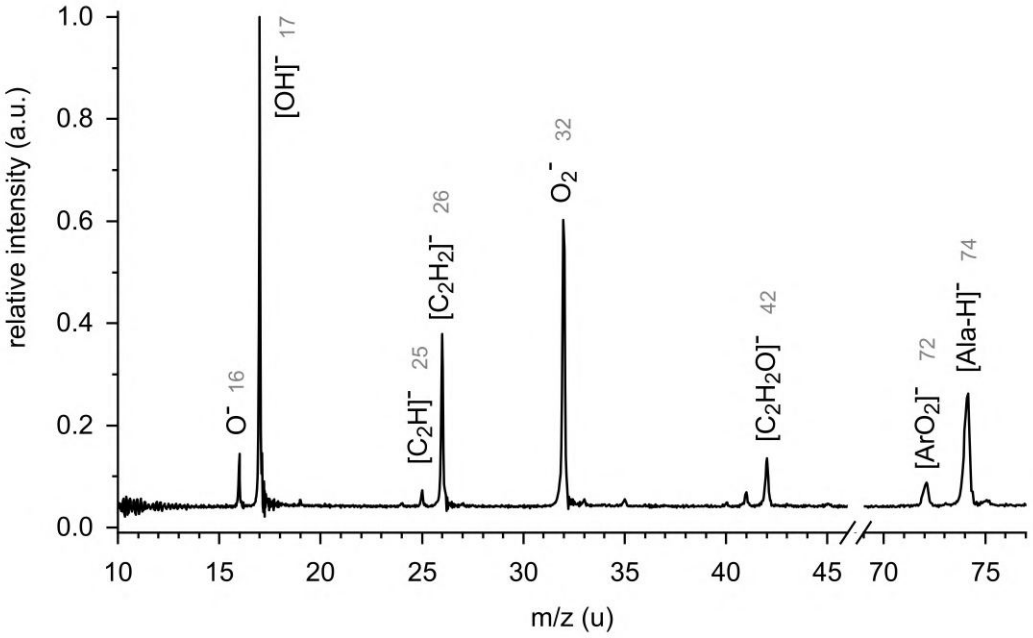

Fig. 3.2.8.: MS from the plasma entrainment source showing typical products of this source (O^-, OH^-, O_2^- and ArO_2^-) as well as Ala-H ($m/$ 74). Various carbon clusters (C_2H^-,$C_2H_2^-$ and $C_2H_2O^-$) can also be considered typical products of this source since they originate from stainless steel sputtering in the plasma region.

3.2.2. Linear Time-of-Flight Mass Spectrometer (ToF-MS)

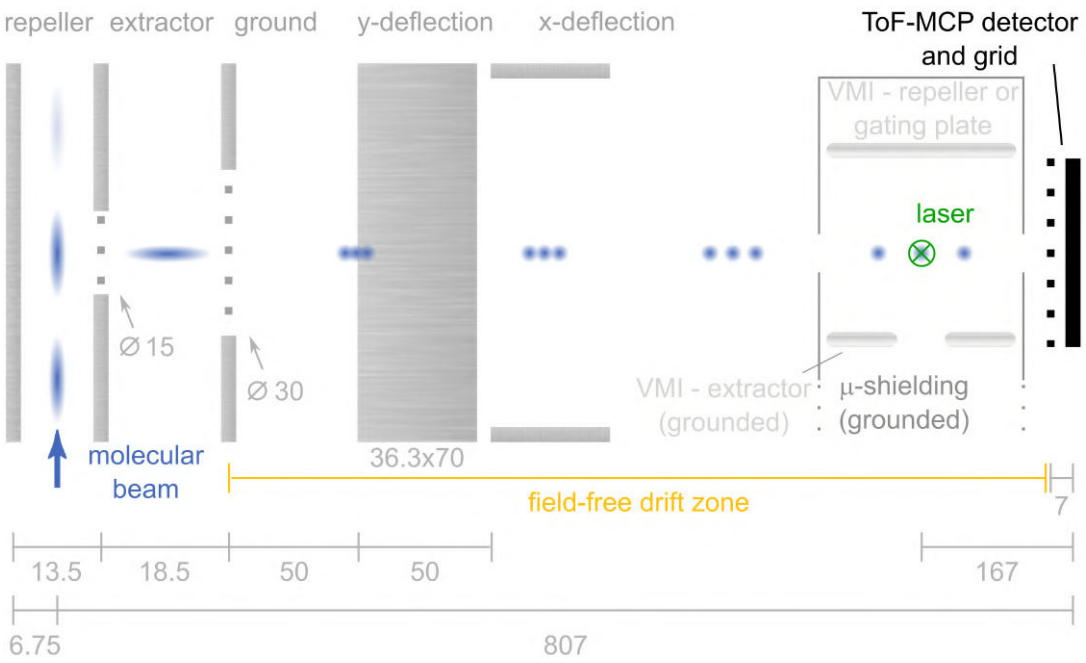

Fig. 3.2.9.: Wiley McLaren-type ToF-MS with deflection plates to guide the anion beam. The different species within one pulse are separated by their time of flight, which can be used to synchronize one specific species with a pulsed laser (green). The species pass through the VMI setup (partly shown) before reaching the ToF-MCP detector. The VMI setup is encased in a grounded μ-metal shielding and its repeller can be used for ion gating. The ToF-MS electrode plates have a dimension of 70x70x1 mm. All distances are given in mm. The figure is not to scale.

Besides the target chiral anion, both the laser ablation and the plasma entrainment source, also produce other products originating from e.g. ion-molecule reactions, clustering, fragmentation etc. leading to various masses and charge states. Therefore, a mass spectrometer is required to isolate the desired substance. One of the available mass spectrometer types is the quite robust and simple linear Time-of-Flight mass spectrometer after the design of Wiley and McLaren (figure 3.2.9)[96]. The voltages on the repeller and the extractor electrodes are pulsed on when the molecular beam is centered in between these electrodes. The anions are thus extracted perpendicularly to the molecular beam, and are separated in time by their mass-to-charge ratio (m/z) in a field-free drift zone after passing through two acceleration stages (repeller-extractor and extractor-ground electrodes). The time of flight distribution can be converted to a mass distribution after adequate calibration. Since this setup is already well established in science and the ToF-MS for this project is described in detail by Grüne in [79] (including calculation of the focal point) just a short description is presented here.

Function of ToF-MS

The physics of charged particles in a field-free drift zone, that were previously accelerated in an electrical field is quite basic: The potential energy of particles with mass m and charge $q = z \cdot e$ (e being the elementary charge and z the charge number) is transformed completely into kinetic energy E_{kin} and is experienced by all ionic particles in the same way. If, furthermore, s is the length of the field-free drift zone and $E = q \cdot U$ the effective accelerating field generated by the effective voltage U then the kinetic energy is expressed as

$$E_{\text{kin}} = \frac{1}{2} m \left(\frac{s}{t}\right)^2 = z \cdot e \cdot U \tag{3.2.4a}$$

$$\rightarrow t = \sqrt{\frac{m}{z}} \frac{s}{\sqrt{2U \cdot e}} \tag{3.2.4b}$$

For singly negative charged particles the equation $z = -1$ holds and U has to be negative. Keeping both the distance s and the acceleration voltage U constant while only focusing on the singly charged particle without initial kinetic energy ($E_{\text{kin},0} = 0$), the arrival time depends solely on their mass m.

It should be noted that the time of flight given in equation 3.2.4b will be lower than the true arrival time since the particles do not start from the ground plate but between repeller and extractor (figure 3.2.9). Hence, the true arrival time is the sum of the time needed to pass through the acceleration stages and the time needed in the field-free drift zone. However, the time of flight in equation 3.2.4b remains a good first approximation of the time of flight.

Resolution

In general, the overall resolution r_{MS} is defined over the peak position in the time of flight or mass spectrum (t or m) and the respective FWHM of the peaks (Δt or Δm)

$$r_{\text{MS}} = \frac{m}{\Delta m} = \frac{t}{2\Delta t}. \tag{3.2.5}$$

The overall resolution of the ToF-MS is restricted by the space and energy resolution. Space resolution depends on the initial space distribution (size of the ion package) while energy resolution is influenced by the initial velocity vectors of two identical ions, which have the same position and speed but opposite flight directions.

Although a single acceleration stage with a subsequent field-free drift zone would suffice for mass-to-charge ratio (m/z) separation, adding a second acceleration zone improves the space and energy resolution of this system clearly [96]. Further design aspects have to be considered to optimize for space and energy resolution, e.g. the distances between electrodes are crucial. For space resolution, the distance between extractor and ground electrode as well as the length of the field-free drift zone should increase. The energy resolution is also improved by an increased field-free drift zone but also demands for a decreased distance between extractor and ground electrode.

Table 3.2.1.: Typical optimized voltages for ToF-MS for different situations. Above dashed line: focus is at ToF-MCP. U_R/U_E is around 1.12. Below dashed line: focus is moved to photodetachment region. U_R/U_E is around 1.14. The photodetachment region is around 17 cm before the ToF-MCP detector. Focusing in this region is important for subsequent VMI measurements.

situation	repeller (V)	extractor (V)
high kinetic energy anions, focus at ToF-MCP	-4000	-3587
lower kinetic energy anions, focus at ToF-MCP	-3010	-2684
focus in photodetachment region	-3010	-2634

This opposite design requirement demands a compromise between space and energy resolution. The length of the field-free drift zone is not restricted by resolution but by the sake of compactness and by the ion loss due to a velocity component perpendicular to the axis of the flight tube. [96]

Once a satisfying design is found and the dimensions are fixed, the resolution will be influenced by the applied voltages, the time the particles spend between repeller and extractor electrode before acceleration as well as the transverse spread of the ion package in the molecular beam. Good space focus or positioning of the focal point is achieved by adjusting the voltage ratio between the repeller and extractor electrode. Also, the decrease of the transverse spread of the ion beam package will improve the space focus. Improved energy focusing can be achieved with the increase of the ratio between the total energy of the ion to its initial energy. The initial energy is mostly thermal energy, which can be reduced by cooling the ion beam. An easier way might be the increase of the acceleration voltage (the voltage applied on the repeller electrode). For the sake of space resolution, the voltage on the extractor will be increased accordingly. Another way to improve the energy resolution is the introduction of a time lag. During the time lag, ions move to new positions due to their initial velocities, which improves the energy resolution but downgrades the space resolution. In the end, a compromise has to be found and influence of time lag on the overall resolution have to be determined for the individual setup. [96]

For the linear ToF-MS used for this project typical voltages for a good resolution are given in table 3.2.1 for different situations. The resolution can be up to $m/\Delta m = 500$.

Calibration of ToF-MS

Calibration of the ToF-MS is performed with a rewritten form of equation 3.2.4b:

$$m_i = c \cdot (t_i + t_{offset})^2 \tag{3.2.6}$$

with $t = t_i + t_{offset}$, where t_{offset} holds all experimental delays (e.g. electronic lag) as well as the time the ions spend in the acceleration stages. The constant c includes all

physical and geometric constants (s, U and e). m_i and t_i are the mass and corresponding flight time for the i-th peak. The identity of at least two peaks in the spectrum need to be known to define both calibration parameters (c and t_{offset}). For the laser ablation source, the gold anion and its clusters are taken for calibration since they are easy to detect in the mass spectrum: Au^- has a strong intensity and the clusters appear in a certain pattern. The plasma entrainment source can be calibrated with its plasma products (e.g. OH^-) and corresponding Ar-clusters ($ArOH^-$). SF_6^- and S^- are taken as an additional calibration species.

With both calibration parameters known, the whole spectrum can be converted from the time domain to the mass(-to-charge) domain. The calibration parameters are pretty stable over long time periods and calibration is only repeated when the voltages (or the geometry) change.

Setup and Abilities

Anions produced in the source need to fly approximately 30 cm (figure 3.2.1) from the nozzle to the perpendicularly oriented ToF-MS and are extracted to the 81 cm (figure 3.2.9) distant ToF-MCP by a set of three electrodes (repeller, extractor, ground). Extractor and ground plate have a high transmitance Ni-mesh to guarantee homogeneous electrical fields in the acceleration stages. Dimensions of the plates and distances between them for this experiment can be found in figure 3.2.9.

The extraction of anions is accomplished by turning on high negative voltages for the repeller and extractor plates with two identically constructed HV switches. If the extractor is switched on 14 ns earlier than the repeller, an enhancement in resolution is observed probably due to a small delay between the high voltage switches.

The already established HV switches (FHI ELAB 3962.3 and 3962.4) were "push" switches, meaning the voltage rises fast but decreases slowly since the voltage drops across a resistor. Later, these switches were replaced with "push-pull" switches (FHI ELAB 4769), which creates a fast rising and falling voltage giving better control over the mass spectrometer.

Two spatially separated pairs of deflection plates, placed after the ground plate of the ToF-MS, are used to guide the ion beam to the MCP detector and rectify the initial direction the anions possess before entering the ToF-MS as well as possible misalignments of the ToF electrodes (figure 3.2.9). Later, these deflection plates were replaced with an Einzel lens. The lens was meant to increase the resolution in the VMI spectrometer, however it never worked satisfactorily and was then only used for deflection.

Ion-gating is a useful tool to remove certain components from the ion beam before they reach the detector of the ToF-MS or in other words let pass only a desired m/z region. The electrical field performing the gating comes from an additional deflection plate, called the gating plate, and is switched by a "push-pull" switch. Only for the m/z region of interest the voltages are switched off to provide a window for ions to pass. This window is normally quite short emphasizing the importance of "push-pull" switches over "push" switches and fast falling voltages. Ion-gating was initially not implemented in this setup but can be achieved by exploiting the repeller (or extractor) of the VMI

spectrometer as the gating plate. The VMI-repeller is encased in a grounded μ metal shielding and is placed perpendicularly to the ToF-MS. It is placed close to the ToF-MCP where m/z separation is sufficient for ion gating (figure 3.2.9). Here, 500 V at the VMI-repeller are sufficient for ion-gating, but 2000 V were also successfully used.

As already described in the beginning of this section, this ToF-MS is not only able to detect anions but also neutrals due to a grid placed before the ToF-MCP detector: The anions pass the grid held at ground potential if no preceding photodetachment is done and are deflected for a grid voltage higher than the ToF-repeller (here: around 500 V more) if photodetachment is performed (green circle with cross in figure 3.2.9). Thus separating anions from the neutrals.

3.2.3. Velocity Map Imaging (VMI)

Next to mass spectrometry, anion photoelectron spectrometry is used to reveal the energy levels of neutrals by photodetaching one of the anion's electrons and recording its kinetic energy, which depends not only on the photon energy but also on the energy level the electron is detached from. The type of photoelectron spectrometer, which is used for this thesis, is the VMI spectrometer. Besides energies, the VMI spectrometer can also measure the momentum of charged particles providing angular information, which is important for PECD measurements. A description of this technique as well as corresponding data handling techniques (reconstruction methods), resolutions and calibration procedures are given here.

Photoelectron spectra and PECD measurements are recorded with a Velocity Map Imaging spectrometer inspired by the design of Eppink and Parker [97]. It is an electron lens system made out of three electrodes (repeller, extractor and ground) like shown in figure 3.2.10. The design reminds of the setup of the ToF-MS, but while for the ToF-MS homogeneous electrical fields between the electrodes are desired, the VMI spectrometer is meant to form an electrostatic lens. This is achieved by removing the meshes from the openings of the extractor and ground electrode[6]. The electrostatic lens forms between extractor and ground electrode and focuses every electron with the same velocity vector (direction and absolute value) on the same point of a detector even if the starting point of each electron is different. Hence, Eppink and Parker called this technique Velocity Map Imaging.

Typical VMI images are closed or open rings with diameters, which increase with increasing electron speed (figure 3.2.10). Open rings look like two half moons, which can be either parallel or perpendicular to the laser polarization axis. The type of ring (closed or open) and the alignment of these half moons is connected to the anisotropy parameter and is reflected in the direction of the electron's velocity vector (figure 2.2.2).

An important property of the VMI spectrometer is that the absolute resolution can be adjusted (to some extent) with the repeller voltage since it determines also the spread in velocity. Best absolute resolutions are achieved with slow electrons, which are yielded with small VMI-repeller voltages. This is discussed further in section 3.2.3.5.

[6]Grid wires also remove signal and cause grid deflections blurring out sharp details in the data.

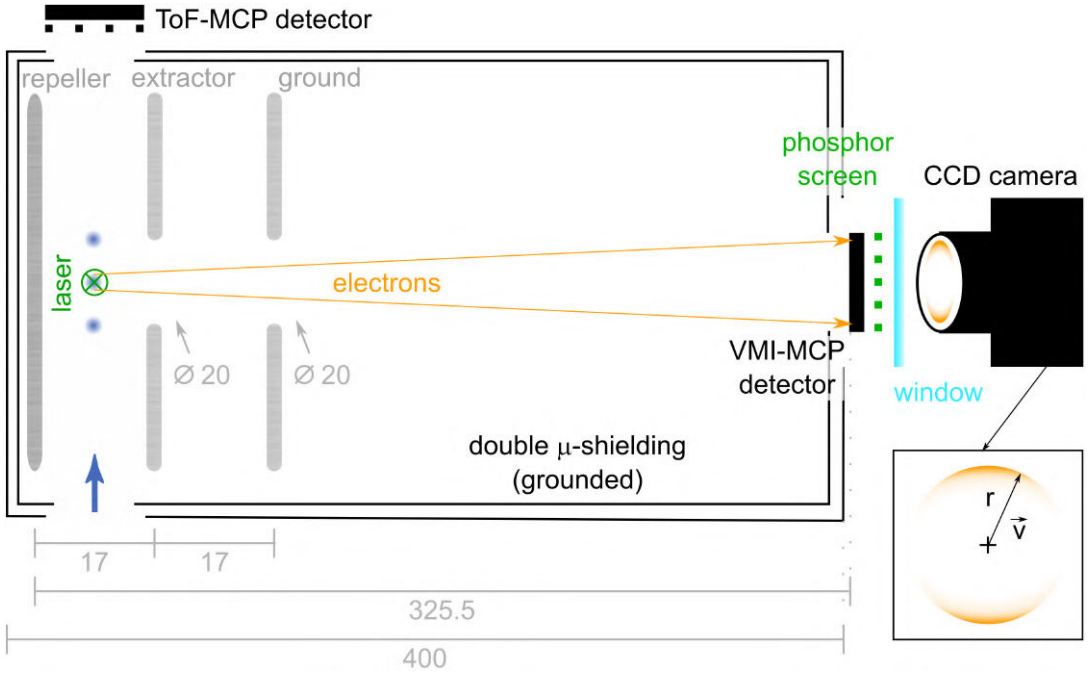

Fig. 3.2.10.: Electron Velocity Map Imaging spectrometer according to Eppink and Parker. The lens setup is covered in a double μ-metal shielding. The molecular (blue) and laser beam (green) meet in the interaction zone between repeller and extractor plate. Electrons (orange) with the same velocity vector are focused on the same point of the detector, which consists of a MCP, a phosphor screen and a CCD-camera. Only the CCD-camera is outside of the vacuum chamber (indicated by the window). A typical VMI image is shown in orange under the CCD-camera: Electrons accumulate in closed or open ring structures, where the diameter is determined by the absolute velocity of the electrons. All electrodes are discs with an outer diameter of ∅ 100 mm and a thickness of 2 mm. Other distances are given in mm. The figure is not to scale.

Since the original publication, several new and more complex designs have emerged to fulfill different purposes like investigating high-lying Rydberg states, which are sensitive to electrical fields and therefore require small extraction fields [98], or the recording of high-resolution data with additional field-correcting electrostatic lenses [99]. Despite the available sophisticated VMI designs, a simple design like the one of Eppink and Parker can suffice for vibrationally-resolved spectra if a cold molecular beam is used in combination with the SEVI method (Slow Electron Velocity Map Imaging) by Neumark *et al.* [100, 101].

The three electrode design from Eppink and Parker is applied here as well and its dimensions are shown in figure 3.2.10. The ion packages interacts with a pulsed laser beam between the repeller and extractor electrodes, leading to photodetachment in the VMI electrodes center, around 170 mm before the ToF-MCP (figure 3.2.1). The released electrons are extracted through switched electric fields to the 317 mm distant detection system composed of a MCP (VMI-MCP) detector with an active diameter of 45 mm, a phosphor screen (P47) and a CCD camera from Basler. During measurement with gold

complexes, the camera model A102f with 1392 x 1040 pixel and a pixel size of 6.45 x 6.45 μm was used but exchanged later for a model with increased resolution. The new model acA1600-20gm has 1626 x 1236 pixel with a pixel size of 4.4 x 4.4 μm and was mainly used for measurements with deprotonated molecules. The VMI electrodes are encased in a double layer μ-metal shielding to suppress interaction of photo-detached electrons with earth magnetic fields. The shielding ends just before the detection system and is on ground potential. The material of the VMI electrodes started out as stainless steel. These electrodes were used mainly for the gold complex measurements[7]. In the case of deprotonated molecules, the electrodes were exchanged with electrodes made out of molybdenum. Molybdenum is paramagnetic and hence can not retain a magnetic field (without an external one), which can disturb the photodetached electrons. Furthermore it has a high melting point making it resilient in the case of high voltage discharges and it does not (quickly) form an isolating oxidation layer if exposed to air.

As mentioned in the beginning of this chapter, the perpendicular setup of the VMI spectrometer allows simultaneously recording the PES with the VMI-MCP detector and the signal of neutrals created in the photodetachment process with the ToF-MCP detector. Unfortunately, the perpendicular setup also causes a spacial displacement of the photoelectron distribution from the center of the detector since electrons detached from the ion package always have a velocity component parallel to the ToF axis. This displacement becomes more important for a smaller acceleration of detached electrons and for lighter investigated molecules but can be reduced by decreasing the acceleration voltage at the ToF plates or can be compensated by applying a tilt to the VMI setup. Here, the VMI spectrometer is tilted and the acceleration voltage of the ToF-MS reduced. However, the decrease of the acceleration voltage is limited since the energy resolution of the ToF-MS gets worse for smaller ToF-repeller voltages (section 3.2.2). Another point is that with a perpendicular setup, the resolution of the VMI spectrometer is coupled to the energy spread of the ions in the molecular beam. The ToF-repeller voltage influences this spread but is, again, limited due to the energy resolution of the ToF-MS.

3.2.3.1. Data Acquisition

The electrons are recorded with a imaging quality MCP detector with an active diameter of 45 mm followed by a P47 phosphor screen, which converts the electron hits into visible light for a CCD camera to record. For noise/background reduction, the VMI-MCP is pulsed to an operating voltage of around 1600 - 1800 V for 0.15 μs during measurements to ensure that only electron signal arising from the photodetachment process is recorded. Compared to other switched potentials in this experiment, the voltage does not fall to 0 V after a measurement but to a standby voltage of around 1200 V, which is below the threshold voltage required to detect electrons. Hence, fast (but gentle) switching is achievable for the VMI-MCP.

[7] The stainless steel plates were later gold plated to elevate the work function and avoid electron background but Nickel was probably taken as intermediate layer (acting as "glue"), which is ferromagnetic.

The data is visualized, collected and saved with a custom LabVIEW program called "VMI Imaging" that was modified for PECD measurements as well as for continuous saving within this project. The measurement program has several measurement modes: normal, continuous, Area-of-Interest (AOI), event and PECD mode. In short, the normal mode records electron hits as spots, which cover several pixel. The size of the spots depend on the camera focus and the voltage applied to the VMI-MCP detector. It is used for calibration measurements due to the fast recording time. If the measurement restarts several times automatically, the continuous mode is used. This allows for rough camera alignment work. AOI mode selects (virtually) the region of interest on the CCD chip of the VMI camera, which will be recorded. The event mode uses centroiding to assign one pixel to one electron hit resulting in superior resolution in comparison to the normal mode, which records spots. It is used for the main measurements with linear polarized light. The PECD mode works in the event mode and saves two alternately recorded data sets simultaneously and individually. Here, the mode is synchronized with the shot-to-shot polarization alternation to separate LCP and RCP data (more details can be found in section 3.2.4). This mode is important, but not restricted to, PECD measurements.

An electron hit is translated into light by the phosphor screen. If a certain intensity treshold is satisfied the electron hit is registered and interpreted by the computer as 1. The hit is saved in a 1236x1060 matrix, which can be illustrated as VMI image. The VMI image of the current experimental cycle is added to the sum of VMI images of previous cycles. Only the resulting sum is stored and used further. In the end, one 1236x1060 matrix is created. If operating in PECD mode two matrices are saved, however the storing concept remains like described for the individual image.

3.2.3.2. Reconstruction of the Original 3D Distribution

Already 35 years before the first VMI spectromter, Herschbach [102] described for reactive collisions in crossed beam experiments reaction products, which have to expand in spheres (originating from the same center) according to the conservation of energy. The radius of these spheres are determined by the (kinetic) energy of the reaction products. Furthermore, the conservation of angular momentum leads to an angular distribution of the products with cylindrical symmetry. All this was derived by applying Newtonian mechanics. Even if Herschbach is not naming it as such, he described what is known today as Newton sphere. The same concept is applicable for other processes as well like photodissociation, ionization or photodetachment [103–105].

For photodetachment, a Newton sphere consists of electrons and expands until it is projected as a 2D distribution on the VMI detector leading to the typical (open and closed) rings visible in VMI images (orange ring in figure 3.2.10). This sphere contains the information about the kinetic energy of electrons in form of the sphere radius r and their angular distribution in the form of polar and azimuth angle θ and ϕ (figure 3.2.11), respectively. Image reconstruction is required to extract this three-dimensional information from the projected 2D detector image.

Methods for Inversion and Fitting Procedures

One of the earliest reconstruction methods is the inverse Abel method, which was already applied by Eppink and Parker [97]. It was first introduced by Niels Henrik Abel [106] and is covered in several text books like from Whitaker [107]. If the y-axis is the direction the extraction field accelerates the Newton sphere, and if the symmetry axis (e.g. laser polarization vector for linearly polarized light) defines the z-axis (figure 3.2.11), then the 2D projection $f(x,z)$ of the 3D distribution $F(x,y,z)$ is given in Cartesian coordinates by

$$f(x,z) = \int_{-\infty}^{\infty} F(x,y,z)dy = 2 \cdot \int_{0}^{\infty} F(x,y,z)dy \tag{3.2.7}$$

where the property of $F(x,y,z)$ being an even function is used. Since the VMI exhibits cylindrical symmetry, $r^2 = x^2 + y^2$, the following relation

$$dy = \frac{r}{\sqrt{r^2 - x^2}}dr \tag{3.2.8}$$

leads to the Abel transform

$$f(x,z) = 2\int_{|x|}^{\infty} \frac{F(z,r)r}{\sqrt{r^2 - x^2}}dr \tag{3.2.9}$$

By performing the inverse Abel transformation

$$F(z,r) = -\frac{1}{\pi}\int_{|r|}^{\infty} \frac{\partial f(x,z)}{\partial x}\frac{1}{\sqrt{x^2 - r^2}}dx \tag{3.2.10}$$

a given projected 2D image yields the desired 3D distribution.

This approach is relatively easy to implement and was successfully applied for particles where the kinetic energy E_{kin} is small compared to the energy of the extraction field E_{U} ($E_{\mathrm{U}}/E_{\mathrm{kin}} \approx 1000$) but showed discrepancies when both energies become more similar ($\frac{E_U}{E_{kin}} \ll 1000$) [108]. Unfortunately, further problems like the computationally costly integration required by the inverse Abel method, a calculation impediment due to the singularity at $r^2 = x^2$, and the tendency of noise amplification owing to the derivation of the 2D image in equation 3.2.10 diminish the allure of this approach [107]. These problems are tackled with the Fourier-Hankel technique, which is based on the Hankel transformation of the Fourier transformed projection of equation 3.2.7. The singularity from before is avoided and noise is reduced. However, the problems with the noise are not completely solved. In fact, noise is accumulated along the center line (coinciding with the symmetry axis) of the reconstructed image. Particularly for PECD measurements this might be a problem since, here, the symmetry axis is defined by the propagation direction of the light and, hence, is the axis where maximal PECD asymmetry is expected.

The BAsis SEt EXpansion (BASEX) method [109] avoids the direct calculation of the cumbersome inverse Abel integral in equation 3.2.10 by employing basis set functions (similar to Gaussian functions) with well-known inverse Abel integrals. Hence, this

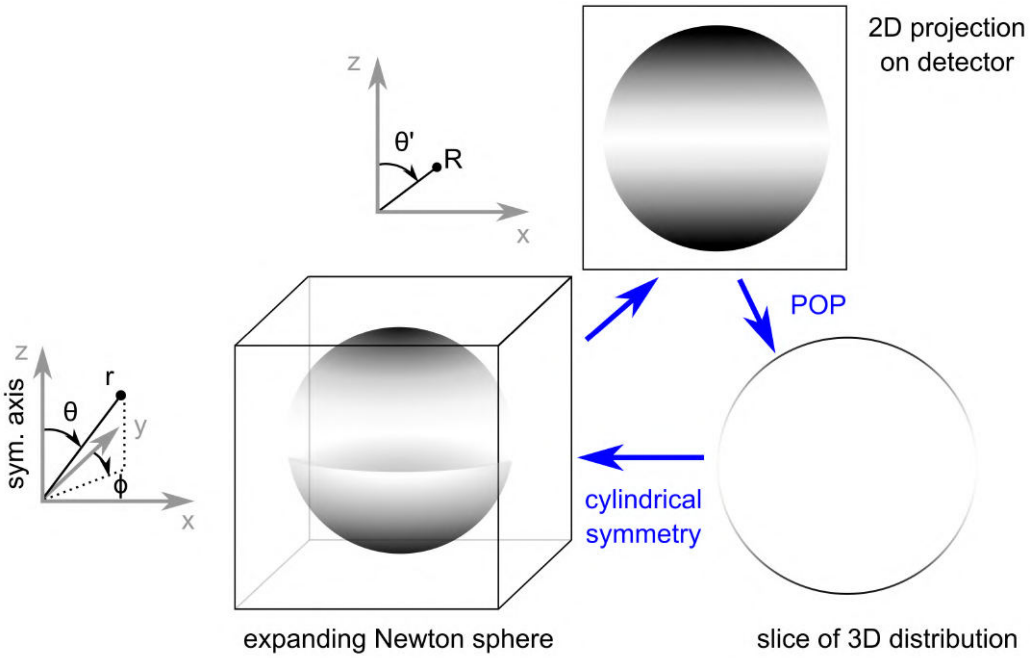

Fig. 3.2.11.: Projection and reconstruction of the 3D distribution. The Newton sphere expands until it is projected on the detector. The 2D projection will contain $\phi \neq 0$ contributions from the 3D sphere, which will be iteratively removed by the POP approach. The full 3D distribution is recovered assuming cylindrical symmetry.

approach is efficient and computationally inexpensive but – among other things – still poses the continuing problem of the accumulation of noise at the center line in the reconstructed image. If prior to inversion with BASEX a transition from Cartesian to polar coordinates is performed to match the given symmetry of the problem, the accumulation of noise at the center line is replaced by a less disturbing accumulation of noise at the center. Furthermore, superior resolution and accuracy, in comparison to the inverse Abel transformation or (Cartesian) BASEX method, makes this method more appealing. Since this method employs BASEX in polar coordinates, it is called pBASEX (polar BASEX) [110].

Another reconstruction method is the Polar Onion Peeling (POP) approach by Zhao *et al.* [108], the successor of the (Cartesian) Onion Peeling Method. The fundamental assumption is that a cylindrical symmetry is present and that the 2D projection contains ϕ contributions from the 3D Newton sphere, which must be "peeled away" in order to reconstruct the 3D distribution (shown in figure 3.2.11). This is achieved by repeated numerical simulations of the 2D image at different values of r with a numerical fit of the experimental data, thus completely evading the costly derivation of the 2D image.

In this approach, the distribution of the Newton spheres is expressed in spherical coordinates (r, θ, ϕ) with an angular distribution independent of ϕ due to the cylindrical symmetry. The corresponding 2D projection on the other hand is described with R, θ' (figure 3.2.11). Since electrons have a radial (speed) distribution described by the

delta function $\delta(r)$, they can contribute to a signal on the 2D distribution, which has a smaller radius than the radius determined by the velocity of the electrons (e.g. at R<r) [108]. This is the influence of the $\phi \neq 0$ components of the Newton spheres on the 2D distribution. If the experiment has more than one transition - or rather many Newton spheres with different radii -, the 2D projection will contain these contributions as well. The only circumference without the influence of other Newton spheres or $\phi \neq 0$ contributions is the outermost ring at $r_{\max}$, which is removed (or "peeled away") from the experimental 2D image by subtracting a simulated image gained from fitting a sine/cosine or Legendre polynomial type function to the experimental image. A "slice" of the 3D contribution containing the largest r contribution and a modified experimental image remain. Afterwards, another simulation of the modified experimental image is calculated and the peeling process starts once more. The slicing and peeling process is performed for every value of r and is repeated until the center of the image is reached. Hence the name "onion peeling". Finally, with cylindrical symmetry the full 3D distribution is obtained. Unfortunately, the permanent calculation of the simulated distribution for every r is time-consuming and slows down the reconstruction process [111]. To speed up the polar onion peeling (POP) method of Zhao *et al.* [108], the ideas of pBASEX are applied to avoid the direct calculation of the simulation of the experimental image and using basis set functions in polar coordinates, as demonstrated by Roberts *et al.* [111]. This method is fast enough to perform POP during data acquisition and thus permits real-time analysis of the 2D images.

All the presented methods to reconstruct the Newton sphere (Abel, BASEX, pBASEX, POP) are briefly compared for photoelectron imaging by León *et al.* [99]. All methods produce a satisfying reconstructed result, with the BASEX method performing a little better than the others. However, since BASEX faces the problem with center line noise it is not suitable for PECD measurements and therefore another procedure is chosen.

From the here mentioned reconstruction methods, only POP by Roberts *et al.* [111] is used in this thesis. However, other methods like rBasex from the PyAbel package [112] and Meveler by Dick [113] are also employed. rBasex can be seen as an update to pBASEX, which enables the representation of Newton spheres as linear combinations of the basis functions. Meveler on the other hand uses a different approach by reconstructing the distribution with probability theory.

Polar Onion Peeling: Reconstruction Method using Fitting Procedures

In this project, the real time POP method from Roberts *et al.* [111] is mainly applied to reconstruct photoelectron spectra measured with linearly and circularly polarized light. Here, the 2D projection is captured by a CCD camera in Cartesian coordinates and needs to be mapped on a polar array to convert to polar coordinates (R, θ') prior to reconstruction [111]. In order to achieve comparable information content, the polar pixel size is chosen similar to the Cartesian pixel size. Thus, the differential area remains almost constant, and the number of polar pixels necessary to form one complete ring at R will scale with R. The intensity of a polar pixel is defined by rotating it by θ' around its pivot point and combining the signals from the four surrounding Cartesian pixels,

which overlap it. Hence the number of angles, at which pixels can be specified, scales linearly with R, leading to a triangular-shaped 2D image in polar coordinates or polar image $p(R, \theta')$ (figure 3.2.12). As described in [111], the polar image can be considered as a sum over individual 2D projections $g(r; R, \theta')$ for all r components of the full 3D distribution

$$p(R, \theta') = \int_0^{r_{\max}} g(r; R, \theta') dr \tag{3.2.11}$$

with $R < r$. The semicolon indicates that the 2D projections are given at a specific radius r. Assuming there is no signal beyond the edge of the detector, the outermost ring contains no ϕ contribution and the substitution

$$g(r; R, \theta') = h(r, \theta) \tag{3.2.12}$$

at $r = R$ can be used whereas $h(r, \theta)$ can be considered as "3D" distribution without the ϕ contribution.

Beginning with the largest radius, $h(r_{\max}, \theta)$ is fitted to the angular distribution:

$$I(\theta) = N(r) \sum_n b_n(r) P_n[cos(\theta)] \tag{3.2.13}$$

where P_n are the n^{th} order Legendre polynomials, $N(r)$ is an intensity factor and b_n are the anisotropy parameters (with $b_2 = \beta$). In this case, n is determined by the physics of the process. The factors $N(r)$ and $b_n(r)$ are the result of the fitting process and lead to the function $g_{\text{fit}}(r; R, \theta')$, which subsequently is subtracted or "peeled away" from $p(R, \theta')$ for every $R \leq r_{\max}$. This procedure is repeated iterative until the center of the image is reached.

The main difference to Zhao *et al.* [108] is that the function $g_{\text{fit}}(r; R, \theta')$ is not calculated but rather obtained with idealized radial distribution functions $d_r(R)$. They are the result of angular integration of isotropic images and create a basis set $D(R, r)$ [111]. $D(R, r)$ only has to be calculated once. $d_r(R)$ are loaded once at the start of the routine.

Given the number of polar pixels at r, $\rho(r, R)$ along with their intensities an idealized isotropic polar image can be computed now:

$$g_{\text{ideal}}(r; R, \theta') = \rho(r, R) d_r(R) \tag{3.2.14}$$

Finally,

$$g_{\text{fit}} = g_{\text{ideal}}(r; R, \theta') N(r) \sum_n b_n(r) P_n[\frac{R}{r} cos(\theta')] \tag{3.2.15}$$

In the case of photoelectron spectra acquired with circularly polarized light, the same reconstruction methods can be used if the symmetry axis is changed to the axis of light propagation instead of polarization direction. Simply put, the image is rotated by 90° prior to reconstruction.

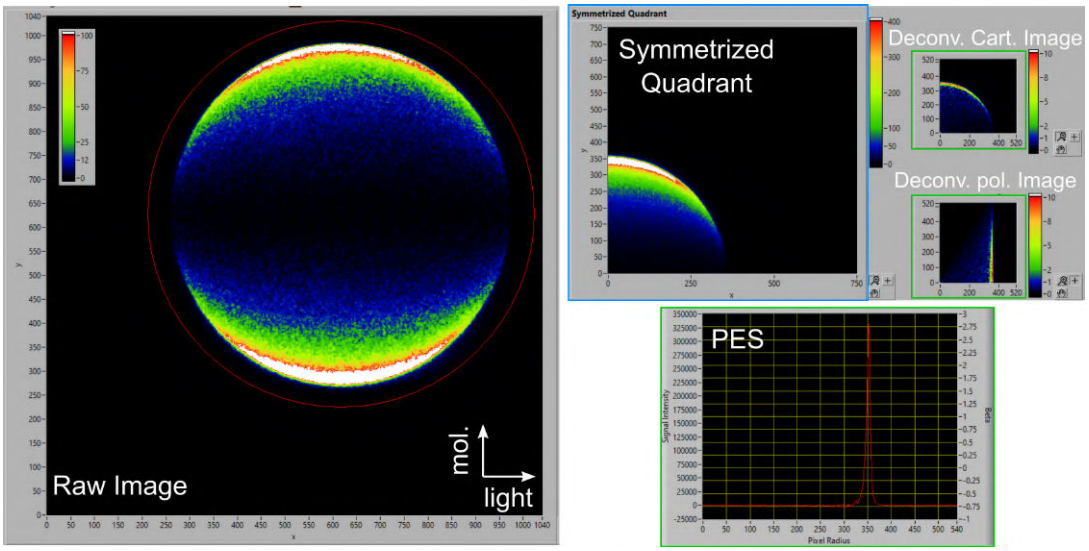

Fig. 3.2.12.: Elements of the reconstruction program "manip_ POP_ v5" used for this thesis. The "Raw image" contains the recorded image. It can be taken as it is or smoothed prior to further processing if it was recorded in event mode (not shown). Symmetrization leads to one quadrant (blue frame). After POP all windows with a green frame are generated: the deconvoluted Cartesian and polar image as well as the radial PES, which is the result of angular integration. The anisotropy parameter is calculated in another subroutine (figure 3.2.13).

3.2.3.3. Implementation of POP

The POP method is incorporated in an existing LabView program "manip_ POP_ v5" (figure 3.2.12), which not only enables reconstruction of the image but also has other features for image preparation. The important steps of the procedure to obtain the radial PES and anisotropy parameter from a recorded image are as follows:

1. The recorded image is loaded and taken as "Raw image". If the image is recorded in event mode, the image is smoothed with a subroutine "Smooth", which performs Gaussian convolution on the raw image (A squared matrix of pixels is assigned to every pixel of the raw image. The size can be set manually).

2. In the case of images recorded with circularly polarized light, the image has be rotated by 90°, which is done with the self written subroutine "RotateData".

3. The center of the (smoothed) raw image is estimated with the help of an artificial red circle (in the raw image of figure 3.2.12)

4. Quadrants of the raw image can be selected

5. The (smoothed) raw image is symmetrized via folding the selected quadrants on top of each other. This creates the "Symmetrized Quadrant" (blue frame in figure 3.2.12)

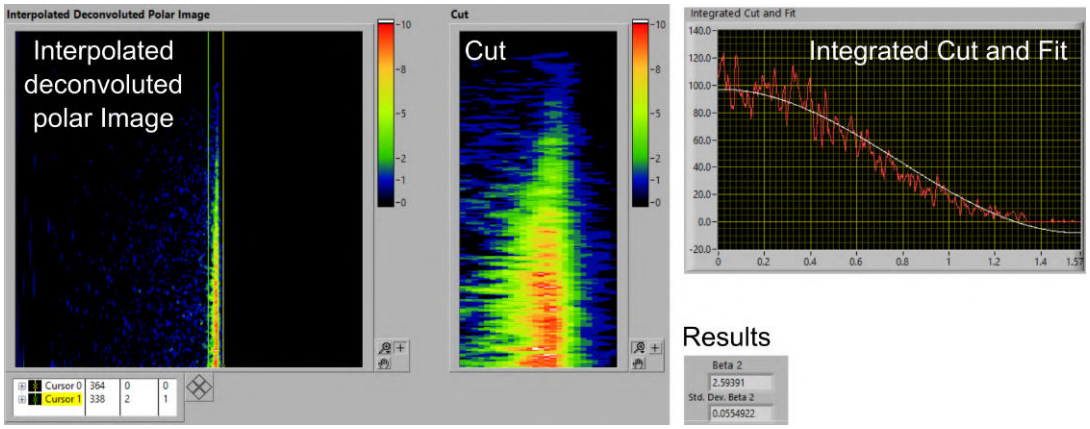

Fig. 3.2.13.: Elements of the "betaplotter", which is a subroutine from the main program "POP" 3.2.12. The interpolated deconvoluted polar image is loaded from the main program. The "Cut" is the zoomed-in area between the cursors of the interpolated deconvoluted polar image and also selects the area, which is considered for the determination of the anisotropy parameter. Integrated cut and fit are shown next to the cut and give the β as well as its standard deviation.

6. Reconstruction with POP is performed, which generates a deconvoluted Cartesian and polar image and the radial distribution, which corresponds to a PES.

7. The PES is saved and loaded as reference spectrum, a new image center is chosen and the procedure is repeated beginning from step 5. The new PES is compared to the reference PES by eye or with the help of a self written subroutine "Gaussfit", which fits a Gauss function to the spectrum and gives for example the FWHM. The new spectrum replaces the reference PES if it is the better spectrum (resolution). This is repeated until the best spectrum is obtained.

A former version of this program was already described and used by Yubero [68] but modified by the addition of the subroutines "Gaussfit" and "Rotate" to analyze the PES within the same program and adapt it for PECD measurements, respectively.

The anisotropy parameter is obtained via the subroutine "betaplotter" (figure 3.2.13) after the best spectrum is found. The deconvoluted polar image is loaded from the main program and is interpolated. Stripes visible in this image correspond to transitions and can be selected via the cursors. In the example of figure 3.2.13 only one stripe is visible since only one transition is recorded with the VMI spectrometer. If the area of interest is chosen with the cursors, a "Cut" is shown, which is a magnified part of the area of interest. Only the cut is used for the fitting procedure and β calculation. Here a non-linear curve fit with the Levenberg-Marquardt algorithm (damped least-squares method) is used. In short: The errors between model function and a data set are determined, squared and added together. If the sum is minimized, the ideal fit is found.

Next to POP other reconstruction methods are used, namely rBasex and Meveler. However, POP will be the main reconstruction program in this thesis and will always be used if not stated otherwise. It is used for all spectra (obtained with linear or circular

polarized light) and for PECD analysis of deprotonated molecules and gold complexes as well as for the anisotropy parameter in gold complexes.

rBasex

In this thesis, rBasex implemented in the PyAbel package is used [112, 114]. Its main application in this thesis is for the anisotropy parameter of deprotonated molecules and the reconstruction of PECD images. rBasex can be seen as an improved version of pBasex. Like pBasex, rBasex uses basis sets in polar coordinates, but applies radial distributions as basis functions from Ryazanov [115]. They are more convenient since they have analytical Abel transformations. The 3D Newton sphere can now be described as linear combination of these basis functions.

A finite number of spherical harmonics $Y_{\mathrm{nm}}(\Theta, \phi)$ (with $m = 0$) describes the 3D Newton sphere at each speed and this can also be described in form of Legendre polynomials $P_n(\cos(\Theta))$. A PAD recorded as $N \times N$ image has only $N_r \times N_a$ degrees of freedom, if N_r is the amount of radial samples and N_a the number of angular terms. N_a is, similar to n from equation 3.2.13, determined by the physics of the process and is usually a small number. N_r is normally $N/2$. Radial distributions obtained from transformed images of other abel-transformed methods correlate with these degrees of freedom.

Despite the similar implementation to pBasex, there are some major differences:

- Projected basis functions are separable into radial and angular contributions since cosine powers instead of Legendre polynomial are used
- Triangular basis functions instead of Gaussian ones, which are more compact; only neighboring functions overlap
- Custom pixel weighting is possible, which helps if part of the images is broken, blocked or occupied by unwanted signal
- Expansion coefficients arise from a simple linear problem, which improves calculation performance
- Less noise in reconstructed images due to restraints on the angular behavior
- Denoising experimental images with low electron counts due to non-negativity constraint

Another important property of this method is that PECD images can be reconstructed and the dichroism parameter can readily be extracted. In contrast to POP, it is designed to be a more adequate method for PECD measurements.

Implementation of rBasex

The program reconstructing the image via rBasex is called “rBasex” and is implemented in python since the PyAbel package is a python package. The program is executed in the python environment of the command promt and guides the user through the different

steps of image preparation, e.g. image transposing and center determination. The center determined by the corresponding PyAbel function can be calculated via various methods including a center-of-mass calculation. Unfortunately, the calculated centers do not lead to a good PES and can merely be taken as a starting point. Like in POP, the true center has to be found iteratively by comparing PES with different centers until the best PES is found. If the center is determined with the POP program beforehand, the POP-center can be used in the rBasex program, which produces better PES than the calculated centers from rBasex.

MEVIR, MEVELER and MELEXIR: Reconstruction with Probability Theory

Alongside the POP method from Roberts *et al.* [111] and rBasex, MEVELER (Maximum Entropy VElocity LEgendre Reconstruction) from Dick [113] – which is based on the maximum entropy concept – is also used for this project. MEVELER is used to extract the anisotropy parameter from measured photoelectron spectra and its results are validated against POP and rBasex. However, POP and rBasex remain the main reconstruction methods and are used for every spectrum in this thesis.

In addition to MEVELER, two other variants based on the same general concept are developed by Dick, called MEVIR (Maximum Entropy Velocity Image Reconstruction) [113] and MELEXIR (Maximum Entropy Legendre EXpansion Image Reconstrution) [116]. Each variant has different advantages and disadvantages: MEVELER and MELEXIR both assume that the velocity distribution of the electrons can be expanded in Legendre polynomials. However, while MEVELER only works with the 0th and 2nd order of these polynomials, MELEXIR employs higher and odd order Legendre polynomials. Because of this, MEVELER is primarily suited for experiments, which use single-photon detachment (or ionization) with linear polarized light while MELEXIR can also be used for spectra from multiphoton experiments and even PECD experiments. MEVIR reconstructs the image without making any assumptions about the velocity distribution (except the assumption of rotational symmetry around the laser polarization axis) and can therefore handle data containing higher and odd order Legendre polynomials. However, similar to other reconstruction methods, MEVIR creates centerline noise and does not handle low intensity data as good as MEVELER and MELEXIR. Nevertheless, all these versions perform better than pBASEX, especially in the low intensity region (0.01 counts per pixel) [113, 116]. A comparison to POP and rBasex is not made in these publications.

According to Dick [113], the following four matrices are introduced for all variants: $\mathbf{F}$ is defined as the velocity map, which is the slice cut through the velocity distribution at $y = 0$. The (forward) Abel transform (in matrix form) of $\mathbf{F}$ creates the simulated image $\mathbf{A}$, which can be compared to the data $\mathbf{D}$. The optimization process is performed on a hidden map $\mathbf{H}$, which is described later.

All variants work on the same basic principle: Instead of applying inversion to the data or approximations by fitting functions, the most likely velocity map for the given data is selected with the help of probability theory. In particular, the method selects the velocity map that maximizes the probability $\Pr(\mathbf{F}|\mathbf{D})$, which denotes the likelihood that

a given velocity map was produced by the given data. Casually speaking, the "trust" one has in the solution **F** based on the actual data **D** is maximized. This conditional probability can be rearranged according to Bayes' theorem

$$\Pr(\mathbf{F}|\mathbf{D}) = \frac{\Pr(\mathbf{D}|\mathbf{F})\Pr(\mathbf{F})}{\Pr(\mathbf{D})} \tag{3.2.16a}$$

$$\Pr(\mathbf{D}|\mathbf{F}) = \frac{1}{Z}\exp(-L) \tag{3.2.16b}$$

$$\Pr(\mathbf{F}) = \alpha S \tag{3.2.16c}$$

$$\Pr(\mathbf{D}) = \text{const.} \tag{3.2.16d}$$

with $\Pr(\mathbf{D}|\mathbf{F})$ being the likelihood that the data **D** is produced given velocity map **F**, $\Pr(\mathbf{D})$ the probability of **D**, $\Pr(\mathbf{F})$ probability of **F**. Z is a normalization constant, L the maximum likelihood estimator, which is a measure for the similarity of the simulated image **A** (obtained from **F**) to **D**. S is the entropy and reflects the information content of the velocity map **F**.

$$S = -\sum_{i=1}^{N_F} F_i \ln \frac{F_i}{eB_i} \tag{3.2.17}$$

for a strictly positive map. B_i is a default map for the situation before data is recorded. If **F** is of dimension NxM, N_F is one of the dimensions of the map **F**.

Maximizing $\Pr(\mathbf{F}|\mathbf{D})$ is equivalent to maximizing $\Pr(\mathbf{D}|\mathbf{F})$ and $\Pr(\mathbf{F})$. In other words, L has to be minimized and S to be maximized. Hence, this is called the maximum entropy concept.

First L is minimized below a certain threshold L_0. For this, from all possible velocity maps, those that create simulated images **A** with the most similarity to the actual data are chosen. The size of this map selection depends on the desired accuracy defined by L_0. From this selection, the map with the smallest information content (= the maximum entropy) is then selected as F to maximize S. Consequently, information not supported by the data is not contained in F.

The optimization process, minimizing L and maximizing S, is performed on a hidden map **H** and gives **F**. The hidden map is connected to **F** via a linear transformation and introduces correlations between adjacent rows of F. Different "layers", with each layer replacing a pixel value by a weighted average of this pixel and its eight adjacent ones, are possible. Often just one, or a few, layers are needed for the reconstruction. However, if working with low intensity measurements (0.01 counts per pixel), the layers increase the quality of the reconstruction and create spectra in a better quality than pBASEX [113].

Since the velocity map in MEVIR is (largely) free of assumption, all information is contained in the velocity map **F** and Legendre polynomials are not needed for the map itself. However, for this kind of experiment, the velocity distribution $Q_n(v)$ is needed, since they give the anisotropy and dichroism parameter. $Q_n(v)$ is obtained from the map and projection with Legendre polynomials and can be expanded in Legendre

polynomials. The anisotropy parameters are then obtained by

$$b_n(v) = \frac{Q_n(v)}{Q_0(v)} \tag{3.2.18}$$

with n being the order of Legendre Polynomials. For an anionic chiral system photodetached via a single photon process only $n = 1$ and 2 will be of importance, where b_1 describes the dichroism parameter for PECD measurements and b_2 the anisotropy parameter (or β).

In MEVELER, the size of matrix $\mathbf{F}$ is reduced by employing a small number of Legendre polynomials[8]. The number of polynomials depends on the type of experiment conducted. In contrast to MEVIR, an assumption about the velocity distribution is made before the optimization process. Hence, a map is not the result of the optimization process but a velocity distribution. The anisotropy parameters are calculated like in MEVIR (equation 3.2.18).

So far only the velocity distribution is expanded with Legendre polynomials but this expansion can be done with the image data as well. This is the idea of the program MELEXIR [116]. Images containing higher order or odd order Legendre polynomials are of better quality and can be reconstructed faster[9] than with MEVELER. Consequently, MELEXIR is technically not only adequate for PES with linear polarized light but also for PECD experiments.

Implementation of MEVELER and MELEXIR

The MEVELER program provided by Dick [113] works via the command promt (cmd) and needs two command lines: one command line for the preparation of the image, which includes quadrant selection, image transposing and the calculation of the image center. The center can either be entered by the user or is calculated by the program by calculating the center of mass. The second command line is responsible for the reconstruction itself. Here, the method (MEVIR, MEVELER or MELEXIR) can be chosen as well as the order of Legendre polynominals and if only even or also odd orders need to be considered (odd order only for MEVIR and MELEXIR). Output files include a summary of the selected options, a reconstructed quadrant of the image (only for MEVELER) and velocity distributions. The velocity distributions are used for the radial PES and anisotropy (and dichroism) parameters. Instead of writing command lines, a LabView program was designed here as operational help, which writes the command line in the command promt depending on the selected buttons.

Comparison: POP, rBasex and Meveler

For the comparison, the PADs of two atomic anions, namely Au^- and S^-, are reconstructed with all three reconstruction methods, POP, Meveler and rBasex. The resulting

[8] In MEVIR the size of $\mathbf{F}$ is the same as for the data matrix

[9] This means reconstruction in real time like the POP method from Roberts [111].

photoelectron spectra as well as the anisotropy parameter are compared in figure 3.2.14 and 3.2.15.

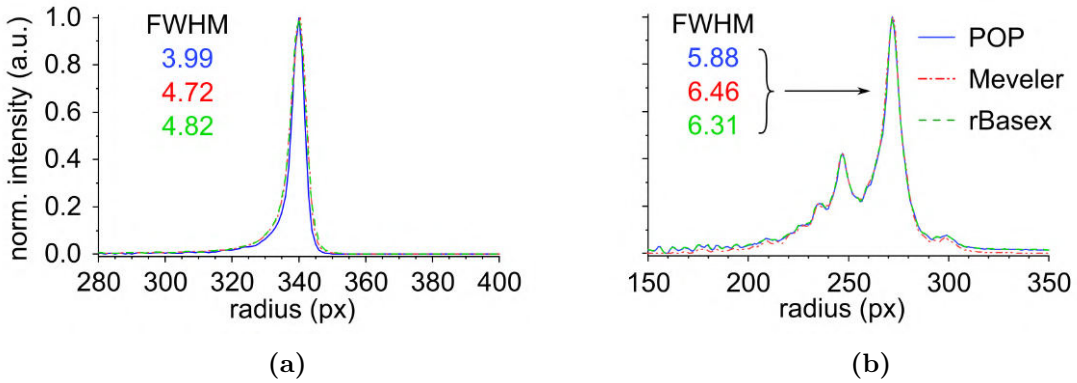

Fig. 3.2.14.: Photoelectron spectra for Au^- (a) and S^- (b) analyzed with different reconstruction methods. The FWHM is given for the most intense peak in the spectrum for each reconstruction method. POP, Meveler and rBasex perform similar in both spectra but POP gives slightly narrower peak widths. In the PES for Au^- POP is visibly better than Meveler and rBasex.

The photoelectron spectra have for all reconstruction methods the same general spectral content and differ only slightly in peak width. However, POP could be declared the "winner" by a small margin since it has the lowest FWHM (best resolution) in the main peak of the Au^- and S^- spectra (figure 3.2.14a).

The easiest case for the analysis of the anisotropy parameter is Au^- since the electron originates from a $6s$ orbital, which corresponds to the transition from $^1S_0$ (anionic ground state) to $^2S_{1/2}$ (neutral ground state) and should have, according to the Cooper-Zare formula (equation 2.2.19a), an anisotropy of 2 regardless of the kinetic energy (parallel transition). This will be used as benchmark for the three reconstruction methods and helps to identify the uncertainty of all methods dependent on the kinetic energy.

Unfortunately, relatively big deviations can be seen for all methods, especially at low kinetic energy for POP and rBasex. The reason for this deviation can not be explained with the way the data was analyzed, e.g. quadrant selection was used, the determined center of the PAD and the correct extractor voltage were confirmed. Furthermore, the circularity of the PAD is checked and higher order anisotropy parameter (e.g. b_4) are considered as "correction parameters" for possible deformations. Last but not least, the data was also plotted over the radius of the transition (not shown) since reconstruction methods based on polar coordinates are known to accumulate more noise in the vicinity of the image center. However, no correlation could be made out. The experimental setup of the VMI seems to be not ideal for anisotropies measured at low kinetic energies.

Meveler seems to give the best performance in the lower kinetic area regime ($E_{\text{kin}} < 1.5$ eV), but it is suspicious that the values given from Meveler are error free and did not deviate from 2 for all digits given (2.0000), whereas POP and rBasex always have at least little deviation. Furthermore, Meveler does not perform differently from the other methods in the S^- case (figure 3.2.15b). This leads to the assumption that Meveler

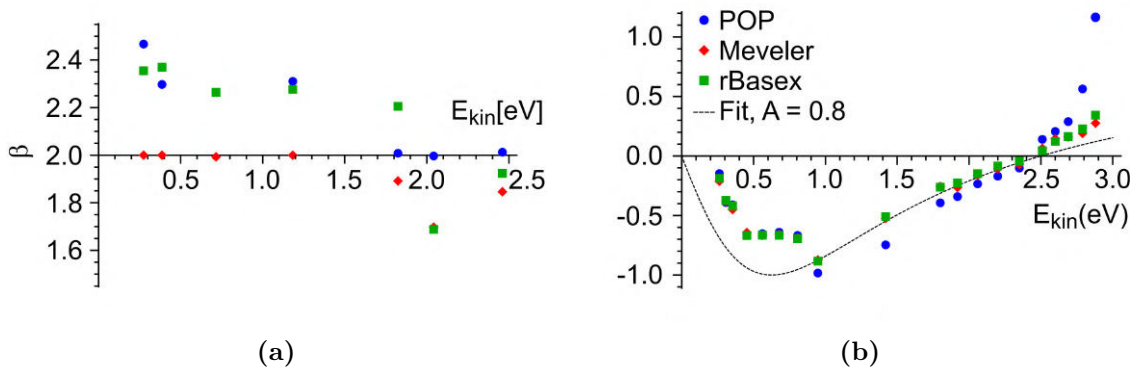

(a) **(b)**

Fig. 3.2.15.: Anisotropy parameter obtained from three different reconstruction methods applied for Au^- (a) and S^- (b). For Au^- the electron originates from an s orbital and should give $\beta = 2$ according to the Cooper-Zare equation (equation 2.2.19a). These deviations between the experimental and theoretical values are used as error for the reconstruction methods. For S^-, the electron stems out of a p orbital. Several unresolved contributions can influence the β parameter especially in the high kinetic energy range but all relevant ones also have p character. Fitting all three data sets to the Cooper-Zare equation leads to similar fit parameters $A \sim 0.8$. The black dotted line represents the Cooper-Zare equation for this fit parameter $A = 0.8$. The legend given for S^- is also valid for Au^-

(forcibly) caps the β parameter for values beyond the limit. In the kinetic energy regime $E_{\text{kin}} > 1.5$ eV, POP seems to give more accurate values than the other methods.

In the case of S^-, the performance of the reconstruction methods is difficult to evaluate since there seems to be no reported value for the anisotropy of S^- or the Hanstrop parameter needed for equation 2.2.19a. However, what is known is that the transition known as electron affinity happens between $^2P_{3/2}$ (anionic ground state) and $^3P_2$ (neutral ground state). Overall, six transitions between an energy of 2.01 and 2.15 eV can be found but are of weaker intensity than the origin band (which give the electron affinity). Due to a too low intensity or energetically close transitions not all of these transitions can be resolved. They are partly resolved for smaller kinetic energies but merge to just one peak if the kinetic energy becomes too high. Concerning the analysis of β, the β at high kinetic energies will probably be a mixture of these different transitions. Luckily, all six transitions are of p character and β will not experience much manipulation due to "orbital mixing".

Despite missing literature values, it seems like all methods perform in a similar manner in the energy regime up to $E_{\text{kin}} = 2.5$ eV. Beyond that region, Meveler and rBasex still give comparable values but POP clearly deviates to higher values. A fit based on the Cooper-Zare formula (equation 2.2.19a) with the Hanstrop parameter A being the fitting parameter leads for all reconstruction methods to $A \approx 0.8$. The corresponding Cooper-Zare formula is given as black dotted line in figure 3.2.15b.

Another aspect is quality of the reconstruction method on the PECD parameter but there are no literature values for PECD on anionic gold complexes and deprotonated molecules, which could be used to judge over the performance of POP, Melexir and

rBasex. However, only POP is used to analyze the PECD value since here rBasex and Melexir, both, give obvious wrong results meaning that the calculated b_1's does not coincide with the raw PECD images. In comparison to POP, rBasex is able to produce reconstructed PECD images directly, which serve for visualization purposes. Melexir should be able to do the same but extracting a reconstructed image is more difficult.

Estimation of Error

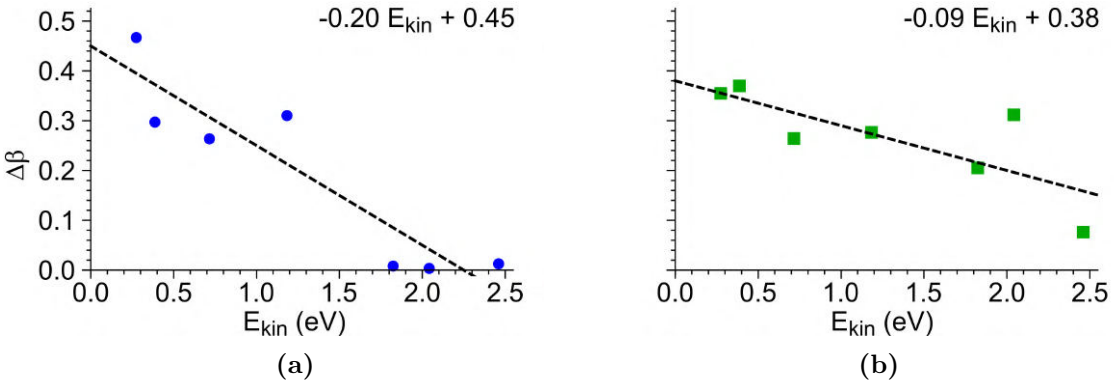

Fig. 3.2.16.: Deviations of the β parameter from the theoretical value ($\Delta\beta = |2 - \beta_{\mathrm{Au}}|$, with β_{Au} being the β parameter from figure 3.2.15a) for POP (a) and rBasex (b). This deviations can be considered as error for the corresponding reconstruction method. The deviations are arbitrarily approximated with a linear error function (black dashed lines) and approximate errors over the whole kinetic energy range.

The size of the experimental error in the determination of β has been estimated from the deviation $\Delta\beta$ from the theoretical value of $\beta = 2$ for the transition $^2S_{1/2} \leftarrow {}^1S_0$ in the photodetachment of Au^-. Only POP and rBasex are considered in the following since Meveler is not used in this thesis for the determination of the β parameter. The deviation $\Delta\beta$ for POP and rBasex are visualized in figure 3.2.16 and are arbitrarily fitted with a linear function:

$$\Delta\beta_{\mathrm{POP}} = -0.20 \cdot E_{\mathrm{kin}} + 0.45 \tag{3.2.19}$$

for POP (figure 3.2.16a) and

$$\Delta\beta_{\mathrm{rB}} = 0.09 \cdot E_{\mathrm{kin}} + 0.38 \tag{3.2.20}$$

for rBasex (figure 3.2.16b). These functions will be used for the gold complexes in chapter 4 and for the deprotonated molecules in chapter 5 to estimate the error of anisotropy parameters for different kinetic energies.

3.2.3.4. Calibration and Optimization

For a meaningful photoelectron spectrum, two important preparations have to be done: voltage optimization and energy calibration. With voltage optimization the goal is to

obtain the best resolved PES. Calibration assigns the radial position a kinetic or binding energy, which is needed in order to be able to assign the measured transition.

Voltage Optimization

To achieve sharp images, the voltage ratio between repeller and extractor needs to be set accurately and has to remain stable during the whole measurement. An appropriate voltage ratio is determined by the VMI geometry and identified in a voltage optimization. For optimization (and calibration) atomic anions are best suited due to their simple and well-known spectra [117]. The aim is to obtain the best resolved atomic spectra with a FWHM that is only determined by the VMI setup. The voltages producing this spectrum are then taken for the main measurement with the target anionic system.

First, the repeller voltage U_R needs to be selected, which determines the maximum of the kinetic energy for the electrons being detected. The repeller voltage is mainly restricted by the limits of the power supply and HV switch. Here, this limit is around 5 kV and corresponds to a maximum kinetic energy of around 5 eV, which can be recorded. The corresponding extractor voltage U_E can be set by performing different measurements with iteratively modified extractor voltages and subsequent comparison between the corresponding reconstructed photoelectron spectra. The ideal extractor voltage is detected when the best-resolved spectrum is attained. In this setup, the optimal voltage ratio U_R/U_E is at around 1.47. An example of this optimization is shown for Au^- with a repeller voltage of 750 V in figure 3.2.17. Here, the best resolved PES is the one with the smallest FWHM at an extractor voltage of 510 V, which corresponds to $U_R/U_E = 1.471$. This voltage optimization needs to be repeated every time the repeller voltage, the light path and/or the extraction time of the electrons is changed.

For the gold complexes Au^- is taken to optimize the voltages. Two exceptions are Au^--Men and Au^--3HTHF at $E_{ph} = 3.49$ eV for which the complex itself was taken for voltage optimization after the binding energy of the complexes had been determined. This is quite unusual but the aim was to get the best (relative and absolute) resolution (section 3.2.3.5) while keeping the transition at large radius and to be able to measure PECD asymmetries at low kinetic energies. Unfortunately, Au^- had no transition in that region and other calibration material like Cu^- did not work out. For the deprotonated molecules S^- is mainly used.

The optimal ratio of ≈ 1.47 for repeller and extractor voltage is used if VMI measurements are performed (VMI mode). However, if the voltages of repeller and extractor are almost equal, the VMI is operating in spatial imaging mode [118]. Here, the detachment (or ionization) coordinate is mapped one-to-one to the detector coordinate. The resulting image is a spatial map of the molecular beam [118]. This mode of operation can reveal deviations of the molecular beam from the center line.

Voltage optimization for a PECD measurement does not only focus on the best resolved spectra but also on the intensity difference of the photoelectron spectra belonging to the image halves for forward and backward direction with respect to the light propagation. Hence, the PAD is reconstructed for the forward and backward direction separately and the intensities are compared with each other. The extractor voltage producing spec-

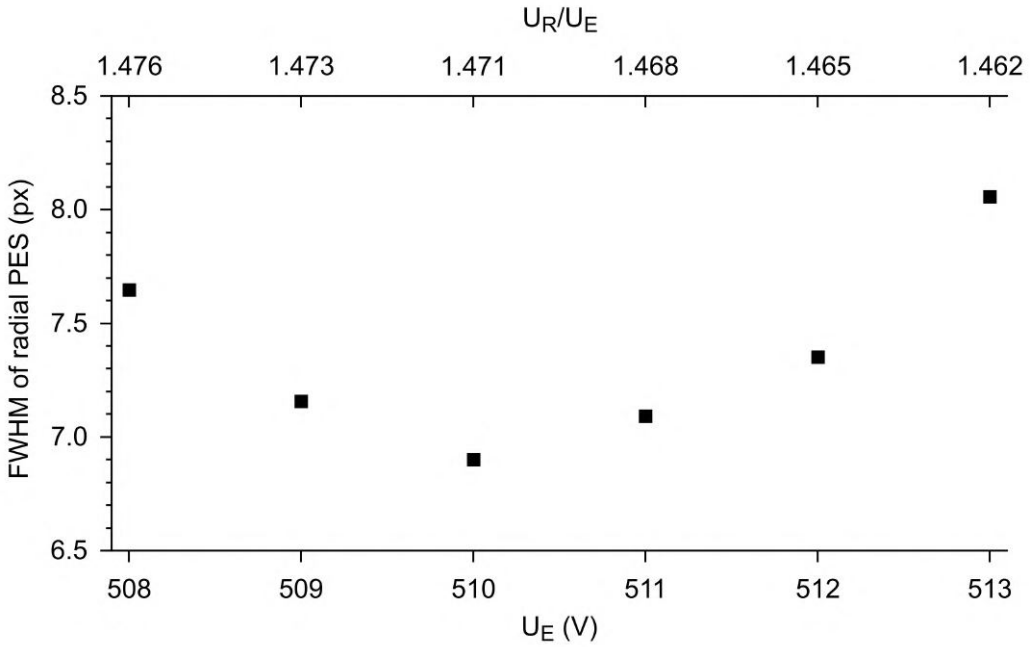

Fig. 3.2.17.: Voltage optimization exemplary on the transition ${}^2S_{1/2} \leftarrow {}^1S_0$ of Au^- with $E_{ph} = 3.024$ eV. The repeller voltage U_R is set to 750 V and the extractor voltage U_E is varied. The FWHM of the transition in the radial PES is determined for each U_E. The best resolved PES is obtained with $U_E = 510$ V, which corresponds to $U_R/U_E = 1.471$.

tra of the same intensity in both halves, for a achiral molecule detached with linearly polarized light, is taken as voltage for the PECD measurement.

At the moment, the reason for this intensity difference despite good voltage optimization is not identified. Many tests were performed to resolve this issue but only lead to theories, which can be excluded: the VMI-MCP detector does not have halves with different qualities. Lens errors, like in an optical lens, could be checked to some extent. Magnetic and electrical stray fields could be excluded and light polarization as well as the measurement mode (Normal, Event) were considered. In the end, similar intensities in both detector halves can only be achieved by adapting the extractor voltage and sacrificing some resolution.

Voltage Stabilization

The use of a wide voltage range in the VMI spectrometer makes a large amount of kinetic energies available to the experiment and opens possibilities for the investigation of many states (with high and low binding energies) at once leading to a "overview" spectrum of the system. On the other hand, small kinetic energies and hence smaller voltages are preferred if a specific state is wished to be studied in more detail since it leads to a better absolute resolution (section 3.2.3.5). Reliably using these different voltage-ranges requires the consideration of voltage resolution and accuracy of the power supplies.

Voltage resolution defines the smallest adjustable voltage interval and needs to be small in order to come close to the ideal voltage ratio $U_R/U_E \approx 1.47$, consequently obtaining a good resolved PES, e.g. for $U_R = 750$ V, the power supply for U_E has to be able to adjust the voltage by (at least) 1 V or else the ideal voltage ratio can not be found (figure 3.2.17). Accuracy on the other hand gives the deviation the output value can have from the set value and describes fluctuation. Keeping the fluctuations small is important for long measurements since voltage drifts can change the quality of the PES during the measurements, e.g. if the power supply drifts by 1 V over time the FWHM can become worse (figure 3.2.17).

During voltage optimization U_E is changed until the ideal, setup specific U_R/U_E ratio is reached. The variation (derivative) of U_R/U_E at the point of ideal U_E becomes smaller for higher U_R. For small U_R a change in U_E of 1 V has a noticeable influence and U_R/U_E will deviate from the ideal ratio resulting in a worse resolved PES (figure 3.2.17). The same can be said for a constant U_E but with changing U_R. Consequently, working with voltage of different order requires different voltage resolutions and accuracies. If voltages of e.g. $U_R = 10$ V are used, power supplies with good resolution and accuracy have to be taken while for e.g. $U_R = 1000$ V less technical requirements can be demanded.

Three different power supplies are used for three diverse voltage ranges that are adapted for voltage resolution and accuracy for the corresponding voltage ranges to provide the VMI voltages. The NHQ215M power supply by ISEG Spezialelektronik GmbH covers the range from 2 to 5 kV. It has an accuracy of $\pm(0.05\%U_{output} + 1V)$ (U_{output} being the set output voltage), which peaks at ± 2.5 V. The resolution is 1 V. However, it becomes highly unstable for lower voltages. The range of 0.1 to 2 kV is provided by SHQ222M from ISEG. Here, the resolution is 0.1 V and accuracy is $\pm(0.05\%U_{output} + 0.4V)$ (maximum accuracy ± 1.4 V). For even lower voltages of 0-120 V, the PLH120-P from LXI is used since the resolution and accuracy is better with 0.01 V and $\pm(0.05\%U_{output} + 0.05V)$ (with maximum accuracy of ± 0.11 V), respectively. To obtain long-term stability a feedback loop is used via a NI AD/DA card and a PID control through a LabView based software [68]. The voltages are stabilized by a capacitor of 0.5 μF before they enter the high voltage switches, which were identical in construction to the ToF-MS HV switches. In order to improve jitter, rise time and noise of electrons on the VMI detector, these switches were replaced by a double push-pull switch with a rise and fall time of around 80 ns. Furthermore, the push-pull switch allows ion-gating in ToF-MS by switching an ion-deflecting electrical field between VMI-repeller and VMI-extractor like it is already explained in section 3.2.2.

Energy Calibration

Energy calibration is necessary to determine, which pixel radius belongs to which kinetic energy to thereby obtain the binding energies of a new (molecular) system. An unambiguous calibration requires a spectrum measured with the optimized voltage ratio.

The raw VMI data after voltage optimization with the corresponding reconstructed image and PES is shown in figure 3.2.18. A total of around $2 \cdot 10^6$ electrons are recorded within almost 3000 experimental cycles in normal mode. The color scale shows the

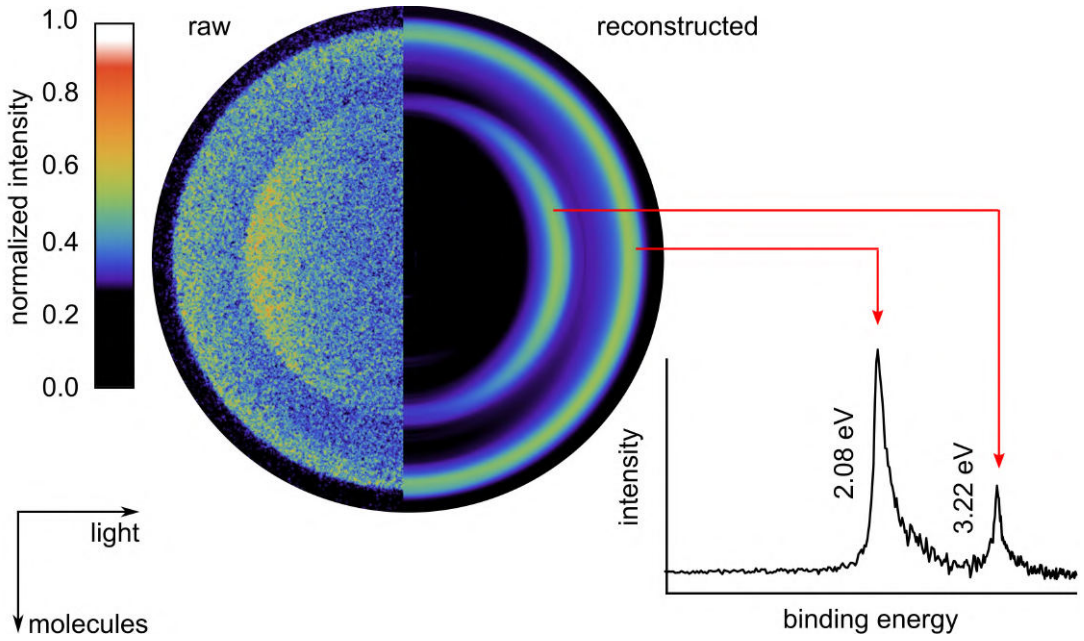

Fig. 3.2.18.: Raw data, reconstructed image and PES obtained with a VMI measurement of the S^- anion at $h\nu = 4.28$ eV. The direction of the laser and molecular beam are given in the left down corner. The radii of the circles give the kinetic energies of the photo-detached electrons and lead to the binding energy since the photodetachment energy is known. Two features can be clearly discerned, which are at 2.08 eV and 3.22 eV. The first feature actually consists of several unresolved transitions but the most prominent is the feature belonging to the electron affinity $^3P_2 \leftarrow {}^2P_{3/2}$ at 2.08 eV. The second feature belongs to $^1D_2 \leftarrow {}^2P_{3/2}$. The angular distribution (here: half moons) disclose the asymmetry parameter β.

normalized number of electron hits ("electron intensity") at each pixel position of the detector. Areas with the most hits are indicated with red or white color, while areas with low hits are black/dark blue. Most of the hits accumulated in a ring-like structure with a radius r_i in pixel (px).

Every ring with radius r_i corresponds to electrons with a specific kinetic energy $E_{\mathrm{kin},i}$.

$$E_{\mathrm{kin},i} = k \cdot r_i^2 \tag{3.2.21}$$

where k is a calibration factor depending on the VMI geometry and the voltages applied to the VMI electrodes.

Using the detachment laser energy $E_{\mathrm{ph}} = h \cdot \nu$, the binding energy $E_{\mathrm{B},i}$ is deduced as:

$$E_{\mathrm{ph}} = E_{kin,i} + E_{\mathrm{B},i} \tag{3.2.22a}$$

$$\rightarrow E_{\mathrm{B},i} = h \cdot \nu - k \cdot r_i^2 \tag{3.2.22b}$$

The constant k is determined in an energy calibration via an initial measurement of a system with well-known energy levels, like atomic anions. The atomic anion is ideally

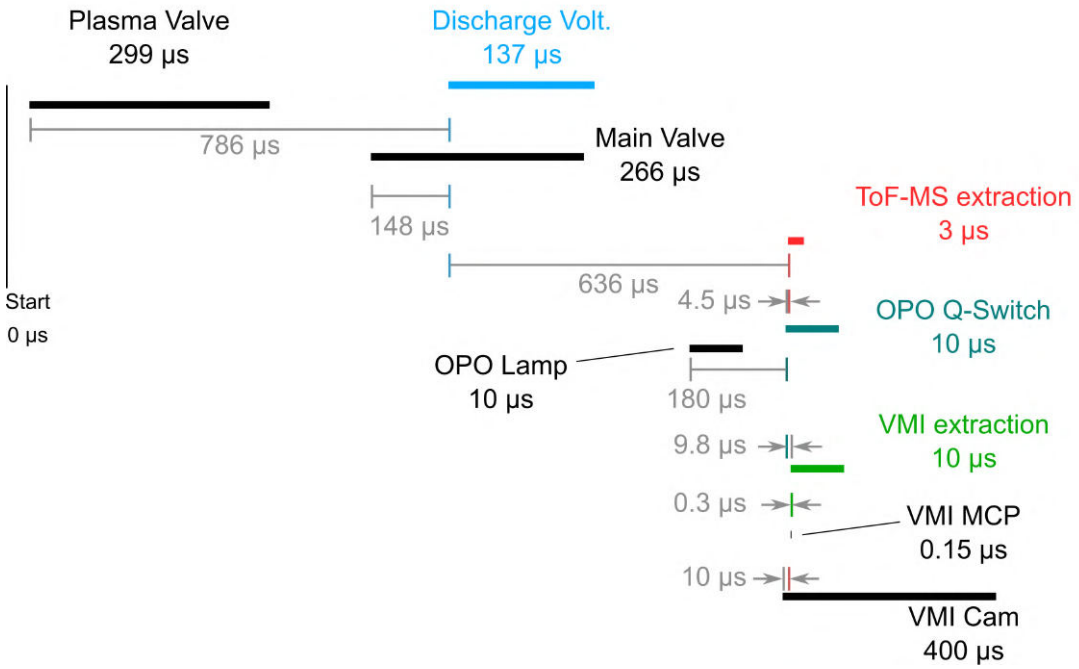

Fig. 3.2.19.: Trigger scheme (not to scale) for the measurement with S^- in figure 3.2.18. Gray values give the length of a trigger signal while the colored values at the trigger labels give the start depending on another trigger signal, e.g. the plasma valve starts 786 μs before the beginning of the the discharge voltage trigger indicated by the blue vertical line below the blue horizontal line and is on for 299 μs.

chosen such that at least one energy level is close to the energy level of interest in the desired molecule as resolution scales with kinetic energy (section 3.2.3.5).

Once k is known, every radius in every raw VMI image can be converted into a kinetic energy, yielding the binding energy as shown in equation 3.2.22b and figure 3.2.18. While k barely changes in day-to-day operation, energy calibration must be repeated every time changes occur at the VMI spectrometer, like electrode voltage changes or variations of the detachment laser's light path.

The calibration is performed using Au^-, S^- and Br^-. Au^- is used for the gold complexes and is easy to obtain with a laser ablation source. For the plasma entrainment source, Br^- and S^- are used and produced by introducing bromobenzene or OCS in the discharge of the plasma valve, respectively. For the measurement of $[Ala\text{-}H]^-$ the VMI spectrometer is calibrated first with Br^- and later with S^-, while for $[Ind\text{-}H]^-$ S^- was exclusively used.

3.2.3.5. Energy Resolution of VMI Images

To assess the quality of a VMI picture or the corresponding PES the resolution must be taken into account. The aim is a PES with well separated features for unambiguous assignment.

Here, resolution is distinguished between absolute kinetic energy resolution ΔE_{kin} and relative kinetic energy resolution res_{r}. The absolute energy resolution describing the spread of the kinetic energy is obtained by

$$E_{\mathrm{kin}} = \frac{1}{2}mv^2 \tag{3.2.23a}$$

$$\rightarrow \Delta E_{\mathrm{kin}} = mv \cdot \Delta v \tag{3.2.23b}$$

and increases with higher velocity. In other words: the best absolute resolution is obtained with slow electrons.

Relative resolution is defined as

$$res_{\mathrm{r}} = \frac{\Delta E_{\mathrm{kin}}}{E_{\mathrm{kin}}} \tag{3.2.24}$$

and improves with better absolute resolution and higher kinetic energies. However, due to the improvement of absolute resolution with low kinetic energies a contradiction is found and a compromise is demanded.

Differentiation of equation 3.2.21 leads to the following relation between kinetic energy and radius.

$$\frac{\Delta E_{\mathrm{kin}}}{E_{\mathrm{kin}}} = 2\frac{\Delta r}{r} \tag{3.2.25}$$

Consequently, transitions at a large radius r have the best relative energy resolution, but low energy electrons have the best absolute resolution. Additionally, low repeller voltages used for slow electrons provide the highest degree of adjacent ring separation.

As already mentioned, in order to ensure voltage stability, three different power supplies are used to cover three voltage ranges: 2-5 kV with NHQ215M, 0.1-2 kV with NHQ222M and 0-120 V with PLH120-P. All three voltage ranges were used for calibration measurements with different atomic anions to demonstrate the reachable energy resolution by Yubero [68]. Here, absolute resolution improves with smaller VMI-repeller voltage (which determines the velocity of electrons) and is best for a repeller voltage of 40 V with $\Delta E_{\mathrm{kin}} = 1.35$ meV. Yubero also shows a smaller relative resolution for a transition at high kinetic energy in comparison to another transition within the same measurement at a smaller kinetic energy. The best relative resolution could be achieved with 3.4%. Overall, both the relative and the absolute resolution improve with smaller repeller voltages.

Here, absolute and relative resolution for Au^- and S^- PES behave like observed for Yubero [68]. However, an extensive investigation of the best possible resolution is not undertaken but the best absolute resolution of 0.01 eV measured here for Au^- can be reported and four out of six transitions for S^- between 577 - 614 nm can be resolved. More details can be found in section 3.2.6.

3.2.4. Laser System and Polarization Techniques

The laser system described and used here provides a wide range of photon energies for photodetachment. Additional optical elements like retarders and a PEM give control over the polarization of the laser beam, which is important for anisotropy (β) and PECD measurements.

The photoelectron detachment of the anions is realized with a laser system operating at 10 Hz and is able to produce ns laser pulses in a range of 0.62 - 5.77 eV. This laser system consists of a Nd:YAG laser (Surelite II, SL II-10 from Continuum) serving as a pump laser for an Optical Parametric Oscillator (OPO Continuum Panther) used for wavelength tuning. The pump laser is operated at its third harmonic (355 nm) and produces pulses with a width of 5-7 ns and a jitter of less than $\pm$1 ns. The light is linearly polarized in horizontal direction and (the third harmonic light) has a pulse energy of around 160 mJ. The subsequent OPO converts the wavelength to 205-2000 nm through a combination of optical parametric oscillation and frequency doubling, leading to a reduction of the initial pulse energy due to the non-linear nature of these processes. The visible range (410-700 nm), called "signal", and IR range (700-2000 nm), known as "idler", only require the optical parametric oscillation process and can reach pulse energies up to 45 mJ and 25 mJ, respectively. The polarization of the signal is vertical while it is horizontal for the idler. For the UV-purple regions (210 - 355 nm and 355 - 420 nm), frequency doubling is used. This further reduces the pulse energy to 3 mJ and <1 mJ, respectively. 355 nm can be taken directly from the pump laser, which passes the attenuator in the OPO but not the non-linear crystals, resulting in a higher output pulse energy for the experiment.

For polarization manipulation waveplates and polarizers are used. Here, achromatic waveplates from Thorlabs are implemented, which cover a large wavelength area: The quarter waveplates (QWPs) cover 260 - 410 nm (AQWP05M-340) and 400 - 800 nm (AQWP05M-600), respectively. The same spectral range can be achieved for the half waveplates (AHWP05M-340 and AHWP05M-600). The polarizer is a Glan-Laser alpha-BBO Polarizer (GLB10, SLAR MgF_2) from Thorlabs and covers 210 - 450 nm. The spectral range above 450 nm is reached with a polarizer from Standa (Glan polarizer, 220 - 2300 nm).

Several broadband mirrors and prisms guide the laser pulse into the VMI chamber. Since reflections could lead to a change in polarization of the incident light if the incidence angle is not 90°, a $\frac{\lambda}{2}$ waveplate and polarizer is used to ensure vertical polarization right before the VMI chamber. Instead of a polarizer, a Brewster window attached to the VMI chamber can be employed, like it was done in earlier experiments with this setup [68, 80]. In this project, the Brewster window is replaced with a flat, UV-graded, fused silica viewport (by VACOM) to allow PECD measurements with circularly polarized light. In general, a $\frac{\lambda}{2}$ waveplate sufficed for the restoration of vertical polarized light.

During the first attempts to measure a PECD signal, the same $\frac{\lambda}{2}$ waveplate is used like for the measurements with linearly polarized light to provide a correct initial polarization for the subsequent static $\frac{\lambda}{4}$ waveplate with fast axis position at 45° or -45° for LCP or RCP light, respectively. In order to check for the quality of circular polarization, a

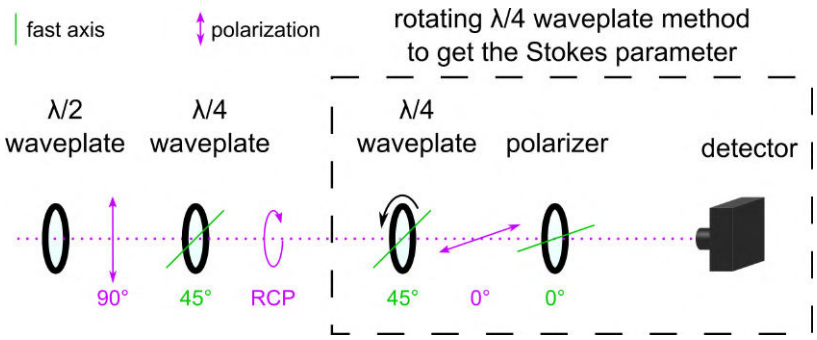

Fig. 3.2.20.: Optical setup to generate LCP/RCP light with a static waveplate and the measurement of the Stokes parameter with the rotating quarter waveplate method (black dashed box). The second quarter waveplate is turned in e.g. 22.5° steps and the modulated intensity is measured at the detector. The position of the fast axis and the intensity lead to the Stokes parameter. Optical elements in the black dashed box are removed for measurements.

second static $\frac{\lambda}{4}$ waveplate, a polarizer and a photodiode were installed to receive and analyze the Stokes parameter with the rotating $\frac{\lambda}{4}$ waveplate method as described in [119]. Of course, the analyzing optical elements were removed for measurements. A scheme of this optical setup is shown in figure 3.2.20.

With this setup, the change between LCP and RCP light is quite slow since the waveplate has to be turned manually. Consequently, signal changes due to short and long term laser intensity fluctuations and drifts of source conditions [120] can add up differently in measurements for LCP and RCP measurements and lead to spurious signal differences, which are not originating from a dichroism effect. In order to alleviate this behavior, a shot-to-shot alternation of the polarization is required. An optical retarder that can create circularly polarized light within the wavelength range of the previously described laser system and that is suitable for quick axis changes with at least 10 Hz is necessary to perform the shot-to-shot measurement.

For this a photoelastic modulator (PEM, Hinds Instruments, Model I/FS50) is added to the experiment. The optical element of a PEM is an isotropic material like fused silica where oscillating strains impose a varying birefringence and, therefore, modify the retardation of a light beam passing through the silica. This oscillation frequency is inherent to the PEM since it depends only on material properties such as length and speed of sound of this material [121, 122]. The model I/FS50 used in this experiment operates at approximately 50 kHz (50.02 kHz to be exact).

The main consequence of this inherent oscillation is the necessity for synchronization with the laser and the whole experiment, which is described below. Another possibility of alternating the polarization in a fast way would be to use Pockels or Kerr cells, but these materials already have an intrinsic birefringence that does not have the same direction as the electrically induced one. Hence, for a laser beam that is only 1-2° off-axis, the light would already experience a superposition of a fraction influenced by the electrically induced birefringence and a fraction influenced by the intrinsic birefringence, which therefore leads to a significant change in polarization. In contrast, the PEM tolerates a

much bigger angle of off-axis beams (50° if a 10% retardation deviation is accepted)[121] and, therefore, facilitates straightforward alignment work.

3.2.4.1. Synchronization

Since the 50 kHz frequency of the PEM is inherent to the mechanical properties of the optical element (e.g. its resonance frequency), no external trigger can be applied and, consequently, the PEM has to be the master clock for the experiment. Also, the 50 kHz needs to be down-modulated to be compatible with the 10 Hz experiment and synchronized in a way that a laser pulse passing through the PEM experiences a $+\frac{\lambda}{4}$ and $-\frac{\lambda}{4}$ retardation, respectively.

In order to gain knowledge about the moment when the PEM is in $\frac{\lambda}{4}$ waveplate mode, a preceding test is conducted as shown in figure 3.2.21: Polarized laser light from a cw HeNe laser first passes through a $\frac{\lambda}{2}$ waveplate with a fast axis at -22.5°. Afterwards, the PEM (fast axis at 0°) and a static $\frac{\lambda}{4}$ waveplate with the same fast axis position of 0° are installed. If the PEM is in the state of $\pm\frac{\lambda}{4}$ retardation, the PEM and the waveplate act together as a $\frac{\lambda}{2}$ waveplate with a changing fast axis. In front of the detector, a polarizer is mounted with a fast axis perpendicular to the first $\frac{\lambda}{2}$ waveplate so that no light can hit the detector until the PEM and the $\frac{\lambda}{4}$ waveplate are installed.

Simultaneously monitoring the 50 kHz driving oscillation from the PEM control (green square wave in figure 3.2.21) and the corresponding phase modulation from the PEM (blue sine wave in figure 3.2.21) facilitates the identification of when the PEM is in $\frac{\lambda}{4}$ retardation state regarding to a fixed signal (here the driving oscillation). The state of $+\frac{\lambda}{4}$ or $-\frac{\lambda}{4}$ retardation is reached when the sine wave of the phase modulation arrives at a maximum or minimum, respectively. Between both these extrema the PEM produces elliptically polarized light, and at zero-crossing it creates a linear polarization with an orientation of 45° (figure 3.2.21). A comparison between the sine phase modulation and the square driving oscillation reveals a clear time delay between maxima/minima of the sine wave with respect to the rising/falling edges of the square wave, and must therefore be considered if the system is triggered at the square wave of the driving oscillation.

A synchronization scheme for a PEM is shown in figure 3.2.21 and is analogous to the asymmetric synchronization described in [120, 123]. The driving oscillation from the PEM controller triggers a pulse-delay generator (Quantum Composer 9420 Series). First, the system mode is set to Duty Cycle with one on-pulse and 9999 off-pulses. Second, two 5 Hz signals are created in channels A and B of the pulse-delay generator by again using duty cycle with one on- and one off-pulse. The pulse length is the same as for the PEMs driving oscillation (20 μs). In order to create a 10 Hz signal in channel C, channel B needs to wait for one pulse (wait function set to one) and combined with the signal from channel A. If the shift Δt_1 between the sine wave of the PEM and the square wave from the PEM controller is taken into account, channel A and B get an extra time delay of Δt_1 and $\Delta t_2 = \Delta t_1 + 20\mu\text{s} + \delta t$, respectively. Here, δt is an adjustable parameter, which is not necessarily zero due to a known effect for PEMs called residual static birefringence [123]. Consequently, channel C creates an almost-10 Hz signal, which offers an interaction of a light pulse with the PEM in the moment of $\pm\frac{\lambda}{4}$ retardation.

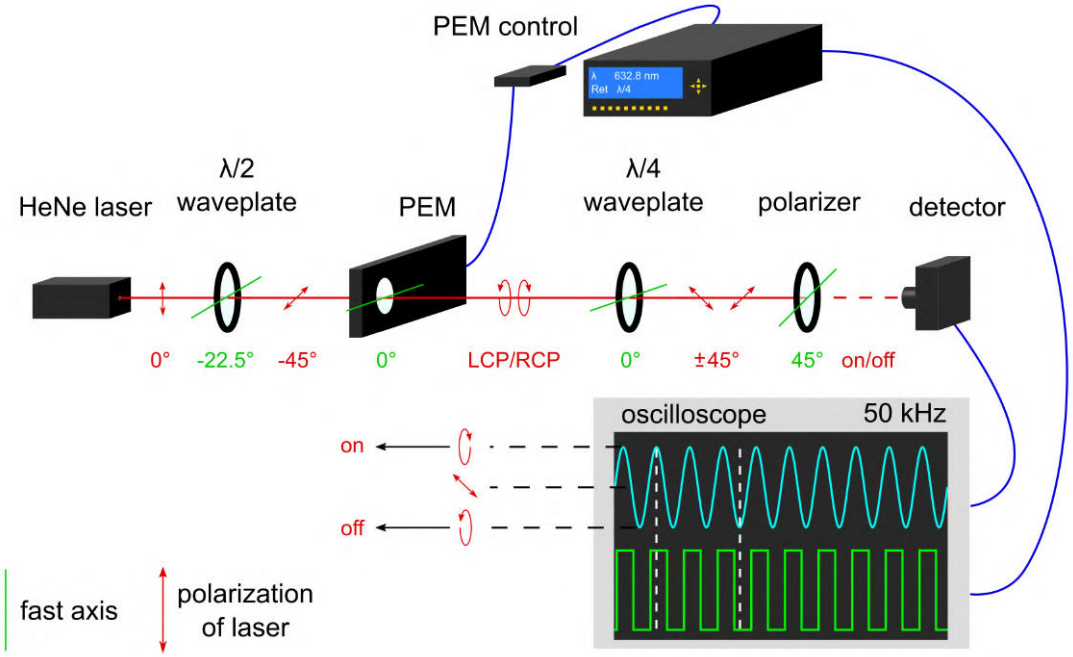

Fig. 3.2.21.: Intensity modulation of a cw laser beam (HeNe laser) by a PEM in quarter waveplate mode. The square wave oscillation of the PEM control is shifted depending on the sine wave received by the detector.

Furthermore, the almost-10 Hz signal now drives the remaining experiment. For data acquisition, channel D is created to distinguish between LCP and RCP measurements. The signal is on (or off) for every second signal of channel C. The signal passes through a digital I/O device of National Instruments (NI USB-6501) to convert it into a digital signal before it is send to a computer. Here, a custom LabVIEW routine separates both measurements by the two states of channel D, and sends the acquired data to different locations (see PECD mode in section 3.2.3.1). For a measurement with linear polarized light the switching is disabled by removing the PEM from the light path and disabling channel D, which stores all data in one file.

3.2.4.2. Testing the PECD mode with the PEM

If the polarization optics are placed before the VMI chamber, the PECD mode mentioned in section 3.2.3.1 can be tested. A similar setup was described earlier in figure 3.2.21 with the main difference being that a pulsed instead of a cw laser is used here. If the PEM is in $+\lambda/4$ (or $-\lambda/4$) retardation state, channel D is in the on (or off) state. However, in this setup, a $\pm\lambda/4$ retardation state of the PEM means that light can either pass through the VMI chamber or is blocked in front of it. Consequently, in a fully running experiment, a photoelectron spectrum is created only in one of the two relevant retardation states of the PEM. If the PECD mode is working, one file contains the photoelectron spectrum while the other file should be empty or only contains noise. Additionally, the PECD mode counts how often the LCP and RCP modes are entered.

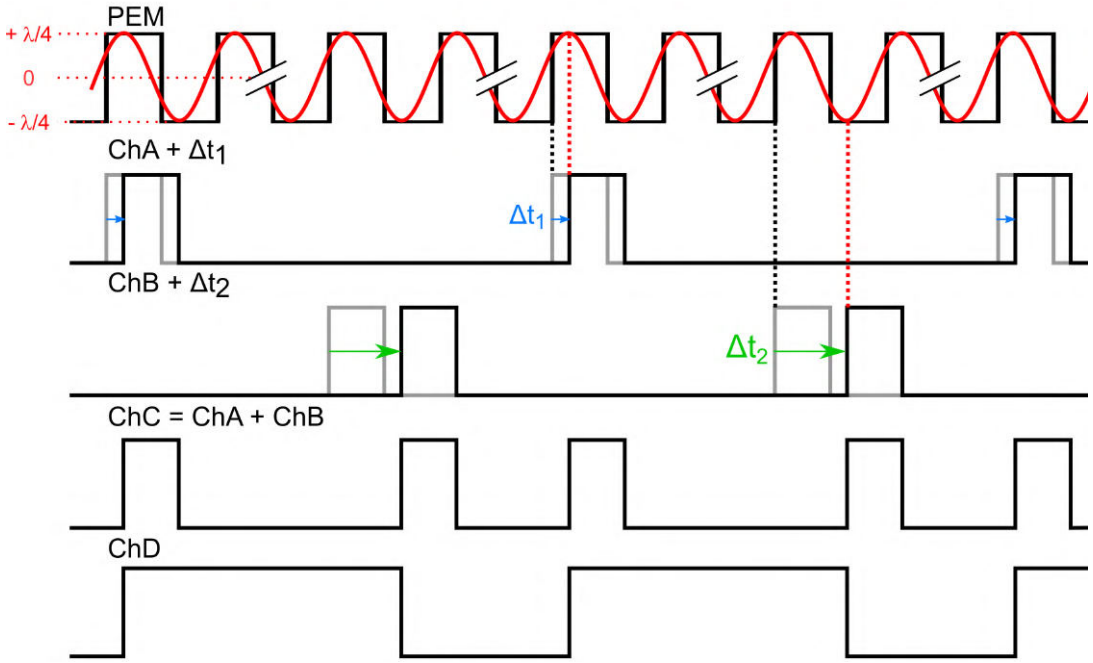

Fig. 3.2.22.: Timing scheme of PEM and how the trigger of the detachment laser is manipulated in order to hit the PEM with the laser when the PEM is in $\pm\frac{\lambda}{4}$ mode. A Time-Delay Generator is triggered by the PEM driving oscillation and creates 5 Hz signals in two separated channels (A and B), which are either synchronized with the maxima or with the minima of the sine wave. Channel C combines both signals to an almost-10 Hz signal. Channel D creates a signal for the computer to distinguish between $\pm\frac{\lambda}{4}$ polarization.

Ideally, these numbers should be equal, especially when working with LCP and RCP light, since an (almost) equal number of electrons in both modes is required for PECD.

3.2.4.3. Quality of Polarization

The quality of polarization is determined by the quality of waveplates, polarizer and PEM. The error for the waveplates is determined by several factors: the waveplates are inserted manually in their rotation mounts and the fast axis is aligned to the zero position with the help of a polarizer and a linear polarized laser. This manually setting is determined by the polarization quality of the used laser. Furthermore, the dial reading of the rotation mounts only offers an accuracy of 1-2°. There are rotation mounts offering indexing in 22.5° steps, which proves helpful for the adjustment of the fast axis but the accuracy of the indexing again influences the error of the fast axis position. Even if the fast axis can be adjusted perfectly, the quality of polarization is influenced by a wavelength dependent retardation. Thorlabs specifies its half waveplates with a deviation in retardance of around 0.45 - 0.54 waves. The QWPs deviate between 0.23 - 0.27 waves in retardance for waveplates in the area of 260 - 410 nm and 0.20 - 0.27 waves for 400 - 800 nm. These will influence the PECD measurements with only the static waveplates as well as the one with the PEM since it is used in combination with these

waveplates. However, with Stokes parameter and an intensity comparison between an off and on pulse, the quality of light polarization can be estimated for the static waveplate and the PEM measurement, respectively.

The quality of light polarization for the static quarter waveplates is determined by the Stokes parameter gained from the rotating $\frac{\lambda}{4}$ waveplate method [119]. The S_3 parameter should be either +1 or -1 regarding the type of circular polarization. Averaged over all experiments using the quarter waveplates a mean S_3 of 0.98 is determined but the value can vary with ± 0.09 between experiments. The polarization quality P (considering all Stokes parameter) is also averaged and has a value of 0.97 ± 0.10. The polarization quality is checked once before the experiment.

For the PEM, the polarization of the light is constantly verified during the experiment by a $\frac{\lambda}{4}$ waveplate, a polarizer and a detector, installed after the VMI chamber. The combination of PEM producing either LCP or RCP light before the VMI chamber and the static quarter waveplate (with a fast axis parallel to the axis of PEM) after the VMI acts as half waveplate with switching fast axis. The subsequent polarizer either blocks or lets the light pass depending on the polarization of the incident light. Consequently, the detector sees a on-off behavior in a 5 Hz pattern.

To estimate the polarization quality, the intensity difference between on and off pulse is measured. Ideally, this difference reaches theoretically its maximum for perfect polarization and has a non-detectable off pulse as well as an on pulse with maximum intensity. However, the off pulse will mostly show a non-zero intensity especially for high light intensities, which the polarizer can not absorb even if set perfectly. Therefore, a new baseline for the off pulse has to be determined before the PECD measurement. First, the initial polarization of the laser needs to be set ($\pm 45°$). Then a polarizer is placed after the VMI in a position, which minimizes the light output (either 45 or 315°). The intensity is read out with an oscilloscope and taken as baseline for the off pulse. Then, the PEM is installed before the VMI chamber and a static quarter waveplate is positioned after the VMI chamber. The intensity of on and off pulse are measured and compared taking the baseline for the off pulse in account.

Especially if working with UV light, the intensity can be completely absorbed by the polarizer resulting in off pulses below the noise level and the only option is to maximize the on pulses. If the noise level is taken for the off pulse intensity the polarization can differ up to 3.3% from the ideal polarization. This represents the worst case scenario for this kind of measurements.

In the case of visible light more intensity is available and the off pulse does not vanish completely. Considering the new baseline of the off pulse, the off pulse barely differs from this base line and the polarization could be considered ideal. However, in the cases where it differed from the base line, the difference between minimum and maximum leads to a 3.5% deviation from ideal polarization. This polarization deviation is comparable to other PECD experiments [72].

3.2.5. Ascertaining a Single Photon Process and its Effectivness

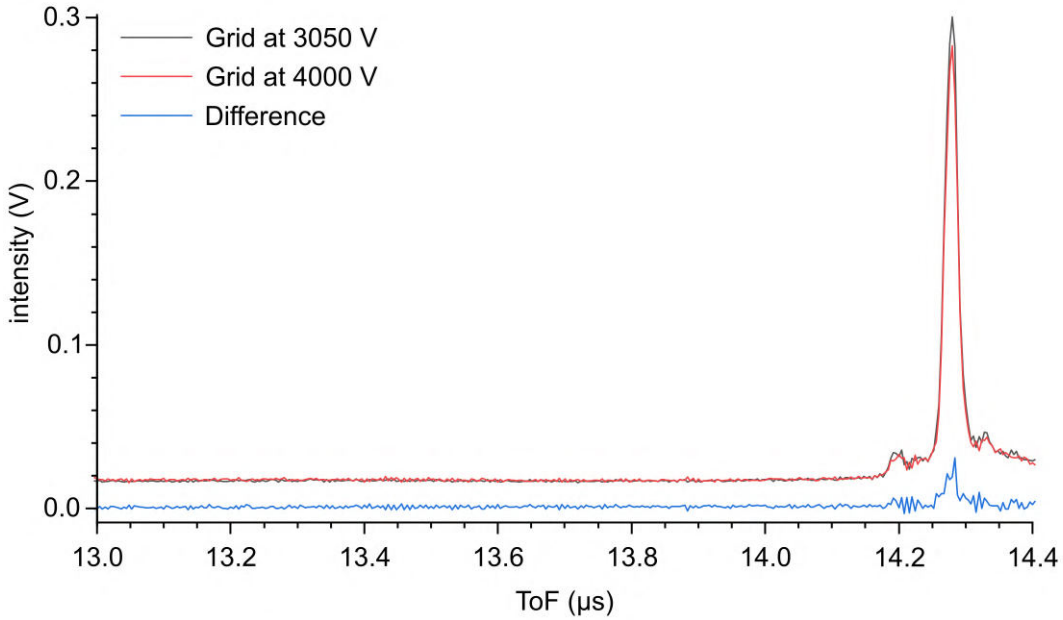

Fig. 3.2.23.: Time of flight spectrum for the neutral signal at different grid voltages. The neutral signal is produced with $E_{\mathrm{ph}} = 4.77$ eV and is not normalized. Intensity differences originate from fluctuations in the source during the change of the grid voltage. The peak at around 14.27 μs corresponds to m/z 133. If cations are present a peak should appear at around 13.95 μs for a grid voltage of 3050 V (black) and at around 13.45 μs for a grid voltage of 4000 V. This assumes that the grid only affects the molecular beam after the μ-metal shielding and that possible cations are not otherwise disturbed, e.g. by anions. μ-metal shielding and MCP are around 70 mm apart. Since there is neither a peak at the estimated time nor a shift of any peak observed, formation of cations is excluded.

The analysis of the photoelectron spectra in this thesis is based on the assumption that an electron is detached via a single photon process from the anion leaving a neutral core behind. These photodetached electrons alone (with the exception of background and noise electrons) should contribute to the PES and PECD signals. If additionally electrons are photoionized from the neutral core leaving cations behind, any PECD signals could also stem from this process, like it is the case in conventional PECD experiments. This measurement would merely have a "photodetachment background" and consequently mask any PECD effect from pure photodetachment.

On the example of deprotonated 1-indanol, two experiments show that neither cations are formed nor that multiphoton processes enabling the creation of cations can be detected. One involves the grid in front of the ToF-MCP detector and the other the measurement of photon energy in dependence of the kinetic energy.

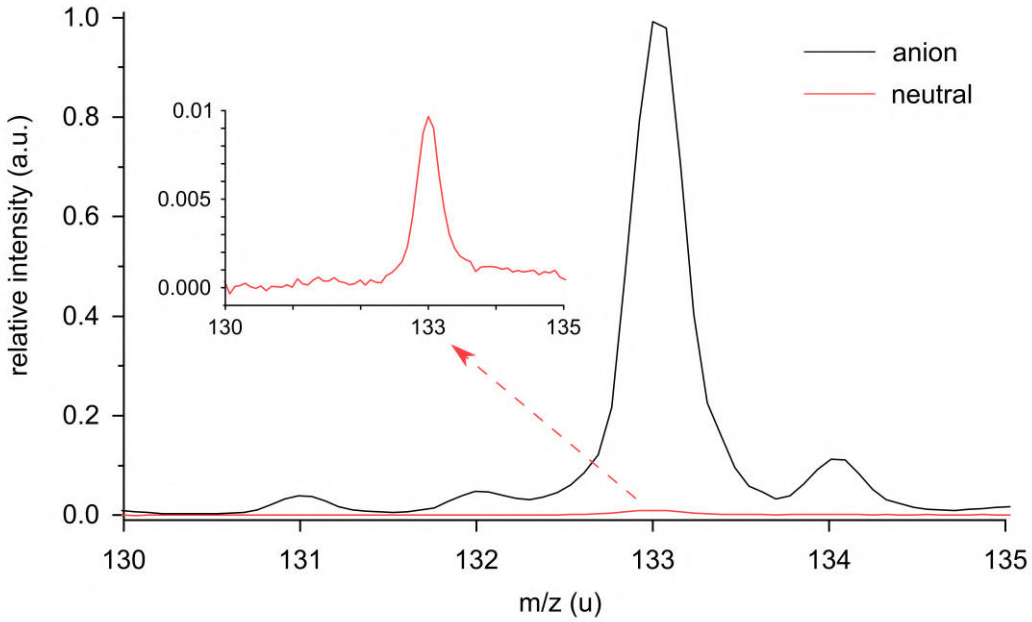

Fig. 3.2.24.: Anion-neutral (signal) ratio for photodetachment at $E_{\mathrm{ph}} = 4.77$ eV. Laser pulse energy before/after VMI chamber around 0.5/0.1 mJ. Anion signal (black) and corresponding neutral signal (red) are measured at the same MCP voltage. The neutral signal is around 1% of the anion signal.

3.2.5.1. Cation Measurement with Grid of ToF-MS

In the experiment, a grid is placed just before the MCP detector for ion detection (figure 3.2.1). Applying a negative potential to this grid can be used to effectively deflect (or reflect) anions before reaching the detector (as described in section 3.2.2). If the anions are accelerated in the ToF-MS to -3010 V, than, with a grid voltage more negative than -3010 V, the anions are deflected, leaving only the neutral signal. If there is also photoionization, cations are formed and accelerated toward the grid. Consequently, a time-of-flight spectrum should show the neutral peak at the same time of flight as the anions and an additional "cation peak" at shorter flight times, which should change position with changing grid voltage.

Figure 3.2.23 shows time-of-flight spectra at different grid voltages. The main feature is the neutral signal of m/z 133 created by photodetachment of $[\mathrm{Ind\text{-}H}]^-$ with $E_{\mathrm{ph}} = 4.77$ eV. Some neighboring peaks matching m/z 132 and 134 also seem to appear but are too small to contribute significantly to the electron signal. Anyway, over the full time scale (figure 3.2.23 only shows an interval of 1.4 μs) no additional peak can be made out and no peak is changing position if the grid voltage is changed. The same result can be obtained with a photon energy of $E_{\mathrm{ph}} = 3.49$ eV (355 nm) where considerably more light intensity is available[10].

[10]Laser pulse energy before/after VMI chamber 3/0.5 mJ.

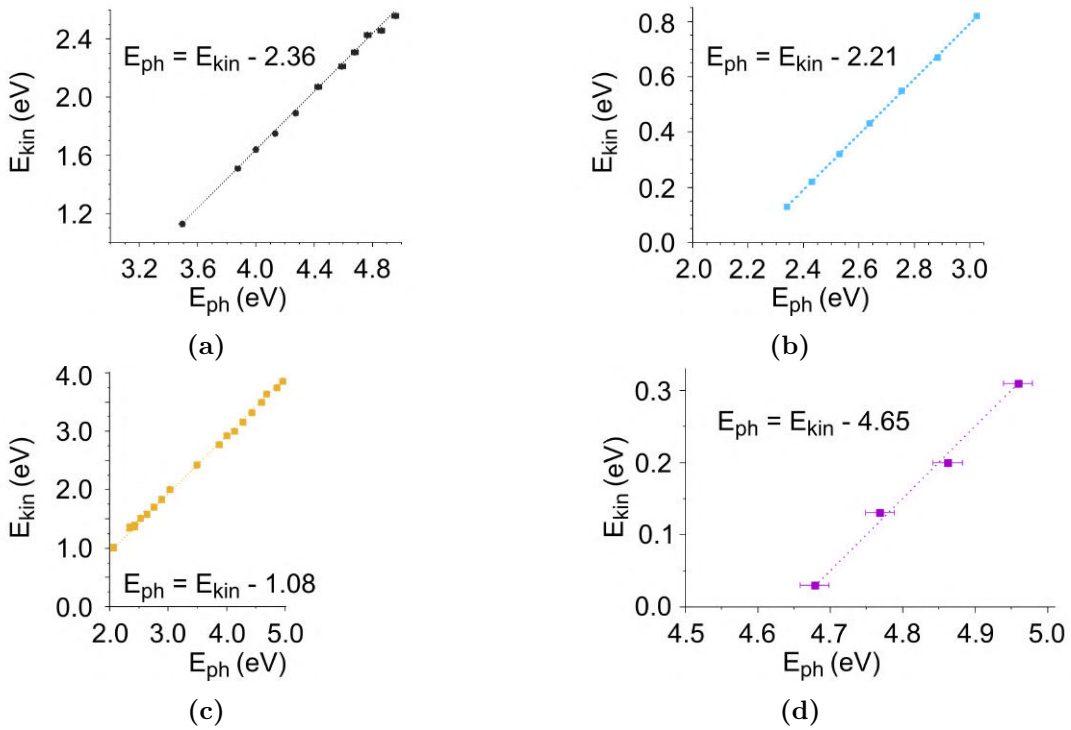

Fig. 3.2.25.: Kinetic energy of the peak maxima in the PES of $[\text{Ind-H}]^-$ plotted over photon energy for some selected transitions. The transitions are labeled B (a), B_1 (b), A (c) and C (d) according to section 5.3.2. The data points can be fitted with a linear function with a slope of 1 and an intercept, which matches the binding energy of the corresponding peak (section 5.3.2). Therefore, a single photon process is assumed.

3.2.5.2. Anion-Neutral Ratio

Comparing the anion and neutral signal of m/z 133 measured with the same MCP voltage, gives an estimate for the effectivness of the photodetachment process. This assumes that neutral and ion signal have (almost) the same detection efficiency at the MCP detector, which is reasonable for high kinetic energies [124, 125]. Other factors like the overlap between molecular and light beam as well as the cross section for photodetachment define the intensity of the neutral signal relative to the anion signal. Since the spot size (and alignment freedom) of the light beam is restricted by light baffles (and an adjustable aperture before the VMI chamber) the light might not hit all molecules if the width of the anion beam should be broader than the light beam leading to an higher anion signal in comparison to the neutral signal.

In figure 3.2.24, the anion signal is compared to a neutral signal generated with a photon energy of $E_{\text{ph}} = 4.77$ eV. The neutral signal is around 1% of the anion signal. A similar result is obtained with $E_{\text{ph}} = 4.13$ eV with almost 1% (not shown). The best anion-neutral ratio is reached with a photon energy of $E_{\text{ph}} = 3.49$ eV (355 nm) with around 6%, using a larger pulse energy. These percentages do not account for the PECD values measured at the photon energies.

3.2.5.3. Kinetic Energy vs Photon Energy

In this project, the first PECD signal was recorded for $[\text{Ind-H}]^-$ at a photon energy of 3.49 eV. Unluckily, some (neutral) alkoxy radicals show optical transitions in a similar energy regime (around 3.5 - 3.8 eV [126]) making resonant absorption feasible after photodetachment. Photoionization via multiphoton processes of the neutral radical Ind-H (after photodetachment) seems possible and the recorded PECD signal could be a result of conventional PECD effects instead of photodetachment. In order to exclude (or prove) multiphoton processes, more photoelectron spectra are recorded and the dependence of the kinetic energies of several peaks on the photon energy is observed.

In a single photon process, the kinetic energy related to a given feature in the PES and photon energy used for the detachment follow Einstein's photoelectric law $E_{\text{kin}} = h\nu - E_{\text{B}}$. Indeed, all peaks evolve in a linear manner when the kinetic energy of the peak maximum is plotted over the photon energies (figure 3.2.25). A linear regression of these data points results in a line with the slope of 1 that crosses the kinetic energy axes at the (in section 5.3.2) experimentally determined binding energies (within the given errors) confirming the single photon process. Furthermore, a multiphoton process would reveal itself by discrete changes of the peak positions in the PES by $h\nu$, i.e. the slope(s) in figure 3.2.25 would change from 1 to n if n photons are required.

If the electrons are the result of a multiphoton process, such shifts or changes should have been seen according to the calculated photoionization energy of the neutral radical Ind-H of 9.321 eV. For example, for the PES recorded at $E_{\text{ph}} = 4.77$ eV two additional photons are needed for the ionization of the neutral Ind-H radical while in the visible region at least four additional photons are required. Even if an arbitrary error of 0.5 eV is assumed for the calculated values, at least one shift should be observable.

In summary, neither cations nor a multiphoton process could be detected, which would have indicated photoionization of neutral species. Consequently, all spectra (and most importantly all presented PECD asymmetries) presented here are the result of photodetachment in a single photon process.

3.2.6. Data Handling

3.2.6.1. PES of gold and sulfur anion

Optimization of the VMI spectrometer voltages and calibration of the PES are done with the gold anion for the gold complex measurements and (mainly) with the sulfur anion for the deprotonated molecules. Exemplary spectra at different photon energies are shown in figure 3.2.27 for Au^- and figure 3.2.30 for S^-.

Gold anion

In general, peaks are represented with Gaussian line profiles. In the case of more complex systems with overlapping vibrations and/or isomeric effects, peaks are approximated with several (overlapping) Gauss profiles. For atomic systems like Au^- only one Gaussian profile is needed to describe one measured electronic transition. An energy level diagram

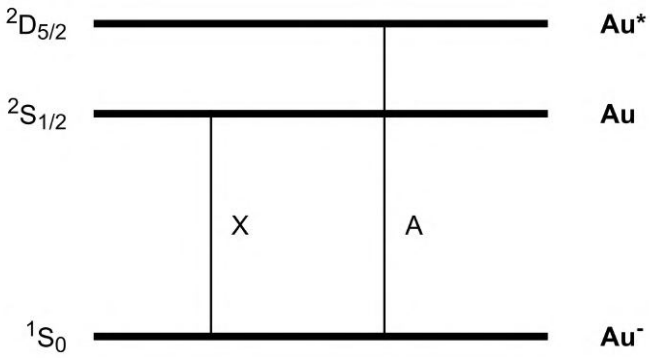

Fig. 3.2.26.: Energy level diagram for photodetachment from Au^-. The transition to the ground state of Au is $^2S_{1/2} \leftarrow {}^1S_0$ and is marked with X. The binding energy is 2.309 eV. The first excited state is reached for the transition $^2D_{5/2} \leftarrow {}^1S_0$ and is indicated with A. The energy is 3.444 eV. [77, 117]

Table 3.2.2.: Energies, resolution and applied VMI voltages for the Au^- spectra. ΔE corresponds to FWHM. * photoelectron spectra are depicted in figure 3.2.27.

E_{ph} (eV)	rep (V)/ext (V)	state	E_B (eV)	E_{kin} (eV)	ΔE (eV)	res_r
4.77*	3700/2475	X	2.31	2.46	0.16	0.07
		A	3.45	1.32	0.08	0.06
4.35	2000/1355	X	2.31	2.04	0.09	0.04
		A	3.45	0.90	0.05	0.06
4.13*	2500/1690	X	2.31	1.82	0.08	0.04
		A	3.45	0.68	0.04	0.06
3.49	1450/989	X	2.31	1.18	0.06	0.05
3.02*	800/538	X	2.31	0.71	0.04	0.06
2.70	800/546	X	2.31	0.39	0.03	0.08
2.58*	500/340	X	2.31	0.27	0.01	0.04

for the detachment from Au^- is given in figure 3.2.26 and the corresponding measured PES is in figure 3.2.27. Dependent on the kinetic energy the FWHM and hence the resolution ΔE varies (figure 3.2.27 and table 3.2.2). As expected (from section 3.2.3.5), the resolution improves with decreasing kinetic energy (figure 3.2.28) and repeller voltage (table 3.2.2). The relative resolution of a peak should be compared to other peaks within the same spectrum. Peak A shows, as expected, an inferior resolution than X since peak A is at smaller kinetic energies than X (section 3.2.3.5). The PES at $E_{ph} = 4.77$ eV behaves slightly in the opposite way.

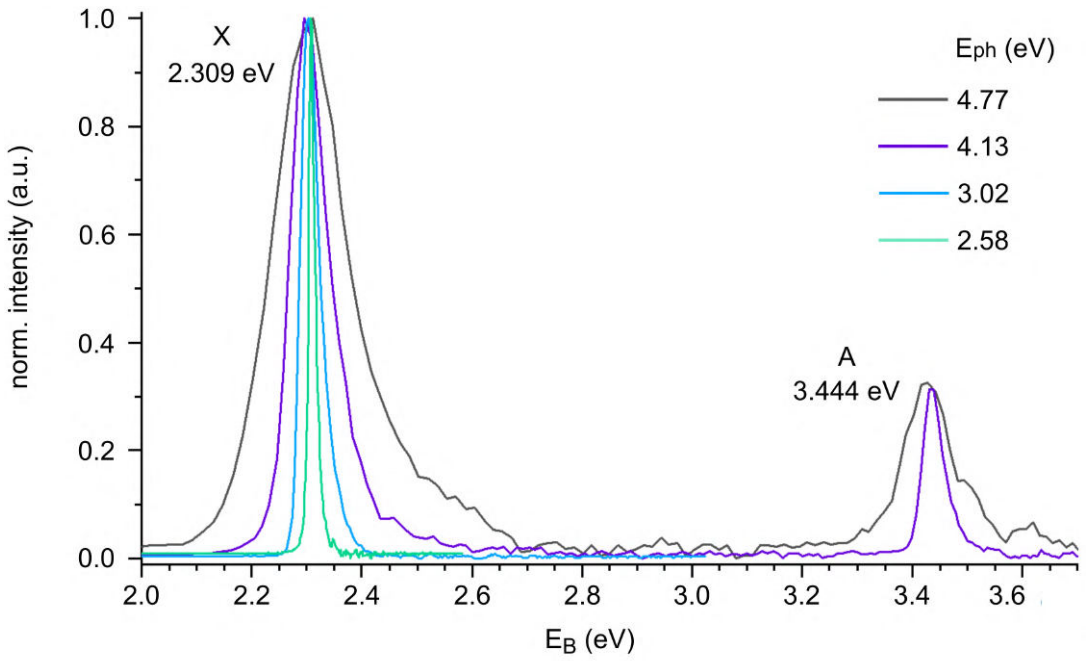

Fig. 3.2.27.: Selected PES of Au^- at different E_{ph} and hence different E_{kin} measured in normal mode. The transition to the ground state (X) is at a binding energy of 2.309 eV and the transition to the first excited state (A) at 3.444 eV. An energy level diagram can be found in figure 3.2.26. The ground and excited state feature smaller FWHMs for smaller kinetic energy and have a better resolution as can be seen in figure 3.2.28. Furthermore a shoulder is observed for PES with high kinetic energy and vanishes the smaller the kinetic energy gets.

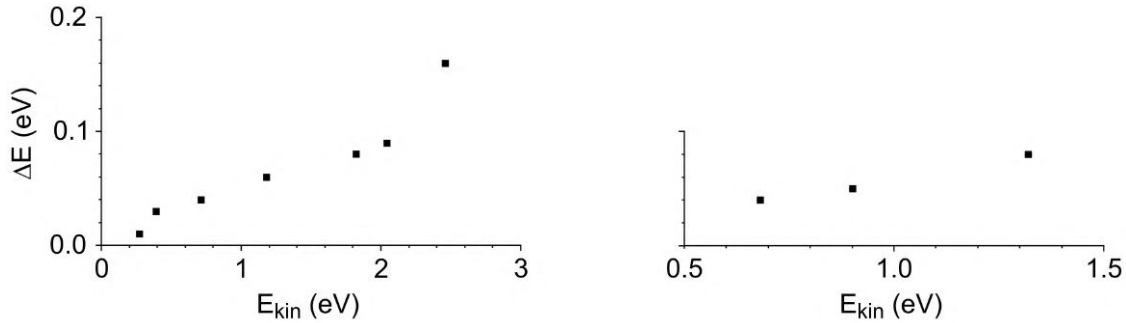

(a) **(b)**

Fig. 3.2.28.: Absolute resolution ΔE plotted over the kinetic energy for the X transition in (a) and the A transition in (b). For smaller kinetic energies ΔE becomes smaller and hence better. The values for these figure can be taken from table 3.2.2.

Besides the expected behavior for the resolution, a shoulder at the side with higher E_B emerges. It is also observed in the literature [127] and appears in PES of other anions like Br^- and F^- (not shown). Since no additional contributions like vibrations can be present, this shoulder is considered to be an experimental artifact or rather an artifact of image processing/deconvolution. This shoulder will be also visible in the PES of Au^--M and the deprotonated molecules and should not be confused with additional overlapping Gaussian peaks origination from isomeric, vibrational or rotational contributions.

Sulfur anion

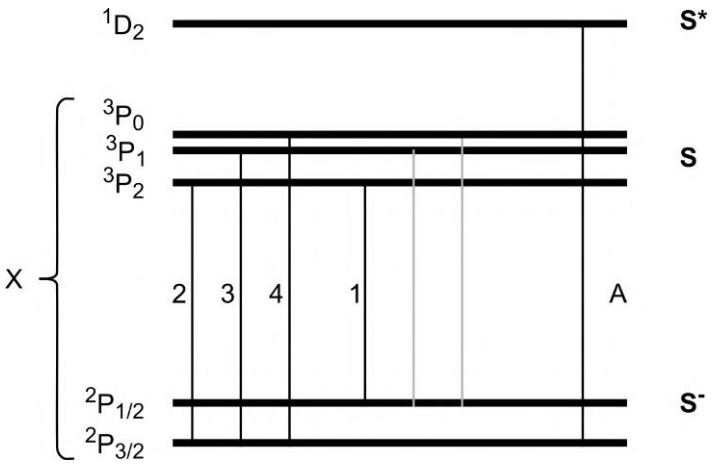

Fig. 3.2.29.: Energy level diagram for photodetachment from S^-. Transition $^3P_2 \leftarrow {}^2P_{3/2}$ ("2") is the electron affinity and has an energy of 2.077 eV. Other transitions, including excited states of the anion and neutral, are given in table 3.2.3. Only the black, labeled transitions can be resolved in this experiment. Since they are energetically close and can not be resolved for PES with high kinetic energies, they are summarized in the label "X". The transition to the excited state "A" is $^1D_2 \leftarrow {}^2P_{3/2}$ and has an energy of 3.222 eV. [77, 117, 128]

A better visualization of improving resolution with decreasing kinetic energy is represented by the sulfur anion. The atomic S^- is known to have six anion to neutral atomic transitions in the visible energy regime (577 - 614 nm), which appear as one peak for E_{ph} = 4.77 eV and start splitting for PES recorded at lower photon (or kinetic) energies (figure 3.2.30a). The best image is obtained for the lowest photon energy (E_{ph} = 2.38 eV) and if the spectrum is measured in event instead in normal mode (figure 3.2.30b). This leads to a PES where four features can clearly be discerned. Two features are unfortunately not resolved but would explain the imperfect Gaussian shape of peak 2 since they are pretty close in energy. A corresponding energy level diagram can be found in figure 3.2.29.

Since only four transitions are resolved an unambiguous assignment of all peaks is not possible before calibration. Consequently, not all peaks can be incorporated in the calibration process. However, the most intense peak (2) can assumed to be the electron affinity at 2.0771 eV [128]. On this basis, the E_B of the other peaks are evaluated,

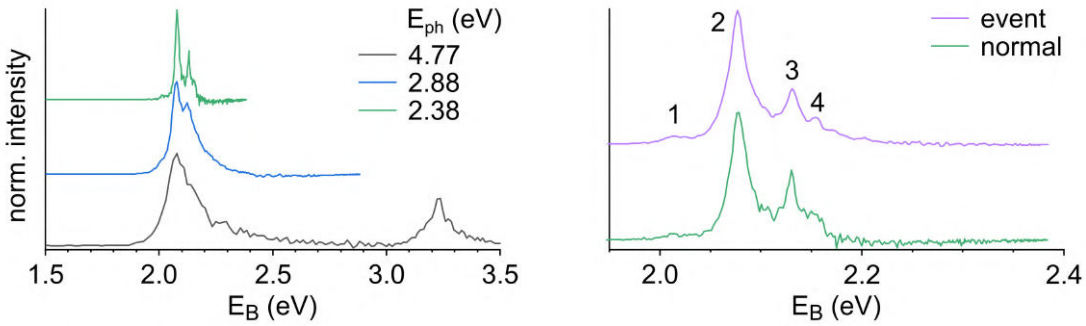

Fig. 3.2.30.: (a) Three PES for S^- in normal mode. For E_{ph} = 4.77 eV (black), two features at 2.077 eV and 3.222 eV are visible corresponding to ground and an excited state, respectively. The ground state peak splits up with smaller photon energy. (b) The best resolved PES (E_{ph} = 2.38 eV) has been measured in normal and event mode. The event mode shows a cleaner PES and up to four features are resolved. Peak 2 has a FWHM of 0.014 and 0.013 eV in normal and event mode, respectively. The assignments and measured energies are given in table 3.2.3.

Table 3.2.3.: Energies and assignment for the S^- spectra at E_{ph} = 2.38 eV from figure 3.2.30. Measured values (meas.) are determined by fitting a Gauss function to the peak. The PES is calibrated on peak 2, which is considered to be the electron affinity. The literature values (lit.) are taken from [77, 117, 128]. An energy level diagram can be found in figure 3.2.29. Not labeled values are not resolved transitions.

label	Transition	E_B (eV) (lit.)	E_B (eV) (meas.)
1	$^3P_2 \leftarrow {}^2P_{1/2}$	2.0171	2.018 ± 0.008
	$^3P_1 \leftarrow {}^2P_{1/2}$	2.0663	not resolved
2	$^3P_2 \leftarrow {}^2P_{3/2}$	2.0771 (EA)	2.0771 (fixed)
	$^3P_0 \leftarrow {}^2P_{1/2}$	2.0882	not resolved
3	$^3P_1 \leftarrow {}^2P_{3/2}$	2.1263	2.131 ± 0.007
4	$^3P_0 \leftarrow {}^2P_{3/2}$	2.1483	2.151 ± 0.006

which does not only provide a save assignment of the remaining peaks but also a quality control of the calibration. In table 3.2.3, the measured values match to the literature values enabling the peak assignment and confirming that the calibration is adequate.

3.2.6.2. Background Signal in VMI data

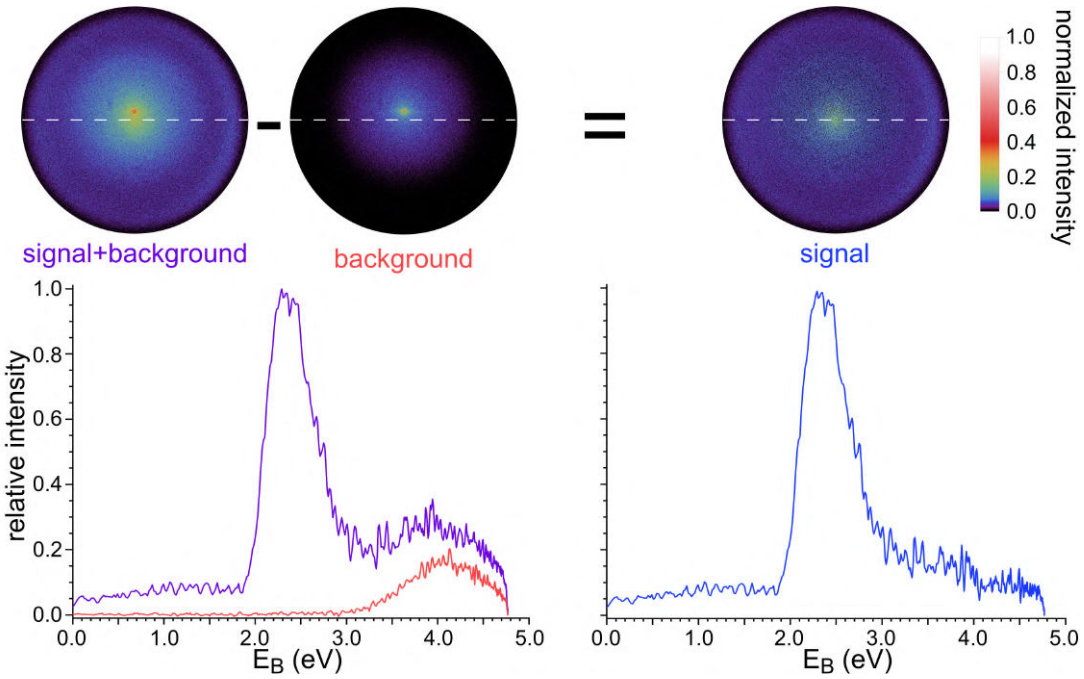

Fig. 3.2.31.: Background signal in VMI data measured in PECD mode. Here, background signal originating from light at $E_{\mathrm{ph}} = 4.77$ eV for a measurement with $[\mathrm{Ala\text{-}H}]^-$ is shown. Up: Raw data from VMI measurements. The data containing the background is subtracted from the data, which contains the signal and background. The result is data with reduced background, called background corrected signal. The dashed line marks a center line of the signal. The background deviates from this line. Down: Corresponding photoelectron spectra to VMI raw data from above. Background signal is clearly visible in the UV region between 3 and 5 eV (red). Hence, the broad peak in this region for the violet spectrum is accounted by background. The blue PES is the background corrected signal. All spectra are normalized relative to the maximum of the violet spectrum.

Background signal measured at the VMI detector accompanies each experiment and can not always be avoided but often reduced to acceptable levels. Here, two main sources of background signal are identified: Background originating from the laser light, especially UV light and background caused by the molecular beam. In both cases the center of the background signal does not coincide with the center of the signal (figure 3.2.31), which hinders the reconstruction of the image. Hence the background has to be minimized or separated from the signal.

Without a molecular beam being present, photoelectrons can be emitted due to scattered light of the metallic surfaces inside the vacuum chamber through the photoelectric

effect. The work function of materials built in the VMI spectrometer is high enough that this background appears only for UV light[11]. This background can be reduced by aligning the path of the light beam such that no or only a few counts reach the VMI-MCP detector while the molecular beam is disabled. The light beam can also be narrowed by a telescope or focused by a lens to avoid contact with the light baffles, which are installed before and after the VMI lens system.

If the background reduction does not suffice, the background signal originating from light can separately be measured by operating the ToF electrodes at 5 Hz while keeping the rest of the experiment at 10 Hz. The PECD mode (introduced in section 3.2.3.1) will then produce a file containing only the background data, which – in combination with the measurement of the signal plus background –, can be used to judge the magnitude and localization of the background. If the background data is subtracted from the data containing signal and background, a background corrected spectrum is obtained (figure 3.2.31). However, caution is advised since background from each trigger cycle is independent from the cycle before. Technically, to be allowed to do this subtraction the background should be measured simultaneously to the signal+background spectrum. The setup is not able to do that but the 5 Hz switching of the ToF plates is "the closest to simultaneity" possible for this experiment.

The other type of background originates from the molecular beam. Here, molecules with high kinetic energy could encounter an obstacle and upon collision eject electrons, which are detected as background. Such an obstacle could be background gas, which is ionized or solid surfaces in form of apertures or μ-metal edges. In the case of collisions with solid surfaces, the background can simply be reduced by redirecting the molecular beam with the deflection plates of the ToF-MS. Background gas can be reduced if the VMI chamber is baked out.

If that is not enough, the background of the molecular beam can be recorded similarly to the background originating from light: Instead of operating the molecular beam at 5 Hz, the light will be operated at 5 Hz. Hence, a PES is recorded normally with a molecular and light beam present in the VMI chamber and a PES where only the molecular beam can be found while the light is off, consequently measuring the background created by the molecular beam. However, the trigger rate of the laser is fixed to 10 Hz and light must be blocked or let through alternatively with a combination of an optical element acting as varying half waveplate and a polarizer. Again, the PECD mode is used to record the two alternatively arriving data sets. In this project, the optical element switching between both polarizations is the PEM, described in section 3.2.4.

Unfortunately, these background reduction mechanism comes with the downside of causing the effective data collection rate to be halved from 10 Hz to 5 Hz. This means that there is an inherent trade-off between the required run length of the experiment and the desired level of background reduction.

Therefore it is preferred to reduce the background with the already mentioned methods e.g. improving the alignment of the path of the light and molecular beam. The

[11] Work function of stainless steel and of μ-metal are around 4 eV and 5 eV [129, 130]. It varies for different metal alloys [131].

background can also be reduced by gating the VMI-MCP detector (which was already described in section 3.2.3.1) and restricting e.g. the recording time.

3.2.6.3. Data Handling for PECD Measurements

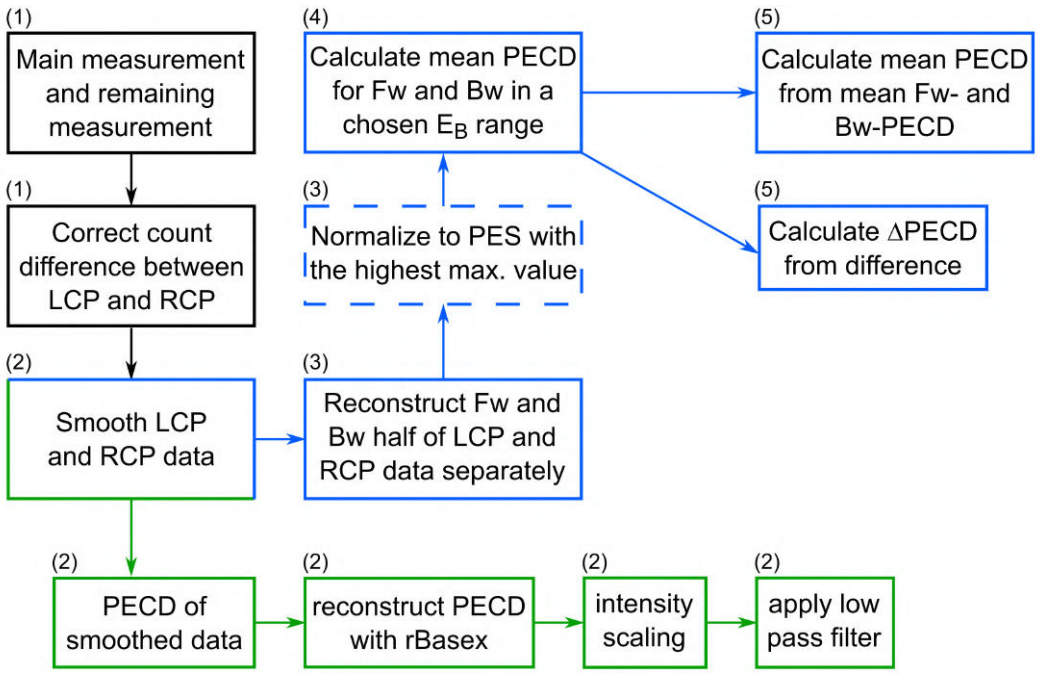

Fig. 3.2.32.: Flowchart for the analysis of PECD data. The first step (1) is the measurement of LCP and RCP data and refers to figure 3.2.33. The second step (2) is the smoothing of the data. For a reconstructed PECD image with rBasex the green path has to be followed (figure 3.2.34). If PECD values are to be extracted from the recorded data POP has to be used and the blue path is taken. The third step (3) is shown in figure 3.2.35. The dashed box is not strictly necessary. The fourth step (4) is illustrated in figure 3.2.36. Figure 3.2.37 shows the below green box of step five.

PECD PADs

The extraction of PECD values from PADs measured with LCP and RCP light and the reconstruction of PECD PADs is illustrated in the flowchart 3.2.32. Five main steps are necessary to get to the PECD value and are all represented in the figures 3.2.33 - 3.2.37.

Step 1: For PECD measurements, two images corresponding to detachment from LCP and RCP light are measured alternatively in the PECD mode. Ideally, both images have the same amount of electron counts after the same amount of measurements cycles (loops), however they always show a count difference of around 0.01 - 3.20%. This count difference neither correlates with the PECD signal nor signal-to-noise ratio or loops. It is probably driven by the cross section of photodetachment and can depend on fluctuations

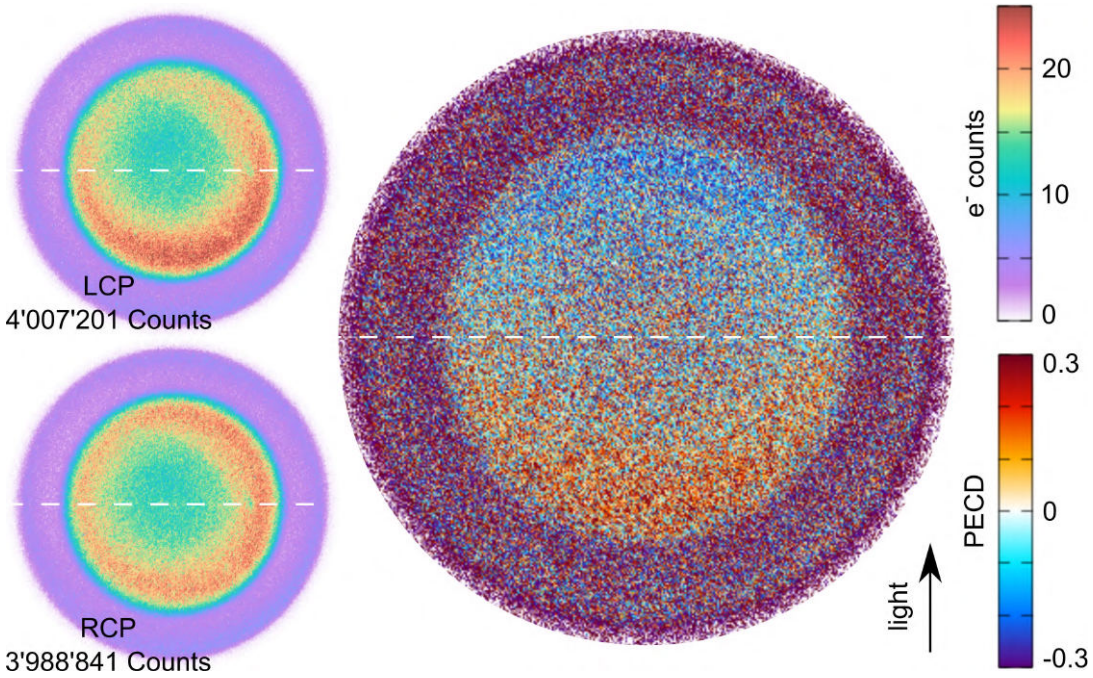

Fig. 3.2.33.: Step 1: Measurement of PECD data. Raw images of the LCP and RCP measurement (left) as well as the resulting PECD image (right) for (R)-[Ind-H]$^-$ at $E_{ph} = 3.49$ eV. Approximately 4 Mio electrons were accumulated for each polarization. No smoothing and no correction of the final counts is applied here.

in molecular and light beam intensity. Also, background fluctuations could have some contribution.

However, this count difference does not necessarily prohibit a PECD signal in the raw images as can be seen in figure 3.2.33. Figure 3.2.33 shows exemplary the PECD measurement of (R)-[Ind-H]$^-$ at $E_{ph} = 3.49$ eV. Despite the missing 0.5% counts in the RCP measurement a PECD asymmetry is visible (on the right of figure 3.2.33). Anyways, for a quantitative analysis the count difference should be reduced to (almost) zero.

To account for this difference, a second PECD measurement is performed right after the first one and stopped when the count difference is met ("remaining measurement"). If the PES of the main measurement (the first measurement) with the lowest electron count is added with the corresponding remaining measurement and compared to the main measurement of the other polarization, the count difference is just a few counts, which is negligible in comparison to the overall electron counts.

Step 2: Both photoelecton distributions are subsequently smoothed in the same way via Gaussian convolution with the "Smooth" subroutine of the main POP program (section 3.2.3.3) and equation 2.2.21 for a PECD image can be applied. The resulting smoothed and count corrected PECD image can be found in the upper, right image of figure 3.2.34.

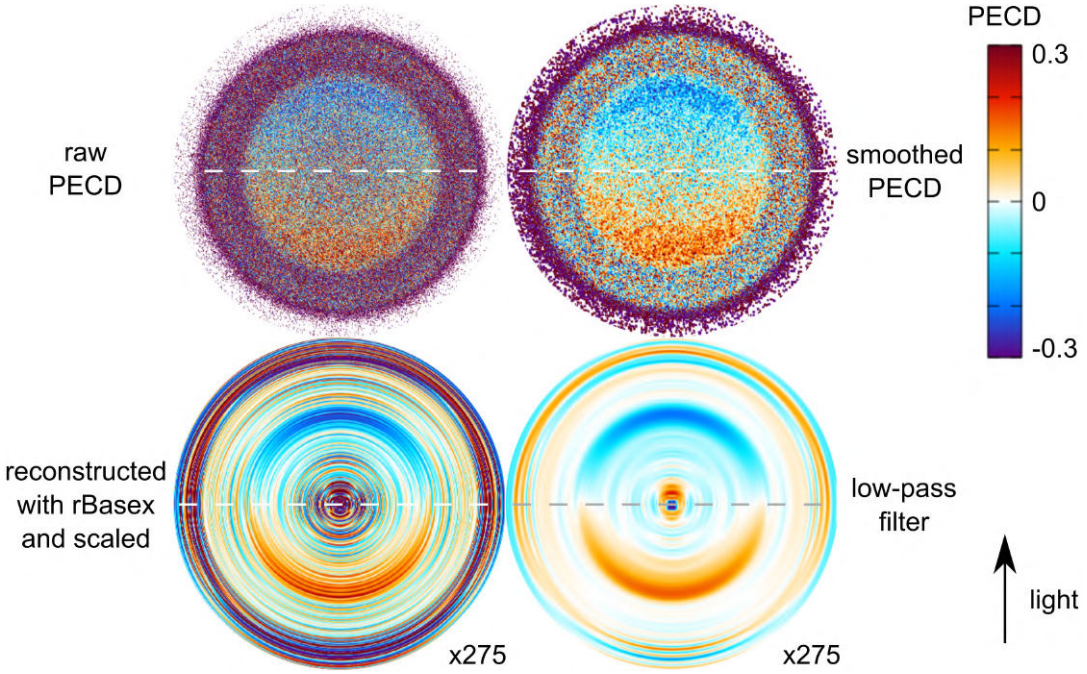

Fig. 3.2.34.: Step 2: Raw PECD image (up, left) from figure 3.2.33 and corresponding PECD image after LCP and RCP data are smoothed (up, right). The reconstruction of the smoothed PECD image via rBasex (down, left) leads to image artifacts in form of rings. The artifacts are alleviated by applying an low-pass filter (down, right).

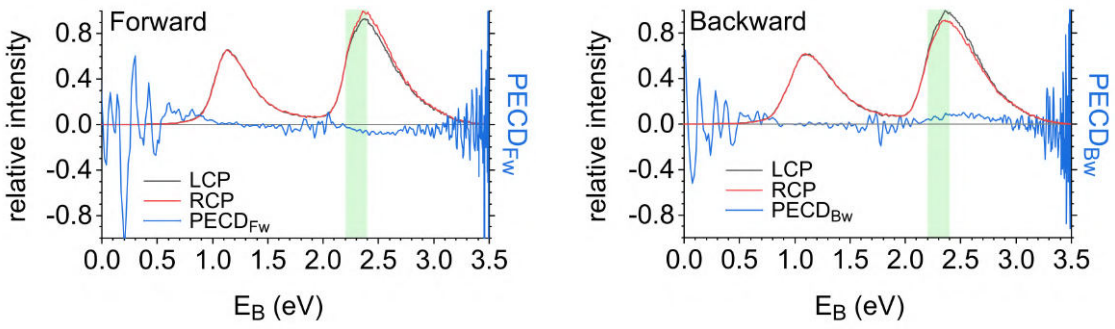

Fig. 3.2.35.: Step 3: Photoelectron spectra of measurements with LCP and RCP light separated in forward (a) and backward (b) direction. Between $E_B = 2$ and 3 eV, PES for LCP and RCP differ clearly in intensity, which also is visible in the PECD function (blue). The intensity difference between LCP and RCP as well as the PECD function switches sign for the other direction. This is recorded under similar conditions as figure 3.2.33 and 3.2.34 but instead of 4 Mio, 70 Mio electrons are accumulated for each polarization for better visualization of the PECD signal. An energy region (green box) is selected for the subsequent analysis.

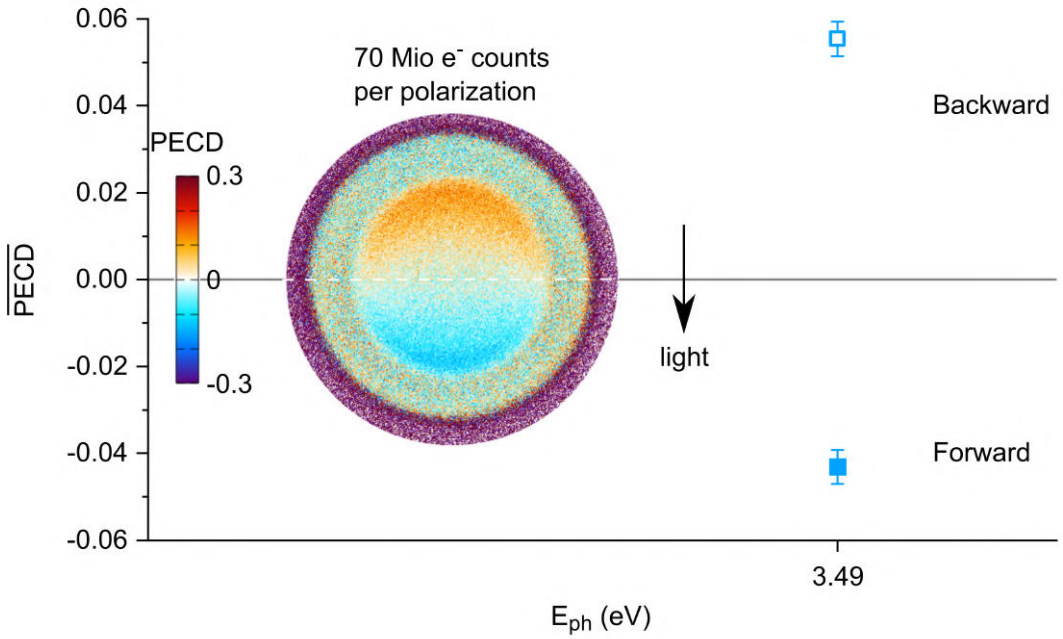

Fig. 3.2.36.: Step 4: Mean PECD values ($\overline{\text{PECD}}$) for forward and backward direction of $[\text{Ind-H}]^-$ at $E_{\text{ph}} = 3.49$ eV in the energy region indicated in figure 3.2.35 with 70 Mio electrons per polarization. Error bars are based on the standard error (SE) of the mean.

For a reconstructed PECD image, rBasex will be used. Unfortunately, this introduces artificial frequencies in form of rings (bottom left of figure 3.2.34) and could be the result of noise/background signal in the raw data. Since these rings are of high frequency a low pass filter, namely the Savitzky-Golay filter [132], will be applied to the reconstructed PECD image, In short, this filter uses convolution to fit a low-degree polynominal with the linear least square method to subsets of the data in an iterative way. One advantage to other methods is the consideration instead of the cutting off of high frequency portions. In the end, this filter leads to an image without high frequencies and it appears smoothed (bottom right of figure 3.2.34).

These images are just for visualization since, unfortunately, PECD values read out from such images do not coincide with the values from the raw or smoothed PECD images due to some internal scaling. The reconstructed as well as the filtered PECD image are shown in the lower part of figure 3.2.34. The PECD "intensity" of the images are scaled with the factor 275 to obtain visually comparable PECD intensities with the raw and smoothed PECD images shown in the upper row.

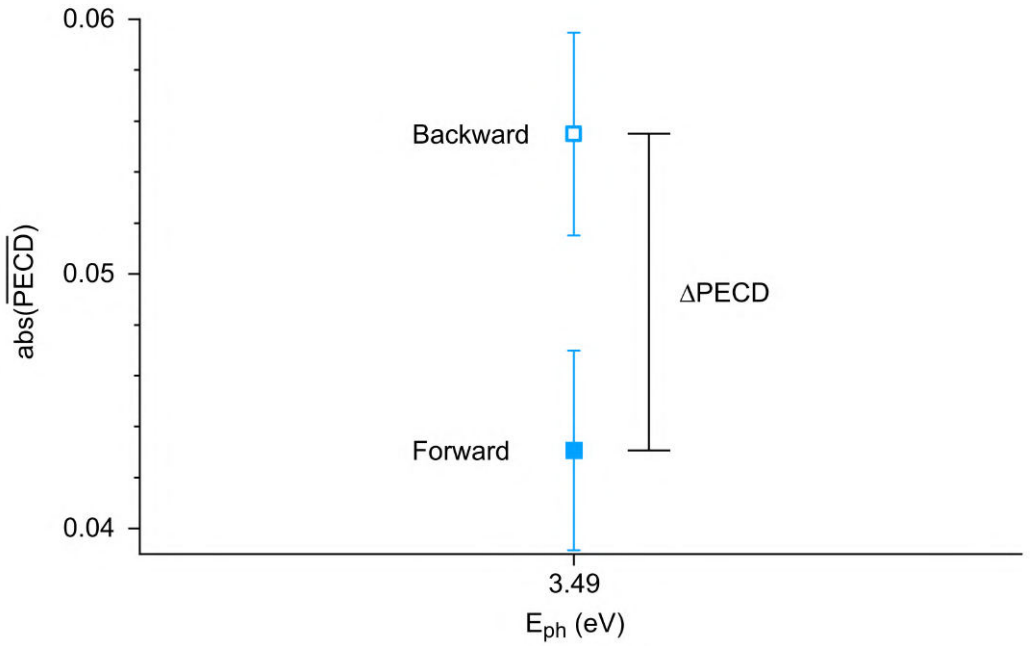

Fig. 3.2.37.: Determination of ΔPECD with the absolute value of the mean PECD ($\overline{\text{PECD}}$) from figure 3.2.36. The forward and backward PECD value should have theoretically the same absolute value but differ clearly. The difference can not be described by the standard error (SE) of mean. Therefore the difference of both values ΔPECD is taken as error to describe the difference in PECD of forward and backward direction.

PECD values

For a quantitative analysis of the PECD data, rBasex and Melexir are theoretically applicable. Although rBasex and Melexir are supposed to reconstruct PECD images and give directly the dichroism parameter, the dichroism parameters obtained here show many (ridiculously high) spikes in value over a broad energy range and also do not coincide with the values obtained from the not reconstructed PECD images even if the spikes are ignored. Again, this could be a result of noise/background in the raw image, which is not handled well in these reconstruction methods. Due to these difficulties, POP will be used for the analysis of PECD data.

Since the main POP program is designed for measurements with linear polarized light, the axis interpreted by POP as symmetry axis coincides with the polarization axis of the light. In order to account for the changed symmetry axis for measurements with circular polarized light, the smoothed PADs are transposed before further processing, which turns the axis for the light path by 90° and hence matches now with the axis POP interprets as symmetry axis.

The reconstruction in POP over the whole PAD would destroy the asymmetry since POP averages over the whole image. While this is not helpful regarding the PECD, it can be used to check on the image quality of LCP and RCP measurement. Both fully reconstructed measurements should lead to PES with equal intensities. For measure-

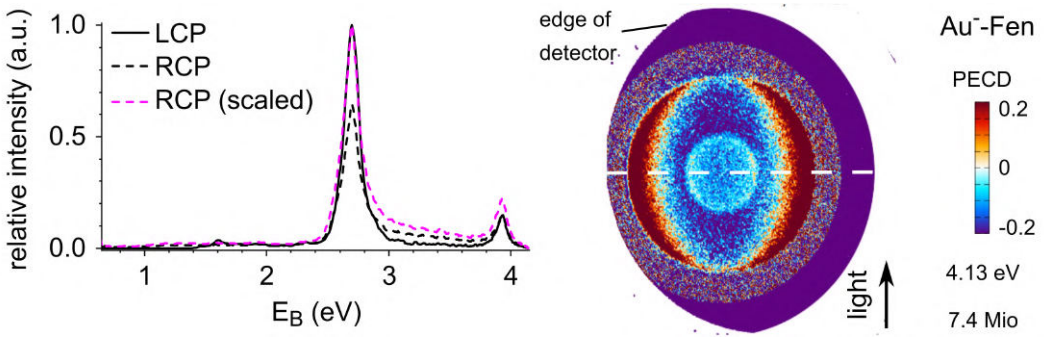

Fig. 3.2.38.: Fully (all quadrants) reconstructed PES of the LCP (black solid) and RCP (black dashed) measurement with POP. Both PES should have the same intensities and shape. However, the RCP PES (black dashed line) needs to be scaled (here with a factor of 1.547) to get equal intensities in the main peak of LCP and RCP (pink dashed line) measurement (left). All PECD measurements with QWPs (and long term signal fluctuations) require such scaling. This concerns the gold complexes. The PECD PAD of the unscaled data is shown on the right. The data is recorded close to the edge of the detector, hence it is cut off on the left side. However, all transitions are contained in the detector image.

ments with quarter waveplates (this concerns mainly the Au^--M measurements), there is unfortunately a quite big difference, like seen for Au^--Fen measured at $E_{ph} = 4.13$ eV in figure 3.2.38. Despite the same amount of electron counts, a scaling factor of 1.547 is needed to make the main peaks equal. The electrons seem to be distributed differently over the PAD for RCP than for the LCP measurement. The cause of the "weird" looking PAD, the corresponding PES and hence the huge scaling factor are explained in more detail in section 4.6 but can be, in short, attributed to long-term drifts. The scaling factors for the deprotonated molecules are around 1, which can be attributed to the shot-to-shot measurements with the PEM and more stable signal intensity. In the case for Au^--M all reconstructed PES (not the PECD PADs) are corrected with a corresponding scaling factor. The PES of the deprotonated molecules are not corrected since the fully reconstructed PES are (almost) equal.

Step 3: To obtain PECD values, the PADs can not be reconstructed fully in POP as explained before but must be separated for each polarization in two image halves corresponding to forward and backward direction (regarding the propagation of the light). The forward and backward half are reconstructed individually for both polarizations, leading in the end to four reconstructed spectra. A comparison of the forward-LCP PES with the forward-RCP PES should show an intensity difference (the PECD signal), which has the same amount but different sign when backward-LCP PES is compared with backward-RCP PES. This is illustrated in figure 3.2.35 for a PECD measurement on (R)-$[Ind\text{-}H]^-$ at $E_{ph} = 3.49$ eV (like before) but with 70 Mio instead of 4 Mio electron counts per polarization due to a less noisy PECD function (blue function in figure 3.2.35).

The PES in figure 3.2.35 are normalized to the maximum value of the PES with the highest intensity for each direction. Hence, two spectra will be at 1 and the other two

will be below 1 according to the PECD difference, e.g. in the forward direction both PES are normalized according to the maximum of the RCP measurement.

Step 4: The PECD asymmetry for each direction is calculated according to

$$\mathrm{PECD_H} = 2\frac{I_{\mathrm{LCP,H}} - I_{\mathrm{RCP,H}}}{I_{\mathrm{LCP,H}} + I_{\mathrm{RCP,H}}} \tag{3.2.26}$$

where H either stands for the forward half (FW) or the backward half (BW). Equation 3.2.26 is another notation of equation 2.2.21 and is obtained for the whole energy range (blue function in figure 3.2.35).

However, certain energy regions are selected to account for the different features, which are available in a spectrum. Here an energy range of 2.187 - 2.376 eV (green box in figure 3.2.35) is used since it contains three transitions, which are not resolved for this photon energy but become resolved when working with visible light [48].

Over the chosen energy range and for each direction, the mean PECD value ($\overline{\mathrm{PECD}}_{\mathrm{Fw/Bw}}$) and the standard error of $\overline{\mathrm{PECD}}_{\mathrm{Fw/Bw}}$ (SE of mean), which is a pure statistical error, are extracted. The result for the measurement for (R)-[Ind-H]$^-$ at $E_{\mathrm{ph}} = 3.49$ eV with 70 Mio electron counts per polarization can be seen in figure 3.2.36.

Step 5: Ideally, both image halves give the same PECD value but are opposite in sign ($\overline{\mathrm{PECD}}_{\mathrm{Fw}} = -\overline{\mathrm{PECD}}_{\mathrm{Bw}}$). Unfortunately, there is a difference in the absolute value of the PECD signal, which points to asymmetries coming from the experimental setup rather than the chiral molecule. This difference can not be explained with the SE of the mean alone (figure 3.2.37). The difference in the PECD signal for both directions could be related to the intensity difference, which was already discovered in PADs measured with linear light when the voltage optimization was described in section 3.2.3.4. Despite the consideration of this intensity difference already in the voltage optimization step, the influence on the PECD asymmetry is clearly visible in figure 3.2.37. Hence, ΔPECD, describing this difference, is considered a machine asymmetry.

To obtain just one PECD value, the overall mean PECD ($\overline{\mathrm{PECD}}$) value of the forward and backward mean PECD ($\overline{\mathrm{PECD}}_{\mathrm{Fw/Bw}}$) is calculated according to

$$\overline{\mathrm{PECD}} = \frac{\overline{\mathrm{PECD}}_{\mathrm{Fw}} - \overline{\mathrm{PECD}}_{\mathrm{Bw}}}{2}. \tag{3.2.27}$$

The PECD value (and its errors) is set to be zero if both image halves give the same sign for the PECD asymmetry, else the SE of the mean and the difference of PECD values for both images halves (ΔPECD) are evaluated to describe the accuracy of the PECD values. However, ΔPECD is in general bigger than the SE of mean (figure 3.2.37) and represent a more realistic error, which is based on experimental conditions rather than statistical ones. The data with SE as error is shown in [48] but ΔPECD will be used here for measurements with non-zero PECD values.

3.2.6.4. PECD with PEM vs QWP

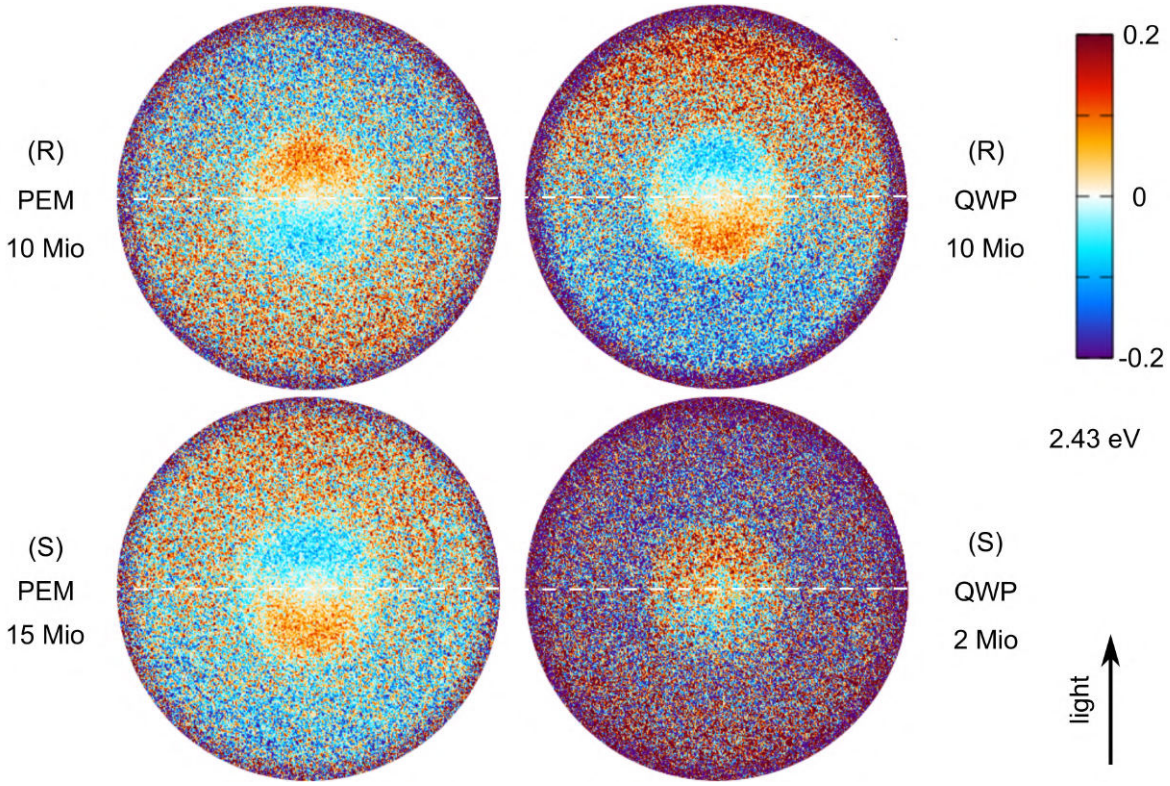

Fig. 3.2.39.: Comparison between PECD measurements performed with QWP and PEM at $E_{\mathrm{ph}} = 2.43$ eV. The QWP is turned once for the polarization change while the PEM changes the polarization shot-to-shot. The PECD asymmetry of the QWP is reversed in contrast to the PEM. The PECD measurement with QWP by itself is consistent since it changes with the enantiomer.

PECD measurements were mainly performed with quarter waveplates for Au^--M and with the photoelastic modulator for the deprotonated species. For Au^--Ala and $[Ind\text{-}H]^-$ quarter waveplates and the photoelastic modulator were used to compare both measurement methods. Since the main difference between both methods is the switch frequency of the light polarization, with the photoelastic modulator switching the polarization in a shot-to-shot manner while the quarter waveplate was only switched manually after one polarization measurement (after 3-4 hours), the influence of long and short term fluctuation on the PECD signal is investigated. The photoelastic modulator is expected to result in PECD signals with higher quality since long term fluctuations are handled better than for the quarter waveplate method. In the following the discussion concentrates on $[Ind\text{-}H]^-$ and not Au^--Ala due to the non-null PECD signal for $[Ind\text{-}H]^-$.

The PECD asymmetry is measured for $E_{\mathrm{ph}} = 2.43$ eV with a quarter waveplate and compared with the PECD measurements with the photoelastic modulator (figure 3.2.39). For all transitions, A, B_1, B_2 and B_3 (which are explained in more detail in section 5.3.2), the mean PECD values are evaluated and shown in figure 3.2.40. In both figures a clear

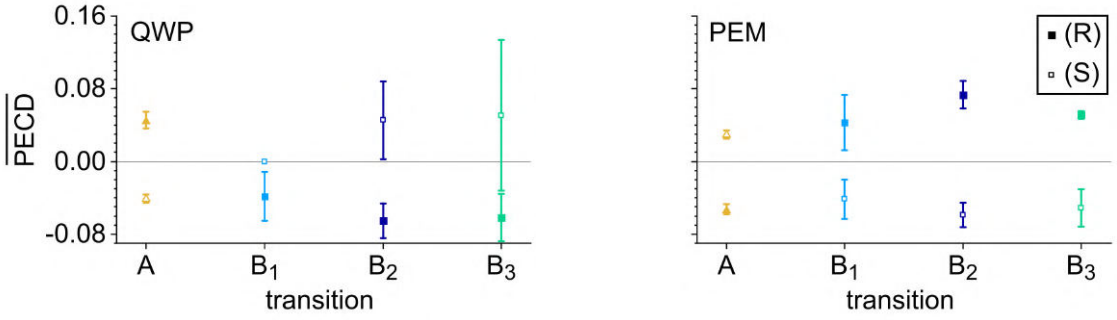

(a) (b)

Fig. 3.2.40.: Mean PECD values for the PECD measurement performed with QWP (a) and PEM (b) at $E_{ph} = 2.43$ eV for the transitions A and $B_{1,2,3}$. Full symbols represent the (R)- and empty symbols the (S)-enantiomer. The mean PECD values are given with ΔPECD as error. The worst quality has the measurement for the (S)-enantiomer with QWP due to the low total electron counts per polarization (2 Mio). The mean absolute PECD values are comparable but the used error is not sufficient in all cases.

but inverted PECD signal can be seen in each measurement, which is probably the result of a mislabeled fast axis of one of the optical elements. One exception is the B_1 feature for the (S)-[Ind-H]$^-$ measured with the quarter waveplate, which shows no PECD signal probably due to low total electron counts/statistics. Considering the error ΔPECD, the photoelastic modulator seems to produce data with smaller error and, hence, gives results of better quality, as was expected.

The reason for the inverted PECD asymmetry for the quarter waveplate measurement is unclear. A measurement with the photoelastic modulator was repeated the same day to confirm the inversion. The way the PEM data is saved is controlled, e.g. if the data saved in the correct file, and determination of the light polarization for the photoelastic modulator and quarter waveplate was confirmed by a different person.

The position of the fast axis of the quarter waveplate and/or the photoelastic modulator could be different from the company label or description. However, to control for the fast axis position an experiment with a chiral molecule with known PECD asymmetry would need to be performed. However, most PECD experiments are performed on neutrals for which this experiment is not designed. A professional polarimeter could also help determining the absolute polarization after both optical elements and determine which optical element could have the (in)correctly set or mislabeled fast axis.

In general, the error is smaller for the (R)-enantiomer than for the (S)-enantiomer since for the (R)-enantiomer a more intense and more stable signal was at hand leading to a better signal-to-noise ratio. Reproducing the source condition for the (S)-enantiomer was not possible which lead to a weaker ion signal and also to lower electron counts (or longer recording time for the same electron counts), e.g. only 2 Mio electrons are recorded for the (S)-enantiomer for the measurement with the quarter waveplate. Signal fluctuations in the case of the (S)-enantiomer can be handled to some extent by the shot-to-shot measurement of the photoelastic modulator but has greater influence on the

measurement with the quarter waveplate. Such fluctuations lead to bigger errors and can also be responsible for the zero mean PECD value for feature B_1 in the measurement with the quarter waveplate for (S)-[Ind-H]$^-$.

In the following, experiments are continued with the photoelastic modulator due to the shot-to-shot measurement method leading to PECD results of better quality than with the quarter waveplate.

3.3. Density Functional Theory

Apart from the experiment, theoretical results can be as important since they help with model development, preparation of the experiment, predictions and analysis/assignment of the experimental observation. For instance in the field of molecular physics, the calculation of molecular properties like bond lengths, dissociation energies and electron affinities are of interest to design and understand experiments, which investigate certain molecules. Such properties are dependent on the molecular structure and can strongly vary between isomers. DFT is one method to obtain the molecular structures and the corresponding molecular properties.

DFT is based on the approximation of the electron density and has – in contrast to ab-initio methods, which are based on the calculation of wave functions – only a small number of spatial coordinates to consider. Furthermore, the number of coordinates does not scale with the number of electrons in the system making it applicable to many-electron systems and reducing the computational cost.

Despite the reduced computational complexity, DFT is based on assumptions and has problems with e.g. strongly correlated systems and liquids [133]. However, DFT has the flexibility to let the user choose between different approximations in form of various functionals and basis sets. Consequently, DFT adapts to the problem at hand and leads to satisfying results in a wide scientific community.

The prediction of structures for systems used in this thesis (gold complexes and deprotonated molecules) as well as their electron affinities, dissociation energies etc are obtained with DFT. Hence, an overview of the basics for DFT is addressed here. An elaborate description or introduction for DFT can be found in e.g. [134–137].

Nonrelativistic, spinless quantum chemical problems can be described by the Schrödinger equation. In these cases, instead of a wave function ψ, a (probability) electron density $n(\vec{r})$ (c.f. equation 3.3.28) is applied to the Schrödinger equation. In comparison to a wave function, the electron density is an experimentally detectable quantity and holds just three instead of $3N$ ($4N$ if spin is considered) spatial variables for an N-electron system.

$$n(\vec{r}) = N \int \cdots \int \left|\psi\left(\vec{x}_1, \vec{x}_2, \ldots, \vec{x}_N\right)\right|^2 ds_1 d\vec{x}_2 \ldots d\vec{x}_N \tag{3.3.28}$$

with $\vec{x}_i$ holding the three spatial coordinates $\vec{r}_i$ and the spin s_i of the i-th electron. $n(\vec{r})$ is the probability of locating one of the N electrons with arbitrary spin s inside the volume element $d\vec{r}_1$. The other $N-1$ electrons have arbitrary spin and locations.

Thomas and Fermi [138] were the first to solve the Schrödinger equation with $n(\vec{r})$. Due to strong approximations applied to the Hamilton operator their model was not able to describe complicated systems like molecules.

Another approach is described by Kohn and Sham [139]. Here, all terms, which require assumptions (unknown terms) are separated from the terms, which are known. What is known is for example operators for non-interacting (ni) reference systems like the kinetic energy operator for a free electron $\hat{T}_{\mathrm{ni}} = -1/2\nabla^2$ (atomic units are used here and will be used in the following equations of this section as well.). The Hamilton operator holding all known terms or terms for non-interacting systems is the Kohn-Sham operator $\hat{H}_{\mathrm{KS}}$. The unknown terms, mostly terms describing interactions like the electron-electron interaction, which require approximations are concentrated in a remainder operator $\hat{V}_{\mathrm{r}}$. The equation rising from the Kohn-Sham approach build the foundation of DFT:

$$\hat{H}n = En \tag{3.3.29a}$$

$$\hat{H} = \hat{H}_{\mathrm{KS}} + \hat{V}_{\mathrm{r}} \tag{3.3.29b}$$

$$\hat{H}_{\mathrm{KS}} = -\frac{1}{2}\nabla^2 + \hat{V}_{\mathrm{ni}} \tag{3.3.29c}$$

with $\hat{V}_{\mathrm{ni}}$ being a local effective potential operator.

In principle, $\hat{H}$ is exact (for a nonrelativistic system without quantum electrodynamics). However, approximations are necessary for the remainder potential and thus $\hat{H}$ becomes an approximation as well. Meanwhile, there is a great variety of approximations from which a system adequate approximation can be chosen.

Unfortunately, even with the Kohn-Sham approach and an electron density, the rewritten Schrödinger equation 3.3.29 can not be solved exactly (except for hydrogen or hydrogen alike systems) and the real electron density remains unknown. However, with the help of the variational principle the ground state wave function ψ_0 and ground state electron density n_0 with corresponding ground state energy E_0 are obtained (and also all excited states with time dependent DFT).

Here, all expectation values, like the energy, are functionals of the electron density $E[n]$ and need to be minimized by searching through all acceptable electron densities until the density with the lowest energy is found. Certainly, this search technique is unrealistic and rather a subset of electron densities has to be scanned. Hence, it could be that the real ground state density is not in the chosen subset but can be approximated by an electron density in this subset.

The minimization of the energy functional requires the self-consistent field (SCF) procedure since the Hamilton operator is dependent on the electron density (the solution) itself via the potential operator. The minimized electron density is an unique density for the system due to the unambiguous assignment to the external potential operator (e.g. the positive background field of the nuclei is considered as external potential for electrons but is not restricted to it) and leads to the lowest energy if the minimized density is the real electron density [140].

3.3.1. Functionals

In the Kohn-Sham approach the Hamilton operator is subdivided into a known and an unknown part. The same can be done for the energy functional:

$$E[n] = T_{\mathrm{ni}}[n] + J[n] + E_{\mathrm{ne}}[n] + E_{\mathrm{r}}[n] \tag{3.3.30a}$$
$$E_{\mathrm{r}}[n] = (T[n] - T_{\mathrm{ni}}[n]) + (E_{\mathrm{ee}}[n] - J[n]) = T_{\mathrm{c}} + E_{\text{non-cl}} \tag{3.3.30b}$$

The known part consists of the non-interacting kinetic energy $\hat{T}_{\mathrm{ni}}$, the energy between nuclei and electrons E_{ne}, and the classical electrostatic electron repulsion energy J for which an explicit form can be given. The remainder energy E_{r} contains all unknown energies – in particular the correlation part of the kinetic energy T_{c} – and all non-classical effects like self-interaction corrections, exchange and correlation.

Approximations are needed for the remainder energy to derive an energy functional, which describes the quantum system with sufficient accuracy and is computationally cheap. The best choice of energy functionals depends on the quantum system at hand with different systems requiring different approximations. Hence, the best way to choose a functional is to apply candidates to both the system of interest and reference systems and to then take the one that matches the experimental data best. One of the first approximations for the remainder functional is the Local (Spin) Density Approximation, L(S)DA, which was introduced by Kohn and Sham [139]. Here, an uniform and homogeneous electron gas is assumed, since the correlation and exchange functional energies are well known for this case. Even the spin is considered. However, it only works well for an ideal metal, but poorly for atoms and molecules. The functional by Perdew and Wang from 1992 (PW92) is a representative of this approach.

A better approximation is the Generalized Gradient Approximation (GGA), which allows (slow) variations of the electron density and can be seen as an extension of the L(S)DA approach. Becke's functional B88 (or B) is an example functional for this approach.

To account for inhomogenities present in molecules, the reduced density gradient is introduced in the GGA approach. An example functional (for the correlation part) is the one from Lee, Yang, Parr (LYP) [141]. Here, instead of a uniform electron gas, the knowledge about the correlation energy of helium is applied.

Another class of functionals are the so-called hybrid functionals. In comparison to the previous methods, these use exact functionals (e.g. from classical effects, uniform electron gas) in combination with approximated functionals (e.g. from non-classical effects like electron-electron correlations, GGA and L(S)DA). An "interaction parameter" determines the amount of interaction in a system and the influence of the approximated functionals on the overall functional. Among the presented approximations, the hybrid functionals are the most accurate ones [134].

Assuming that the exchange-correlation functionals of both the non-interacting and the fully interacting system contribute with equal parts (half-half combination), the exchange-correlation functional can be written as

$$E_{\mathrm{xc}}^{\mathrm{B3LYP}} = (1-a)E_{\mathrm{x}}^{\mathrm{L(S)DA}} + aE_{\mathrm{xc}}^{\mathrm{ni}} + bE_{\mathrm{x}}^{\mathrm{B88}} + cE_{\mathrm{c}}^{\mathrm{LYP}} + (1-c)E_{\mathrm{c}}^{\mathrm{L(S)DA}} \tag{3.3.31}$$

with E_{x} as the pure exchange functional, E_{c} as the pure correlation functional, E_{xc} as the exchange-correlation functional and the three interaction parameters: a, b and c. Equation 3.3.31 is the wide-spread B3LYP functional (Becke, 3 parameters, Lee, Yang, Parr), with the exchange energy functional from Becke and the correlation energy functional from Lee, Yang and Parr (LYP) [141]. It belongs to the class of hybrid functionals.

So far, all discussed methods do not include dispersion effects and thus are not appropriate for problems involving hydrogen bonding, bonding of noble gases, protein folding, or other highly polarizable systems like Au^-. This is because methods like GGA are local, while dispersion is a non-local, pure correlation effect. The dispersion correction of Grimme [142] is a widely implemented solution for this problem due to its robustness, speed, simplicity in programming and satisfying accuracy. For this method, atomic dispersion corrections ($\propto R^{-6}$) are added to standard functionals (GD)[143]. Later damped dispersion correction terms were used and the GD functional was generalized as well as reparametrized (GD2) [144]. The most recent and advanced functional of Grimme uses structure-dependent dispersion coefficients (GD3) [142]. It handles all elements from Z=1 to Z=94 consistently, and reproduces the asymptotic behavior for finite systems (molecules) exactly.

If GD3 is used for e.g. B3LYP, the functional is written as B3LYP-D3. This is the functional, which is chosen to calculate the gold complexes and deprotonated species in this thesis.

3.3.2. Basis Sets

The application of DFT requires another ingredient: the basis sets, which yield the Kohn-Sham orbitals ϕ_i. Almost all computational procedures are based on the linear combination of atomic orbitals (LCAO) ansatz

$$\phi_i = \sum_{\mu=1}^{L} c_{\mu,i}\eta_\mu \tag{3.3.32}$$

with η_μ being a finite basis set with L functions. The density in that case is

$$n(\vec{r}) = \sum_{i}^{N} \left|\phi_i^2(\vec{r})\right| = \sum_{i}^{N}\sum_{\mu}^{L}\sum_{\nu}^{L} c_{\mu,i}c_{\nu,i}\eta_\mu(\vec{r})\eta_\nu(\vec{r}). \tag{3.3.33}$$

In order to solve the Kohn-Sham equation properly, all ϕ_i's should be considered such that $L = \infty$ (exact limit) but practically L is finite (basis set limit) and should be chosen big enough to achieve the desired accuracy. There are different kinds of basis sets, which are designed for different problems: While Gaussian-type orbitals (GTO) feature

great computational advantages, Slater-type orbitals (STO) are more appropriate from a physical point of view and model the behavior for $r \to 0$ and $r \to \infty$ better. However, a STO is difficult to handle computationally. Because of that, contracted Gaussian Functions (CGF) are introduced to combine the advantages of GTO (computationally cheap) and STO (better treatment of radial behavior). Another basis set is the double-zeta one, which assigns two functions per orbital. If chemical reactions are of interest, the computational costs are reduced by applying the double-zeta basis set only to the valence orbitals while the core orbitals use smaller, simpler basis sets (split-valence type basis sets). This basis set can easily be extended to triple- or quadruple-zeta and is used by the Dunning basis sets denoted cc-pVTZ and cc-pVQZ (correlation-consistent polarized valence triple/quadrupole zeta), respectively. Additionally, basis sets can be expanded by polarization functions, which contain higher angular momenta. These functions describe also unoccupied states in atoms/molecules, e.g. the p state in hydrogen. These are the augmented basis sets (aug), which are appropriate for molecules since the atomic orbitals are allowed to distort and thus can adapt to the molecular environment.

When modeling heavier elements such as gold, relativistic effects like the stronger coupling between the spin of the electron and the orbital angular momentum or the velocity-dependent mass have to be considered. The last effect is particular important since it results in core contractions, which must be considered for core states and their influence on chemically relevant valence shells in every model for such systems. For this, the core states are substituted by a potential imitating the core states and its influence on valence states [137]. This is the effective core potential (ECP) or pseudo-potential (PP). Since valence electrons are shielded from the core by the inner electrons, relativistic effects become negligible and non-relativistic basis sets like aug-cc-pVTZ can be applied.

3.3.3. Energies

Once, a functional and basis set are chosen, structure optimization lead to the ground state energy $E_\mathrm{g}(M)$ of a system (e.g. a molecule) M. Additional frequency calculations lead to vibrational frequencies, confirm the convergence of the calculation and give the zero-point energy (ZPE). The ZPE-corrected ground state energy of M, called $E(M)$, is then given by

$$E(M) = E_\mathrm{g}(M) + \mathrm{ZPE} \tag{3.3.34}$$

and will be used predominantly.

The molecular constants of a diatomic system like VDE, ADE, dissociation energy D_0 etc. can be explained with the aid of two interatomic potentials, which are approximated by Morse potentials. Here, VDE and ADE describe transitions between two Morse potentials while D_0 is explained by following one Morse potential to higher bond lengths. In an analogous way, the interatomic potential(s) can be applied to an anionic pseudo-diatomic model, which is created if one of the atoms is replaced by a neutral molecule, called M, and the other atom by an anion, called A^- (figure 3.3.1). In simplest terms, this system can still be treated as diatomic system in a Morse potential.

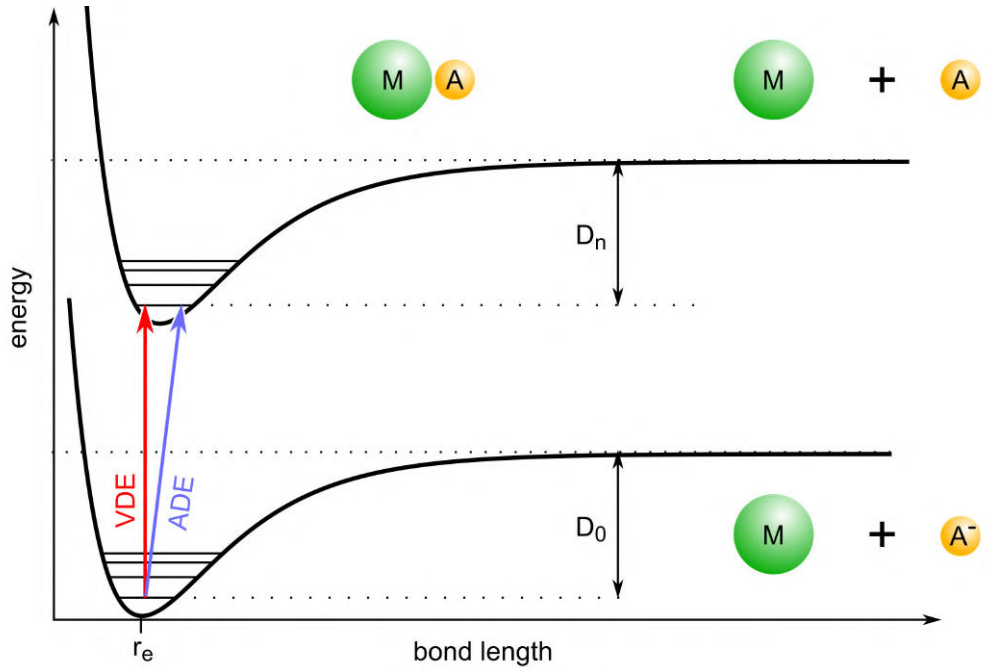

Fig. 3.3.1.: Simplified potential scheme for electron detachment illustrating the definition of VDE, adiabatic detachment energy (ADE), dissociation energy D_0 of the anionic diatom, dissociation energy D_n of the neutral diatom and equilibrium bond length r_e. If structural changes happen after photodetachment, r_e changes and VDE≠ADE.

If two elements form a diatomic molecule, the system is stable in the well of the interatomic potential and has the energy E. During the dissociation process, the diatomic molecule follows the interatomic potential to longer bond length until the bond breaks and the constituent parts are separated (figure 3.3.1). The energy required for this process is the dissociation energy D_0. For the anionic pseudo-diatomic system (A^--M), D_0 is the energy difference between the complexed system $E(A^-\text{-M})$ and the sum of the separated elements $E(A^-)$ and $E(M)$

$$D_0 = E(A^-) + E(M) - E(A^-\text{-M}) \tag{3.3.35}$$

Analogously, a dissociation energy for the neutral complex D_n can be defined

$$D_n = E(A) + E(M) - E(A\text{-M}) \tag{3.3.36}$$

If the neutral complex is not allowed to relax to its optimized structure than the corresponding energy $E^*(A-M)$ leads to an excited dissociation energy of the neutral complex

$$D_n^* = E(A) + E(M) - E^*(A\text{-M}). \tag{3.3.37}$$

Another process an anionic diatomic system can undergo is electron photodetachment, where an electron is removed, leaving behind the neutral diatomic system. Computationally, an electron detachment energy can be computed from the energy difference of

the anion and neutral diatomic system, where constraining the neutral geometry to the same geometry of the anion provides the vertical[12] detachment energy (VDE) (equation 3.3.38).

$$\mathrm{VDE}(\mathrm{A^-M}) = E^*(\mathrm{AM}) - E(\mathrm{A^-M}) \tag{3.3.38}$$

Allowing the neutral diatomic system to relax to its stable configuration yields the ADE (equation 3.3.39).

$$\mathrm{ADE} = E(\mathrm{AM}) - E(\mathrm{A^-M}) \tag{3.3.39}$$

Since ADE arises from the structural change after photodetachment and VDE assumes an unchanged structure, the difference VDE - ADE gives a relaxation energy for the neutral case, an energy needed to reach the ground state structure from an excited state.

In experimental photodetachment studies, it is quite reasonable to assume no structural changes after photodetachment since such changes are too slow for this kind of process (Born-Oppenheimer approximation). In other words, r_e, the minimum of the interatomic potential, should be the same for both Morse potentials and VDE should be equal to ADE. Here, the resulting measured electron binding energy E_B is compared to VDE.

The shift (ΔVDE), the difference between the VDE of the pseudo-diatomic system and the VDE of the bare atomic anion $\mathrm{A^-}$ is defined in equation 3.3.40.

$$\Delta\mathrm{VDE} = \mathrm{VDE}(\mathrm{A^-M}) - \mathrm{VDE}(\mathrm{A^-}) \tag{3.3.40}$$

It gives (approximately) the interaction strength between $\mathrm{A^-}$ and M. The corresponding measured value is called ΔE_B.

In general, many isomers belong to the same pseudo-diatomic system $\mathrm{A^-}$-M. They are considered as stable system if the (ground state) energy or the inner energy of the system is negative. Relative stability between isomers can be judged by comparing the ground state energies or the ZPE-corrected minimum energies $E_0(\mathrm{A^-M})$ (E_min + zpe = E_0) with each other. The isomer with the lowest minimum energy is considered to be the most stable isomer and is called E_0(most stable $\mathrm{A^-M}$). All other $E_0(\mathrm{A^-M})$ are given relative to this energy and only the difference to E_0(most stable $\mathrm{A^-M}$) is considered further (equation 3.3.41).

$$E_0 = E_0(\mathrm{A^-M}) - E_0(\text{most stable } \mathrm{A^-M}) \tag{3.3.41}$$

3.3.4. Choice of Functional and Basis Set

From the vast functional/basis set combinations that are exist, B3LYP-D3/aug-cc-pVTZ(-PP) is used as main calculation method on Gaussian16 (g16) [145]. This decision was made after testing 12 different functional/basis set combinations on reference systems ($\mathrm{Au^-}$ and $\mathrm{Au^-}$-$\mathrm{H_2O}$) and one of the here investigated gold complexes ($\mathrm{Au^-}$-Fen). The calculated results are compared to the experimental

[12]The transition from the anion to the neutral configuration describes a vertical line (figure 3.3.1)

values of the reference systems (Au^- with E_B = 2.309 eV [77] and Au^--H_2O with E_B = 2.76 eV [146]) and the gold complex Au^--Fen ($E_B = 2.69 \pm 0.02$ eV, section 4.3 or [51]).

Out of the 12 functional/basis set combinations, B3LYP-D3/aug-cc-pVTZ(-PP) gave energies, which generally differ the least from literature and experimental values (not shown). In particular, the literature and experimental values for Au^-, Au^-H_2O and – the most stable – Au^--Fen deviate by only 0.09 eV, 0.05 eV and 0.11 eV, respectively. Some readers might think that 0.11 eV is a significant deviation. Better results could be achieved if more functionals and basis sets were tested. However, this is a time consuming process and hence was omitted here. Furthermore, in section 4.4.1 it is demonstrated that there seems to be a simple linear relationship between the calculated and the experimental results, which helps to predict experimental values more accurately than the calculated results do and is also faster than searching for the perfect functional-basis set combination.

For an orbital composition analysis, Hartree-Fock (HF) is used in combination with aug-cc-pVTZ(-PP). Instead of electron densities, wave functions are used, which normally lead to more precise information on the (molecular) orbitals, e.g. their composition from different atomic orbitals. Orbitals with corresponding energies and orbital composition analysis are obtained with the help of the Multiwfn software [147].

4. Gold Complexes of Chiral Molecules[1]

Fig. 4.0.1.: The four molecules used to create Au^--M, in skeletal representation (a subset of figure 3.1.1). All molecules are chiral and have a non-superposable mirror image (not shown). The stereogenic center is highlighted with a * and their absolute configuration is given.

This chapter will have two main foci: nonconventional hydrogen bonds of the type $Au^- \cdots$H-C,N,O and the first PECD measurements on gold-chiral complexes Au^--M with M being the chiral molecule fenchone (Fen), menthone (Men), 3-hydroxytetrahydrofuran (3HTHF) or alaninol (Ala) (figure 4.0.1). Of particular interest is the bond $Au^- \cdots$H-C and if the interaction between molecule and Au^- is strong enough for recognizable PECD signals.

4.1. Introduction and Motivation

The gold complexes were the first targets for the anion PECD measurements. The idea behind these complexes were to create an anionic chiral system, which is easy to produce and without (strongly) altering the chiral molecule itself yet providing an electron source (Au^-) from which an electron can easily be photodetached. The detached electron would then interact with the chiral environment provided by the molecule and lead to the PECD effect. While PECD measurements were the main focus in the beginning, analyzing PES measured with linear polarized light and DFT calculations showed further interesting results towards (unconventional) hydrogen bonding.

Historically, hydrogen bonds are interactions, between hydrogen and either oxygen, nitrogen or fluorine, the most electronegative elements. However, evidence for hydrogen bonds with alternative elements, which retained the hallmark properties of a hydrogen bonded system accumulated over time [148–157]. Hence, the IUPAC redefines hydrogen

[1]This chapter is in part based on the article J. Triptow, G. Meijer, A. Fielicke, O. Dopfer, M. Green, "Comparison of Conventional and Nonconventional Hydrogen Bond Donors in Au– Complexes", 2022, in: The Journal of Physical Chemistry A, ACS Publications, in press DOI: 10.1021/acs.jpca.2c02725

bonds by discarding the idea of the use of specific atoms in favor of specific properties, like geometric, energetic and electronic ones [158].

Now, IUPAC defines a hydrogen bond as an attractive interaction between three elements: the hydrogen (H), which is covalently bound to an atom called the hydrogen donor (X), interacts with an atom called the hydrogen bond acceptor (Y). X and Y are both electronegative atoms with Y having electron donor character. In general, a hydrogen bond is written as X-H$\cdots$Y. A hydrogen bond is also considered a three-center-four-electron (3c-4e) bond [159, 160].

Some of the properties defined by the IUPAC are:

1. The bond X-H$\cdots$Y is almost linear: $\angle$XHY = 110 - 180°
2. H$\cdots$Y length is smaller than the van-der-Waals radii of H and Y
3. Commonly, the bond length X-H increases for a hydrogen bond, leading to a redshift in the stretching frequency of X-H
4. Involved forces are electrostatic (dipole-dipole interaction), inductive, dispersive. Their contribution can depend on the charge character of proton donor and acceptor [161]
5. The electron density topology usually shows a bond path and a (3,-1) bond critical point between H and Y

The IUPAC lists more than the here given properties like NMR characteristics but they are not considered here since it is not possible with this experimental setup to test them all and does not need to be fulfilled completely to call a bond a hydrogen bond anyways [158]. This also concerns the measurement of the red shift for the stretching frequency in point 3 since there is currently no setup for vibrational measurements. However, the bond length is monitored via DFT calculations.

This more universal definition of the hydrogen bond motivated many studies to non-conventional hydrogen bonds. Especially transition metals have been found to be good hydrogen acceptors [157, 162–166]. Brammer explained this property with electron rich transition metals with filled d shells [149]. Especially, the class of late transition metals, to which Au belongs, should be the best hydrogen acceptors.

Originally, Au^- was chosen under the aspect of PECD measurements but it turned out to be a good candidate for hydrogen bonding as well: The gold atom is relativistic meaning that the atomic and ionic radii are contracted [137] leading to greater accessibility for hydrogen donors. Furthermore, the relativistic effects are responsible for gold being one of the most electronegative transition metals with 1.92 (Allen scale), which is similar to heavy halogens. Au also has a high polarizability and behaves like a Lewis base. The neutral atom, as well as, the anionic gold have been found to form (nonconventional) hydrogen bonds [127, 167], whereas the additional charge in the anion strengthen the interaction leading to so called charge assisted hydrogen bonds [168–170].

Hydrogen bonds of the type $Au^-\cdots$H-X normally concerned conventional hydrogen donors like O, N and F. Smaller systems found moderate and strong bonding [146,

171–175]. Also, more complex systems like microsolvation and nucleaobases can be found mainly with the common donor atoms [127, 176, 177]. Few studies focus on the nonconventional donors and bonds like $Au^- \cdots$ H-C. The problem is that they are either overshadowed by other, stronger hydrogen bonds or that they can not conclusively be identified as hydrogen bonds [152, 177, 178].

Although, there are only a few studies on $Au^- \cdots$ H-C hydrogen bonds, the importance of such interaction can be significant. In catalysis, $Au^- \cdots$ H-C is expected to be an important secondary interaction [178, 179]. Important molecules in biology and chemistry often have no conventional hydrogen donors and can only offer H-C like fenchone and menthone. They only have a ketone as functional group, which can not act as hydrogen donor. These molecules are part of a larger group of compounds, which are being used for green synthesis of gold nanoparticles [180–182].

The other two investigated molecules, 3-hydroxytetrahydrufuran (3HTHF) and alaninol, can be considered as comparative molecules since they can offer in both cases OH and additionally NH in the case of alaninol. 3HTHF is considered a standard in measuring hydrogen bonding [183, 184]. Alaninol even shows internal hydrogen bonding in the form of N$\cdots$H-O or O$\cdots$H-N, depending on the isomer.

An analysis of these different complexes not only provides insight into the general characteristics of nonconventional hydrogen bonding with gold, but also provides insight into the potential of the interaction between the photoelectron source (Au^-) and the chiral component (Fen, Men, 3HTHF and Ala) being "chiral". In other words, this analysis gives a first look into the possibility of PECD asymmetries of these complexes. The sections about hydrogen bonding are already partly published in [51].

4.2. Mass Spectra

The utilization of a gold target in the laser ablation source produces mass spectra, which peaks at multiples of m/z 197 corresponding to Au_m^- as evident in figures 4.2.1. If in addition chiral molecules are introduced, the gold complexes Au^--M can form (figures 4.2.1)[2]. In particular, peaks appear in the spectrum at m/z 349 for Au^--Fen (figure 4.2.1a), m/z 351 for Au^--Men (figure 4.2.1b), m/z 285 for Au^--3HTHF (figure 4.2.1c) and m/z 272 for Au^--Ala (figure 4.2.1d), where m/z consists of a contribution of the gold anion m/z 197 and the corresponding molecule (m/z 152 for fenchone, 154 for menthone, 88 for 3HTHF and 75 for alaninol).

Along side the desired complex Au^--M, different kinds of clusters (Au_m^--M_n) are observed. In particular, Au_m^--Fen_n with $m = 1$ and up to $n = 4$ (highlighted in green in figure 4.2.1a) are observed as well as $m = 2$ with up to $n = 2$ (highlighted in blue). Also Au_m^--Fen_n with $m = 3$ and $m = 1$ are visible in the mass spectrum (highlighted in red). Similar combinations are visible in the other mass spectra containing the other chiral molecules.

[2]The presented spectra of figure 4.2.1 are not necessarily optimized for the target complex in order to show various other features.

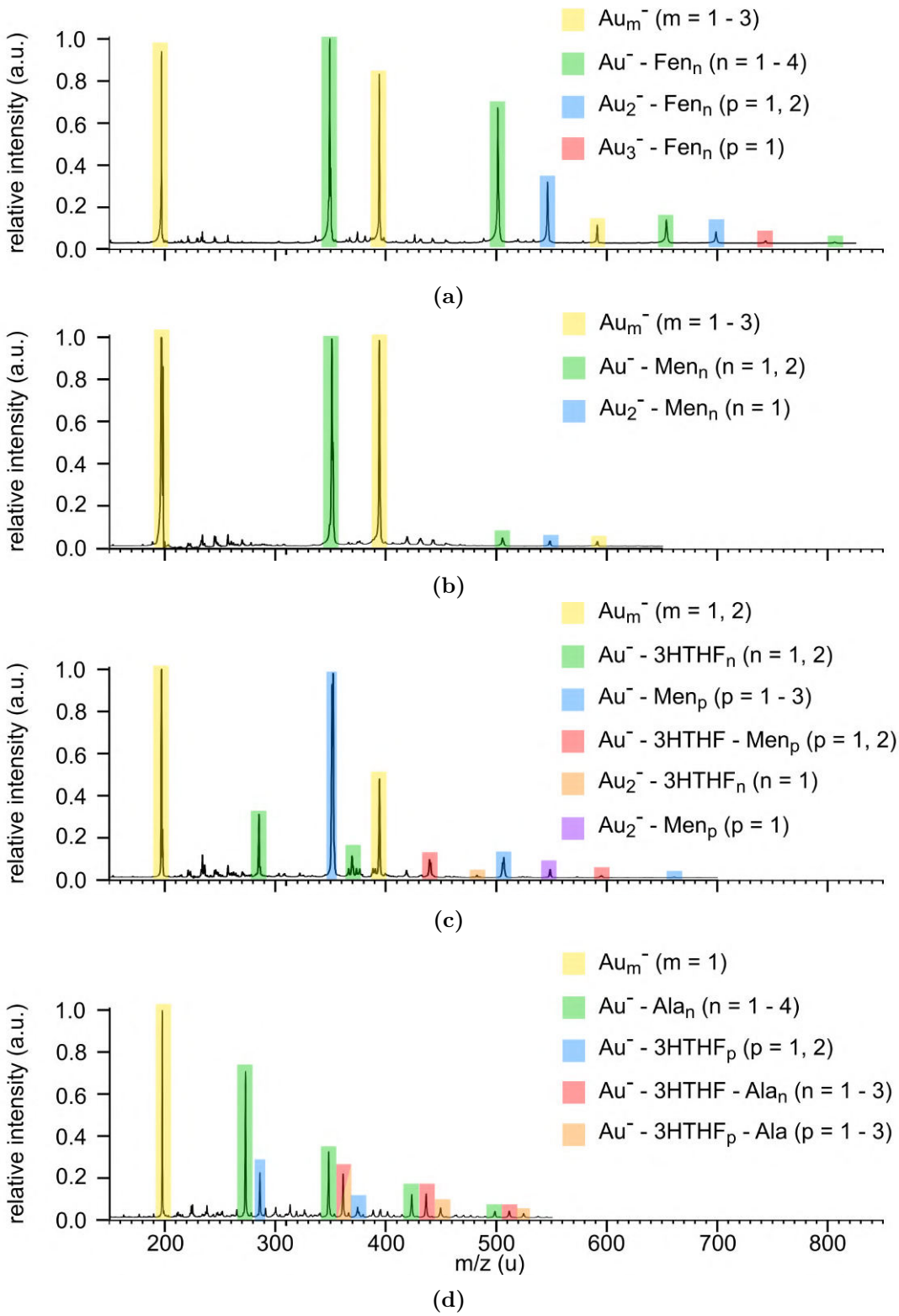

Fig. 4.2.1.: Mass spectra of gold complexes. Au^- (m/z 197) and clusters in yellow. Target complex Au^--Fen at m/z 349 (a), Au^--Men at m/z 351 (b), Au^--3HTHF at m/z 285 (c), Au^--Ala at m/z 272 (d), with molecule cluster in green. Various mixtures in other colors.

It is also possible, that one mass spectrum shows peaks of two different complexes Au_m^--M_n and Au_m^--M'_n, e.g. the mass spectrum of the target complex Au^--3HTHF (figure 4.2.1c) shows Au_m^--$3HTHF_n$ and Au_m^--Men_n. Additionally, complexes with multiple chiral precursors Au_m^--M_n-M'_p ("mixed complexes") are possible (figures 4.2.1c and 4.2.1d). Au_m^--M'_n and the mixed complexes observed in figure 4.2.1c and figure 4.2.1d arise from residual molecules from previous measurements.

Other peaks in the mass spectra that are not marked in figure 4.2.1 can be assigned to impurities: Au_m^- complexes with carbon clusters, like Au_m^--C_n(-H) are assigned to the small peaks between m/z 209 and 258, after Au^-, and between m/z 406 and 454, after Au_2^-. In addition, the peak at m/z 229 in figure 4.2.1a is assigned to Au^--O_2. Furthermore, molecules like C_n(-H), H_2O and O_2 can combine with the target complex Au_m^--M, which is observed in figure 4.2.1a between m/z 364 - 381. While the oxygen could be coming from the air, the carbon could have its origin from the steel wool used to clean the gold rod or from sputtering in the laser ablation region. Fragments of organic molecules could also be a reason. In general, despite the variety of anions that are visible in the mass spectra, mass selection enables the isolation of the desired complex prior to photodetachment.

4.3. Photodetachment of Gold Complexes with Linear Polarized Light

4.3.1. Photoelectron Spectra

Photoelectron spectra of the complexes measured at $E_{\mathrm{ph}} = 4.13$ or 4.35 eV give an overview and are compared to the PES of Au^- in figure 4.3.1. Several features and properties are visible in the PES of the gold complexes: The dominant peaks (X and A) belong to the electronic transitions of the gold complexes and show a difference Δ to the respective Au^- transitions, which will be called "shift". Corresponding binding energies, E_{B}, and shifts, Δ, are extracted from the high resolution spectra, discussed in section 4.3.1.1, and are summarized in table 4.3.1. The shift is directly related to the strength of the bond of the molecule with Au^- and will be discussed in section 4.3.1.2. Secondary features are visible for the complexes Au^--Fen and Au^--Men at around $E_{\mathrm{B}} = 2.31$ eV

Table 4.3.1.: Photoelectron transitions for the different Au^--M with errors and shifts Δ to Au^- based on PES (figure 4.3.1). X indicates the ground and A the excited state.

System	$E_{\mathrm{B,X}}$ (eV)	Δ_{X} (eV)	$E_{\mathrm{B,A}}$ (eV)	Δ_{A} (eV)
Au^-	2.309	0	3.45	0
Au^--Fen	2.707 ± 0.009	0.398	3.93 ± 0.01	0.48
Au^--Men	2.775 ± 0.008	0.466	4.05 ± 0.03	0.60
Au^--3HTHF	2.99 ± 0.04	0.68	4.22 ± 0.04	0.77
Au^--Ala	3.00 ± 0.02	0.69	4.22 ± 0.02	0.77

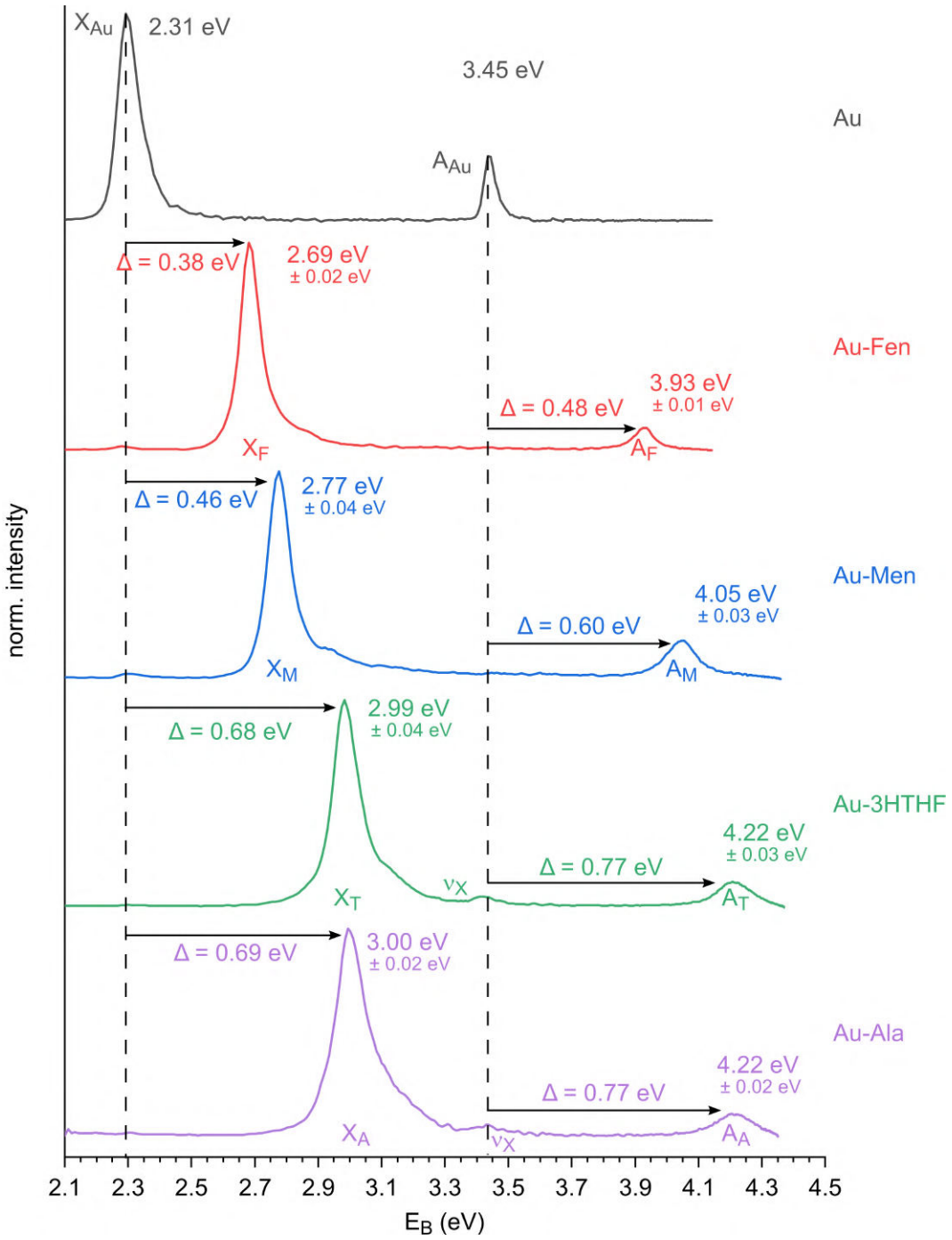

Fig. 4.3.1.: PES with linear polarized light at $E_{\mathrm{ph}} = 4.13$ eV (300 nm) or 4.35 eV (285 nm) for all Au^--M in comparison to PES of Au^-. The PES for the complexes look similar to the one of Au^- but are shifted by Δ, which correlates with the strength of the Au^--M interaction.

as well as for Au^--3HTHF and Au^--Ala at around $E_{\mathrm{B}} = 3.4$ eV. In the case of Au^--Fen and Au^--Men, the complex is metastable and leads to an Au^- contribution in the PES of the complex. The feature in the PES of Au^--3HTHF and Au^--Ala can be attributed

to an O-H (or N-H) stretch vibration, which is supported by DFT calculations (section 4.5.2). Both features will be discussed in section 4.3.1.3.

4.3.1.1. Resolution

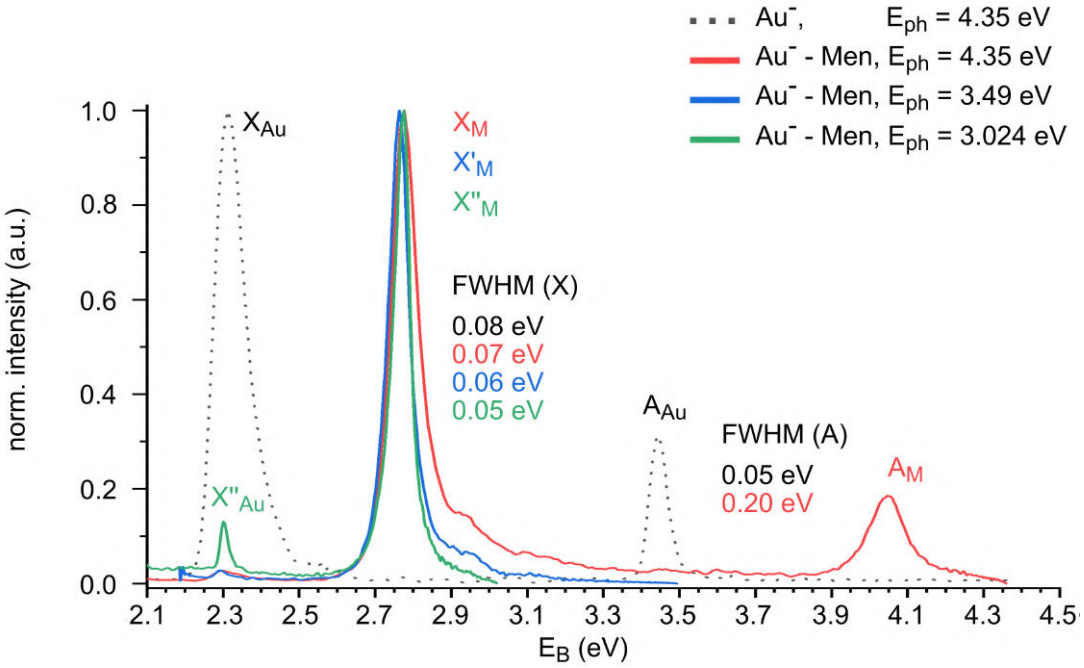

Fig. 4.3.2.: PES with linear polarized light at different photon energies E_{ph} for Au^--Men compared to Au^-. The peaks corresponding to the ground state are labeled X_{Au} for Au^- and X_M (or X'_M and X''_M) for Au^--Men. The excited stated are labeled accordingly with A. If the spectrum is measured at a different photon energy ' is added to the label. For Au^--Men the first transition (X) is around $E_B = 2.77$ eV and the second (A) around 4.04 eV. The small transition around 2.31 eV in the blue PES arises from Au^- indicating a metastable state of the complex. FWHM gets smaller with smaller E_{ph}. Au^- is measured in normal mode while Au^--M is measured in event mode.

Apart from the PES presented in figure 4.3.1, more PES measured at smaller photon energies are also recorded with the VMI spectrometer since they show an improved absolute resolution of single peaks (section 3.2.3). The smallest photon energy for Au^--Fen and Au^--Men is 3.024 eV. For Au^--3HTHF the smallest photon energy is 3.49 eV. Au^--Ala is only measured at $E_{ph} = 4.35$ eV. In all PES with different E_{ph} an improved absolute resolution is evident, which is only shown exemplary for Au^--Men in figure 4.3.2. The binding energies of table 4.3.1 are derived from these PES. For the high intensity peak in figure 4.3.2, there is a clear narrowing of the band, but the increase in absolute resolution did not reveal additional spectral structure. Therefore, representative spectra of the Au^- anion and Au^--M complexes, which show all observed transitions, at comparable resolutions, are provided in figure 4.3.1.

Spectra measured with relatively high photon energies show, at ground state peaks, a shoulder on the side of higher binding energies. If this shoulder contains unresolved vibrational or isomeric features, measurements at lower kinetic energies should resolve this features according to absolute resolution. Instead of resolving any features, the shoulder vanishes for smaller kinetic energies (figure 4.3.2). A shoulder with the same behavior was visible in the PES of Au^- from section 3.2.3.5 and can be attributed as an artifact of a not perfect image reconstruction.

However, even if high resolution spectra could not resolve additional features, the PES of Au^--3HTHF and Au^--Ala probably contain vibrational or isomeric features due to a broadened FWHM of X in comparison to Au^- PES measured at similar kinetic energies. Especially for Au^--Ala, the FWHM could be dominated by isomeric effects since for alaninol itself already 25 isomers could be found [75]. In contrast, the FWHM of the X peak of Au^--Fen and Au^--Men seem similarly broadened to the X peak of the Au^- PES for high E_{kin} (> 1 eV). However, the Au^- PES could be broader than it could be since it is measured in normal mode and not like the gold complexes in event mode, which reduces the resolution as could be seen for S^- in figure 3.2.30b. For lower E_{kin} (< 0.5 eV), the X peak for Au^--Fen and Au^--Men shows bigger broadening. In the end, the PES of all gold complexes could contain more or less some unresolved vibrational or isomeric features.

Comparing the corresponding excited state peaks (A), all Au^--M show an increased FWHM with respect to the Au^- peaks. Vibrational states and isomeric effects seem to dominate this broadening.

Furthermore, it is important to consider the relative resolution or rather peaks with similar kinetic energy as uncertainty in the resolution scales with electron kinetic energy (section 3.2.3.5). Consequently, peaks corresponding to ground states are expected to have better relative resolution than corresponding excited states. In contrast to the absolute resolution, not a comparison between spectra of different photon energies is made but a comparison between peaks within one spectrum. Hence, at least two peaks (ground state and excited state) need to be in one spectrum, which is only fulfilled for spectra measured with at least $E_{ph} = 4.22$ eV. The expected better resolution for ground state transitions can be observed in all the spectra (exemplary shown in figure 4.3.2 for Au^--Men).

4.3.1.2. Blue shift Δ

The PES of Au^- given as reference in figure 4.3.1 and 4.3.2 are measured with 4.13 eV (300 nm) and 4.35 eV (285 nm), respectively. These photon energies are sufficient to probe the transitions from the anionic electronic ground state $^1S_0$ to the neutral ground state $^2S_{1/2}$ (X_{Au} in figure 4.3.1) and to the excited state $^2D_{5/2}$ (A_{Au} in figure 4.3.1), which corresponds to a detachment from the $6s$ orbital with $E_B = 2.309$ eV and from the $5d$ orbital with $E_B = 3.445$ eV, respectively (figure 3.2.26).

As expected, all Au^--M spectra resemble the spectrum of Au^- indicating a photodetached electron that was mainly localized at Au^- before photodetachment. The main difference to the Au^- spectra is the (blue) shift Δ to higher electron binding energies,

which is seen in figure 4.3.1 and table 4.3.1. Apparently, the Au^--M without conventional hydrogen bond donors (i.e. fenchone and menthone) show smaller blue shifts. Similar blue shifts of the ground state peaks (X) were already reported for related molecules by several research groups [127, 146, 152, 176, 185]. Interestingly, blue shifts related to the excited states (A) are larger than for the first transition and are also reported in [127].

The Born-Haber cycle is given by

$$\mathrm{Au} + \mathrm{e}^- + \mathrm{M} + E_\mathrm{B}(\mathrm{Au}) \rightarrow \mathrm{Au}^- + \mathrm{M} \tag{4.3.1a}$$

$$\mathrm{Au}^- + \mathrm{M} + D_0 \rightarrow [\mathrm{Au}]^-\mathrm{M} \tag{4.3.1b}$$

$$[\mathrm{Au}]^-\mathrm{M} - E_\mathrm{B}(\mathrm{AuM}) \rightarrow \mathrm{AuM} + \mathrm{e}^- \tag{4.3.1c}$$

$$\mathrm{AuM} + \mathrm{e}^- - D_\mathrm{n} \rightarrow \mathrm{Au} + \mathrm{e}^- + \mathrm{M} \tag{4.3.1d}$$

with E_B being the electron binding energy, D_0 the dissociation energy of the anionic complex and D_n being the dissociation energy for the neutral complex. In equation 4.3.1, the shift reflects (in zeroth order of approximation) the interaction between Au^- and the molecule M – or in other words, the dissociation energy – if the interaction between Au and M is neglected.

Assuming the complex is held together solely by the extra electron, detaching it leads to a neutral complex (Au-M) with a negligible dissociation energy. Hence D_n is set to zero and the dissociation energy must be $E_\mathrm{B}(\mathrm{AuM}) - E_\mathrm{B}(\mathrm{Au}) = |\Delta E_\mathrm{B}| = |D_0|$. This is just a rough estimation and hence the shift reflects the interaction of Au^--M, or in other words the dissociation energy, only approximately. However, it seems that a larger shift can be connected to higher dissociation energies.

From the perspective of hydrogen bonding with Au^-, the electronegativity values EN for the atoms in the molecules (in Allen scale [186]: EN(H) = 2.30, EN(C) = 2.54, EN(O) = 3.61 and EN(N) = 3.07) shows that O has the strongest electron withdrawn ability and leaves the largest partial positive charge at its hydrogen. Consequently, the interaction between Au^- and a hydroxy group is stronger than with other groups leading to larger dissociation energies and, according to the approximation made in the Born-Haber cycle ($\Delta E_\mathrm{B} \approx D_0$), to larger blue shifts in the ground and also in excited states.

For Au^--Fen and Au^--Men blue shifts of around 0.40 eV and 0.47 eV are found respectively, which is much bigger than what was calculated for Au^--CH_4 [152] with 0.047 eV. Other gas phase studies focusing on $Au^- \cdots$ H-C interactions in similar complex systems like done here seem not to be available for a comparison.

The blue shifts for Au^--3HTHF and Au^--Ala are around 0.7 eV in both cases. In comparison to Au^--H_2O, Au^--CH_3OH, Au^--C_2H_5OH and Au^--C_3H_7OH this blue shift is about 0.2 eV higher indicating to a stronger interaction between Au^- and molecule [127, 146, 176, 187].

In these studies, smaller blue shifts were observed, in comparison to the complexes studied, herein. This is assumed to be due to the number of attractive interactions that can be sustained: with such small molecules, only a single H-bond interaction is expected, where as the complexes here are much larger, and as will be shown later (section 4.4),

can sustain numerous hydrogen bonding interactions. The amount of bonds and the cooperation between them stabilize the system and leads to a higher blue shift.

On the other hand, nucleaobase-Au^- show much higher blue shifts of 0.92 - 1.12 eV [177]. These systems also show more than one bond to Au^- and are characterized by medium or strong $Au^- \cdots$ H-N hydrogen bonds.

The blue shifts of the excited states Δ_A are around 0.1 eV larger than the shifts of the ground state. Before this work, no satisfying explanation to this effect was given in the literature. An explanation will be ventured in section 4.4.3.2. In summary, charge transfer mechanisms could lead to a more diffuse $6s$ orbital and hence to the deshielding of the $5d$ orbital in Au^-. This lowers the energy for transition A.

The blue shifts in the PES are a clear indicator for the influence of the molecule on the detached electron. Hence, the electron "feels" the molecular potential (more or less) of each complex but it is not clear to what extent the chirality is felt by the electron and how it is expressed in the PECD effect.

4.3.1.3. Secondary Features

Two secondary features are visible in the PES of the gold complexes:

First, spectra from Au^--Fen and Au^--Men both feature an unusual peak at 2.30±0.01 eV and 2.31±0.01 eV, respectively (figure 4.3.1, more pronounced in figure 4.3.2 for $E_{ph} = 3.024$ eV (410 nm)). This peak matches the transition from the $6s$ orbital of Au^- at 2.309 eV. Thus, despite the huge m/z difference for Au^- and Au^--M, both substances seem to enter the interaction zone of the VMI spectrometer simultaneously (hence reach the ToF-MS detector at the same time) and are photodetached with the same laser pulse. This leads to the assumption of a metastable fraction of Au^--M, which falls apart in the acceleration region of the ToF-MS. However, this offers the opportunity to verify in retrospect the quality of optimization and calibration to some extent[3] and can confirm a relatively flawless running experiment since every (major) error will be reflected in the extra Au^- peak.

Second, for Au^--3HTHF and Au^--Ala, a tiny peak around 3.4 eV or around 0.4 eV higher in energy than the main peak X, emerges. It is labeled ν_X in figure 4.3.1. The energetic position of this peak leads to two possibilities:

It can be the first excited transition A of Au^-. Au^--Fen and Au^--Men already showed that the complex might be meta stable and transitions from the bare Au^- can appear but this always concerned the X peak and never the A peak. If ν_X should be the A peak of Au^-, the X peak should also be visible and be of much stronger intensity. However, this is not observed, which makes this theory unlikely.

A more likely explanation is ν_X being the stretch vibration of O-H. A similar peak is observed in Au^--H_2O and it is assigned to the water stretch frequency [146]. Furthermore, DFT calculations support this assumption but will be discussed later in section 4.5, where experimental and computational results are compared. In the case of Au^--Ala, the calculations indicate also to a N-H vibration.

[3] This does not replace a real calibration, since the intensity is too small

4.3.2. Beta Parameter

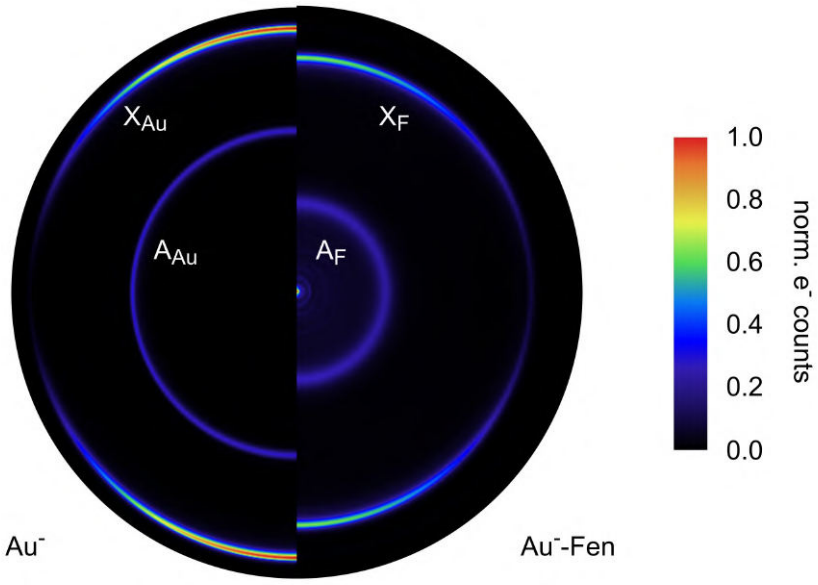

Fig. 4.3.3.: Exemplary reconstructed PAD of Au^- and Au^--Fen to visualize the angular distribution of the electrons. Both spectra are taken at $E_{ph} = 4.13$ eV and lead for Au^--Fen to the red spectrum shown in figure 4.3.1. The different positions of rings between both PADs correspond to different electron binding energies. The PAD of Au^--Fen features noise in the center, which originates from the light and accumulates after hours of measurement. Au^- does not show this noise since the signal-to-noise ratio is much higher and the PAD can be taken in several minutes. Hence, the noise can not accumulate. Both PADs are normalized to their highest intensity value. Transitions are labeled according to figure 4.3.1.

The anisotropy parameter β is extracted from the photoelectron spectra with POP and rBasex for all Au^--M. Since both methods produce (almost) identical results only the POP data is depicted here in figure 4.3.4.

As already known for the isolated Au^-, the anisotropy parameter is (in theory) exactly 2 for all kinetic energies since the electron detachment for the first transition happens out of the $6s$ orbital. Electrons from other orbitals than pure s orbitals show a dependence on the kinetic energy E_{kin}. Such a dependence is seen in the anisotropy parameters of each Au^--M (figure 4.3.4). Some points could be, within the errors, 2 but most data points are around $1 < \beta < 2$ indicating to a photoedetachment process from an s orbital, which is disturbed by the complexing molecule. The disturbing elements could be the $2p$ orbitals from the carbons, oxygen and nitrogen, which mix with the $6s$ orbital of Au^-. The disturbance of the molecules might be subtle but is still large enough to be recognized with the current setup.

The second transition A shows anisotropy parameter around zero indicating to a more uniform distribution in the low kinetic energy region. This anisotropy parameter is probably determined by the $5d$ orbital of Au^- being disturbed by the molecule.

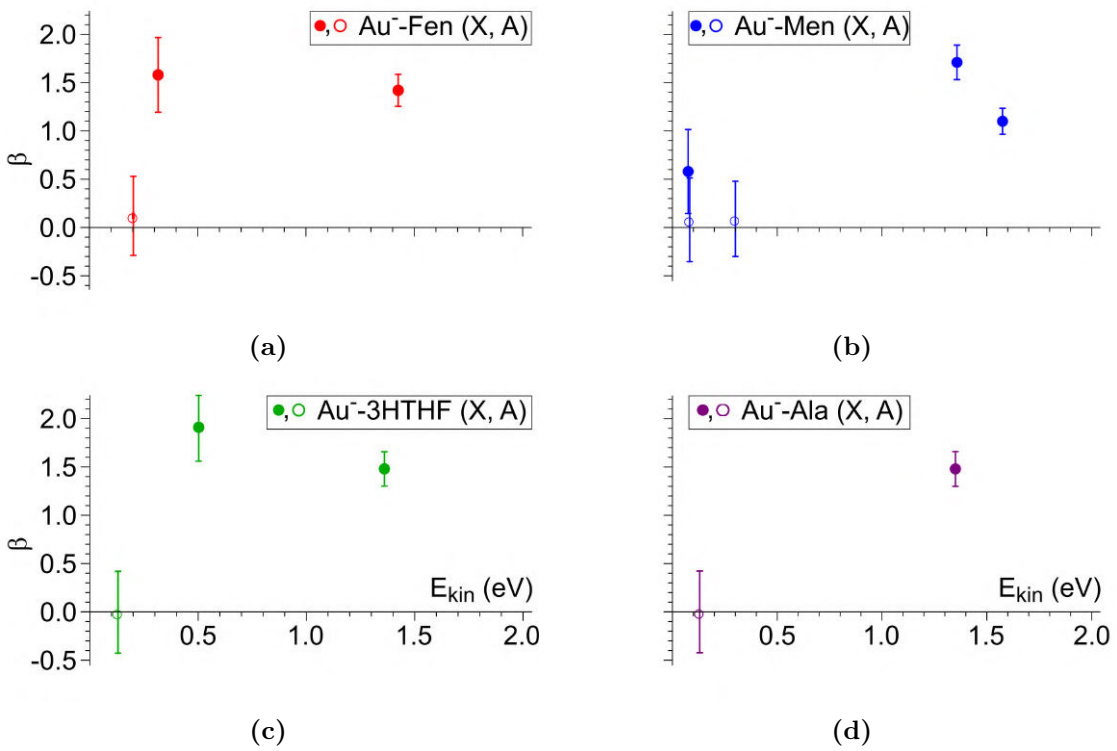

Fig. 4.3.4.: Anisotropy parameter β for X and A transition of Au^--Fen (a), Au^--Men (b), Au^--3HTHF (c) and Au^--Ala (d) obtained with POP.

Orbital images of the gold complexes in combination with an orbital composition analysis will help understanding the anisotropy parameters. However, this will be discussed in more detail in section 4.5.

The change in beta, in conjunction with the blue shifts observed in the complex spectra, provide evidence for the influence of the chiral molecule on the detaching electron. However, it is still unclear whether the photodetachment will carry a chiral signal (i.e. PECD signal).

4.4. Computational Results

4.4.1. Calculated Structures of Gold Complexes

4.4.1.1. Stabilization

The initial molecular geometries – which are taken to prepare Au^--M for calculations – are shown in figures 4.4.1 for fenchone, 4.4.3 for menthone, 4.4.7 for 3HTHF and 4.4.9 for alaninol. They are arranged and labeled according to their stability (or minimum energy E_0).

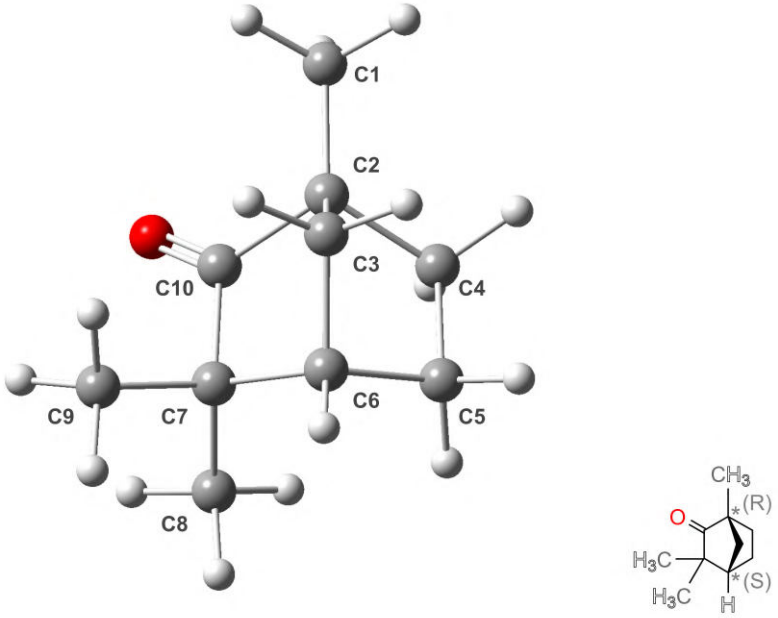

Fig. 4.4.1.: Structures for fenchone optimized with B3LYP-D3/aug-cc-pVTZ(-PP). This is the only possible isomer due to the bicyclic structure of fenchone [32].

Especially the most stable configurations were initially extracted from the literature [32, 75, 188, 189], calculations were repeated with the level of theory given in the literature and a comparison of rotational constants confirms the reproduction of these structures. Apart from isomers given in the literature, other structures were extracted from websites like "PubChem". This concerns for example the "chair" structure of menthone 4.4.3d. In the end, all structures were optimized with B3LYP-D3/aug-cc-pVTZ in combination with harmonic frequency calculations to fit with the upcoming Au^--M calculations.

Due to its bicyclic structure, fenchone has no torsional flexibility, leading to only one possible conformation [32]. This structure is shown in figure 4.4.1.

In contrast, menthone, 3HTHF and alaninol, possess more than one isomer. For menthone, four different isomers were found: M1.0 - M3.0 have almost a flat structure and differ from each other by a rotated isopropyl group [188], whereas the structure of M4.0 resembles a "chair", due to the bending of the adjacent methyl group out of the plane of the central ring. M1.0 (figure 4.4.3a) is the most stable configuration. M2.0-M4.0 are structures, which lie 0.008, 0.029 and 0.094 eV above M1.0.

For 3HTHF, four isomers were reported in [189] from which just two are considered here. Among them, the most stable structure H1.0 and an isomer located 0.02 eV above H1.0 (figure 4.4.7). Both isomers are depicted in two different views: The top view for H1.0 shows clearly the orientation of the hydroxy hydrogen pointing inside the ring and towards the ether oxygen (O2), which might stabilize the system due to the internal hydrogen bond O2$\cdots$H-O1. The side view shows the form of the ring and the upwards

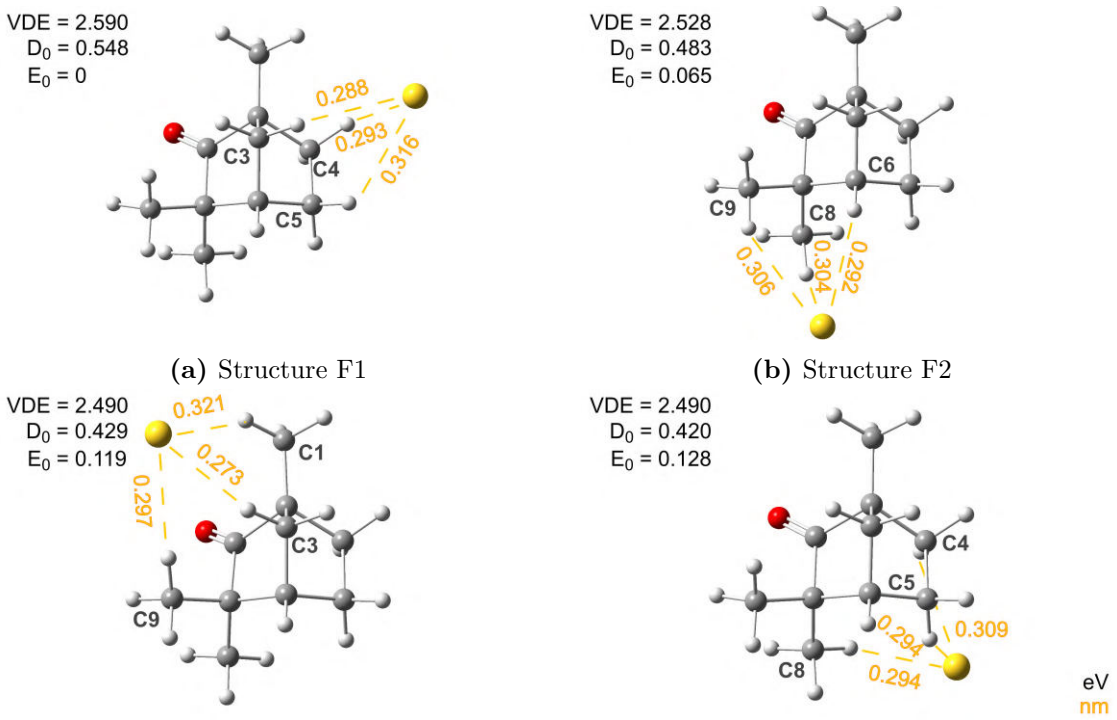

(a) Structure F1 **(b)** Structure F2

(c) Structure F3 **(d)** Structure F4

Fig. 4.4.2.: Optimized structures for the complex Au^--Fen with various positions of the gold atom adjacent to the chiral core obtained with B3LYP-D3/aug-cc-pVTZ(-PP) as well as the distances to Au^- in nm (yellow) and energies VDE, E_0, D_0 in eV (black).

bending of the ether oxygen due to the hydrogen bond. This type of structure is called a C2-endo structure and corresponds to the most predominant furanose ring structure, which can be found in nucleotides [189].

For H2.0, the hydroxy hydrogen is pointing outside the ring, leading to a vanishing interaction to the ether oxygen. Furthermore, the interaction between the ether oxygen and the hydroxy oxygen is increased, which may support the ring puckering (side view of H2.0). This is the C4-endo structure.

According to Fausto *et al.* [75], there can be up to 25 different isomers for alaninol within a relative energy range of just 0.3 eV. Here, only five isomers are considered, which mainly differ from each other by the rotation of the OH group and secondary by the arrangement of hydrogens at the nitrogen. Among them, the most stable configuration A1.0 in figure 4.4.10a. The stability of the system seems to be determined by two internal hydrogen bonds of the type N···H-O and O···H-N. For the most stable conformer A1.0 and the two isomers below A2.0 and A3.0, the hydrogen bond N···H-O appears in different strengths. In A4.0, no N···H-O but instead O···H-N emerges, which reduces the stability of the system since N induces a smaller partial positive charge in its hydrogens than O. A5.0 is the least stable isomer since neither N···H-O nor O···H-N can be observed as a bond rotation causes the hydroxy and amino groups to be separated.

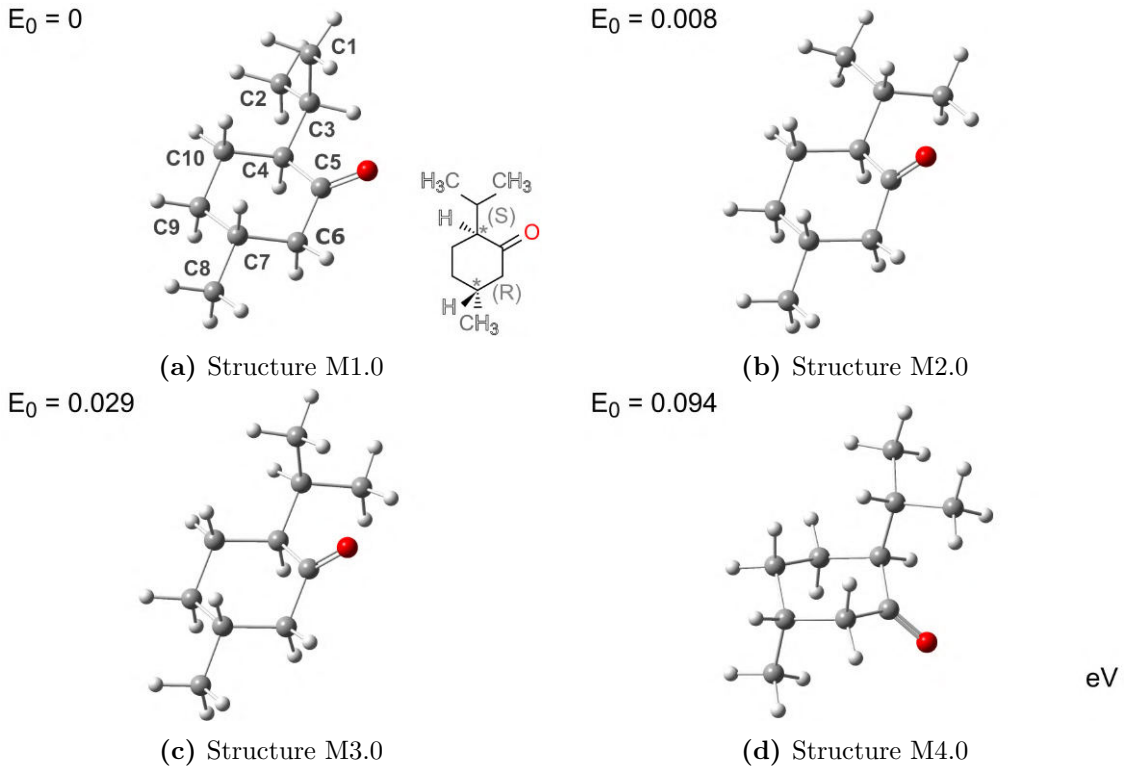

(a) Structure M1.0 **(b)** Structure M2.0

(c) Structure M3.0 **(d)** Structure M4.0

Fig. 4.4.3.: Optimized structures for menthone obtained with B3LYP-D3/aug-cc-pVTZ(-PP). E_0 is the minimum energy given relative to the most stable structure M1.0. M1.0-M3.0 correspond to the structures given in [188] and differ by a rotated isopropyl group. M4.0 resembles a "chair" and is the least stable structure studied here.

Au^--M are prepared for all molecules (and their isomers) in the same manner: the neutral molecule was fixed in one orientation and Au^- was manually placed at six different positions around it, then a geometry optimization was performed. After optimization, the initial structures converged to the gold complexes presented in figure 4.4.2 for Au^--Fen, figures 4.4.4 - 4.4.6 for Au^--Men, figure 4.4.8 for Au^--3HTHF and figures 4.4.10 - 4.4.13 for Au^--Ala. The optimized structures of the most stable Au^--M are given in the appendix A.1. Alongside the Au^--M structures, bond lengths and angles of the three (sometimes four) shortest $Au^- \cdots H$ bonds as well as energies like VDE, D_0 and E_0 are extracted. They are given partly in the figures and completely in the corresponding tables 4.4.1 - 4.4.2. Both, figures and tables, are arranged by stability or in other words, according to E_0, starting with the most stable Au^--M isomer.

The label of the different Au^--M isomers are assigned depending on the initial molecular isomer and the stability of the complex: In the case of Au^--Fen, the complexes are labeled with F1 - F4, with F1 being the most stable complex and F4 the least stable one. For the other Au^--M two numbers are needed: the first number always indicates the parent molecular isomer and the second number is assigned according to their stability. For example, the gold complexes Au^--3HTHF are labeled H1.x (with x = 1 - 4) and H2.x (with x = 1, 2) according to the base structures H1.0 and H2.0, respectively. In

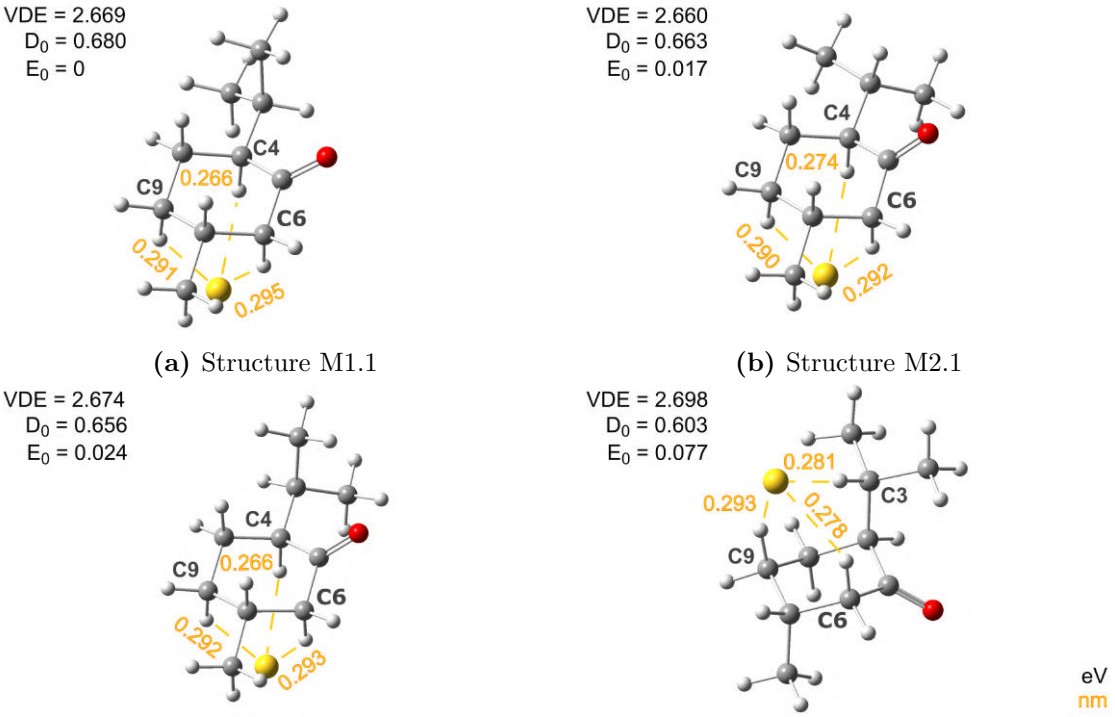

(a) Structure M1.1 **(b)** Structure M2.1

(c) Structure M3.1 **(d)** Structure M4.1

Fig. 4.4.4.: First group (1) of optimized structures for the complex Au^--Men with various positions of the gold atom adjacent to the chiral core obtained with B3LYP-D3/aug-cc-pVTZ(-PP). This are the most stable isomers for Au^--Men. Predominantly, Au^- binds with the ring of menthone. Distances to Au^- are given in nm (yellow) and energies VDE, E_0, D_0 in eV (black).

the group of H1.x isomers, the most stable one is H1.1 and the least stable one H1.4, while H2.1 is the most stable complex in the group of H2.x. Other Au^--M are labeled accordingly.

In general, two main stabilization effects can be discerned, which correlates with the type of molecule in the complex: The complexes with ketone groups (Au^--Fen and Au^--Men) are stabilized by geometry while the complexes with conventional hydrogen bond donors (Au^--3HTHF and Au^--Ala) are stabilized through the strong electron withdrawing ability of these donors.

The stability for Au^--Fen and Au^--Men seems to be determined by the position of the Au^-. In general the Au^- seems to avoid the ketone group, which can probably be explained by the negative partial charge sitting on the oxygen. For Au^--Fen the distance of Au^- to O is between 0.5 - 0.6 nm and a bit bigger for Au^--Men with 0.5 - 0.7 nm. One could expect that the stability is increased for the isomers with the largest distance of Au^- and O but this is not what can be observed here: The most stable isomer of Au^--Fen shows the largest distance but the smallest distance is seen for F3 and not F4. In Au^--Men the least stable isomers show the biggest distances between Au^- and O and the most stable isomer even has the shortest one. Overall, the ketone group is avoided

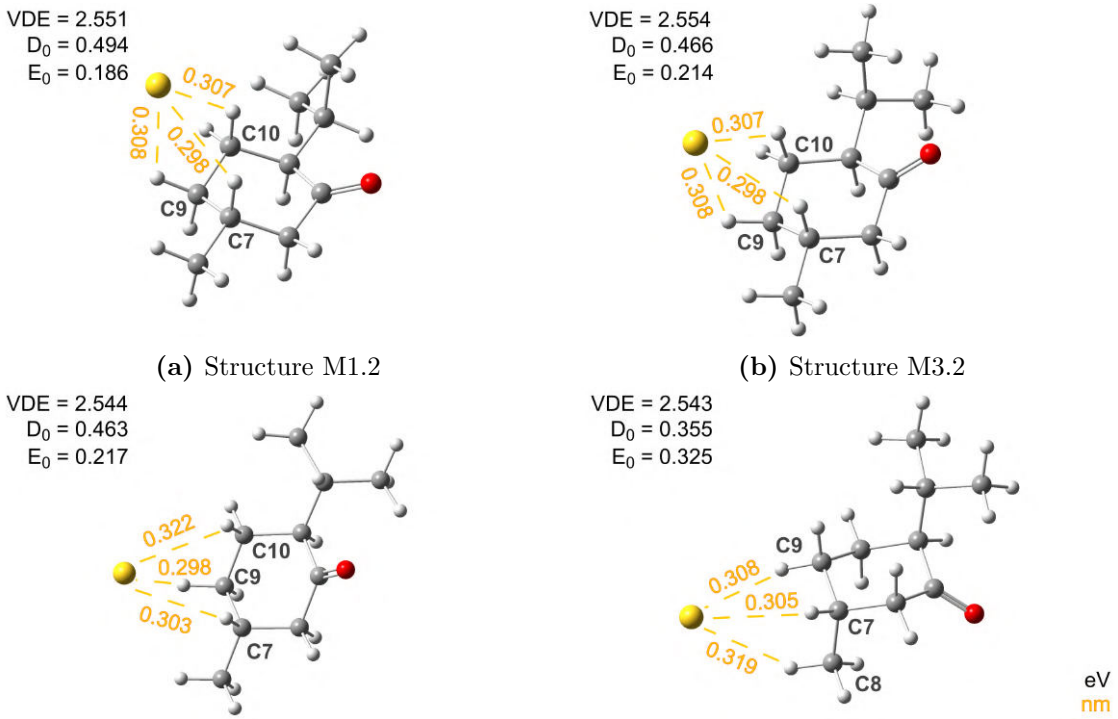

(a) Structure M1.2 **(b)** Structure M3.2

(c) Structure M2.2 **(d)** Structure M4.2

Fig. 4.4.5.: Second group (2) of optimized structures for the complex Au^--Men with various positions of the gold atom adjacent to the chiral core obtained with B3LYP-D3/aug-cc-pVTZ(-PP). This are the second stable isomers of Au^--Men. Au^- binds predominantly to the boarder of the ring of menthone. Distances to Au^- are given in nm (yellow) and energies VDE, E_0, D_0 in eV (black).

by Au^- but the attractive forces of the positively partial charged hydrogens seems to have a bigger influence on the position of Au^- at the molecule than the repellent effect from the oxygen.

Something similar can be observed for Au^--3HTHF: Here, not a ketone group needs to be avoided but the ether oxygen, which is part of the ring structure. However, the reason will stay the same with the oxygen holding a negative partial charge, which repels the Au^-. Especially H1.3, H1.4 and H2.2 show this effect clearly: the oxygen always bends away to the other side of the ring plane (ring puckering). Even more, in H2.2, the hydroxy group is pointed away from the ring center and exposes O1 to the ether oxygen. Normally, this leads O2 to bend to the other side of the ring plane but here it rather stays on the same side with O1 than to be on one side with Au^-.

Another aspect regarding the stability of Au^--Fen and Au^--Men is the position relative to ring structures: If Au^- connects with H atoms of C's, which are part of a ring structure the most stable isomers are formed. This is the case for F1, where Au^- bonds with hydrogens of C's, which form a rather deformed ring. For F2 - F4, Au^- connects to hydrogens from carbons not being part of a closed structure (ring).

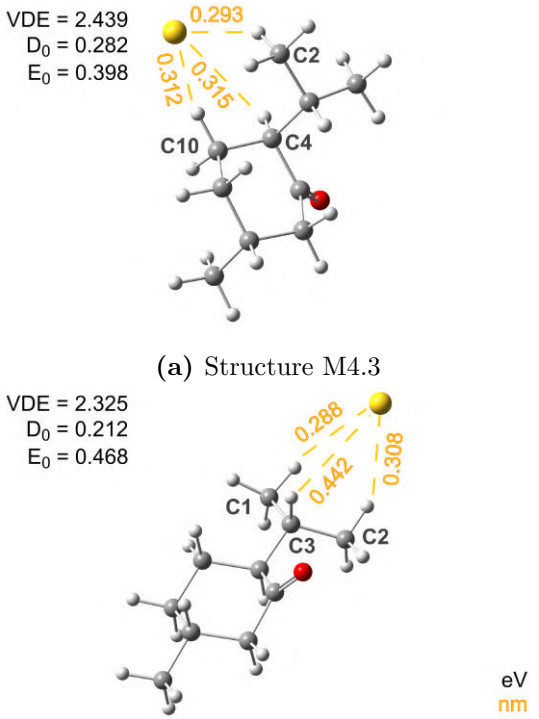

(a) Structure M4.3 **(b)** Structure M1.3

(c) Structure M2.3

Fig. 4.4.6.: Third group (3) of optimized structures for the complex Au^--Men with various positions of the gold atom adjacent to the chiral core obtained with B3LYP-D3/aug-cc-pVTZ(-PP). This are the least stable isomers for Au^--Men. Here, the system is the least stable if Au^- binds to the isopropyl group. Distances to Au^- are given in nm (yellow) and energies VDE, E_0, D_0 in eV (black).

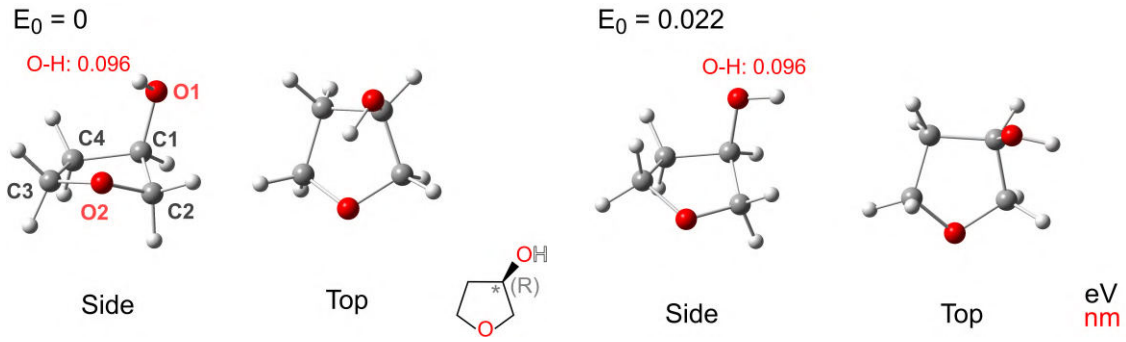

(a) Structure H1.0 **(b)** Structure H2.0

Fig. 4.4.7.: Structures for 3HTHF optimized with B3LYP-D3/aug-cc-pVTZ. The bond lengths of O-H are given in nm (red) and the minimum energies E_0 in eV. The structure with the lowest E_0 is structure H1.0. H1.0 and H2.0 are discerned by ring puckering (up view) and the orientation of the hydroxy group (side view). For H1.0, H is pointing inside the ring and towards the ring oxygen, which stabilize the structure.

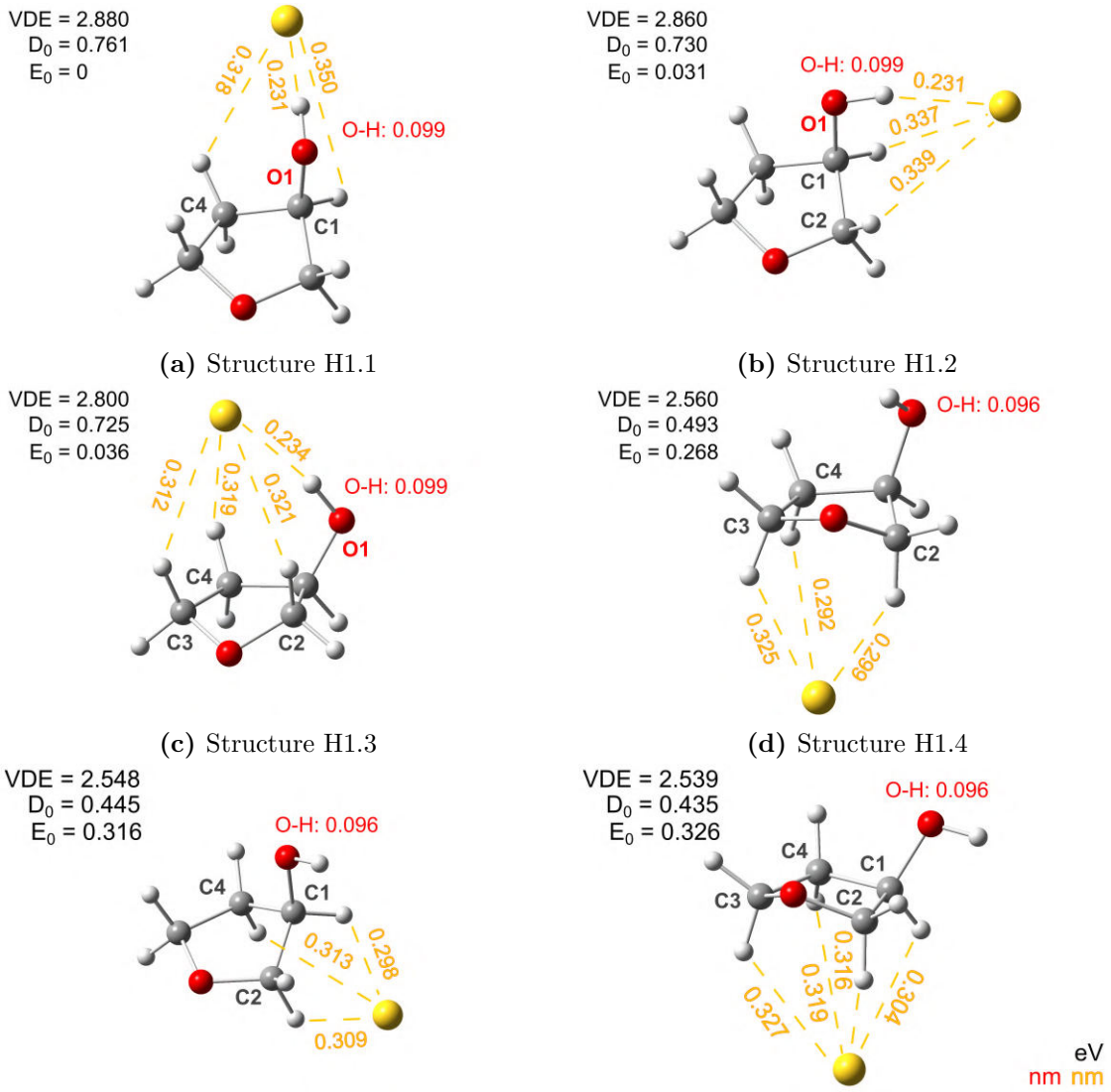

(a) Structure H1.1 **(b)** Structure H1.2

(c) Structure H1.3 **(d)** Structure H1.4

(e) Structure H2.1 **(f)** Structure H2.2

Fig. 4.4.8.: Optimized structures for the complex Au^--3HTHF with various positions of the gold atom adjacent to the chiral core obtained with B3LYP-D3/aug-cc-pVTZ(-PP) resulting from the initial molecule H1.0 or H2.0. The isomers are arranged according to E_0. H1.1 - H1.3 show a hydrogen bond between Au^- and the hydroxy group ($Au^- \cdots$H-O), which increases the OH bond length (compare to figure 4.4.7) and decreases the hydrogen bond length of $Au^- \cdots$H-O in comparison to $Au^- \cdots$H-C. They are the most stable structures and belong to the first group of isomers. H1.4, H2.1 and H2.2 do not have $Au^- \cdots$H-O resulting in less stable structures and an unchanged OH bond length. These are the second group. Distances are given in nm (yellow or red). The VDE, E_0 and D_0 energies are given in eV (black).

Due to the better arranged structure, this effect is observed more easy in Au^--Men: The most stable isomers belong to structures where Au^- interacts mostly with the ring part of the molecule (figure 4.4.4). Here, the most H can participate in the Au^- bonding

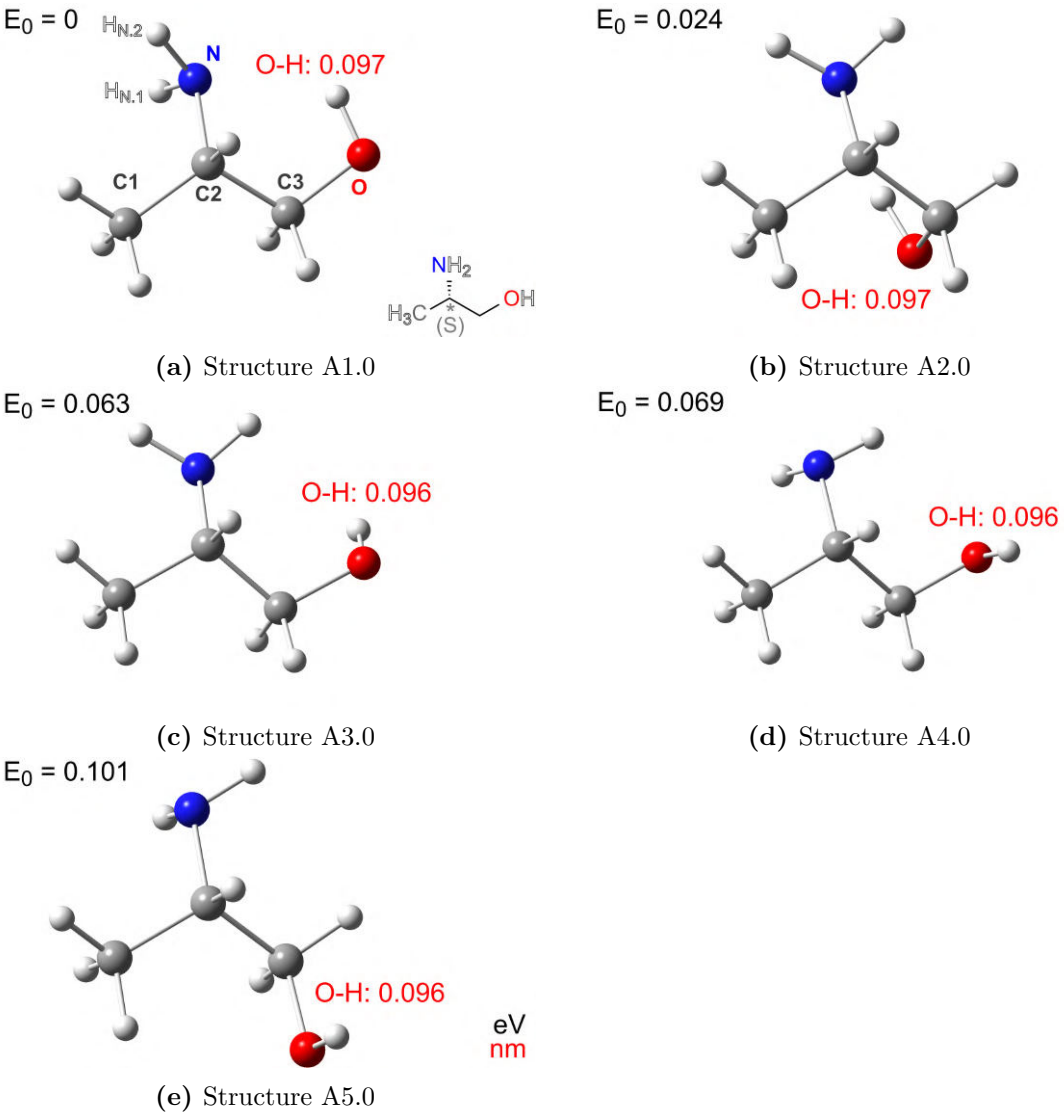

(a) Structure A1.0 **(b)** Structure A2.0

(c) Structure A3.0 **(d)** Structure A4.0

(e) Structure A5.0

Fig. 4.4.9.: Structures for alaninol optimized with B3LYP-D3/aug-cc-pVTZ. Given are the OH bond lengths in nm (red) and minimum energies E_0 in eV. The structure with the lowest E_0 is structure A1.0, with H of the hydroxy group pointing directly at N.

stabilizing the bond. The fourth stable isomer is a structure obtained from M4.0 (the "chair" structure). If the gold is "sitting down" a quite stable complex (M4.1) is created from the least stable molecular structure. If Au^- binds at the boarder of the ring part of the molecule (figure 4.4.5) less stable isomers are created, which is accompanied by increased hydrogen bond length between Au^- and CH. The least stable isomers are created if Au^- is bound to the isopropyl group instead to the ring (figure 4.4.6).

Something similar could be expected from Au^--3HTHF due to the 5-membered ring but here only the least stable isomers show a connection between Au^- and the ring part of the molecule. The stabilization effect by the ring seems to be secondary if an O-H group is involved (e.g. compare H1.1 with H2.2 in figure 4.4.8).

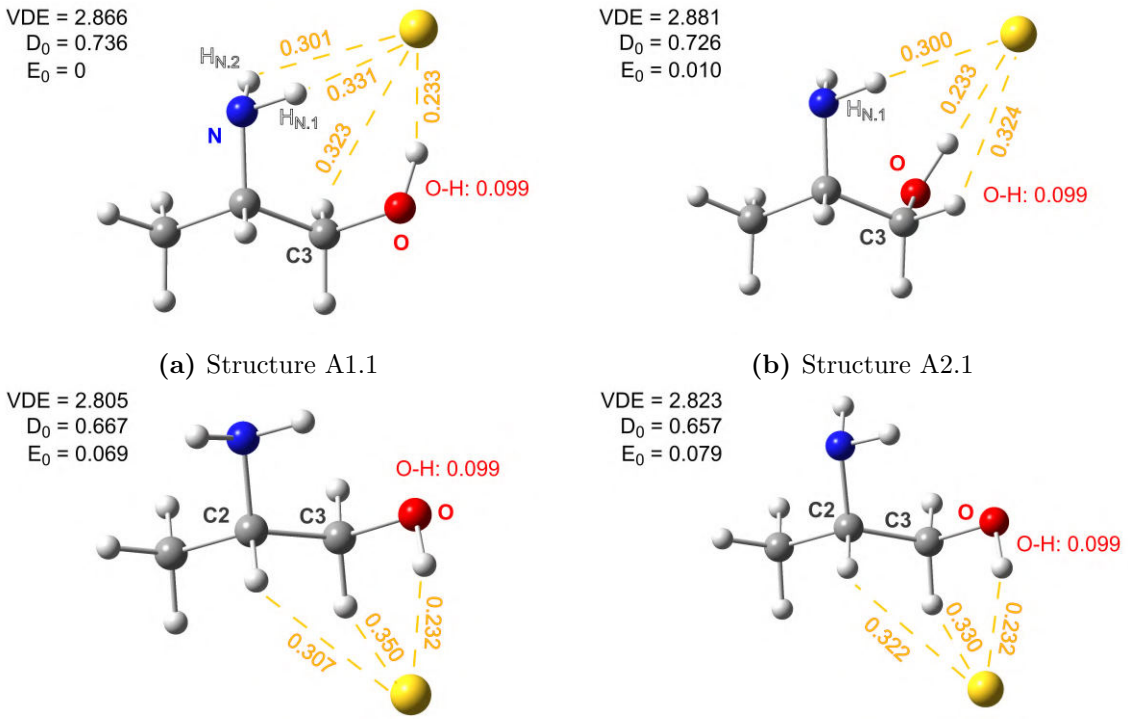

(a) Structure A1.1 **(b)** Structure A2.1

(c) Structure A3.1 **(d)** Structure A4.1

Fig. 4.4.10.: First group (1) of optimized structures for Au^--Ala with various positions of Au^- adjacent to the chiral core obtained with B3LYP-D3/aug-cc-pVTZ(-PP). They are ordered according to E_0 and are the most stable ones of the Au^--Ala complexes. Common in all configurations is the existence of the hydrogen bond $Au^- \cdots$H-O, which leads to an extended OH bond length and a shorter hydrogen bond in $Au^- \cdots$H-O (in comparison to $Au^- \cdots$H-C or $Au^- \cdots$H-N). In addition to $Au^- \cdots$H-O, A1.1 and A2.1 feature a hydrogen bond of the type $Au^- \cdots$H-N. Distances are given in nm (yellow or red) and energies in eV (black).

Structure H1.1 is the most stable isomer of Au^--3HTHF with the hydrogen of the hydroxy group pointing outside the carbon ring and towards Au^-. It could be generated with the structure H1.0 and H2.0. Indeed all complexes generated by H1.0 could also be produced by H2.0 indicating to a low energy barrier for conversion between H1.0 and H2.0. This is also supported by the small E_0 difference of 0.022 eV (figure 4.4.7b). The interaction between molecule and Au^- is strong enough to overcome the energy of 0.022 eV, which is needed to convert H1.0 into H2.0 or vice versa (or to cause OH rotation and ring puckering).

In general, Au^--3HTHF and Au^--Ala show a clear trend regarding stabilization: The most stable isomers are the ones with a hydrogen bond between Au^- and the hydroxy group $Au^- \cdots$H-O (H1.1 - H1.3 in figure 4.4.8 as well as all isomers in figure 4.4.10 and 4.4.11) while isomers without that hydrogen bond (no $Au^- \cdots$H-O) are the least stable isomers (H1.4, H2.1, H2.2 in figure 4.4.8 and all isomers in figure 4.4.12, 4.4.13). This can be expected from bonds including one of the strongest hydrogen donors.

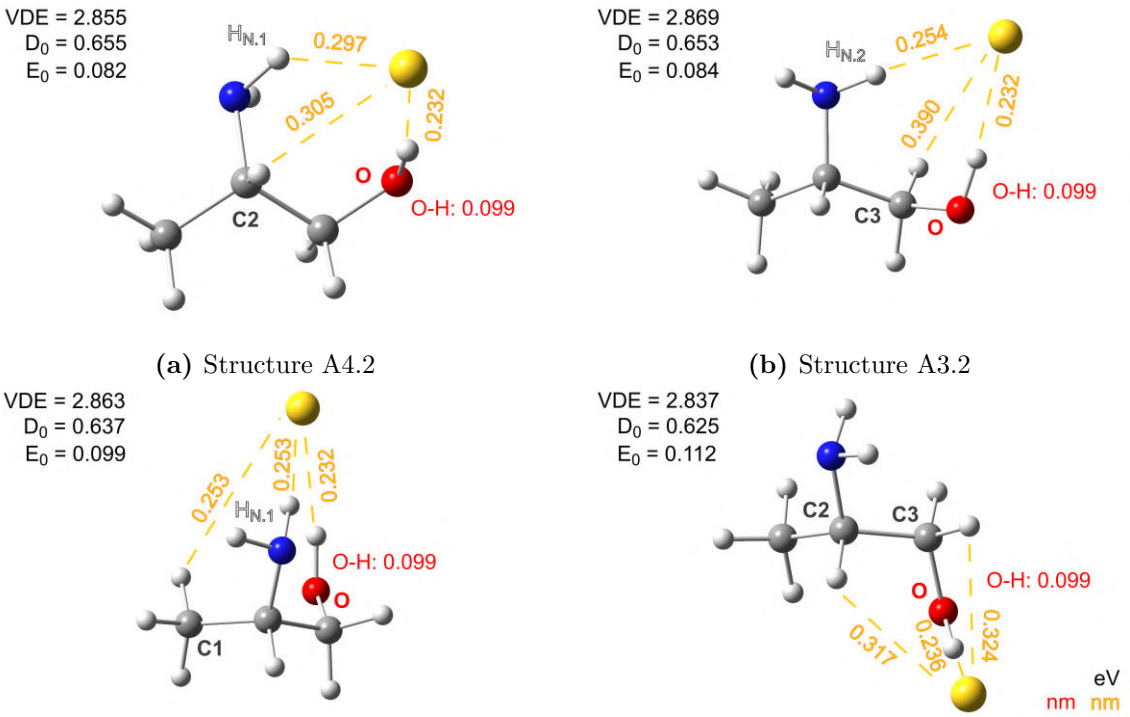

(a) Structure A4.2 **(b)** Structure A3.2

(c) Structure A2.2 **(d)** Structure A5.1

Fig. 4.4.11.: Second group (2) of optimized structures for the complex Au^--Ala with various positions of Au^- adjacent to the chiral core obtained with B3LYP-D3/aug-cc-pVTZ(-PP). This are the second most stable isomers of the Au^--Ala complexes. As for the first group, the hydrogen bond $Au^- \cdots$H-O exists. A4.2, A3.1 and A2.2 also have the hydrogen bond $Au^- \cdots$H-N. The hydrogen bond to N is shorter than for $Au^- \cdots$H-C or for the first group in figure 4.4.10 indicating a stronger interaction between the hydroxy hydrogen and N. Distances are given in nm (yellow or red) and energies in eV (black).

Comparing E_0 between the groups of isomers with and without $Au^- \cdots$H-O for Au^--3HTHF, the isomers show a difference of around 0.3 eV emphasizing the importance of the $Au^- \cdots$H-O hydrogen bond for stabilization. This energy jump between both groups of isomers is much smaller for Au^--Ala, especially if the first subgroup of isomers without $Au^- \cdots$H-O (A1.2, A1.3, A2.3 and A2.4 in figure 4.4.12) is considered. Looking at the hydroxy group, a slightly increased bond length of 0.097 and 0.098 nm is observed in contrast to the undisturbed OH bond of 0.096 nm. Au^- is too far away to be responsible for this kind of extension. However, a (internal molecular) hydrogen bond of the type N$\cdots$H-O, like observed in A1.0 - A3.0, can be responsible for the slight extension and give some stabilization. If this internal molecular hydrogen bond is not present, the energy jump in E_0 between both groups is around 0.2 eV (compare figure 4.4.11 and 4.4.13).

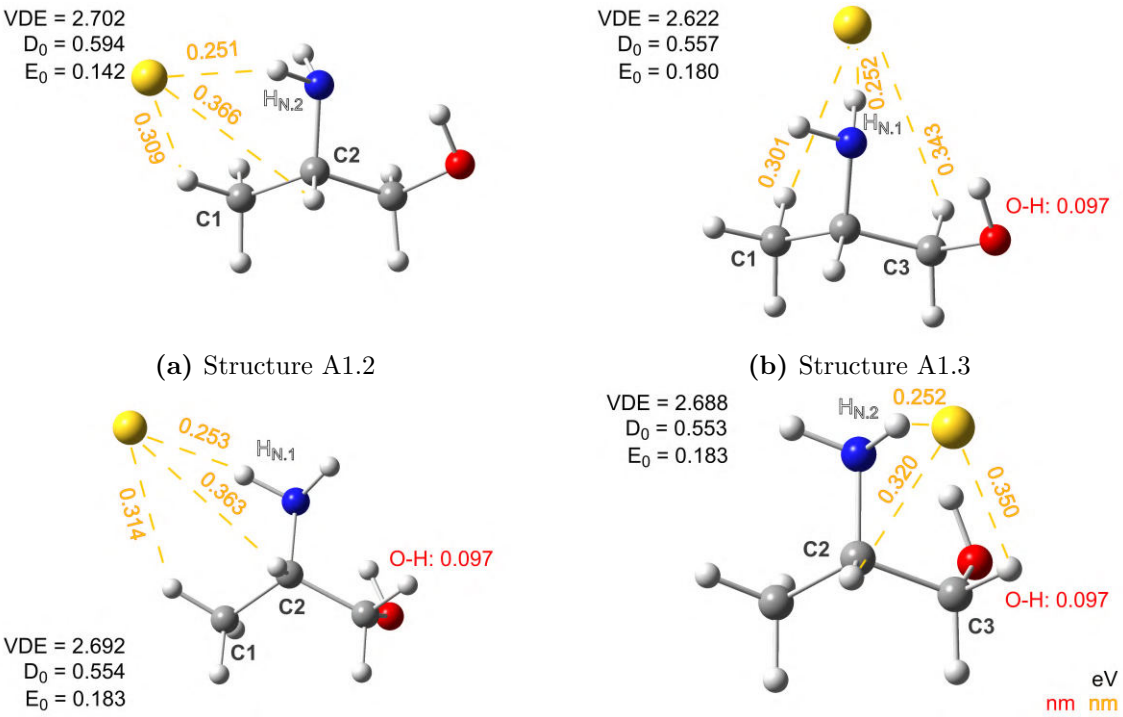

(a) Structure A1.2 **(b)** Structure A1.3

(c) Structure A2.3 **(d)** Structure A2.4

Fig. 4.4.12.: Third group (3) of optimized structures for the complex Au^--Ala with various positions of Au^- adjacent to the chiral core obtained with B3LYP-D3/aug-cc-pVTZ(-PP). In contrast to the first two groups, no $Au^- \cdots$H-O hydrogen bonds are observed. Instead, hydrogen bonds with $Au^- \cdots$H-N occur. Like in the second group, the hydrogen bond in $Au^- \cdots$H-N is shorter in comparison to $Au^- \cdots$H-C bonds. Since Au^- is too far away from the hydroxy group, the OH bond length is determined by the influence of N, which increases the bond length slightly (figure 4.4.9). Distances are given in nm (yellow or red) and energies in eV (black).

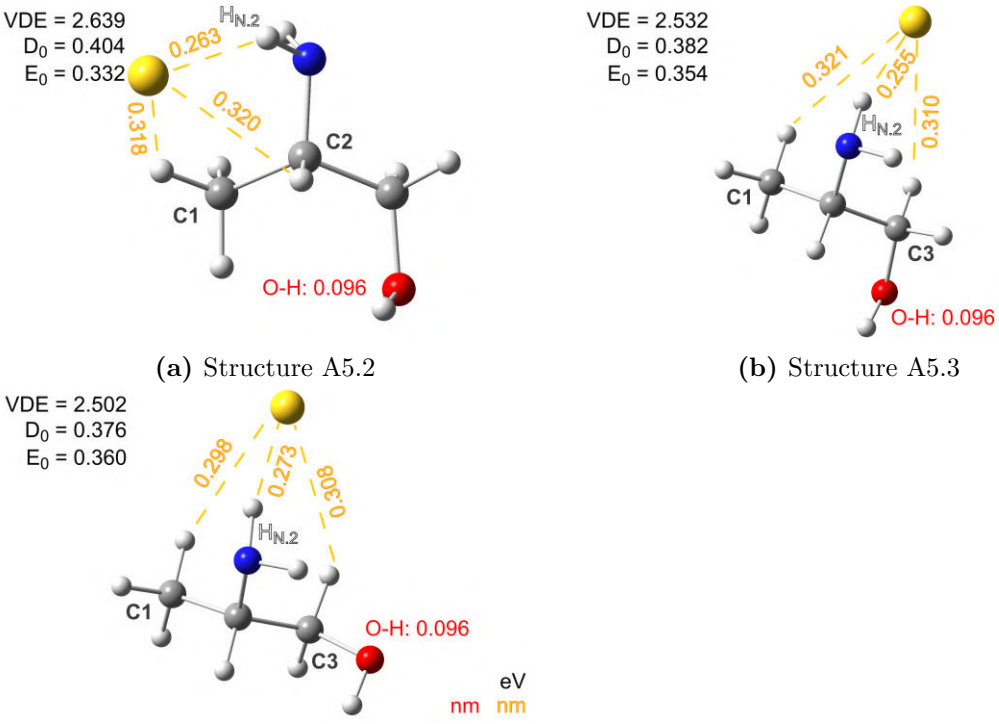

(a) Structure A5.2

(b) Structure A5.3

(c) Structure A4.3

Fig. 4.4.13.: The fourth group (4) of optimized structures for the complex Au^--Ala with various positions of Au^- adjacent to the chiral core obtained with B3LYP-D3/aug-cc-pVTZ(-PP). Like for the third group, no hydrogen bonds of the type $Au^- \cdots$H-O occur and the hydrogen bonds $Au^- \cdots$H-N are shorter in comparison to $Au^- \cdots$H-C. The difference to the third group is the bond length of the OH group, which is the uninfluenced bond length since neither N nor Au^- interact with the hydroxy group. The distance between Au^- and CH hydrogens is around 0.3 nm. Distances are given in nm (yellow or red) and energies in eV (black).

4.4.1.2. Geometric Properties Supporting H-bonding in Au^--M

According to the IUPAC definition and listed properties for a hydrogen bond mentioned in the beginning of this chapter, the bond length between hydrogen and hydrogen acceptor is usually smaller than the sum of the van-der-Waals radii of both atoms. Van-der-Waals radii can be extracted from Bondi and Batsanov in [190] but relevant sums are 0.272 nm for conventional hydrogen bonds involving X-H$\cdots$O and 0.333 nm for the nonconventional bonds X-H$\cdots$Au, where X is an hydrogen donor, e.g. O, N or C. Here, the van-der-Waals radius of neutral Au is taken, not the one of the anion, which might lead to a (slightly) smaller radius than for the anion case.

Normally, bond lengths of H$\cdots$O in a hydrogen bond are around 0.18 - 0.20 nm [191], fulfilling the IUPAC definition. In the nonconventional case of O-H$\cdots$Au, the bond length also meets the condition set by IUPAC for some systems [127].

The more common case with O as hydrogen acceptor fulfills this condition always for Au^--3HTHF and Au^--Ala: All bonds involving O lead to a $Au^-\cdots$H bond length of around 0.23 nm, a bond length, which also fulfills the length condition as if Au^- would be an O. Concerning N, this property is also easily satisfied by the last two groups of Au^--Ala with the length staying below 0.275 nm, where N is the only/primary hydrogen bond donor (figure 4.4.12 and 4.4.13). Mostly the bond length is around 0.25 nm. However, the most stable group (the first group) of Au^--Ala barely fulfills the condition with bond length of 0.3 nm or higher where N operates as a secondary H-bond donor, second to O. (figure 4.4.10).

Considering the $Au^-\cdots$H-C systems, most bond lengths stay below the limit of 0.333 nm. In the case of Au^--Fen all bond length are below that limit and also all Au^--Men complexes except two examples in the least stable ones fulfill this condition. Even in the systems with $Au^-\cdots$H-O and $Au^-\cdots$H-N bonds, there are complexes with $Au^-\cdots$H-C with a bond length smaller than 0.333 nm. Among them are the most stable ones, e.g. H1.1, H1.3, A1.1 and A2.1.

The smallest bond length of the type $Au^-\cdots$H-C can be found in M1.1 and M3.1 with 0.266 nm. It is no match for the $Au^-\cdots$H-O bond length but is comparable to $Au^-\cdots$H-N (compare with figure 4.4.13).

Another aspect for hydrogen bonds is the bond angle $\angle$X,H,Au^- with X being either O, N or C. For a H-bond, the bond has to approach linearity (110 - 180°). Bonds of the type $Au^-\cdots$H-O easily satisfy this condition since the angles are all between 159 - 175°. The bonds involving N can be comparable to $\angle$O,H,Au^-, but can also be pretty small with one bond not fulfilling the angle condition. The angles are between 102 - 175°.

$\angle$C,H,Au^- satisfy in most cases the angle condition, too, but with a smaller average bond angle compared to those mentioned above. In Au^--Fen and Au^--Men where C does not need to compete with O or N the angles are between 128 - 168° for Au^--Fen and 84 - 173° for Au^--Men. Only two bonds are not fulfilling the angle condition. They are in the two least stable Au^--Men and do not fulfill the bond length condition from earlier. In general, $Au^-\cdots$H-C bond angles are comparable in linearity to the $Au^-\cdots$H-O and $Au^-\cdots$H-N bonds. If $Au^-\cdots$H-C has to compete with the other bond types the angle is in general smaller and is between 86 - 143° (Au^--3HTHF and Au^--Ala).

Table 4.4.1.: Bond lengths and angles for selected Au^--M. The most stable isomer of each isomer group is chosen as representative of this group. Number in brackets give the values for the undisturbed molecule (no Au^-). X = C, N or O. Other isomers can be found in the appendix A.3.

Complex	H-bond	length (nm) X-H	length (nm) H$\cdots$Au$^-$	angle(°)
F1	C3-H$\cdots$Au	0.109	0.288	151.2
	C4-H$\cdots$Au	0.109	0.293	134.9
	C5-H$\cdots$Au	0.109	0.316	128.4
M1.1	C4-H$\cdots$Au	0.111(0.110)	0.226	161.0
	C6-H$\cdots$Au	0.110	0.295	144.3
	C9-H$\cdots$Au	0.109(0.110)	0.291	144.8
M1.2	C7-H$\cdots$Au	0.110	0.298	130.7
	C9-H$\cdots$Au	0.109	0.308	117.7
	C10-H$\cdots$Au	0.109	0.307	130.1
M4.3	C2-H$\cdots$Au	0.109	0.293	149.3
	C4-H$\cdots$Au	0.109	0.315	125.3
	C10-H$\cdots$Au	0.109	0.312	119.3
H1.1	C1-H$\cdots$Au	0.109	0.231	92.2
	C4-H$\cdots$Au	0.109	0.318	124.8
	O-H$\cdots$Au	0.099(0.096)	0.231	164.6
H1.4	C2-H$\cdots$Au	0.110	0.299	139.5
	C3-H$\cdots$Au	0.109	0.325	121.9
	C4-H$\cdots$Au	0.109	0.292	131.1
A1.1	C3-H$\cdots$Au	0.110	0.323	107.1
	N-$H_{N.1}\cdots$Au	0.102(0.101)	0.331	102.0
	N-$H_{N.2}\cdots$Au	0.102(0.101)	0.301	122.4
	O-H$\cdots$Au	0.099(0.097)	0.233	163.5
A4.2	C2-H$\cdots$Au	0.109(0.110)	0.305	121.1
	N-$H_{N.1}\cdots$Au	0.102(0.101)	0.297	138.5
	O-H$\cdots$Au	0.099(0.096)	0.232	170.0
A1.2	C1-H$\cdots$Au	0.109	0.309	136.2
	C2-H$\cdots$Au	0.109	0.366	94.9
	N-$H_{N.2}\cdots$Au	0.103(0.101)	0.251	157.9
A5.2	C1-H$\cdots$Au	0.109	0.318	128.7
	C2-H$\cdots$Au	0.110	0.320	111.5
	N-$H_{N.2}\cdots$Au	0.102(0.101)	0.263	149.6

Interestingly, the most linear bond for $Au^- \cdots$H-C of 173.1° can not be found in the most stable isomer M1.1 but in M4.1 indicating that the stability is not driven by a solitary $Au^- \cdots$H-C bond but rather is a collaboration of several $Au^- \cdots$H-C bonds. This is in contrast to isomers involving $Au^- \cdots$H-O bonds. This bond is always the most linear bond and the corresponding isomer belongs to the most stable isomers.

Beside the bond length to Au^-, internal bond lengths like O-H, N-H and C-H are monitored to study the influence of Au^- on this kind of bonds. The bond lengths disturbed and undisturbed by the Au^- can be found for selected Au^--M in table 4.4.1 and in the appendix A.3 for all other isomers (table A.6 - A.15).

For hydrogen bonding, it is usual to find an elongated bond between the donor and H in comparison to the undisturbed bond. Without the perturbation of Au^-, the OH bond length is around 0.096 nm for 3HTHF isomers (figure 4.4.7) and for alaninol isomers except for the most stable isomers A1.0 and A2.0 (figure 4.4.9). A1.0 and A2.0 have an extended bond length of 0.097 nm due to the internal hydrogen bond N$\cdots$H-O. Both, OH bond lengths are within literature values [75, 189, 192]. If Au^- is interacting with the molecule, the bond length is increased clearly to 0.099 nm, which can be expected for the common hydrogen donor O.

Another hydrogen donor is N, which can be found in alaninol. It forms weaker hydrogen bonds than the common donor O can offer but is nevertheless accepted as hydrogen bond. The bond elongation is about 0.001-0.002 nm. Especially in the first two groups of Au^--Ala (table A.12 and A.13) the elongation is mostly 0.001 nm since the N donor is in competition with the O donor weakening the hydrogen bond involving the N and hence lead to a smaller elongation. In contrast to the last two groups (table A.12 and A.13), which have no hydrogen bonds with the O, most complexes show an increased elongation of 0.002 nm.

Bonds involving C change the bond length maximal by 0.001 nm. Some seem to be longer and even shorter after the bond with Au^- (e.g. M1.1 in table A.7). This could be due to rounding the values but in general the elongated bonds match with the elongation seen in the N-H bond.

From a geometric point of view, all complex types demonstrate characteristics of hydrogen bonding indicating to a stronger (and potentially directional) interaction between chiral molecule and Au^-. This interaction is expected to be stronger and more perturbing than weak van der Waals forces and might help the photoelectron to sense the chiral potential facilitating a PECD effect.

4.4.2. Calculated Energies of Gold Complexes

4.4.2.1. Global Energies

Table 4.4.2.: ZPE corrected energies calculated with B3LYP-D3/aug-cc-pVTZ(-PP) for Au^--Fen and Au^--Men. VDE(Au^-) = 2.215 eV. $E_B(Au^-)$ = 2.309 eV. D_0 and D_n are always related to the respective most stable molecular isomer. The structures are ordered by E_0. Hence, isomers of Au^--Men can be grouped according to the connectivity of Au^- to Men: Au^- connects with (1) the ring structure (figure 4.4.4), (2) the border of the ring (figure 4.4.5) and (3) isopropyl group of Men (figure 4.4.6).

Au^--Fen

Exp		E_B	ΔE_B				
		2.707	0.398				
DFT	E_0	VDE	ΔVDE	D_0	ADE	VDE-ADE	D_n
F1	0	2.590	0.373	0.548	2.550	0.040	0.214
F2	0.065	2.528	0.313	0.483			
F3	0.119	2.490	0.275	0.429			
F4	0.128	2.490	0.275	0.420			

Au^--Men

Exp		E_B	ΔE_B				
		2.8	0.5				
DFT	E_0	VDE	ΔVDE	D_0	ADE	VDE-ADE	D_n
(1)							
M1.1	0	2.669	0.454	0.680	2.606	0.063	0.289
M2.1	0.017	2.660	0.445	0.663			
M3.1	0.024	2.674	0.459	0.656			
M4.1	0.077	2.698	0.483	0.603			
(2)							
M1.2	0.186	2.551	0.336	0.494			
M3.2	0.214	2.554	0.339	0.466			
M2.2	0.217	2.544	0.329	0.463			
M4.2	0.325	2.543	0.328	0.355			
(3)							
M4.3	0.398	2.439	0.224	0.282			
M1.3	0.456	2.326	0.111	0.224			
M2.3	0.468	2.325	0.110	0.212			

Table 4.4.3.: ZPE corrected energies calculated with B3LYP-D3/aug-cc-pVTZ(-PP) for Au^--3HTHF and Au^--Ala. VDE(Au^-) = 2.215 eV. $E_B(Au^-)$ = 2.309 eV. D_0 and D_n are always related to either H1.0 or A1.0, respectively. Isomers are ordered by E_0 and hence can be grouped according to the connectivity of Au^- to the molecule: Au^- connects with the hydroxy group of 3HTHF and Ala in (1), respectively (figures 4.4.8a - 4.4.8c and 4.4.10). Also for (2) in the case of Ala but $Au^- \cdots$ H-O is not observed in (2) for 3HTHF as well as (3,4) for Ala.

Au^--3HTHF

Exp		E_B	ΔE_B				
		2.99	0.68				
DFT	E_0	VDE	ΔVDE	D_0	ADE	VDE-ADE	D_n
(1)							
H1.1	0	2.880	0.665	0.761	2.845	0.035	0.131
H1.2	0.031	2.860	0.645	0.730			
H1.3	0.036	2.800	0.585	0.725			
(2)							
H1.4	0.268	2.560	0.345	0.493			
H2.1	0.316	2.548	0.333	0.445			
H2.2	0.326	2.539	0.324	0.435			

Au^--Ala

Exp		E_B	ΔE_B				
		3.00	0.69				
DFT	E_0	VDE	ΔVDE	D_0	ADE	VDE-ADE	D_n
(1)							
A1.1	0	2.866	0.651	0.736	2.386	0.480	0.565
A2.1	0.010	2.881	0.670	0.726			
A3.1	0.069	2.805	0.590	0.667			
A4.1	0.079	2.823	0.608	0.657			
(2)							
A4.2	0.082	2.855	0.640	0.655			
A3.2	0.084	2.869	0.654	0.653			
A2.2	0.099	2.863	0.648	0.637			
A5.1	0.112	2.837	0.622	0.625			
(3)							
A1.2	0.142	2.702	0.487	0.594			
A1.3	0.180	2.622	0.407	0.557			
A2.3	0.183	2.692	0.477	0.554			
A2.4	0.183	2.688	0.473	0.553			
(4)							
A5.2	0.332	2.639	0.424	0.404			
A5.3	0.354	2.532	0.317	0.382			
A4.3	0.360	2.502	0.287	0.376			

Energies extracted from the various isomers of the gold complex can be found in the tables 4.4.2 - 4.4.3. Like the figures, the isomers are ordered according to their minimal energy E_0 in ascending order.

However, ordering the isomers according to the VDE in descending order would lead for Au^--Fen and Au^--3HTHF to the same order. The isomers in Au^--Men would change places within the respective groups (figure 4.4.14a), e.g. M4.1 would be on the first position instead of M1.1. In these cases, the VDE seems to correlate with the general placement of Au^- relative to the molecule and hence correlates with E_0. Au^--Ala would behave a bit differently: isomers with $Au^- \cdots$H-O would rearrange within the first two groups (1) and (2), e.g. A3.2, a member of (2), would be on the second position instead of A2.1 and hence be in (1). The same could be observed for the group without $Au^- \cdots$H-O (3,4). Especially in the first two groups, if one $Au^- \cdots$H-N is among the three closest bonds, the corresponding isomer shows the largest VDE values (points above the blue horizontal line in figure 4.4.14b) while isomers without $Au^- \cdots$H-N have lower VDE values (below the blue line). Hence, the VDE seems to be primarily determined by $Au^- \cdots$H-O and secondary by $Au^- \cdots$H-N. From group (1) only A1.1 and A2.1 and from (2) A2.2, A3.2 and A4.2 are above the blue horizontal line. The difference between these subgroups is the strength of the $Au^- \cdots$H-N bond, which is for (1) weaker than for (2) according to the bond length. This seems to be important for E_0 and less for the VDE.

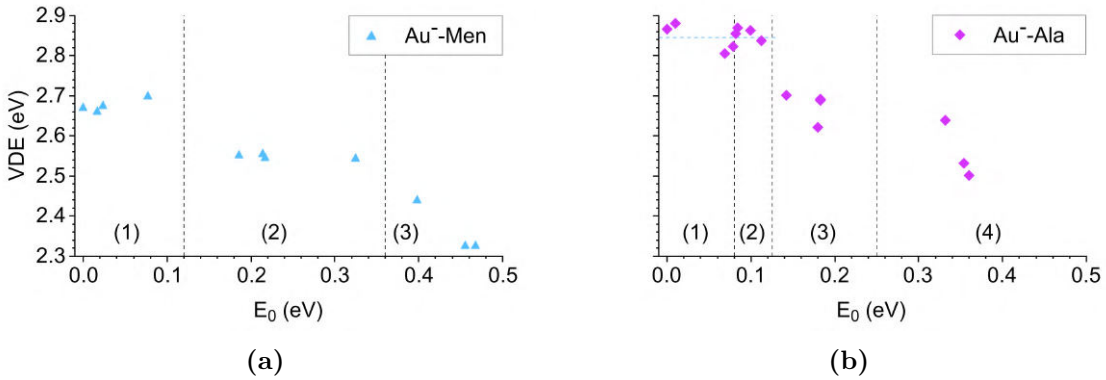

Fig. 4.4.14.: VDE vs minimum energy E_0 of (a) Au^--Men and (b) Au^--Ala. Vertically black dashed lines are set arbitrarily to separate the different isomer groups. Group (1) and (2) of Au^--Ala are further subdivided with an horizontal blue dashed line above which isomers show $Au^- \cdots$H-N bonds. From (1) only A1.1 and A2.1 are above the blue line and differ from (2) by the weaker $Au^- \cdots$H-N bond according to the bond length to Au^-.

After photodetachment, the influence of Au is decreased due to the missing charge and the complex can experience different structural changes before reaching a relaxed state. The energy needed for this changes is ADE-VDE, which is given for only the most stable isomers of all Au^--M. For Au^--Fen and Au^--Men, VDE-ADE is only 0.038 and 0.063 eV implying a relatively small structural change of the complex after photodetachment. For Au^--3HTHF a difference of 0.035 eV is needed. Without the additional charge, the molecule in H1.1 (which resembles H2.0 more than H1.0) could transform

in a molecule, which resembles more H1.0. In that case, around 0.022 eV are required for the transformation from H2.0 to H1.0 (E_0 in 4.4.7). The remaining 0.013 eV could be needed for additional hydrogen rotation. The largest structural change appears in Au^--Ala with VDE-ADE = 0.480 eV. Once the charge is removed, alaninol in A1.1 seems to need big structural changes to reach the relaxed configuration.

4.4.2.2. (Local) Hydrogen Bonding Energetics

An analysis of the geometric properties of these complexes gives a qualitative assessment of the hydrogen bonding in these complexes, but examining the local energetics of these complexes, meaning the influence of individual hydrogens, could provide a more quantitative understanding. Considering the whole complex, the dissociation energy is a good first hydrogen bond strength estimator. However, with the help of Bader's quantum theory of atoms in molecules (QTAIM or just AIM) [161, 193] analysis, strengths of the individual hydrogen bonds can be estimated more precisely. Solely considering the dissociation energy D_0 of an isomer with conventional bond donor and another with a nonconventional hydrogen donor shows that the latter is not necessarily weaker bound. For example, A1.1, the most stable isomer of the Au^--Ala, has an $Au^- \cdots$H-O only shows a dissociation energy difference to M1.1 of 0.056 eV (table 4.4.2 and 4.4.3). Even more interesting is the fact that D_0 of M1.1 is only smaller for the first two most stable isomers of Au^--Ala, hence being more stable than some of the isomers, which show a $Au^- \cdots$H-O bond (e.g. A4.1).

This small energy difference between the different types of complexes and even the superiority of M1.1 over some isomers from Au^--Ala show the importance of identifying hydrogen bond donors, the effect of cooperativity of several hydrogen donors on the total bond energy and the influence of different forces like electrostatic forces, dispersion and induction.

A first approximation of the individual hydrogen bond energy eb_{HB} can be done under the assumption of $D_0 = -E_{HB}$ with E_{HB} being the sum of all hydrogen bonding interactions between molecule and Au^-. If only one H is contributing to the bond with Au^- and all other bonds are negligible then the individual hydrogen bond energy is simply $-E_{HB}$. However, this is just the lower limit (considering the minus sign) and probably an overestimation of the magnitude. At the opposite end of the spectrum, if three hydrogens equally participating in the bond with Au^-, the individual contribution is $-E_{HB}/3$, which can be considered as the upper limit if the minus sign is considered and represents a lower limit of an overestimation. This arises from the assumption that there are no other energetic contribution to the dissociation energy except the ones from hydrogen bonding.

Considering only the most stable isomers, the individual H-bond energy range for each complex is [-0.55,-0.18] eV for Au^--Fen, [-0.68,-0.23] eV for Au^--Men, [-0.76,-0.25] eV for Au^--3HTHF and [-0.74,-0.25] eV for Au^--Ala. An energy of at least -0.2 eV is considered to be a moderate strength in hydrogen bonds [158], which seems to be possible for all complexes. Au^--Fen and Au^--Men will probably show energies, which are closer to $-E_{HB}/3$ since all bonds have the same hydrogen donor and will be equally strong. On

the other hand, Au^--3HTHF and Au^--Ala could be closer to the other limit since they possess the pretty dominant hydrogen donor O.

This is an overestimation, as it assumes all attractive forces and contributions to the dissociation arise from solely the hydrogen bonding. Therefore, an AIM analysis is performed to further confirm the hydrogen bond.

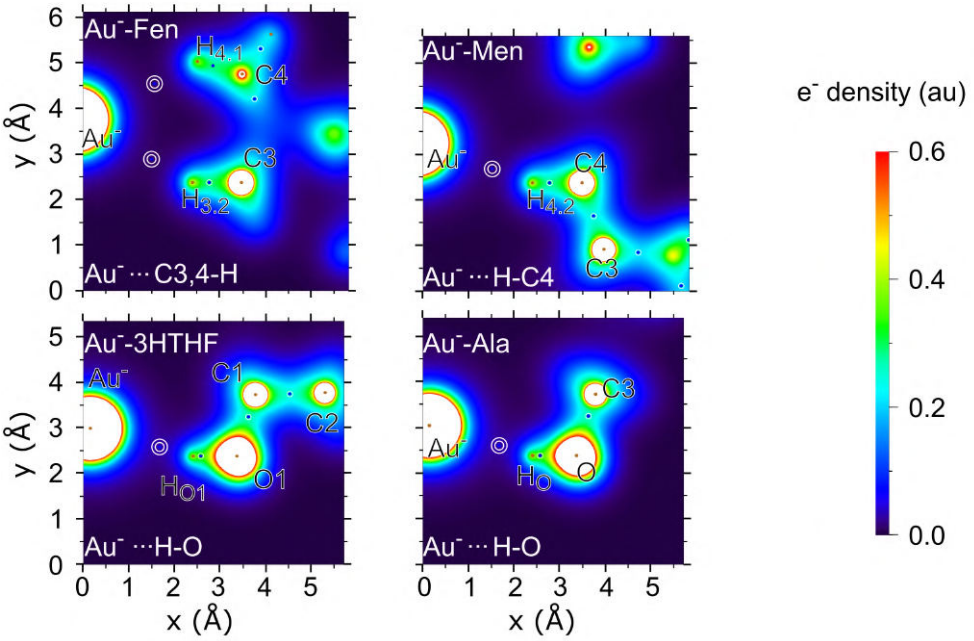

Fig. 4.4.15.: Electron density of the most stable gold complexes after AIM analysis. White areas (density beyond scale) and brown dots (nuclear critical points) mark the atom positions. Bond critical bonds are blue dots with white circles. The one with two big white circles is the bond critical point considered in table 4.4.4. Ring and cage critical points are masked. Only hydrogen bonds with the strongest bcp's are considered here. H label according to figure A.1.

AIM analysis The result of the AIM analysis is given in form of electron densities ρ and critical points in figure 4.4.15 for selected bonds of the most stable gold complexes. Critical points are positions where the derivation of the density is zero and hence mark extrema in the charge density. They can be categorized into four types:

- (3,-3) or nuclear critical point (npc): ρ is a local maximum. It overlaps (almost perfectly) with the nuclear positions of (heavy) atoms.
- (3,-1) or bond critical point (bcp): Saddle point in ρ with ρ being a maximum in two room directions and a minimum in one room direction. It occurs between attractive atom pairs.

- (3,+1) or ring critical point (rcp): Like bcp a saddle point but with ρ being a minimum in two room directions and a maximum in one room direction. It marks the center of ring systems and displays steric effects.

- (3,+3) or cage critical point (ccp): ρ is a local minimum. It describes cage systems like pyramid shaped molecules.

Of special interest are the bcp's since conclusions about type and strength of a bond can be derived, which helps to judge about the (hydrogen) bonds in the gold complexes. However, caution is advised for bcp's since, contrary to their name, bcp's do not always indicate a (chemical) bond [194]. A bcp can also appear if two non-bonded atoms are close together simply due to their topology. To avoid this confusion between bcp's and (chemical) bonds, Shahbazian [194] suggests to call bcp's, line critical bond (lcp). Here, bcp is used further to avoid confusion between the two abbreviations LCP and lcp.

In figure 4.4.15, the positions of the atoms are clearly visible by white areas, which mark values beyond the density scale and by brown dots representing nuclear critical points. Bond critical points are blue dots with a white ring and the one with two rings is the one of interest. Table 4.4.4 lists all relevant bcp's (two white rings) with corresponding densities and energies (according to Emamian *et al.* [161]) for the most stable gold complexes.

For Au^--Fen, four bcp's concerning Au^- and one completely without Au^- could be found. Interestingly, the one not involving Au^- shows the highest density but it is possible that this bcp does not indicate a true bond due to the repellent character of both partially positively charged hydrogens. Four bcp's for Au^--Men are revealed from which the one with the lowest density does not include Au^- but the ketone group. Au^--3HTHF and Au^--Ala show each two bcp's, which all include Au^- and different hydrogen donors. The found bcp's agree more or less with the most likely bonds found via $Au^- \cdots H$ bond length and angles.

Emamian *et al.* [161] studied 42 different hydrogen bond complexes (28 neutral and 14 charged complexes) of various hydrogen bond strength and could not only classify this strength from very weak to strong but also establish a relationship between electron density and individual H-bond energies. Due to the variety of H-bond complexes studied by Emamian *et al.*, gold complexes will be compared to their electron densities and energies. This enables also a categorization of the gold complex' hydrogen bond strengths according to Emamian *et al.* [161].

The determined electron densities of bcp's of charged systems by Emamian *et al.* [161] are at least 0.03 au (atomic units[4]), which is not reached by any bond of Au^--M (table 4.4.4). The bond of the type $Au^- \cdots$H-O from Au^--3HTHF and Au^--Ala come close but stay under that value. This could be due to the different kind of complex: Emamian *et al.* [161] did not study charged complexes involving Au^- but mostly conventional hydrogen acceptors (and Cl, S), which may have greater influence on the H-bond than unconventional anions like Au^-. However, comparing the densities of bcp's of the $Au^- \cdots$H-O bonds to the ones of the gold(I)$\cdots$indazol-3-ylidene complex from Park

[4]Not to be confused with arbitrary units a.u.

Table 4.4.4.: Bond critical points (bcp) calculated with AIM for the most stable conformers and ordered according to the density ρ_{bcp}. The density ρ_{bcp} is given in atomic units (au). The bond energies for a single hydrogen bond eb_{HB} are calculated according to equation 4.4.2 and given in eV. Bonds with * are shown in figure 4.4.15. The bcp in C5-H$\cdots$H-C8 of Au^--Fen might not correlate to a true bond.

System	bcp	ρ_{bcp} (au)	eb_{HB} (eV)
Au^--Fen	C5-H$\cdots$H-C8	0.0120	-0.2192
	$Au^-\cdots$H-C3*	0.0103	-0.1947
	$Au^-\cdots$H-C4*	0.0098	-0.1875
	$Au^-\cdots$H-C5	0.0067	-0.1428
	$Au^-\cdots$H-C1	0.0033	-0.0938
Au^--Men	$Au^-\cdots$H-C4*	0.0156	-0.2711
	$Au^-\cdots$H-C9	0.0100	-0.1903
	$Au^-\cdots$H-C6	0.0094	-0.1817
	O$\cdots$H-C1	0.0089	-0.1745
Au^--3HTHF	$Au^-\cdots$H-O1*	0.0282	-0.4526
	$Au^-\cdots$H-C4	0.0066	-0.1413
Au^--Ala	$Au^-\cdots$H-O*	0.0273	-0.4397
	$Au^-\cdots$H-N	0.0089	-0.1745

and Gabbai [167] (ρ_{bcp} = 0.026 and 0.017 au), which are confirmed moderately strong hydrogen bonds, reveals that the here determined densities are greater. Of particular interest is the gold(I)$\cdots$indazol-3-ylidene complex with a bcp of a smaller density of 0.017 au since it is comparable to the $Au^-\cdots$H-C4 bond of Au^--Men.

Emamian [161] estimates the bond energy of each bond with a linear fit to the electron density ρ_{bcp} of a specific bond critical point gained from fitting experimental and DFT calculated results. The relationship between the individual bond energy eb_{HB}, given in kcal/mol, and ρ_{bcp}, given in atomic units (au) is presented in equation 4.4.2.

$$eb_{HB} = -332.34 \cdot \rho_{bcp} - 1.0661 \tag{4.4.2}$$

The fit is based on a calculation with B3LYP-D3(BJ)/ma-TZVP [161] and equation 4.4.2 might vary for different DFT methods. Since, in this work a slightly different functional and another basis set is used, equation 4.4.2 might show a different deviation than given by Emamian [161]. However, a test calculation with F^--H_2O shows that B3LYP-D3/aug-cc-pVTZ and B3LYP-D3(BJ)/ma-TZVP lead to similar dissociation energies (around 0.014 eV difference) indicating that the deviation given by Emamian could still be similar in the here presented case. This test calculation is presented in table A.5.

The energies of the individual bonds with Au^- are comparable and equally distributed for Au^--Fen and Au^--Men like it can be expected for bonds involving the same atoms (C, H, Au^-). This confirms the assumption from earlier when the individual bond energy was estimated based on D_0, which also led to similar numbers like given in table 4.4.4.

Table 4.4.5.: Calculated O-H and asymmetric N-H stretch frequencies for Au^--3HTHF and Au^--Ala. Calculated frequencies from the optimized neutral complex and isolated molecules are given. All calculated frequencies are given in cm^{-1} and are scaled with a factor of 0.9636.

Vibration (cm^{-1})	Au^--3HTHF	Au^--Ala
OH stretch in Au^--M	3104.83	3147.26
OH stretch in Au-M	3627.49	3633.11
OH stretch in isolated M	3643.05	3582.18
NH stretch in Au^--Ala		3380.01
NH stretch in Au-Ala		3431.10
NH stretch in isolated Ala		3441.21

In contrast, Au^--3HTHF and Au^--Ala show energies that are not described well by the estimation done with D_0. It was correct to assume that the atom with the highest electronegativity will have the strongest contribution but the energy of these bonds is lower than the maximum assumed energy of D_0. The bond involving the atom with lower electronegativity has an energy smaller than estimated with $D_0/3$. In general, estimating the individual bonding energies with the help of D_0 and AIM leads to lower values for AIM. This is pronounced for Au^--3HTHF and Au^--Ala while the AIM result of Au^--Fen and Au^--Men is more comparable to the estimation with D_0.

Redshift Apart from bond strength, a hydrogen bond can also be identified by a redshift upon hydrogen bonding, according to IUPAC. Such redshifts can be calculated for the O-H and N-H bond. However, it remains experimentally not accessible due to the experimental resolution.

The calculated frequencies can be found in table 4.4.5 and are scaled by a factor of 0.9636, which is determined from [195]. The ratio of the B3LYP-D3/aug-cc-pVTZ calculated frequencies of the asymmetric and symmetric stretch frequencies of H_2O and corresponding experimental values hereby define this scaling factor.

The relevant redshift is between the isolated molecule and the anionic complex. For Au^--3HTHF and Au^--Ala, the frequency drops for O-H around 538 and 435 cm^{-1}, respectively. Something similar is observed in the N-H bond but weaker: the frequency falls in total by around 61 cm^{-1}. In general, this is the redshift, which is typical for hydrogen bonds according to IUPAC.

A smaller redshift of around 16 and 10 cm^{-1} can also be observed for the O-H bond in the neutral complex Au-3HTHF and the N-H bond in Au-Ala, respectively. Hence, a weak H-bond seems to be possible for the neutral complex as well indicating that the charge is not necessary for a H-bond itself but is definitely enhancing it.

For a H-bond, an unusual blueshift of around 51 cm^{-1} can be found for the O-H bond in the neutral complex Au-Ala. The O-H frequency is probably altered in the molecule due to the internal hydrogen bond N$\cdots$O-H in the isolated molecule, which is broken in the gold complex. In contrast to the internal bond, the neutral Au seems to create a weaker H-bond, which only becomes stronger if the charge is added to the gold.

4.4.3. Bond Character

Hydrogen bonds in charged complexes are governed mainly by electrostatic and induction forces [161]. This includes charge transfer ΔQ and polarization α. With the help of a natural bond orbitals (NBO) analysis, it is determined if the interaction between Au^- and molecule is of global nature (in the context of the complex' size) or if the bond character is driven by local properties (e.g. by single atoms of the complex). In order to achieve that, the quantities are considered in combination with the stability of the complex or the dissociation energy.

4.4.3.1. Global Property: Dipole Moment and Polarizability

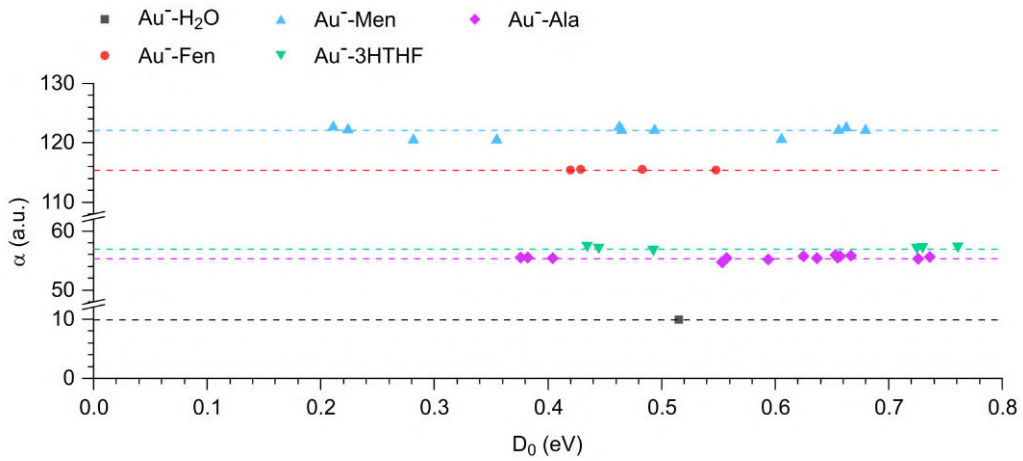

Fig. 4.4.16.: Polarizability α of the excited molecules dependent on the dissociation energy of Au^--M. The dashed colored lines are the α of the respective most stable molecular isomer. All excited isomers M* of the same molecule are polarized in the same way in the vicinity of Au^-. The polarizability of M* differ not at all or just slightly (Au^--Men) from the polarizability of the most stable molecular isomer.

Here it is hypothesized that, molecules with a strong polarizability α should be the most stable systems, i.e. having the largest dissociations energies D_0 due to the relationship between dispersion forces and α. Also, molecules with a strong magnitude in dipole moment and a dipole vector pointing towards Au^- should attract Au^- the most hence leading to the most stable Au^--M.

While the polarizability and the magnitude of the dipole moment can readily extracted after the DFT calculation, the dipole angle needs some more consideration: The orientation of the dipole moment from the excited molecule is depicted by GaussView and a bond parallel to the dipole vector is located, e.g. the O-C bond in fenchone. Now, the corresponding gold complex is considered: a "gold vector" is defined, which has the same origin as the dipole vector from M* but ends at Au^- (inset of figure 4.4.17e). The angle between the dipole and gold vector is the dipole angle and is plotted over D_0 (figures 4.4.17e - 4.4.17h).

Figure 4.4.16 present the correlation between the polarizability α of the excited molecule M^* over D_0. The stability does not rise with α but shows an (almost) constant relationship to α. The dashed line indicates α of the most stable molecular isomer (e.g. A1.0 in violet) and is in almost all cases not differing from α of M^*. Hence, if Au^- forms the external polarizing field, all isomers of the same molecules will displace their charges in an (almost) equal amount in the vicinity of Au^-. The only difference is the polarizability of the different molecules with the largest molecules (fenchone in red and menthone in blue) having larger α than the smaller ones (3HTHF in green and alaninol in violet). This is a known tendency since larger molecules offer more volume to the electrons to occupy.

In figure 4.4.17 the magnitude and angle of the dipole moment μ of the excited molecules M^* is compared to D_0 of Au^--M. The expected correlation of a strong dipole moment (magnitude μ) pointing in the direction of Au^- ($\phi = 0°$) leading to the most stable systems is not observed here. Au^--Fen and Au^--Men stay more or less constant for the magnitude μ and even show the inverse expected correlation for ϕ. For Au^--3HTHF and Au^--Ala no correlation at all seems to exist. Since neither the magnitude nor the direction of the dipole show the expected correlation to D_0, the breakdown of the multipole expansion has to be assumed. It is valid at great distances but not for short ones like 0.3 nm, which is observed for these complexes.

Global properties like the polarizability and the dipole moment of the whole molecule seems to have no expected influence on the stability of the system or on the charge transfer. Rather local effects, like the amount of hydrogen atoms participating in Au^- bonding (compare figures 4.4.4 - 4.4.6) or local charge displacements of H in the vicinity of Au^-, seem to have the dominant role.

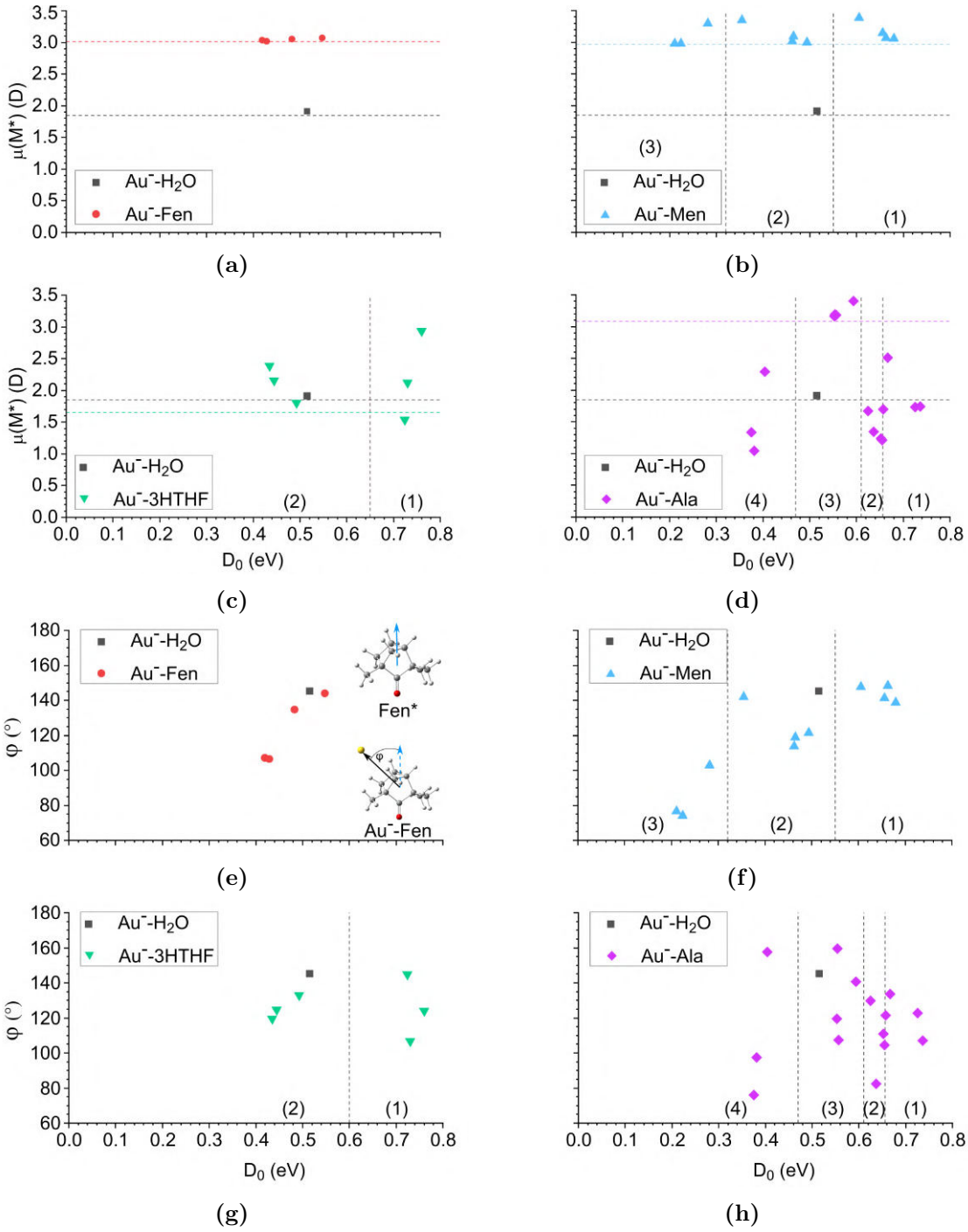

Fig. 4.4.17.: Magnitude (a-d) and angle (e-h) of the dipole moment of the excited molecules dependent on the dissociation energy of Au^--M. Horizontal dashed lines in (a-d) indicate the dipole moment of the most stable molecule (water in black, the other molecules in their respective colors) for comparison. Vertical dashed lines are set arbitrary between the different groups of gold complexes, according to the energy tables 4.4.2 - 4.4.3. The inset of (e) shows the definition of the angle between the dipole vector (blue, solid) (obtained from Fen* and copied to Au^--Fen (blue, dashed)) and the gold vector (black solid). The dipole vector is parallel to the C-O bond, which can be used as reference. In (e-h) 0° means that dipole vector and gold vector are parallel.

4.4.3.2. Localization and Transfer of the Excess Charge

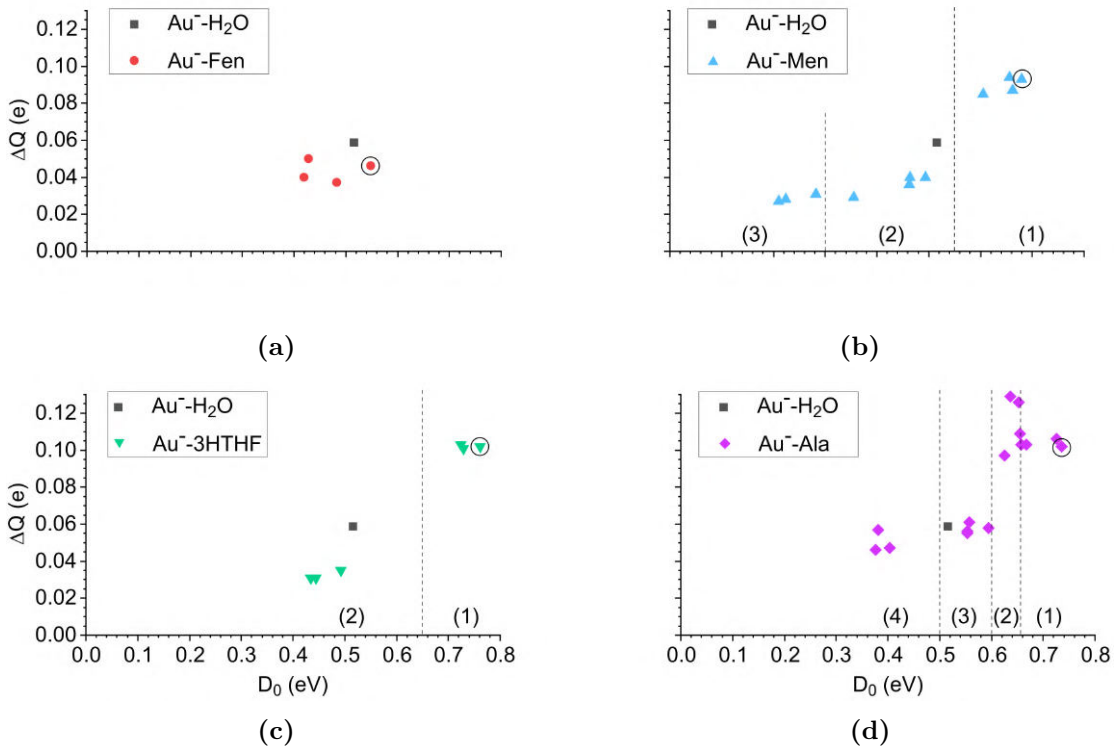

Fig. 4.4.18.: A comparison of charge transfer ΔQ and dissociation energy D_0. Black circles mark the most stable structures. Vertical black dashed lines are set arbitrarily between the different isomer groups according to the energy tables 4.4.2 - 4.4.3.

A NBO analysis reveals that the extra charge mainly remains localized at the gold part of the complex but is slightly reduced due to the "electron sharing" with or "charge transfer" to the molecule (around 0.9 e remains at Au). The amount of negative charge being transferred from Au^- to the molecule, the charge transfer ΔQ, is calculated as the difference of the charge located at the gold anion Q_{Au^-} and the charge of a bare gold anion Q = -1: $\Delta Q = |-1 - Q_{Au}|$. ΔQ (and Q) are measured in units of e.

ΔQ is compared to the dissociation energy (figure 4.4.18), and the blue shift ΔVDE (figure 4.4.19). In general, ΔQ rises with increasing ΔVDE or D_0 indicating that a stronger bond correlates to the "electron sharing" with the molecule. Due to this correlations, properties plotted against D_0 will in general show the same behavior as when plotted over ΔQ, e.g. dipole moment and polarizability plotted over ΔQ will still not show the expected behavior. In figure 4.4.19, the most stable structures are among the structures with the largest ΔVDE and ΔQ but do not necessarily feature the strongest electron bond or the most "electron sharing". The same can be said about the VDE due to the linear relationship to ΔVDE. Anyways, the most stable structures are among the structures with the largest VDE and ΔQ.

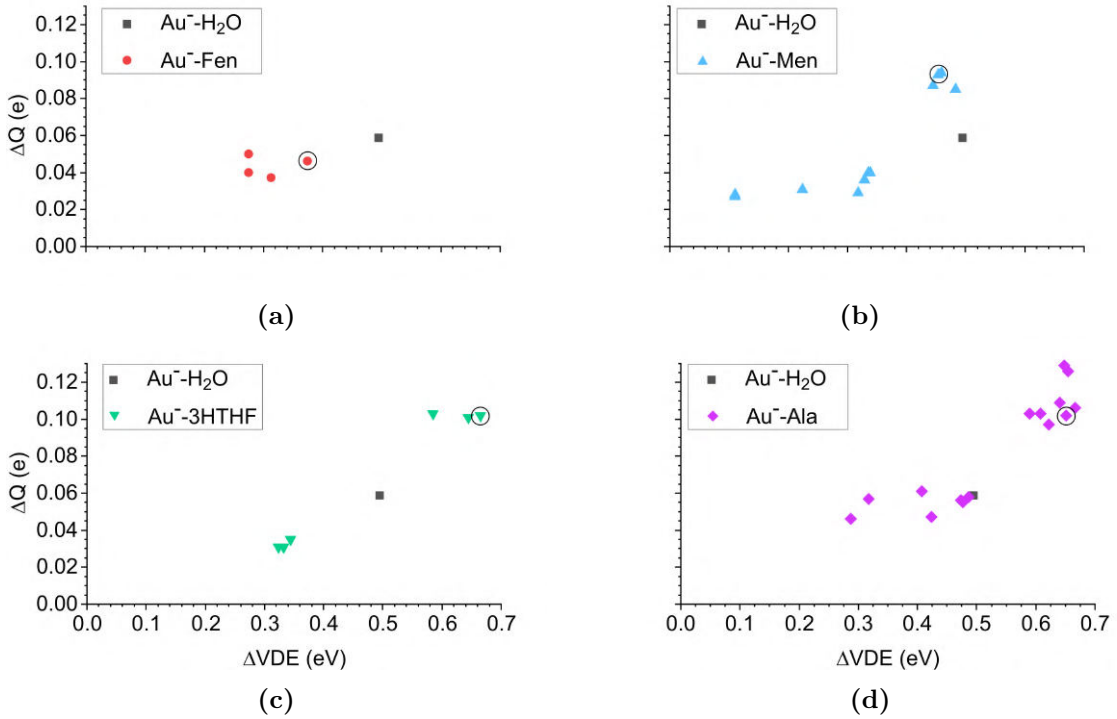

Fig. 4.4.19.: A comparison of charge transfer ΔQ and ΔVDE. The most stable structures are marked with black circles.

To further understand the bond character a more detailed look on the charge distribution and charge modification (due to Au^-) among the other atoms within the complex is performed. In figure 4.4.20 the charge distribution is shown for the most stable structures F1, M1.1, H1.1 and A1.1. The charge of the atoms may differ, slightly, within the same kind of gold complex but the trend of charge distribution remains the same. As already mentioned, the negative charge or excess electron remains mainly concentrated at the gold atom (around -0.9 e). The hydrogens are weakly positively charged (dark green), whereas the carbons tend to have almost no or a weak negative charge (dark red). One exception is the C binding to O in fenchone and menthone: It clearly holds a positive charge while the oxygen holds a negative one. In the case for Au^--3HTHF and Au^--Ala, all hydrogens are mainly positively charged. However, the hydrogen in the hydroxy group is a bit more positive than the others. In general, the charge distribution matches with what can be expected if the electronegativities of the atoms are considered.

The change of NBO charges upon Au^- bonding can also be seen in figure 4.4.20. Here, all hydrogens relevant for the bond with Au^- according to bond length and angle are depicted with their charges when Au^- is bond and in brackets when Au^- is not there. In general, all charges are more positive if Au^- present. Two exceptions are a hydrogen at H1.1 and another at A1.1: In the case of H1.1, AIM does not reveal a bcp between that hydrogen and Au^- indicating that there is no H-bond formed with Au^-. For A1.1, the difference arises from breaking the internal H-bond when going from bare molecule to the gold complex.

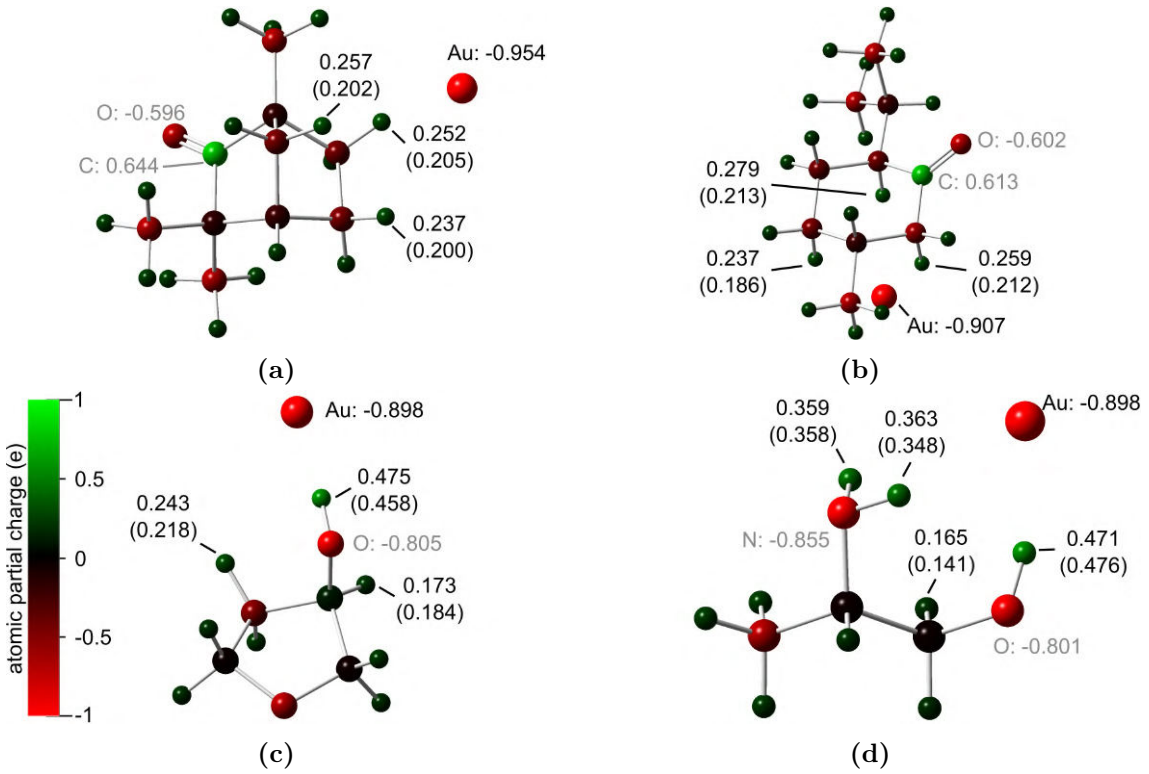

Fig. 4.4.20.: NBO of the most stable structure for the different Au^--M: F1 (a), M1.1 (b), H1.1 (c) and A1.1 (d). Given are atomic partial charges (NBO charges) in units of the elementary charge (e) from +1 (green) to -1 (red). The negative charge or the electron remains mainly with Au^-. Black numbers are relevant for (hydrogen) bonding with Au^-. Numbers in brackets give the charges of the bare molecule (no Au^-).

In the case of the most stable isomers, figure 4.4.18 and 4.4.19 already show that complexes with an OH group show a (slightly) bigger charge transfer ΔQ than gold complexes with a ketone group. The same can be observed in figure 4.4.20. This can be explained by the different strong interactions between Au^- and the different participating atoms in the hydrogen bond. In figure 4.4.20, the charge increase in the hydogens is greater in magnitude than what can be explained by the lost charge of Au^- indicating an enhanced H-X bond polarity due to induction, an important force in hydrogen bonding.

The NBO analysis revealed the electron donation character of the complexes. In all cases electron donation happens predominately from the $6s$ orbital of Au^- into the σ^* orbital of all X-H bonds: the CH bonds of Au^--Fen and Au^--Men, the OH and CH of Au^--3HTHF as well as significantly into OH and secondary into NH and CH from Au^--Ala. Such a donation behavior is typical for three-center-four-electron (3c-4e) bond, which is expected for a hydrogen bonds.

4.5. Experiment vs Computational Results

All the energies obtained from the previous presented structures will be compared to the experimental values to verify if the generated structures are appropriate for describing the Au^--M system that have been observed. Since, just the (electron) binding energy is measured in these experiments, only a comparison between E_B and VDE (figure 4.5.1a) as well as the resulting shifts to Au^-, Δ (figure 4.5.1b) are possible. A comparison between experiment and calculated value is not restricted to peak X but can be extended to peak ν_X and A as well if frequency calculations and Koopmans' theorem [196] are used, respectively. Here, D_0, D_n and E_0 do not have an experimental counterpart.

4.5.1. Peak X and Blue Shift

The comparison between the binding energies of peak X in figure 4.5.1a, as well as the shifts in figure 4.5.1b, for the most stable isomers show that the calculated binding energies and shifts underestimate, in all cases, the experimental values. This is indicated by a linear fit without offset and a slope of slightly larger than one (1.04 for the most stable systems).

If instead the VDE of the most stable isomers is replaced with the best matching VDE, the comparison between VDE and E_B gives a worse fit, e.g. not matching the error bars of the data points. The fit for the most stable complexes seems to be more reliable and hence the factor 1.04 is recommended for an estimation of experimental values given the calculated values. The proximity of the fit parameter to 1 is another indicator of the adequate choice of functional and basis set for these systems.

The DFT calculations can also be used to test the assumption from section 4.3.1, that the shift ΔVDE or ΔE_B from the Au^- PES can be fully described by the dissociation energy due to the negligence of D_n^* (equation 3.3.37). For this test, the Born-Haber cycle

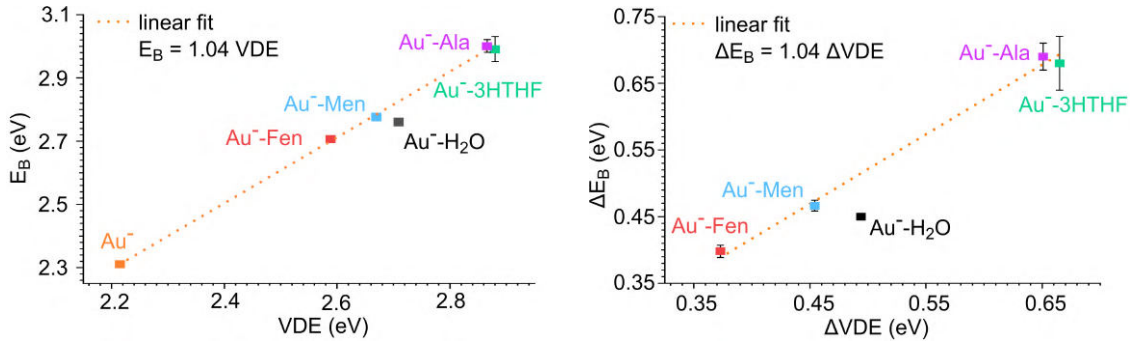

Fig. 4.5.1.: (a) Experimental electron binding energy (E_B) over the calculated electron binding energy (VDE) of the most stable structure and (b) the corresponding shifts ΔE_B over ΔVDE. A linear fit with slope 1.04 (orange dotted line) shows in both cases how the experimental energies are underestimated by the calculated ones. The experimental values for Au^--H_2O are taken from Zheng *et al.* [146] while the VDE is calculated with B3LYP-D3/aug-cc-pVTZ-PP.

introduced in equation 4.3.1 of section 4.3.1 is applied. All concerned energies, VDE of Au^- and Au^--M as well as the dissociation energies for Au^--M and Au-M have to compensate each other to close the Born-Haber cycle: $\mathrm{VDE}(Au^-) + D_0 - \mathrm{VDE}(Au^-\text{-M}) - D_n^* = 0$. Instead of D_n, D_n^* has to be chosen to close properly the cycle since the VDE energy assumes detachment without relaxation into the neutral ground state[5]. The compensation of energies and closing of the Born-Haber cycle can exemplary be done with the most stable isomers. In general, the excited dissociation energy of the

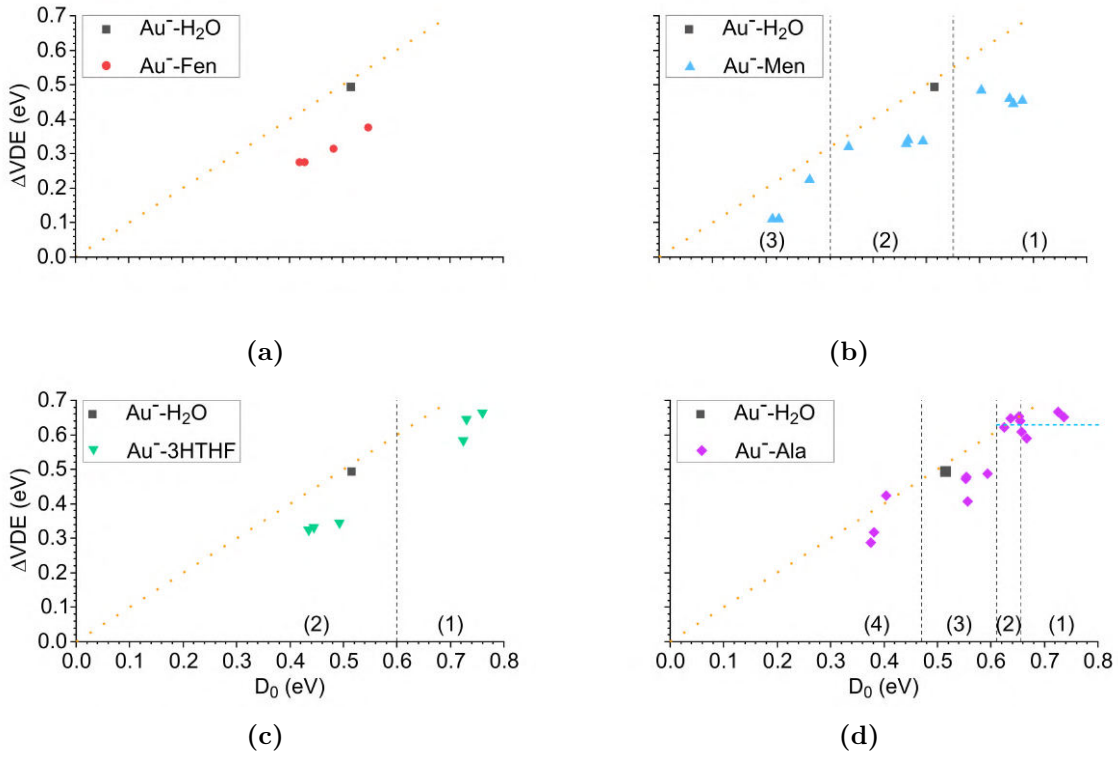

Fig. 4.5.2.: ΔVDE vs dissociation energy D_0. If the dissociation energy of the neutral complex is negligible, the points would follow the orange dotted line with slope of 1 (Born-Haber cycle). Vertically black dashed lines are set arbitrarily to separate the different isomer groups. Group (1) and (2) of Au^--Ala are further subdivided with an horizontal blue dashed line above which isomers show $Au^- \cdots$H-N. (b) and (d) are related to figure 4.4.14 since ΔVDE and VDE as well as D_0 and E_0 are only shifted by system specific constants.

neutral D_n^* is a quite small value but non-zero. Hence, D_0 alone can not compensate completely the VDE shift $\Delta\mathrm{VDE} = \mathrm{VDE}(Au^-) - \mathrm{VDE}(Au^-\text{-M})$. Figure 4.5.2 illustrates this difference and relationship between D_0 and ΔVDE. Approximately, large shifts lead to high D_0 but are by a value of D_n^* below the dissociation energy (or being by a value of D_n^* below the orange dotted line indicating the line of equality). In conclusion, the assumption made in section 4.3.1 about the dissociation energy of the neutral being weak

[5]The cycle can also be closed without exchanging D_n with D_n^* but then ADE instead of VDE has to be taken.

and maybe even negligible does not quite fit. Nevertheless, figure 4.5.2 shows clearly that larger D_0 also lead to larger ΔVDE, which validates the statement of section 4.3.1 that the most stable isomers lead to the largest shifts. Since the calculations matches pretty well with the experimental values (figure 4.5.1), the same statements can probably made for the experimental values even if not all values of the Born-Haber cycle are experimentally measured.

4.5.2. The Peak ν_X in Au^--3HTHF and Au^--Ala

In the spectra of Au^--3HTHF and Au^--Ala a peak at 3.42 and 3.43 eV is visible, respectively. The other two complexes do not reveal such a peak. This peak was already discussed in the experimental section 4.3.1.3 and it is assumed that it could be a O-H stretch vibration, which motivated the label ν_X. Here, this assumption is supported by DFT calculations:

A similar peak is observed for Au^--H_2O at around 3900 cm^{-1} (0.49 eV) [146]. A test calculation for Au^--H_2O gives a scaled[6] calculated frequency of around 3700 cm^{-1} for the water stretch vibration, which is in line with literature values and supports the use of the here applied DFT method and basis set.

For Au^--3HTHF and Au^--Ala, the peaks are higher in energy to the X transition by 0.43 eV in both cases. This corresponds to a transition of 3470 $\pm$ 330 cm^{-1} for Au^--3HTHF and 3470 $\pm$ 250 cm^{-1} for Au^--Ala above the ground states of these complexes.

The scaled calculated frequencies (in table 4.4.5) deviate around 200 cm^{-1} from the experimental value and fall all within the confidence area of the experimental value indicating a relatively good match to the O-H stretch vibration in Au^--3HTHF and Au^--Ala. For Au^--Ala, the asymmetric stretch vibration of N-H also fits pretty well and could be another possibility for the ν_X peak. A Franck-Condon simulation is not conducted but according to the harmonic frequency calculations from the gaussian calculations the O-H vibration should be more probable.

4.5.3. Peak A and Molecular Orbitals

Examining the molecular orbitals can provide information to compare the binding energy of peak A to DFT calculations as well as give further insight into the observed anisotropy of photodetachment. The molecular orbitals for the most stable Au^--M are shown in figure 4.5.3 for HOMO and in figure 4.5.4 for HOMO-1. The HOMO and HOMO-1 of all Au^--M are dominated by the $6s$ and $5d$ orbital of Au^-, respectively. However, they are deformed slightly in the complex due to the different (and mostly) p type atomic orbitals of the molecule.

Orbital energies are extracted with Multiwfn after an orbital composition analysis (table 4.5.1). The detachment energy of the excited peak A is then estimated with Koopmans' theorem [196] given by

$$\mathrm{VDE}(A) = \mathrm{VDE}(X) + (E_{\mathrm{HOMO}} - E_{\mathrm{HOMO-1}}) \tag{4.5.3}$$

[6] scaling factor 0.9636 from [195]

Table 4.5.1.: Orbital energies and their difference to the corresponding orbital of Au^- Δ for the most stable Au^--M are given in eV. Orbital composition shows only contributions to the orbital, which are bigger than 0.5%. In all cases, only Au shows a contribution of greater than 0.5%.

System	Orbital	orbital energy (eV)	Δ (eV)	orbital composition (%)
Au^-	HOMO	-0.04		
	HOMO-1	-1.18		
Au^--Fen	HOMO	-0.58	0.54	Au, 6s, 99.1
	HOMO-1	-1.77	0.59	Au, 5d, 99.9
Au^--Men	HOMO	-0.72	0.68	Au, 6s, 98.7
	HOMO-1	-1.96	0.77	Au, 5d, 100.0
Au^--3HTHF	HOMO	-0.77	0.73	Au, 6s, 98.3
	HOMO-1	-1.93	0.75	Au, 5d, 99.7
Au^--Ala	HOMO	-0.80	0.76	Au, 6s, 98.2
	HOMO-1	-1.99	0.81	Au, 5d, 100.0

Table 4.5.2.: Experimental (E_B) and calculated (VDE) energies from the most stable complexes compared to each other. VDE(A) is calculated with the orbital energies from table 4.5.1 and Koopmans' theorem.

System	E_B(X) (eV)	VDE(X) (eV)	E_B(A) (eV)	VDE(A) (eV)
Au^-	2.309	2.215	3.45	3.3603
Au^--Fen	2.707±0.009	2.590	3.93±0.01	3.7789
Au^--Men	2.775±0.008	2.669	4.05±0.03	3.9055
Au^--3HTHF	2.99±0.04	2.880	4.22±0.04	4.0450
Au^--Ala	3.00±0.02	2.866	4.22 ±0.02	4.0522

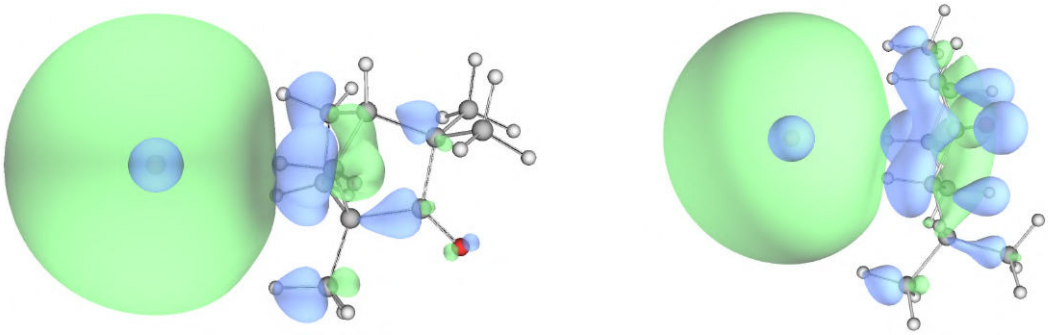

(a) HOMO of F1

(b) HOMO of M1.1

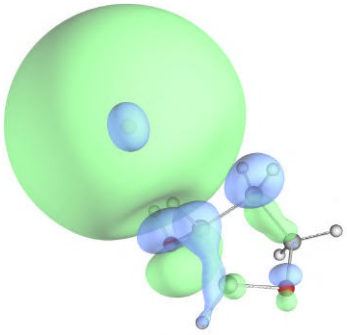

(c) HOMO of H1.1

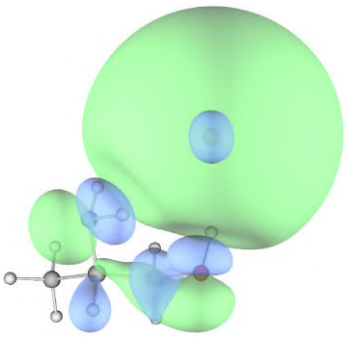

(d) HOMO of A1.1

Fig. 4.5.3.: HOMO of most stable Au^--M. The molecular orbitals are created with the program Multiwfn. Blue and green refer to positive and negative regions. The isosurface value is 0.01 for all figures. The *s* orbital of Au^- is deformed slightly by molecular orbitals.

with VDE(A) being the estimated detachment energy of A, VDE(X) the already determined VDE of transition X and E_{HOMO} as well as $E_{\text{HOMO-1}}$ being the orbital energies given in table 4.5.1. The results are summarized in table 4.5.2.

In all cases, the calculated energy is lower than the experimental evaluated binding energy. For the X transitions this was already determined before but not in comparison to the excited state A. Au^- shows for X and A the same deviation of 0.9 eV. The deviation in the X transition for the gold complexes ranges from around 0.11 to 0.13 eV, while a stronger deviation of 0.14 - 0.17 eV is observed in A. Such different deviations can be expected from Koopmans' theorem since it assumes unaltered orbitals (no reorientation) as well as identical relativistic energies (only relevant for inner electrons) and electron correlation energies between (an)ion and molecule [197]. Especially the assumption of identical correlation energies contributes to the different deviations of X and A since this energy is not only different in ion and molecule but can also be different between states of the ion/molecule [197]. However, the deviations from the experimental values are still relatively low validating the use of Koopmans' theorem for these gold complexes.

In the experiment, a greater shift in binding energy is observed for the A peak than for the X peak in comparison to the Au^- peaks. This shift is observed in other works as well (e.g [127]) but no satisfying explanation has been provided. Given what has been determined about the complexes herein, an explanation will be attempted: If electrons

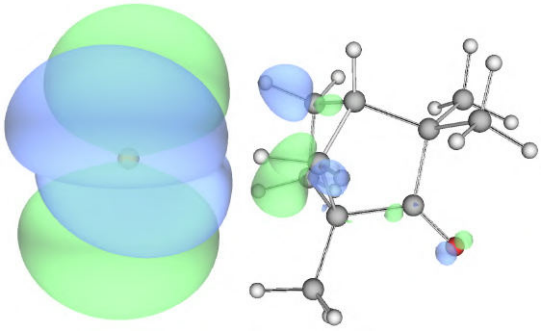

(a) HOMO-1 of F1

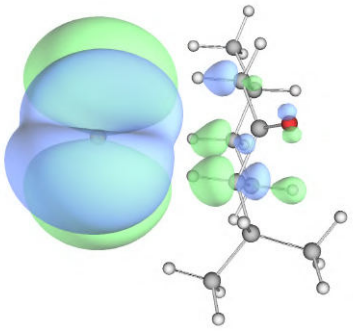

(b) HOMO-1 of M1.1

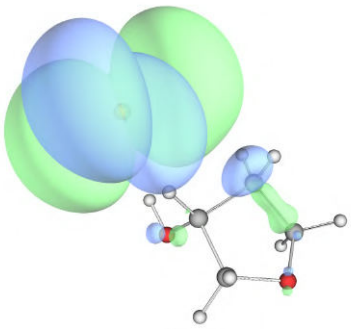

(c) HOMO-1 of H1.1

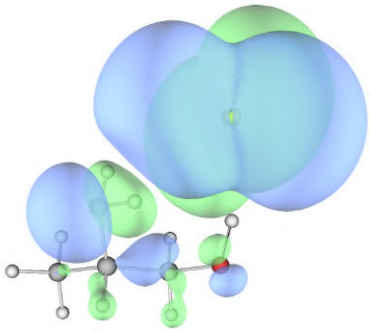

(d) HOMO-1 of A1.1

Fig. 4.5.4.: HOMO-1 of most stable Au^--M. Colors are defined like in figure 4.5.3. The isosurface value is 0.004. The d orbital of Au^- is deformed slightly by molecular orbitals.

are shared upon complexation, the energy of the HOMO is lowered, which leads to a more diffuse $6s$ orbital. Hence, deshielding the $5d$ orbital, which lowers the HOMO-1 orbital energy and blue shifts peak A. This is supported by the calculated HOMO and HOMO-1 orbital energies in table 4.5.1.

A more qualitative way to analyze the individual orbital contributions to the whole system is an orbital composition analysis (table 4.5.1). Only orbitals with a contribution of bigger than 0.5% are shown, which is only fulfilled by the gold atom. In all cases, the contribution of gold is between 98 and 100% emphasizing the dominance of the gold orbital over the whole system. Hence, the excess electron will mainly originate from Au^- instead of the molecule, which is consistent with the results in the discussion about the charge transfer.

Considering the results of the anisotropy parameter from section 4.3.2, the orbitals match to what one would expect from the experimental β values for the X transition. β is around 1 and 2, which indicated to a system still dominated by the $6s$ orbital of Au^- but being disturbed by the molecule. This is affirmed by the orbital image in figure 4.5.3, which shows the $6s$ orbital of Au^- deformed by the molecular orbitals.

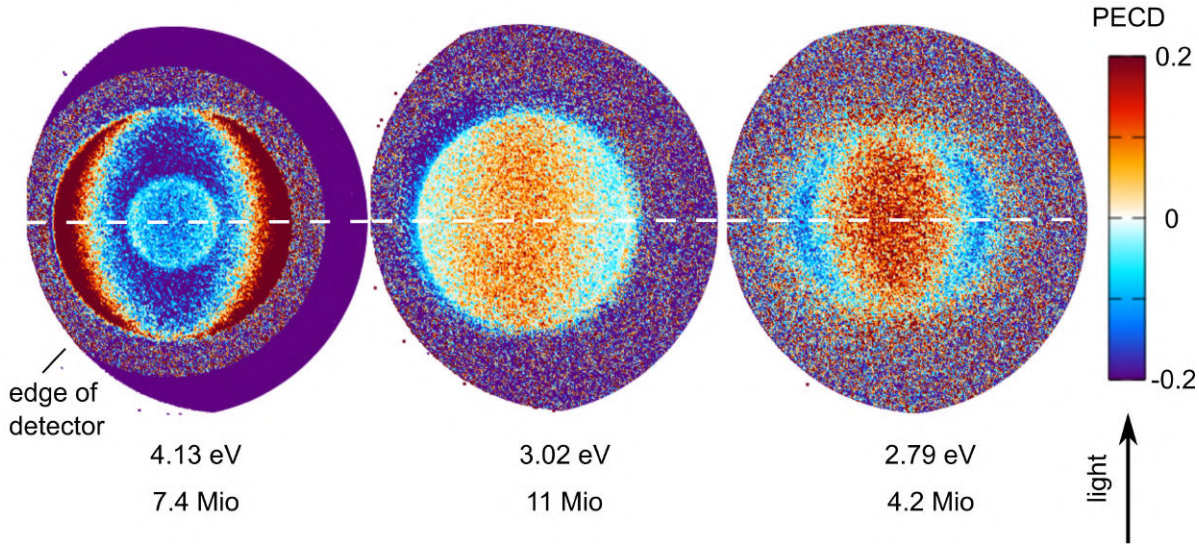

Fig. 4.6.1.: PECD PADs of Au^--Fen (not scaled). Images are recorded close to the edge of the detector (clipped circle on the left of each image). Below the PADs are the photon energy and electron counts per polarization. The light propagates from down to up. The forward and backward half are separated by a dashed line.

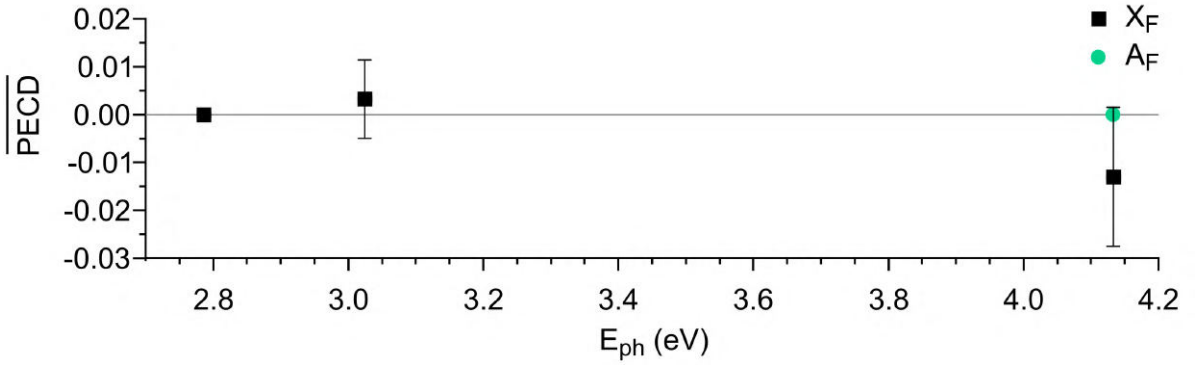

Fig. 4.6.2.: Mean PECD of Au^--Fen. LCP and RCP spectra were scaled before PECD values are calculated.

4.6. Photoelectron Circular Dichroism

The results and analysis of the previous section have confirmed the interaction and influence between Au^- and four chiral molecules, but also revealed that the probed electron mostly retains the character of an electron from atomic Au^-. The question if this interaction is enough to elicit a chiral response (i.e. PECD asymmetry) in the photodetachment is answered here.

The PECD results for Au^--M can be found in figures 4.6.1 - 4.6.8 containing the (unscaled) PECD PADs and mean PECD values, which where obtained by scaling the RCP PES according to table A.16 before PECD evaluation (section 3.2.6). The mean

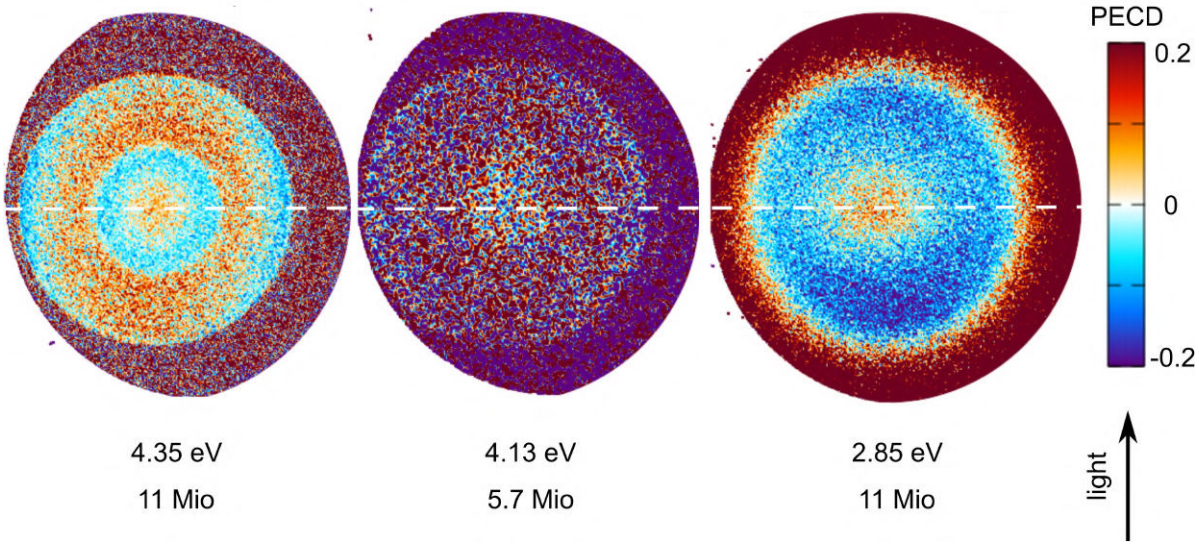

Fig. 4.6.3.: PECD PADs of Au^--Men. Below the PADs are the photon energy and electron counts per polarization. The light propagates from down to up. The forward and backward half are separated by a dashed line.

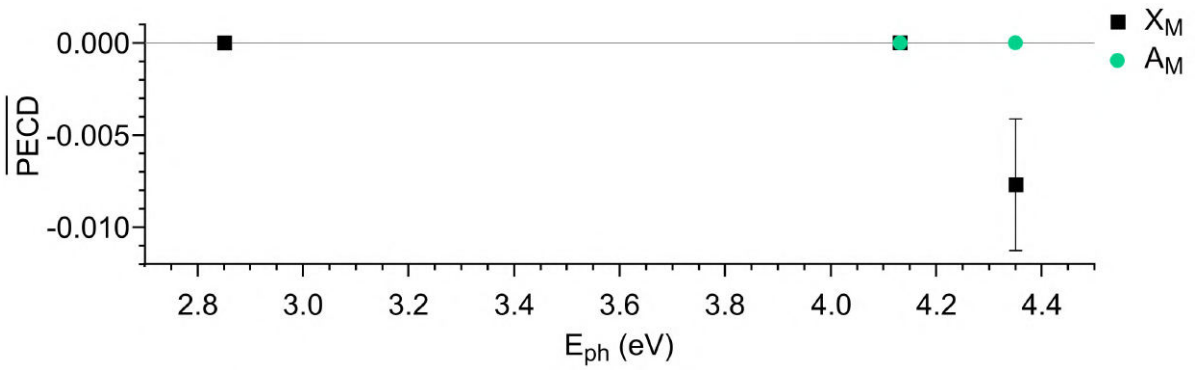

Fig. 4.6.4.: Mean PECD of Au^--Men. LCP and RCP spectra were scaled before PECD values are calculated.

PECD value is evaluated over the FWHM of all peaks. Measurements for all Au^--M are performed with quarter waveplates (4.6.1 - 4.6.7(up) and 4.6.8a). For Au^--Ala, a measurement with the photoelastic modulator, with shot-to-shot polarization switching were additionally performed to assure that the null-PECD result is not a consequence of the quarter waveplates (figures 4.6.7(down) and 4.6.8b).

Except for the measurements with the PEM and the left PAD in figure 4.6.5, PADs show a weird red-blue (positive and negative PECD values) pattern: It seems like the colors are accumulating at positions of transitions or background, e.g. first PAD in figure 4.6.1 for Au^--Fen shows how red (positive PECD values) accumulates where the transition is located while the region between the transitions is blue. If the PAD is fully reconstructed (all four quadrants considered), then the corresponding PES looks like the black curves in figure 3.2.38 of section 3.2.6. Here, the LCP-PES shows clearly a higher

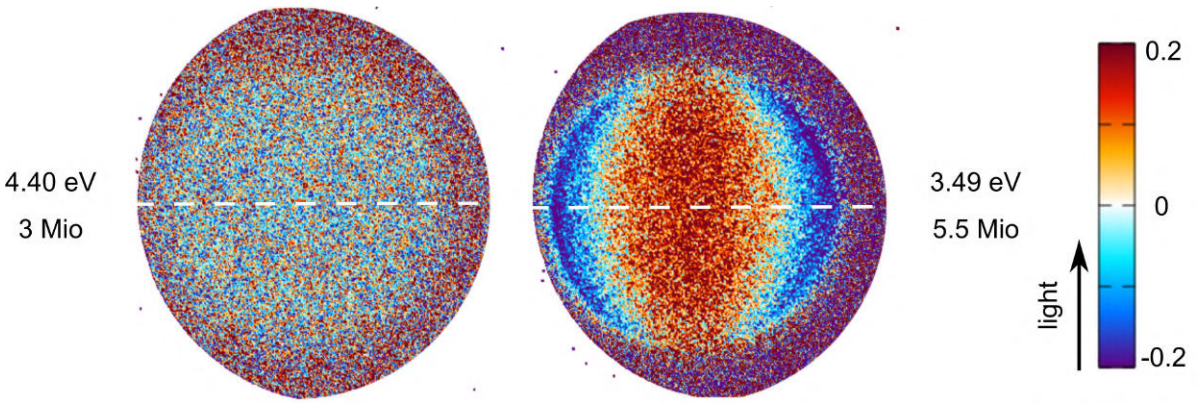

Fig. 4.6.5.: PECD PADs of Au^--3HTHF. Next to the PADs the photon energy and electron counts per polarization are given. The light propagates from down to up. The forward and backward half are separated by a dashed line.

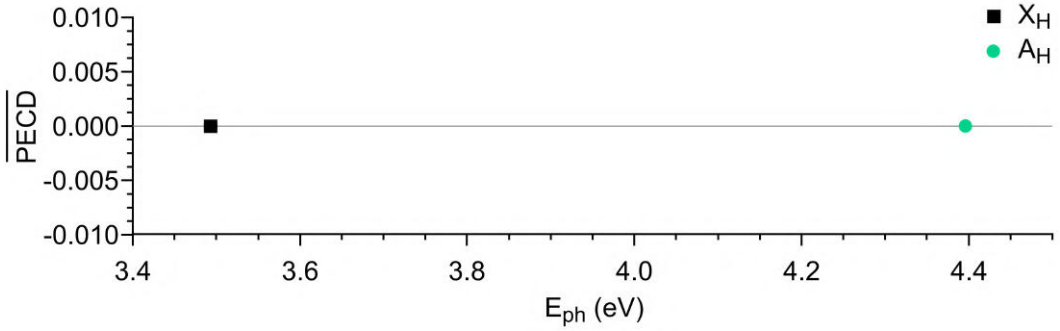

Fig. 4.6.6.: Mean PECD of Au^--3HTHF. LCP and RCP spectra were scaled before PECD values are calculated.

intensity in the main transition (corresponding to red in the PAD) but less signal in the region between the transitions (around 3.0 - 3.8 eV, blue region in PAD) in comparison to the RCP-PAD. Since both images have the same electron counts, the electrons seem to be differently distributed indicating to a worse signal-to-noise ratio in the RCP-PAD in comparison to the LCP-PAD. This is supported by the needed loops, which is clearly higher for the RCP-PAD than for the LCP-PAD. Since the PADs recorded with QWPs are measured in series and not alternatively, and signal is optimized with respect to the signal intensity, different experimental conditions existed probably during the measurement of the LCP and RCP-PAD (long term effect). From the view of measurement, alternatively switching the polarization and recording the PADs avoids this since both PADs are equally affected by changed experimental conditions as can be seen in figure 4.6.7 (compare the four upper PADs with the four lower PADs). This is also reflected in the scaling factors, which are generally closer to 1 than for the QWP measurements (table A.16). However, the PEM was not available during the measurements shown in figures 4.6.1 - 4.6.7(up) and scaling the RCP-PAD according to table A.16 is used.

PADs of Au^--Ala (figure 4.6.7 (up)) look a bit different, like the colors accumulating in different quadrants (left image in third row of figure 4.6.7) or still accumulating in the transition/background manner like above but the transition ring is "closing" in the upper half of the image (right image in third row and left image of fourth row of figure 4.6.7). If the color accumulation is related to the transition, then this indicates to an incorrect anisotropy (β) since the ring should be symmetric around the Fw-Bw axis (white dashed line). Despite checking the polarization before PECD measurements, the polarization seems not to be ideal in these kind of images or changed during the measurement. A better approach would be to constantly monitor the quality of polarization to recognize such changes in time like it is done in the measurements with the PEM.

Overall, the data does not indicate that a (real) PECD signal was measured for any of the Au^-- M complexes. Most mean PECD values are either set to zero since forward and backward direction give the same sign or are zero within the SE. Only two points, namely Au^--Men at $E_{ph} = 4.35$ eV (figure 4.6.4) and Au^--Ala at $E_{ph} = 3.02$ eV (figure 4.6.8a) seem to reveal a PECD asymmetry but are on closer inspection not real:

For Au^--Men the determined PECD signal is rather small at -0.8% and the SE is small enough to not reach zero. However, looking at the corresponding PAD image in figure 4.6.3, the expected PECD pattern is not visible (even if the PAD is scaled like it is done before PECD value evaluation). The SE seems not to be an adequate error description for this measurement.

Au^--Ala gives seemingly a mean PECD value of around 3% at $E_{ph} = 3.02$ eV but shows not the typical PECD pattern in the PAD (left PAD in second row of figure 4.6.7): Blue is predominantly on one side but as no corresponding red part on the other side. Furthermore, the red part is not contained within one image half but spills over to the other half. This could be due to wrong/changed polarization. Additionally, the measurement was repeated for smaller VMI-repeller voltages to focus on the corresponding region (right PAD in second row of figure 4.6.7 and of figure 4.6.8a) and also with the PEM (right PAD in the last row of figure 4.6.7 and 4.6.8b) but the earlier PAD pattern and the PECD signal could not be reproduced, probably because polarizations are set more correctly in the latter cases.

While no PECD asymmetry could be measured for neither quarter waveplates nor the photoelastic modulator, the measurements involving the PEM result in better null-PECD PAD, meaning they are distributed like one would expect for a noisy PAD. Hence, using the PEM seems to be more promising for a PECD measurement since non-PECD-asymmetries are not contained in the PAD and will not overlapping with any real PECD signal.

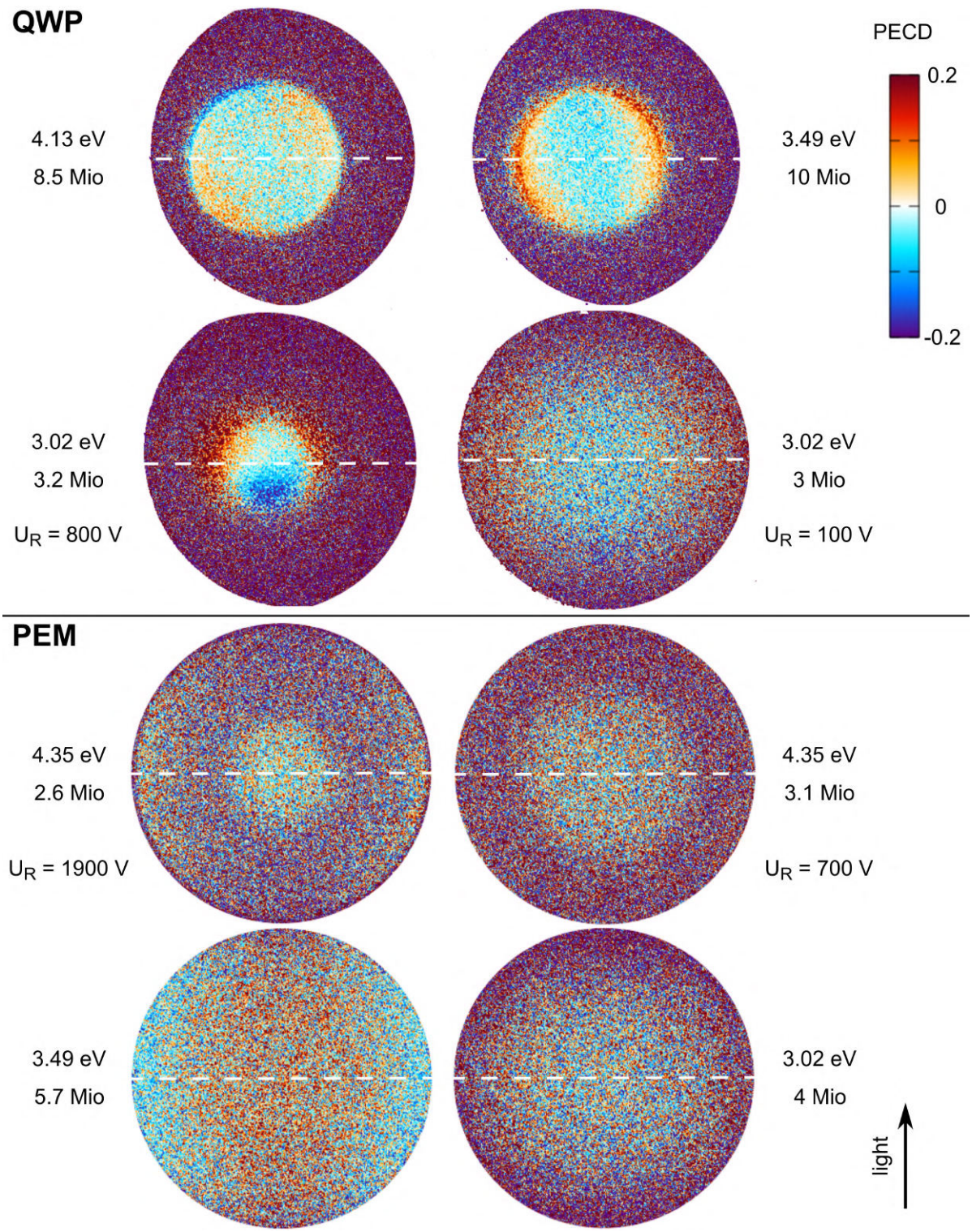

Fig. 4.6.7.: PECD PADs of Au^--Ala recorded with QWPs (up) and PEM (down). Next to the PADs the photon energy and electron counts per polarization are given. The light propagates from down to up. The forward and backward half are separated by a dashed line. U_R is the used repeller voltage of the VMI spectrometer.

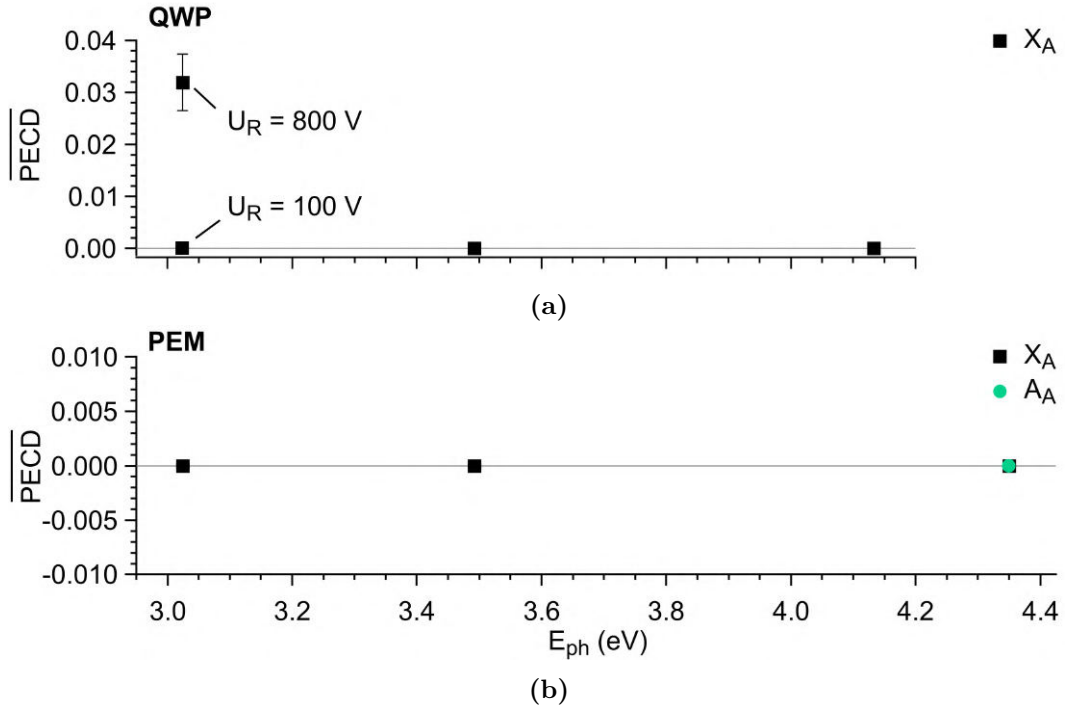

Fig. 4.6.8.: Mean PECD of Au^--Ala measured with (a) QWP and (b) PEM. LCP and RCP spectra were scaled before PECD values are calculated. U_R is the repeller voltage of the VMI spectrometer.

Possible Reasons for the null-PECD Result

The null-PECD results for Au^--M elicit the question of why no PECD effect is observed despite having a chiral system. Several reasons can be considered for potential explanation:

1. PECD signal under the detection limit of this setup
2. Unlucky selection of chiral molecules and kinetic/photon energy
3. The photodetached electron does not feel the chiral potential of the molecule (enough)
4. Contributions by too many isomers and/or vibrational states with different PECD asymmetries, which superimpose and cancel each other out

The detection limit depends from the noise or background level, which can depend on several factors like different noise from light (dependent on photon energy and alignment) or molecular beam. The amount of electron counts also plays an important role since more electrons mean a smaller statistical error. Here, 2.6 - 11 Mio electrons per polarization are recorded but it was not known if this is sufficient to measure the PECD signal at that time. As will be shown in section 5.4.2 with $[Ind\text{-}H]^-$, the smallest measured PECD signal still being over the standard error (SE) is around 1% and required 4 Mio electron counts per polarization. With 40 Mio electron counts per polarization a PECD asymmetry of around 0.5% could be measured. If the PECD values for gold complex are below 1% (or 0.5%) than it is excessively difficult to measure.

Another instrumental limitation are the artificial asymmetries in the PECD measurements with QWPs, which are probably caused by long term fluctuations or unstable anion signal. This could be clearly avoided with a shot-to-shot measurement with the PEM. However, even with the PEM a PECD signal could not be measured.

Every chiral system should show a PECD asymmetry but not every chiral molecule will show a strong one. Additionally, since the PECD asymmetry is dependent on the kinetic (or photon) energy, the PECD effect can become quite small. An unlucky combination of a bad chiral system and kinetic energy could lead to a non-detectable PECD effect.

Of course, chiral molecules were chosen such that a (large or) measurable PECD asymmetry (or a chiral response in the case of Men) exists in the neutral case too avoid such an scenario. Especially fenchone is known to have a strong PECD asymmetry of around 8 - 16% for valence shell [28, 29] in the neutral case. However, the situation might change to the worse for the anionic system or within the gold complex.

Regarding the kinetic energy, low kinetic energy electrons are known to result in PECD signals while (too) high kinetic energy electrons do not have time to probe the chiral molecule and result in no PECD asymmetry. In the neutral case the limit was around 10 or 20 eV (section 1.2). However, for the anion case the assumption of having only short-range interactions guided to the conclusion that even slower electron are needed for PECD signals in anions to ensure enough interaction time. However, what slow means was not known when the Au^--M measurements started. PECD measurements were

conducted for 0.1 eV $< E_{\mathrm{kin}} <$ 1.6 eV to stay (hopefully) in the slow regime necessary for anion PECD signals.

Other reasons for the electron not to feel the chiral environment of the molecule apart from being too fast could be the distance of the electron to this chiral environment or the strength of localization on the achiral part of the system: The DFT calculations of Au^--Fen and Au^--Men give distances of around 0.3 nm between the gold anion and the hydrogens of the chiral molecule. If the short-range interactions necessary for PECD effect are already negligible at this distance, the electron will not feel the chirality of the molecule. The distance between gold anion and molecule can become shorter for molecules with stronger H-bond donating functional groups, as seen for Au^--3HTHF and Au^--Ala. These complexes had $Au^- \cdots$H-O bond distances of 0.23 and 0.25 nm but these distances might not suffice for the short range interactions. However, the hydrogen bond length to Au^- corresponding to the distance of the detached electron to the chiral molecular is just an approximation since neither the extension of the atom nor the uncertainty in position of the electron is considered.

The localization of the negative charge stays mainly with the gold (0.9 e). However, a measurable influence of the chiral molecule is happening since the anisotropy parameter of the gold complexes is not 2, which would be the case for the pure gold anion. The localization could still be strong enough for the electron to not feel the chiral environment of the molecule effectively and hence does not produce a detectable PECD asymmetry.

With DFT calculations from section 4.4 several structures for the gold complex are revealed. Such structures are often energetically close and one can assume that several conformers are produced in the laser ablation source. Unfortunately, for PECD measurements, this might be not ideal as the PECD effect is known to be sensitive to even slight structural changes. PECD asymmetries can be different for all conformers and even cancel each other out. (Of course, the opposite effect of enhancing each other is also possible.) Hence, adding Au^- to the chiral molecule could have been not ideal, since it leads to many isomers due to the various possible binding positions, e.g. for Au^--Fen four isomers are calculated despite having just one molecular isomer (Fen).

A similar problem is on hand if vibrational states are considered, since – beside conformer sensitivity – PECD asymmetries can feature different values for different vibrational states. Unfortunately, the experiment is neither able to cool down the complexes efficiently to reduce the amount of isomers and vibrational states nor can it resolve the isomers and vibrational states. Therefore, target molecules that can assume many different conformations and are expected to have significant thermal population are most likely not the most ideal targets for initial anion PECD studies.

4.7. Summary for Gold Complexes

Gold complexes (Au^--M) were the first target systems for anion PECD experiments in this project. The idea was to complex a chiral molecule with an electron source (Au^-) such that the chiral molecule remains (mainly) unaltered and that leads to a chiral response in the photodetachment of the electron from the Au^--M. Apart from PECD

measurements, gold complexes could be used to make statements about (unconventional) hydrogen bonding.

Four different gold complexes, namely Au^--Fen, Au^--Men, Au^--3HTHF and Au^--Ala are produced in gas phase. PES (with linear polarized light) and DFT calculations revealed the interaction between Au^- and the chiral molecule: Blue shifts and anisotropy parameter indicated to an influence of the chiral molecule, however, the photodetached electron remained mainly controlled by the unchiral part of the complex, the Au^-.

Many isomers of the Au^--M are calculated with DFT and could be created in the experiment. They are used to characterize the interaction as hydrogen bonding and can provide quantitative predictions. Regarding hydrogen bonding, even $Au^- \cdots$ H-C fulfills the IUPAC requirements for hydrogen bonding and can be called as such.

Unfortunately, no PECD signal could be seen for the gold complexes. While many possible reasons are discussed, it is not clear what the main cause for the null-PECD signal could be since these measurements started before any other (published) anion PECD studies on this topic. At the start, there was no guiding principle and one had to find the needle in the hay stack: What are good chiral systems/kinetic energies? Is the detection limit of the experimental setup sufficient? How many electrons should be recorded? Is a PECD effect for anions even possible?

Due to the various problems emerging from gold complexes for the PECD effect (e.g. electron too strongly localized), another system – without any additionally attached anion – should be chosen. Deprotonated chiral molecules are a possible choice: Here, the charge is directly located in the molecule and should sense the chirality of the molecule much better. Of course, due to structure sensitivity of PECD signals, it should have a distinctive deprotonation side. Hence, fenchone and menthone are not suited since deprotonation is (almost) equally probable at every position. On the other hand, chiral molecules with hydroxy groups are ideal since deprotonation happens most likely at only one position: the hydroxy group.

5. Deprotonated Chiral Species[1]

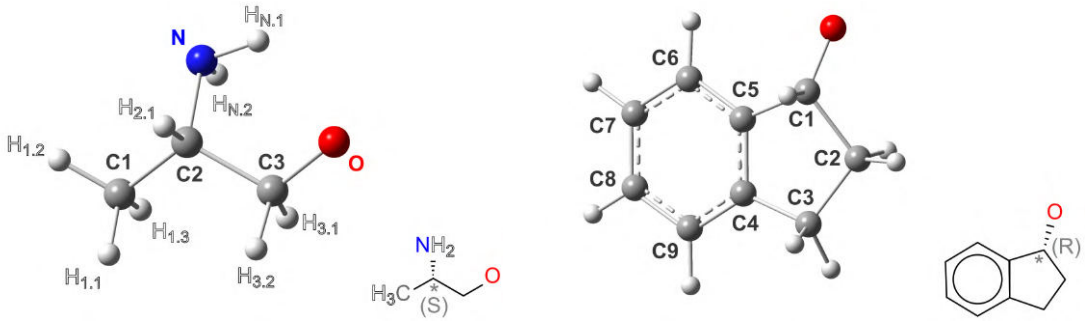

(a) Ala-H **(b)** Ind-H

Fig. 5.0.1.: 3D structures of deprotonated alaninol $[Ala\text{-}H]^-$ and deprotonated 1-indanol $[Ind\text{-}H]^-$ with corresponding skeletal structures and labels.

The second approach pursued for the creation of chiral anions is the deprotonation of chiral molecules. In contrast to the gold complexes, the chiral molecule is altered due to the removal of the hydrogen but detachment happens now directly in the chiral molecule. This could enhance the electron's sensing of the chiral field. Here, $[Ala\text{-}H]^-$ and $[Ind\text{-}H]^-$, which are deprotonated at the hydroxy group are of main interest (figure 5.0.1).

However, not only the chiral system was changed, also several experimental modifications were undertaken. The source was changed to a plasma entrainment source to adapt to the new kind of chiral anions. Furthermore, the software controlling the experiment was updated from KouDa to SDaq since new hardware components like new computers and a new VMI camera were integrated. Also, all polarisation optics changed the positions such that the light does not need to pass through further prisms after the PEM and only a window separates the PEM and the VMI interaction zone.

In addition, some improvements to the VMI system and VMI images were tested like the gold platting of the stainless steel VMI plates to rise the working function and hence minimizing the electron background/noise in the UV regime. Unfortunately, this was not successful and it is assumed that nickel was used during the gold plating process as

[1]Results of $[Ind\text{-}H]^-$ are, to a large part, published in the article J. Triptow, A. Fielicke, G. Meijer, M.Green, "Imaging Photoelectron Circular Dichroism in the Detachment of Mass-Selected Chiral Anions", 2022, in: Angewandte Chemie International Edition, Wiley Online Library, in press DOI: 10.1002/anie.202212020

intermediate "glue" layer. A material, which is ferromagnetic and is unwanted in VMI systems. In the end, new VMI plates made out of molybdenum were installed.

Two einzel lenses were added, one before and one after the extraction region of the ToF mass spectrometer to reduce the waist of the anion beam and also to improve the resolution of VMI measurements but could not give noticeable improvement. One einzel lens replaces the deflection plates of the ToF-MS and now are only used for deflection.

Most of the changes happened during the measurements with alaninol. There are for example mass- and photoelectron spectra of $[Ala\text{-}H]^-$ created with the laser ablation and plasma entrainment source. Deprotonated 1-indanol was used when all experimental modifications were finalized.

5.1. Mass Spectra

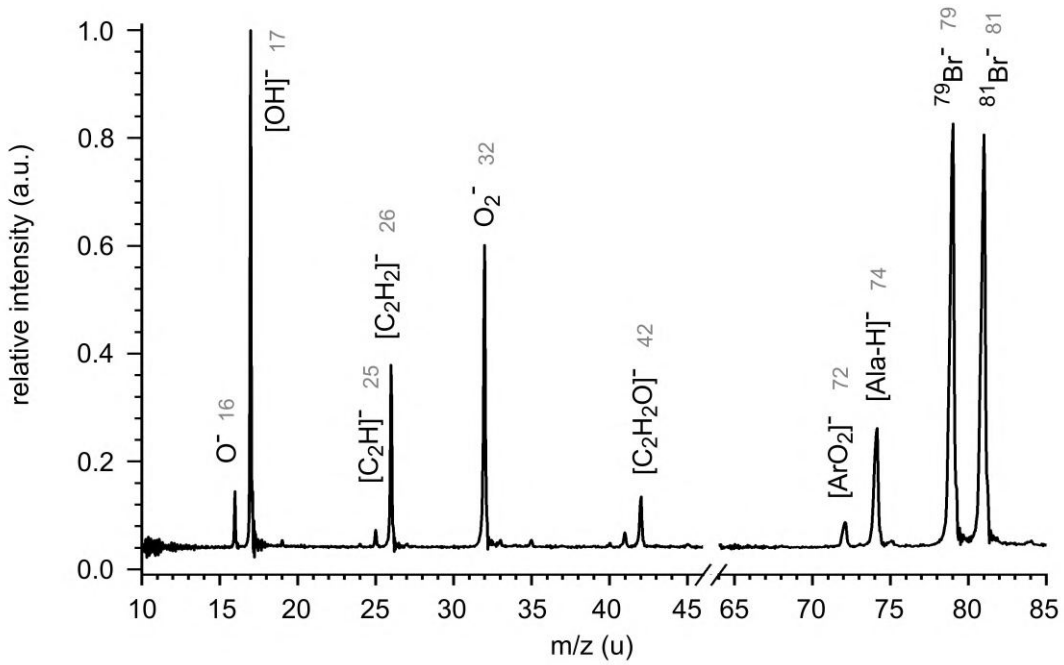

Fig. 5.1.1.: Mass spectrum obtained with plasma entrainment source with the target molecule $[Ala\text{-}H]^-$ at m/z 74. Also, OH^-, O^-, O_2^- and $[ArO_2]^-$ are assigned, which are typical for this kind of source (section 3.2.1.2). Isotopes of Br^- at m/z 79 and 81 originate from bromobenzene and serve for the calibration of subsequent VMI measurements. The break in the m/z axis marks strong electronic noise originating from high HV switches that has been removed from the picture.

Mass spectra for $[Ala\text{-}H]^-$ and $[Ind\text{-}H]^-$ created in the plasma entrainment source are presented in figure 5.1.1 and 5.1.2, respectively. Typical for the plasma entrainment source are the plasma products O^- at m/z 16 and OH^- at m/z 17. C_2H^- at m/z 25 visible in both mass spectra as well as other carbon-containing anions like $C_2H_2O^-$ in figure 5.1.1 probably stemming from sputtering carbonaceous deposits or from fragments

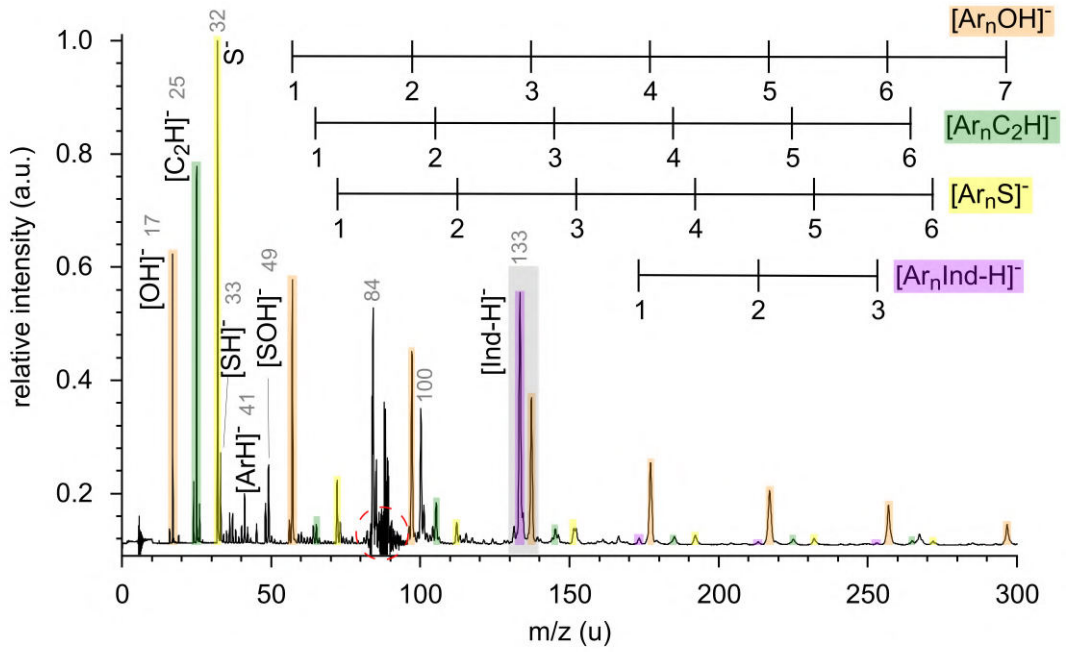

Fig. 5.1.2.: Mass spectrum obtained with plasma entrainment source using 1-indanol, showing $[\text{Ind-H}]^-$ at m/z 133 and corresponding clusters with Ar (purple). Also S^-, used for calibration, is visible at m/z 32 and its clusters with Ar (yellow). Typical plasma entrainment products like $[\text{Ar}_n\text{OH}]^-$ (orange) and $[\text{ArH}]^-$ can be found. Also, argon clusters of small carbon containing molecules (green) appear. The red dotted circle indicates noise produced by HV switches. The gray area is enlarged and shown in figure 5.1.3.

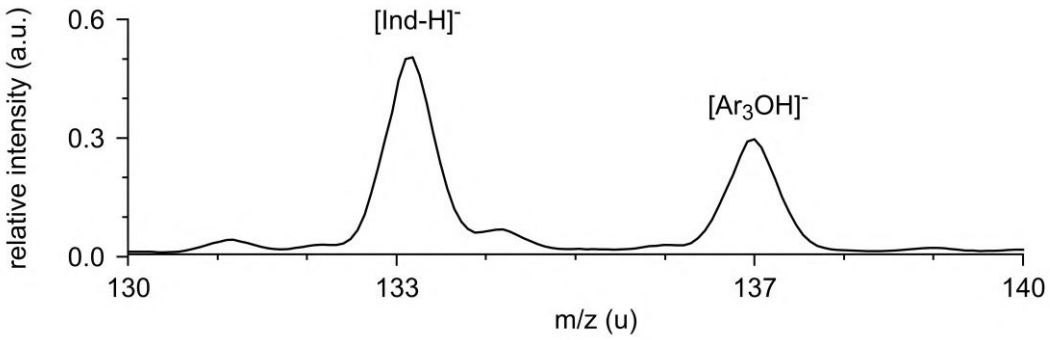

Fig. 5.1.3.: Enlarged part of the mass spectrum from figure 5.1.2 in the region around $[\text{Ind-H}]^-$ at m/z 133. The resolution for m/z 133 is about $m/\Delta m = 211$.

of the organic molecules. Furthermore, Ar complexes of the produced molecular anions can be detected (figure 5.1.2).

In the following experiments, Br^- (m/z 79 and 81 in figure 5.1.1) and S^- (m/z 32 in figure 5.1.2) are used to calibrate the kinetic energy scale of the VMI spectrometer. They are introduced via bromobenzene or OCS and can be confirmed by their respective isotopes and natural abundances, i.e. ^{79}Br and ^{81}Br with an abundance of 51% and 49%

as well as $^{34}S^-$ with 5%. This is especially important for S^- since O_2^- also appears at m/z 32. Another indicator for S^- is a peak at m/z 33, which is assigned to SH^- since $[O_2H]^-$ is unlikely. Additionally, S^- and Br^- can later be confirmed by anion PES.

At m/z 74 in figure 5.1.1 and m/z 133 in figure 5.1.2 (or 5.1.3) are the deprotonation products of alaninol and 1-indanol. m/z 133 only appears after heating the reservoir to around 100 °C, which corresponds to the sublimation temperature of 1-indanol and hence supports the assignment. In the case of 1-indanol, clustering with argon is also observed.

Figure 5.1.3 shows a cutout of figure 5.1.2 and covers an area of m/z 130 - 140, which includes $[Ind\text{-}H]^-$ at m/z 133 and $[Ar_3OH]^-$ at m/z 137. The resolution at m/z 133 is about $m/\Delta m = 211$, which is sufficient to separate the neighboring peaks and to ensure that only m/z 133 is probed by the laser.

5.2. Computational Considerations

5.2.1. Isomers

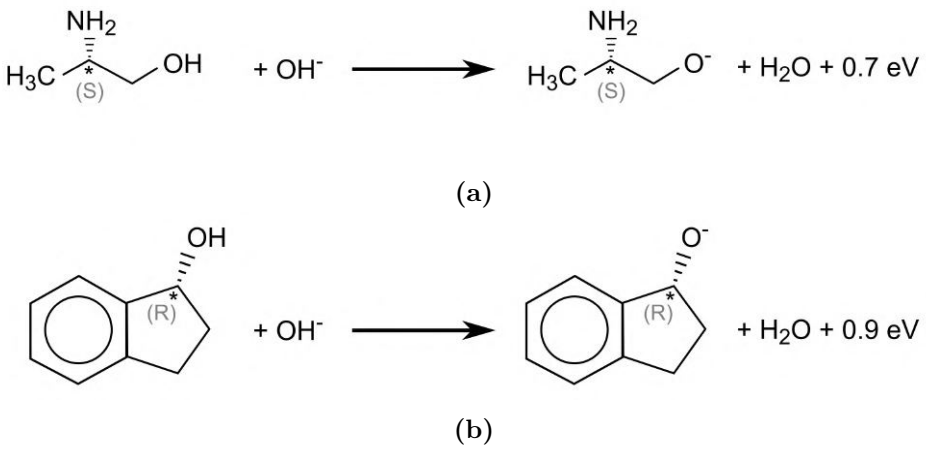

Fig. 5.2.1.: Deprotonation process of alaninol (a) and 1-indanol (b). The hydroxy group is deprotonated with OH^- forming the molecular anion, water as well as an excess energy of 0.7 eV for alaninol and 0.9 eV for 1-indanol. The excess energy is calculated with B3LYP-D3/aug-cc-pVTZ for the most stable conformer.

The conformeric landscape of neutral alaninol has been discussed before (figure 4.4.9 of section 4.4.1) and will be the basis for the DFT calculations of $[Ala\text{-}H]^-$. All molecular isomers of figure 4.4.9 are considered in the calculations but the results will mostly be presented for the most stable isomer since the results are similar (e.g. orbitals).

While for alaninol 25 isomers are predicted [75], only six conformers are found for 1-indanol. They can be separated into two groups based on the position of the C2 atom (figure 5.0.1b) relative to the ring plane and are called equatorial (eq) or axial (ax) position (figure 5.2.3). The eq and ax group each contain three conformers, which differ

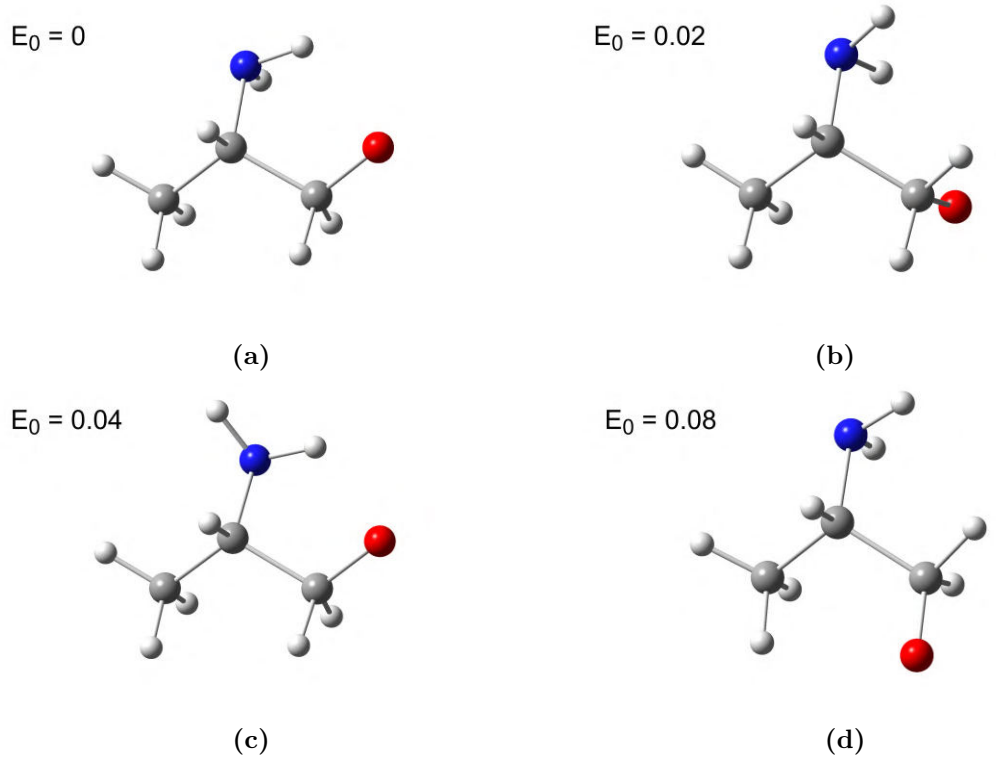

Fig. 5.2.2.: Four conformers of $[Ala\text{-}H]^-$: AH-1 (a), A-H2 (b), A-H3 (c), A-H4 (d) calculated with B3LYP-D3/aug-cc-pVTZ. The energies, E_0, are relative to the lowest energy conformer and given in eV. Arrangement and label are according to their relative energy.

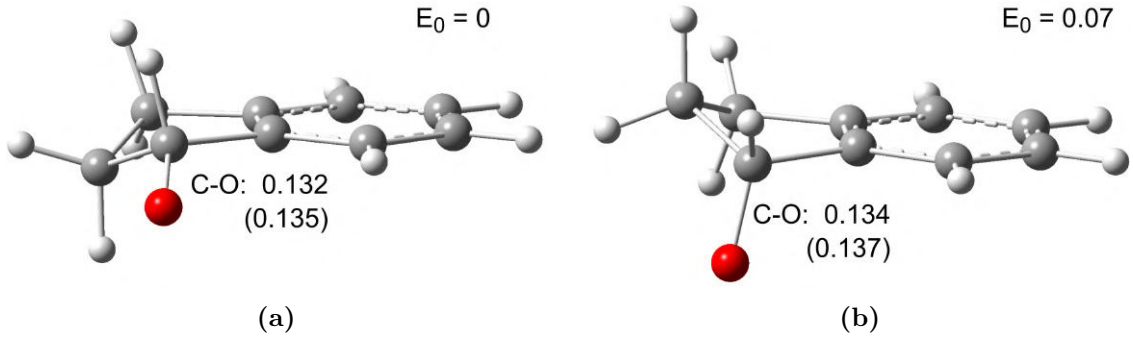

Fig. 5.2.3.: Two conformers of $[Ind\text{-}H]^-$ calculated with B3LYP-D3/aug-cc-pVTZ. (a) is the equatorial (eq.) and (b) is the axial (ax.) form. Distances of C-O are given in nm for $[Ind\text{-}H]^-$ and in brackets for the optimized neutral radical Ind-H. For comparison, the C-O bond lengths in the neutral 1-indanol conformers are 0.142 nm for eq and 0.144 nm for ax, respectively.

by the orientation of the H atom. In a supersonic expansion of Ar, however, only a single conformer (eq) has been detected [198, 199].

The deprotonation process with OH^- is shown in figure 5.2.1 for the loss of H^+ at the most acidic site, i.e. the OH group. Furthermore, water and an excess energy calculated to be around 0.7 eV for alaninol and 0.9 eV for 1-indanol (for the most stable conformer)

Table 5.2.1.: Isomers of $[Ala\text{-}H]^-$ obtained by deprotonation of the most stable conformer of neutral alaninol. Different deprotonation sites (dep. site) are used. The label correspond to figure 5.0.1a. Tautomers above the dashed line are energetically possible according to the excess energy of 0.7 eV for formation of the most stable tautomer (figure 5.2.1a).

dep. site	E_0 (eV)	VDE (eV)
H_O	0	2.080
$H_{N.1}$	0.478	1.670
$H_{N.2}$	0.484	1.774
$H_{1.1}$	1.172	0.950
$H_{1.2}$ and $H_{1.3}$	1.185	0.923
$H_{2.1}$	1.226	0.856
$H_{3.1}$	1.507	0.413
$H_{3.2}$	1.630	0.568

are formed. All isomeric anions with a smaller relative energy than the excess energy can be created as well. Next to the most stable isomer of $[Ind\text{-}H]^-$, the equatorial form, the axial configuration reappears since it is only ≈ 0.07 eV higher in energy (figure 5.2.3b).

After deprotonation and optimization four different conformers of $[Ala\text{-}H]^-$ are formed (figure 5.2.2) since A1.0 and A4.0 result into the same deprotonated structure, A-H1, which is the most stable conformer. The other three deprotonated conformers are energetically close to A-H1 (within 0.1 eV, figure 5.2.2) and may be formed during the deprotonation process, too. Probably, even more conformers for $[Ala\text{-}H]^-$ can be expected since only a subset of the 25 alaninol conformers is considered. If around three OH orientations per base structure are estimated, around eight conformers could survive after deprotonation (presupposed they fulfill the energy requirement set by the excess energy). For $[Ind\text{-}H]^-$, on the other hand, only two conformers are expected: eq. $[Ind\text{-}H]^-$ and ax. $[Ind\text{-}H]^-$, which should lead to a less complicated PES in comparison to $[Ala\text{-}H]^-$. The structures of the most stable isomers of $[Ind\text{-}H]^-$ and $[Ala\text{-}H]^-$ can be found in the appendix B.1.

5.2.2. Tautomers

Aside from deprotonation of the O-H group, deprotonation can also occur at other sites leading to tautomers. If the excess energy for deprotonation at the O-H group is considered (table 5.2.2), three more tautomers for $[Ala\text{-}H]^-$ and two for $[Ind\text{-}H]^-$ may be expected to be observable in the experiment. These tautomers have VDEs, which are at least 0.3 eV ($[Ala\text{-}H]^-$) or 1 eV ($[Ind\text{-}H]^-$) lower compared to the ground state isomer and hence should be easily differentiated in a photoelectron spectrum. To avoid confusion between the lowest isomer and tautomers, $[Ind(O)\text{-}H]^-$ is used to mark the deprotonation from the hydroxy group and $[Ind(C\mathit{i})\text{-}H]^-$ for deprotonation from the

Table 5.2.2.: Relative energies (E_0) and VDE's of tautomers formed by deprotonation of equatorial 1-indanol at different sites (dep. site). The atom labels correspond to figure 5.0.1b. H_O would be the hydrogen bonded to the oxygen (not shown in figure 5.0.1b). Tautomers above the dashed line are energetically possible according to the excess energy of 0.9 eV for formation of the most stable tautomer (figure 5.2.1b). C3 and C2 each hold two hydrogens, which lead to the same structure when deprotonated. * indicates the stereogenic center.

dep. site	E_0 (eV)	VDE (eV)
O	0	2.185
C3	0.466	1.047
C1*	0.603	0.949
C6	0.966	2.110
C2	1.001	1.122
C9	1.214	1.704
C8	1.322	1.617
C7	1.329	1.628

i-th C atom, e.g. $[Ind(C1)\text{-}H]^-$ and $[Ind(C3)\text{-}H]^-$ mean a deprotonation at C1 and C3, respectively. $[Ala\text{-}H]^-$ is handled similar.

For tautomers with an intact OH group a variety of conformers associated with the O-H orientation exist, similar to the neutral molecules, e.g. in total 12 conformers for $[Ind\text{-}H]^-$ and even more for $[Ala\text{-}H]^-$. Thus, the spectral signatures of the tautomers predicted at around 1.7 eV ($[Ala\text{-}H]^-$) or 1 eV ($[Ind\text{-}H]^-$) may contain contributions from several conformers of similar energy.

Achiral tautomers are formed by deprotonation at the sterogenic center, i.e. $H_{2.1}$ in alaninol or C1 in 1-indanol. In the case of alaninol, formation of such isomer is energetically not feasible (table 5.2.1). However, for 1-indanol, the formation of an achiral tautomer is energetically possible. A PECD asymmetry for $[Ind\text{-}H]^-$ photodetachment in the energy region around 1 eV, therefore, may attributed to the tautomer $[Ind(C3)\text{-}H]^-$.

5.2.3. Orbitals

For the lowest energy isomers of $[Ala(O)\text{-}H]^-$ (A-H1) and $[Ind(O)\text{-}H]^-$ (eq) deprotonated at the OH group, the HOMO, HOMO-1 and HOMO-2 orbitals are exemplary visualized in figure 5.2.4 and figure 5.2.5, respectively. The orbitals of other isomers look similar (not shown). The figures are created with Multiwfn [147].

Since HOMO and HOMO-1 are the O's lone pair after deprotonation, the HOMO and HOMO-1 of each conformer are mainly concentrated at the oxygen atom. HOMO-2, on the other hand, is located predominately at other positions: at the nitrogen in the case of $[Ala(O)\text{-}H]^-$ and the ring structure for $[Ind(O)\text{-}H]^-$.

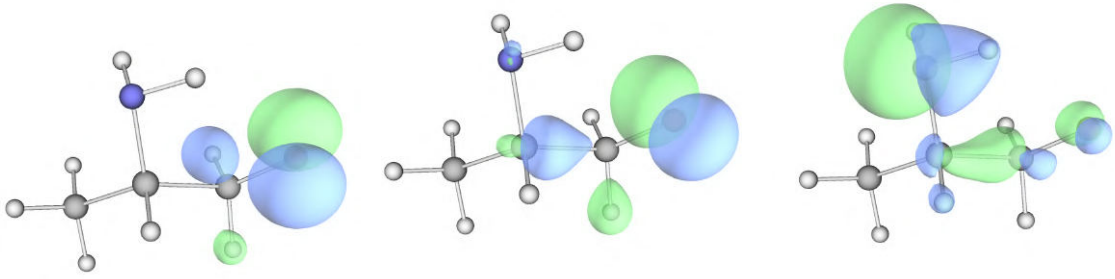

(a) (b) (c)

Fig. 5.2.4.: Valence orbitals of the most stable isomer of $[\text{Ala(O)-H}]^-$ (A-H1). HOMO (a) and HOMO-1 (b) are mainly localized at the oxygen atom, HOMO-2 (c) at the nitrogen atom. All in all, the other isomers follow the same trend (not shown). Isosurface value is 0.08.

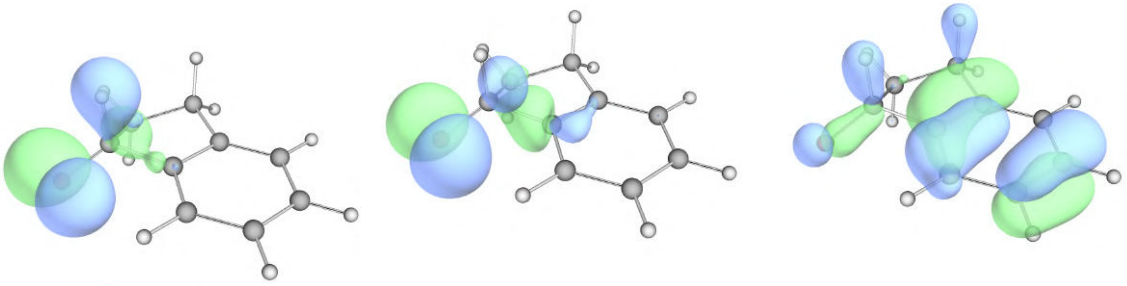

(a) (b) (c)

Fig. 5.2.5.: Orbitals of eq. $[\text{Ind(O)-H}]^-$. HOMO (a) and HOMO-1 (b) are concentrated at the oxygen, while HOMO-2 (c) is determined by the ring structure. Orbitals of ax. $[\text{Ind(O)-H}]^-$ look similar (not shown). Isosurface value is 0.05.

An orbital composition analysis reveals in more detail, which atomic orbitals contribute to the corresponding molecular orbitals: The most dominant participant atoms and their contributions are given in table 5.2.3 for the HOMO and HOMO-1 of A-H1 as well as in 5.2.4 for the HOMO, HOMO-1 and HOMO-2 of eq. $[\text{Ind(O)-H}]^-$.

The strongest contributor for the HOMO in both molecules is the oxygen atom ($2p$) with around 73% for A-H1 and around 64.5% for eq. $[\text{Ind(O)-H}]^-$. The hydrogen atom ($1s$) bound to the C, which is connected to the oxygen (for $[\text{Ind(O)-H}]^-$ this corresponds to the stereogenic center) is the second strongest contributor with 12% for A-H1 and 10% for $[\text{Ind(O)-H}]^-$. Overall, the HOMOs of both molecules are of $1s/2p$ character with a fractional p character of $f = 0.845$ for A-H1 and 0.860 for eq. $[\text{Ind(O)-H}]^-$. The same is valid for HOMO-1 of eq. $[\text{Ind(O)-H}]^-$ but with $f = 0.913$. These results are important for the s-p-mixing model from Sanov, which will be applied to the anisotropy parameter (or β) analysis of both molecules.

Table 5.2.3.: Orbital composition (comp.) analysis for HOMO and HOMO-1 of A-H1. The atom labels are according to figure 5.0.1. * marks the stereogenic center. The atoms are ordered according to their contribution to the HOMO. Main contributor is oxygen with around 73% for HOMO and 74% for HOMO-1. Contributions with less than 1% are not shown. The sum of the total values is not 100% since contributions from other atomic orbitals are not shown.

atom	type	HOMO comp. (%)	HOMO-1 comp. (%)
O	$2p$	73.0	74.1
$H_{3.1}$	$1s$	12.0	1.1
C2*	$2p$	5.5	4.4
C3	$2p$	3.3	3.3
N	$2p$	1.6	1.8
$H_{3.2}$	$1s$		12.4
total	s	14.8	14.9
total	p	84.5	84.5

5.2.4. Calculated Detachment Energies

Electronic Transitions

Vertical detachment energies are calculated to be 2.080 and 2.185 eV for the most stable conformers of $[Ala(O)\text{-}H]^-$ and $[Ind(O)\text{-}H]^-$, respectively (table 5.2.5 and 5.2.7). The energy difference to other conformers is rather small with maximal differences of around 0.092 eV for $[Ala(O)\text{-}H]^-$ and 0.084 eV for $[Ind(O)\text{-}H]^-$ but these are still within the resolution of this experiment. However, the smallest energy difference for $[Ala(O)\text{-}H]^-$ is only 0.005 eV and it will be quite difficult to resolve these conformers experimentally. Other conformers, which can be expected for $[Ala(O)\text{-}H]^-$ but are not considered here, aggravate the situation, since it can be assumed that their are in a similar energy range.

The adiabatic energies are smaller by 0.105 eV for eq. $[Ind(O)\text{-}H]^-$ and 0.080 eV for ax. $[Ind(O)\text{-}H]^-$ indicating that the axial configuration is closer to its most stable form after photodetachment. With an ADE smaller by 0.169 eV the $[Ala(O)\text{-}H]^-$ is the furthest away from its equilibrium structure.

Based on the VDE, Koopmans' theorem and orbital energies the detachment energies of HOMO-1 and HOMO-2 for $[Ala(O)\text{-}H]^-$ (table 5.2.6), for both conformers of $[Ind(O)\text{-}H]^-$ (table 5.2.8) and for the tautomers $[Ind(C1)\text{-}H]^-$, $[Ind(C3)\text{-}H]^-$ (table 5.2.9) are estimated. However, the orbital energies for all HOMO's and some HOMO-1's obtained from Multiwfn for A-H1 are positive. This indicates to an electron self interaction error common in DFT. $[Ind\text{-}H]^-$ only shows this behavior for the HOMO's of the tautomers, else all orbital energies are negative.

Between HOMO and HOMO-1 of $[Ind(O)\text{-}H]^-$, the energy difference is 0.118 eV for eq. $[Ind(O)\text{-}H]^-$ and 0.035 eV for ax. $[Ind(O)\text{-}H]^-$. Assuming the existence of both conformers in the molecular beam, the energy range between around 2.1 and 2.3 eV can

Table 5.2.4.: Orbital composition (comp.) analysis for HOMO, HOMO-1 and HOMO-2 of eq. Ind(O)-H. The atom labels are according to figure 5.0.1. * marks the stereogenic center. The table is ordered according to the contribution of atomic orbitals to the HOMO. Main contributor is oxygen with around 64.5% for HOMO and 76.7% for HOMO-1. Three carbon atoms contribute to HOMO-2 with similar amounts. Contributions with less than 1% are not shown. The sum of the total values is not 100% since contributions from other atomic orbitals are not shown.

atom	type	HOMO comp. (%)	HOMO-1 comp. (%)	HOMO-2 comp. (%)
O	$2p$	64.5	76.7	12.3
H (of C1*)	$1s$	10.3	4.6	
C2	$2p$	8.0	2.1	
C1*	$2p$	3.0	1.8	
C8	$2p$	3.0		22.4
C4	$2p$	2.2		19.3
C5	$2p$	1.8	8.0	24.7
C6	$2p$	1.6		2.5
C2	$2s$	1.4		
C5	$2s$		2.1	
C7	$2p$			12.9
H (of C3)	$1s$			1.9
C3	$2p$			1.2
total	s	13.1	8.1	2.8
total	p	86.0	91.3	96.8

Table 5.2.5.: Energies calculated with B3LYP-D3/aug-cc-pVTZ for four conformers of $[\text{Ala(O)-H}]^-$ given in eV. Energies are zero point corrected.

$[\text{Ala-H}]^-$	E_0	VDE	ADE
A-H1	0	2.080	1.911
A-H2	0.019	2.085	
A-H3	0.042	2.070	
A-H4	0.077	1.993	

Table 5.2.6.: Detachment energies from orbitals calculated with Koopmans' theorem for $[Ala(O)\text{-}H]^-$ given in eV.

$[Ala\text{-}H]^-$	VDE (HOMO)	HOMO-1	HOMO-2
A-H1	2.080	2.209	4.489
A-H2	2.085	2.203	4.525
A-H3	2.070	2.242	4.421
A-H4	1.993	2.041	4.574

Table 5.2.7.: Energies calculated with B3LYP-D3/aug-cc-pVTZ for $[Ala(O)\text{-}H]^-$ given in eV. Energies are zero point corrected.

$[Ind\text{-}H]^-$	E_0	VDE	ADE
eq	0	2.185	2.080
ax	0.069	2.101	2.021

Table 5.2.8.: Detachment energies from orbitals calculated with Koopmans' theorem for $[Ind(O)\text{-}H]^-$ given in eV.

$[Ind\text{-}H]^-$	VDE (HOMO)	HOMO-1	HOMO-2
eq	2.185	2.303	4.728
ax	2.101	2.136	4.547

Table 5.2.9.: Detachment energies from orbitals calculated with Koopmans' theorem for the tautomers $[Ind(C1)\text{-}H]^-$ and $[Ind(C3)\text{-}H]^-$ given in eV. C1 is the stereogenic center.

tautomer	VDE (HOMO)	HOMO-1	HOMO-2
$[Ind(C1)\text{-}H]^-$	0.949	4.089	4.368
$[Ind(C3)\text{-}H]^-$	1.047	4.125	4.539

already contain four transitions, which needs to be resolved properly due to the small energy differences.

In the case of $[Ala(O)\text{-}H]^-$, the energies of the respective orbitals are pretty similar. For the here considered isomers, the difference in HOMO-1 can be as small as 0.003 eV and for HOMO-2 as small as 0.04 eV (5.2.6). Since more isomers with similar energetics can be expected, the PES may contain features of several overlapping isomers, which will probably difficult to resolve.

Vibrationally Excited States

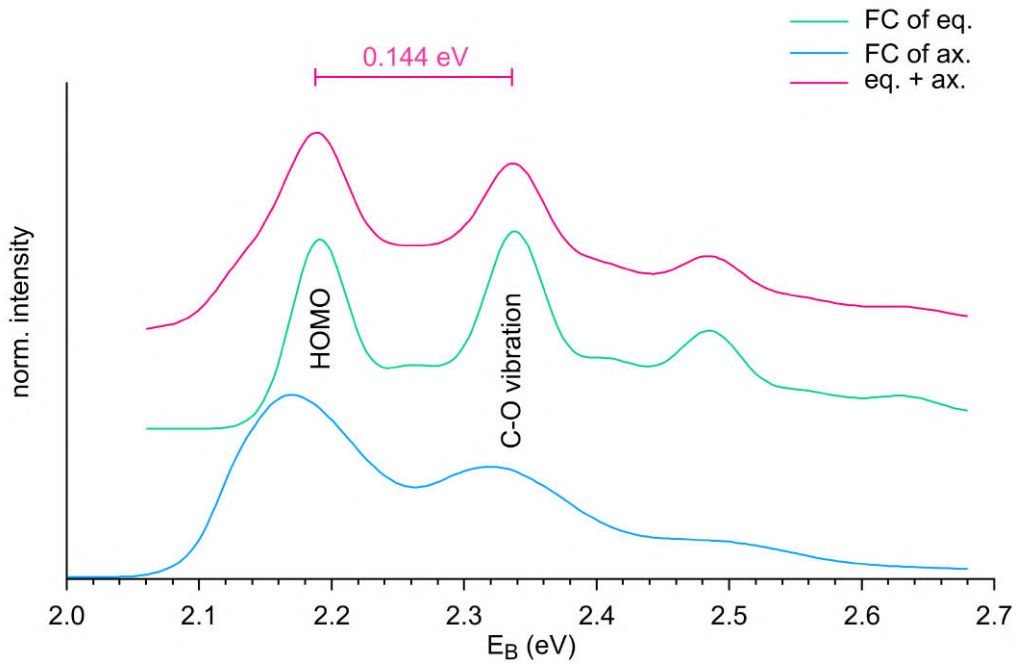

Fig. 5.2.6.: FC simulation for eq. $[Ind(O)\text{-}H]^-$ (green) and ax. $[Ind(O)\text{-}H]^-$ (blue). The FC spectra are shifted in energy such that the first peak of eq. $[Ind(O)\text{-}H]^-$ matches the calculated VDE of around 2.19 eV. The combination spectrum assumes a ratio of 1:1 between both conformers (red) and resembles the spectrum of the eq. $[Ind(O)\text{-}H]^-$ the most. The difference between the first peak (HOMO) and the second peak (C-O vibration) is about 0.144 eV (scaled with 0.9687 [200]). HOMO-1 is not considered.

Next to electronic transitions, vibrations are considered, which can broaden the PES or give additional distinct features. Vibration frequencies are coupled to the geometry like bond lengths, however their probability or activation is determined by how much the geometry changed upon the transition from the anion $[Ind(O)\text{-}H]^-$ to the (optimized) neutral radical Ind(O)-H and how the respective wave functions overlap (Franck-Condon (FC) principle in section 2.2.1). Major geometry changes happen in the 5-member ring, especially around the stereogenic center (C1) while the 6-member ring stays basically the same. The most important change is the C-O bond length, which

becomes longer by 0.003 nm in both isomers of Ind(O)-H compared to $[Ind(O)\text{-}H]^-$ (figure 5.2.3). This change is related to the detachment from the HOMO (and HOMO-1) meaning the detachment of a localized electron from the oxygen (figure 5.2.5). Consequently, oxygen orbitals are altered, which in the end influences the bond length to C1. The calculated (B3LYP-D3/aug-cc-pVTZ) and scaled[2] frequencies related to the elongated bond lengths are around 1058 cm^{-1} (0.13 eV) for eq. Ind(O)-H and 1075 cm^{-1} (0.13 eV) for ax. Ind(O)-H. A Franck-Condon simulation performed on both conformers confirms the activation of these frequencies and also their energy positions (figure 5.2.6).

The FC simulation is performed with Gaussian 16 with a simulation temperature of 300 K on $[Ind(O)\text{-}H]^-$. A simulation with 0 K gives basically the same result. Tautomers are not considered. For each peak a Gaussian distribution with HWHM of 160 cm^{-1} (0.02 eV) is used, which produces spectra with similar resolution than the experimental spectra. The first two prominent peaks of the eq. and ax. $[Ind(O)\text{-}H]^-$ belong to the HOMO and to a vibrational mode, which is dominated by the C-O stretch (figure 5.2.6). Another smaller third feature appears at around 0.14 eV higher in energy than the C-O stretch feature. The FC simulation shows that this peak is partly attributed to a vibrational progression of the C-O stretch vibration.

In the case of ax. $[Ind(O)\text{-}H]^-$, there are more significant vibrational contributions, which broaden the spectrum clearly. Since the energies of eq. and ax. $[Ind(O)\text{-}H]^-$ are pretty similar and the combination spectrum is dominated by the eq. $[Ind(O)\text{-}H]^-$, the influence of the ax. $[Ind(O)\text{-}H]^-$ to the experimental spectrum will be difficult to determine. However, arbitrary a ratio of 1:1 is assumed like in [48] and in figure 5.2.6.

The transition from HOMO-1 is close to the one of HOMO in the case of eq. and ax. $[Ind(O)\text{-}H]^-$ (table 5.2.8) and hence should be considered for further interpretations. However, this requires the optimization of the excited neutral, which is beyond the scope of this work. The interpretation is consequently restricted to the HOMO.

In the end, three different contributions (HOMO, HOMO-1 and the CO stretch) for each isomer might appear in the experimental spectrum. However, since HOMO-1 is not considered in the FC calculations not all possible features might be calculated. The calculated features are energetically similar and good resolution is required.

5.3. Photoelectron Spectra with Linear Polarized Light

5.3.1. Photoelectron Spectra of Deprotonated Alaninol

Photoelectron spectra measured with linear polarized light are plotted over the binding energy in figure 5.3.1. The measured values are given in table 5.3.1 and features are assigned according to previous calculations.

One broad feature, called A, centered at $E_B = 2.23 \pm 0.09$ eV is visible in both spectra and matches the calculated VDE for HOMO and HOMO-1 of several $[Ala(O)\text{-}H]^-$ isomers. Due to the close energies predicted in table 5.2.6, both HOMO and HOMO-1, of the calculated structures may be contained in this peak. Additionally, more conformers,

[2]Scaling factor is 0.9687 [200]. The same scaling is used in the previous chapter 4.

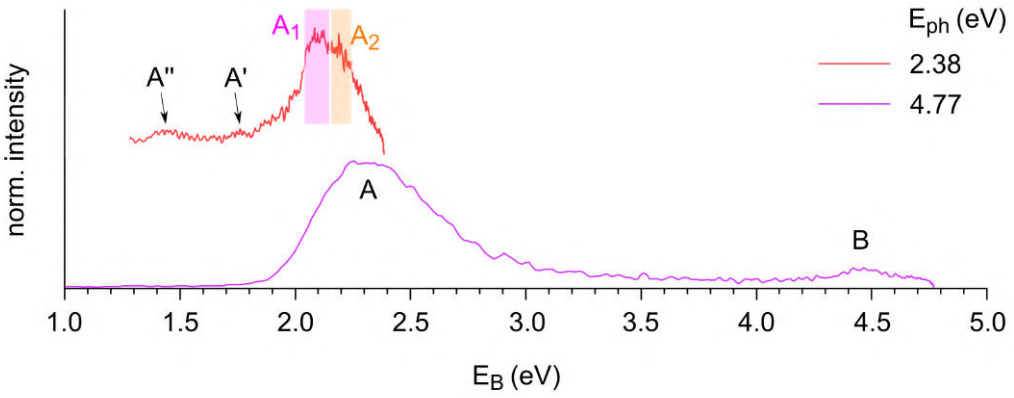

Fig. 5.3.1.: PES of $[Ala\text{-}H]^-$ plotted over the electron binding energy for E_{ph} = 2.38 eV and 4.77 eV. More PES are recorded for E_{ph} = 2.76 eV, 3.02 eV and 3.49 eV (not shown).

Table 5.3.1.: Electron binding energies for the signals seen in the PES of $[Ala\text{-}H]^-$ and possible assignments according to computational results.

peak	E_B	assignment
A"	1.44 ± 0.02	-
A'	1.76 ± 0.01	tautomers ($H_{N.1}$, $H_{N.2}$)
A	2.23 ± 0.09	HOMO and HOMO-1
A_1	2.099 ± 0.07	HOMO
A_2	2.163 ± 0.006	HOMO-1
B	4.47 ± 0.02	HOMO-2

not considered in the calculation, as well as vibrational substructure can be expected but can not be resolved in this spectrum leading to the relatively broad feature (covering an energy area of ≈ 0.7 eV).

For a photon energy of 2.38 eV, peak A seems to split in two peaks, which are referred to as A_1 and A_2. Feature A_1 is centered at E_B = 2.10 ± 0.07 eV and matches way better the calculated VDE of the HOMO from $[Ala(O)\text{-}H]^-$ isomers. A_2 is centered at E_B = 2.163 ± 0.006 eV but could be adulterated in intensity and energy due to the close proximity of the cutoff energy/center of PAD. Anyways, this feature could be assigned to the HOMO-1 (table 5.2.6).

Other clear features visible in the same spectrum are A' and A" at E_B = 1.76 ± 0.01 eV and E_B = 1.44 ± 0.02 eV, respectively. While A' matches well with the calculated VDE of the tautomers, which are deprotonated at the nitrogen atom ($[Ala(N)\text{-}H]^-$), the assignment for A" is not clear since it does not match with any calculated electron binding energies (table 5.2.6).

The last feature is B, which is only visible in the spectrum measured at 4.47 eV. It is probably the excited state of HOMO-2.

5.3.2. Photoelectron Spectra of Deprotonated 1-Indanol

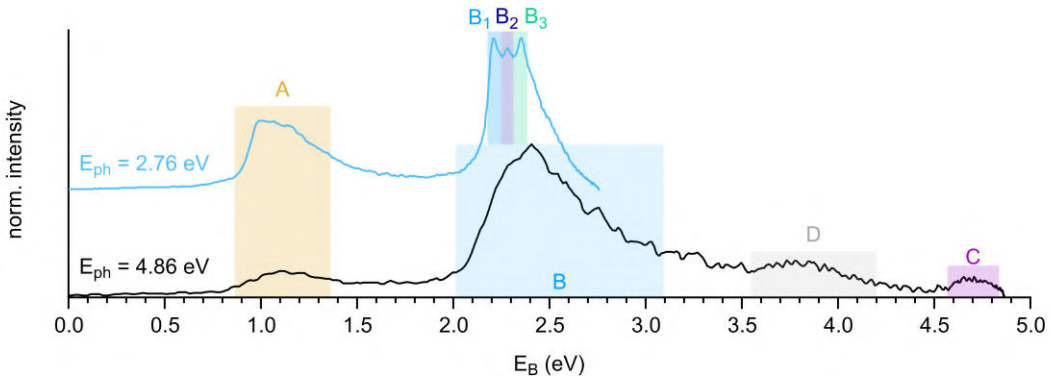

Fig. 5.3.2.: Photoelectron spectra of $[Ind\text{-}H]^-$ plotted over the binding energy for photon energies of 2.76 (blue) and 4.86 eV (black). Energies and assignments are given in table 5.3.2.

Table 5.3.2.: Experimental determined binding energies for $[Ind\text{-}H]^-$ with possible assignment according to computational results.

Peak	E_B (eV)	assignment
A	1.06 ± 0.05	VDE (HOMO) of tautomers (C1*, C3)
B_1	2.21 ± 0.01	VDE (HOMO of eq. $[Ind(O)\text{-}H]^-$)
B_2	2.28 ± 0.01	HOMO-1 of eq. $[Ind(O)\text{-}H]^-$?
B_3	2.35 ± 0.01	C-O vibration of $[Ind(O)\text{-}H]^-$
C	4.64 ± 0.02	HOMO-2 of $[Ind(O)\text{-}H]^-$
D	3.78 ± 0.02	HOMO-1 of tautomers?

For $[Ind\text{-}H]^-$, in total, 18 photoelectron spectra have been recorded in the photon range of 2.34 - 4.96 eV. Exemplary, two spectra are presented in figure 5.3.2 in dependence of the binding energy for photon energies of 2.76 and 4.86 eV. The energies and possible assignments according to computational results can be found in table 5.3.2.

The UV-PES, represented by the black PES in figure 5.3.2, show four features: peak A spans over 0.9 - 1.5 eV and matches to the VDE's of the tautomers deprotonated at C3 and C1*. B occupies the energy region from around 2 - 3 eV and contains – according to the previous calculations – the HOMO and HOMO-1 for equatorial and axial $[Ind(O)\text{-}H]^-$ as well as possibly the excitation of a C-O stretch vibration. Between 4.5 and 5 eV, feature C is visible and can be assigned to HOMO-2. Feature D, in the region of 3.5 - 4.2 eV could be the HOMO-1 of the tautomers (table 5.2.9).

With smaller photon energies, photoelectron spectra gain a better absolute resolution as can be seen in the vis-PES, represented by the blue PES in figure 5.3.2. The B peak splits into three subfeatures located at 2.21 ± 0.01 eV (B_1), 2.28 ± 0.01 eV (B_2) and

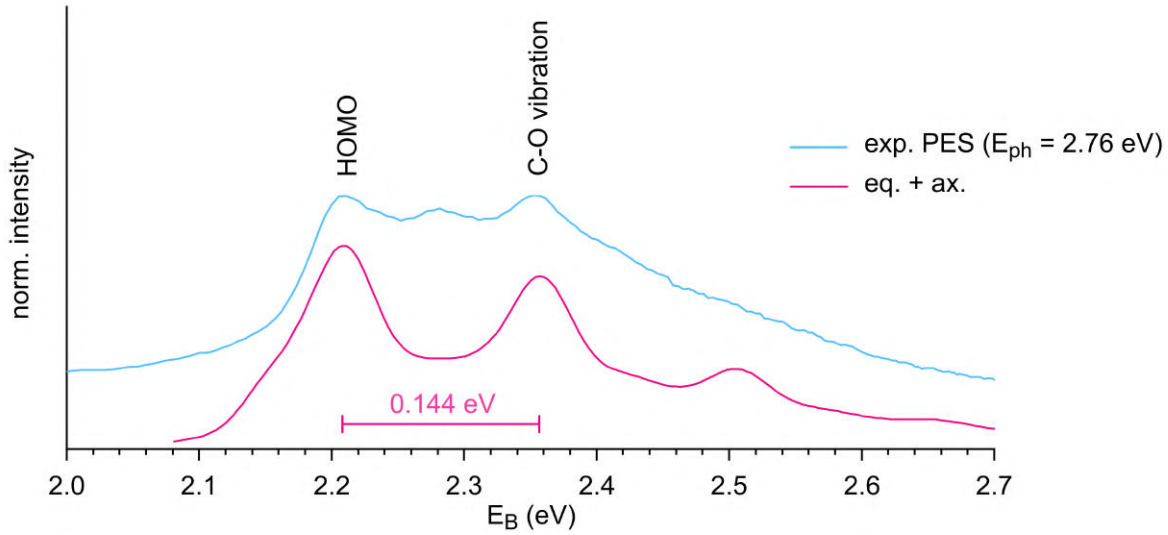

Fig. 5.3.3.: Comparison of the experimental spectrum (blue) with the combined FC simulation of eq. and ax. $[Ind(O)\text{-}H]^-$ from figure 5.2.6 (red). The FC simulated spectra is energetically shifted to match with the experimental spectrum. HOMO-1 is not considered in the FC simulation but could explain the peak between "HOMO" and "CO vibration" in the exp. PES.

2.35 ± 0.01 eV (B_3) (table 5.3.2). B_1 matches well with the calculated VDE of eq. $[Ind(O)\text{-}H]^-$ (2.185 eV) or with the detachment energy from the HOMO.

The experimental spectrum resembles the combination spectrum of eq. and ax. $[Ind(O)\text{-}H]^-$, but also the simulated spectrum of eq. $[Ind(O)\text{-}H]^-$. Assuming that the PES is dominated by eq. $[Ind(O)\text{-}H]^-$, B_2 can be assigned to the HOMO-1 of the eq. $[Ind(O)\text{-}H]^-$ (calculated to be 2.303 eV). The observation of the HOMO-1 is supported by the observation of HOMO-2, which is assigned to peak C.

B_3 lies around 0.14 eV above B_1, which matches with the Franck-Condon simulation with a (scaled) band spacing of 0.14 eV (figure 5.2.6).

Overall, the FC simulation matches with the experimental spectrum (figure 5.3.3): The first two peaks in the FC simulation fit well to features in the experimental spectrum but the third peak at higher binding energy, including the vibrational progression of the C-O stretch, has no visible counterpart. It is either not resolved or has a too low intensity. The observed band pattern and their widths agree better with the FC simulated spectra of eq. $[Ind(O)\text{-}H]^-$ than with the ax. $[Ind(O)\text{-}H]^-$, which is broader due to a richer vibrational structure (figure 5.2.6). The contribution of the ax. $[Ind(O)\text{-}H]^-$ to the low binding energy part of the HOMO peak is not clearly visible but the current experimental resolution might not be sufficient to resolve that. A contribution of the ax. $[Ind(O)\text{-}H]^-$ to the experimental spectrum is difficult to assign. Attempts to obtain better resolved spectra, i.e. by using a photon energy of 2.43, 2.64 and 3.02 eV in combination with smaller repeller voltages able to catch a maximum kinetic energy of around 1.1, 1.3 and 2.5 eV, respectively, did not lead to additional features in the spectrum. The contribution of ax. $[Ind(O)\text{-}H]^-$ remains unknown.

5.3.3. Anisotropy Parameter

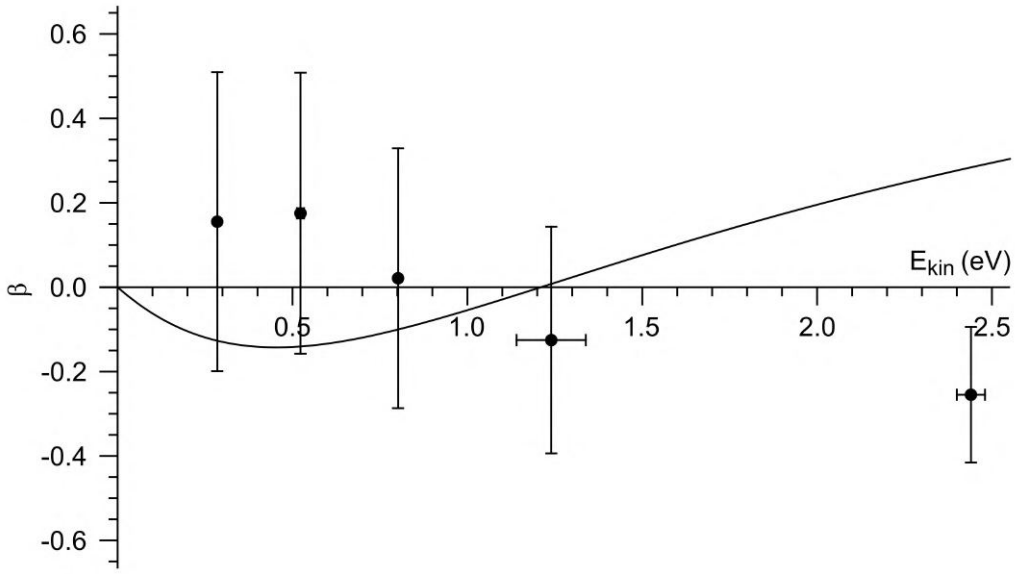

Fig. 5.3.4.: Anisotropy parameter for peak A of $[Ala\text{-}H]^-$ determined with rBasex. The error of E_{kin} is calculated with Gaussian error propagation and the one of β is estimated by the error function 3.2.20 determined from Au^- spectra. The attempted fit is determined with the *s-p* mixing model of Sanov and is based on the assumption that the anisotropy parameter is predominantly described by oxygen orbitals.

Anisotropy parameters are measured for the photoelectron spectra of $[Ala\text{-}H]^-$ (figure 5.3.4) and $[Ind\text{-}H]^-$ (figure 5.3.5 and 5.3.6) but are – in contrast to the spectra – obtained with rBasex rather than POP. As mentioned in section 4.3.2, POP and rBasex lead to similar results but an anisotropy analysis with POP becomes difficult for energetically close transitions like it is the case for B_1, B_2 and B_3 for $[Ind(O)\text{-}H]^-$. The problem is that only two transitions (B_1 and B_3) are visible in the analysis program for the anisotropy parameter (figure 3.2.13) even if all transitions appear in the radial PES after reconstruction. The problem might be that B_2 is lost in the background of the peak edges of its neighboring peaks and also in noise background. rBasex does not show this problem. All transitions are available for the β analysis. For $[Ala\text{-}H]^-$ this is not a problem since the features are not as resolved as for $[Ind\text{-}H]^-$, nevertheless for both anions rBasex is used.

The error for the kinetic energy is based on Gaussian error propagation and the assumption that there are uncertainties of ± 1 px for the peak position as well as ± 1 nm for the wavelength of the laser. If the error bar is not visible in the plots, the error is smaller than the dot size as can be seen in the first two data points of figure 5.3.4 as well as in figure 5.3.5 and 5.3.6. By means of the Au^- spectra, an equation for the error of rBasex (equation 3.2.20) was established and used in figure 5.3.4 - 5.3.6 to estimate the error for the anisotropy parameter.

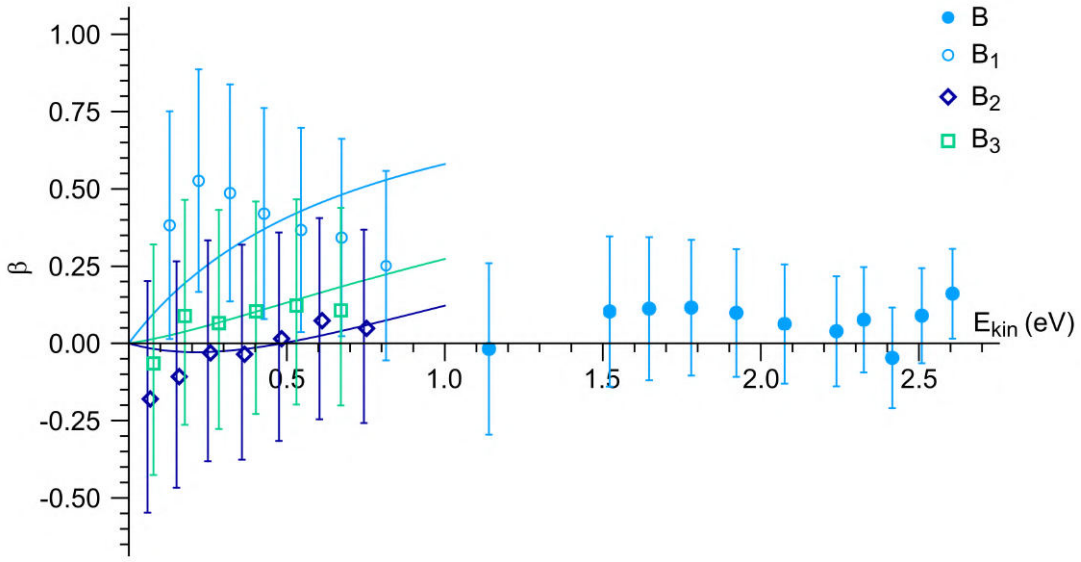

Fig. 5.3.5.: Anisotropy parameter for feature B of $[Ind(O)\text{-}H]^-$. The black dots correspond to data obtained at high photon energy, mostly in the UV, where peak B was not further resolved, while at lower photon energy contributions of B_1 (blue), B_2 (red), and B_3 (green) could be separated. For low E_{kin} a fit is attempted according to the *s-p* mixing model of Sanov and assume that β is dominated by the oxygen orbitals. The fits are in the same color as the corresponding data points. The error for β is based on the error function 3.2.20 determined from Au^- spectra. The error of E_{kin} is smaller than the dot size.

Ramond *et al.* [201] investigated alcoxyides, like CH_3O^- at an kinetic energy of around 1.8 eV. They can show anisotropy parameters of around 1 or -0.9. The sign seems to be determined by the symmetry of the vibronic state. However, the spectra presented here do not resolve vibronic states. Furthermore, peak B of $[Ind\text{-}H]^-$ and peak A of $[Ala\text{-}H]^-$ are not resolved at the kinetic energy of 1.8 eV. If vibronic states are present in $[Ala\text{-}H]^-$ and $[Ind\text{-}H]^-$ similar to Ramond *et al.* [201] but unresolved than the different β values overlap. Depending on the amount of vibronic states in a specific symmetry, β might tend to be more positive (e.g. 1), more negative (e.g. -0.9) or around 0 if they cancel each other out. For $[Ind\text{-}H]^-$ the anisotropy parameter is 0.12 or 0.10 for a kinetic energy of 1.78 or 1.92 eV, respectively. For $[Ala\text{-}H]^-$, β could be negative around that energy. In the case of the alkoxides of Ramond *et al.* [201], this would indicate to different symmetries in (dominating) vibrational states between $[Ala\text{-}H]^-$ and $[Ind\text{-}H]^-$.

Attempted fits of the *s-p*-mixing model from Sanov to the data points under consideration of some simplifications are included in figure 5.3.4 (black) and in figure 5.3.5 and 5.3.6 (colored). The simplifications concern B/A (ratio of Hanstrop parameter describing different detachment channels) as well as f (the fractional p character), which were introduced in section 2.2.2, and are based on the assumption that only the most stable conformers (A-H1 or eq. $[Ind(O)\text{-}H]^-$) are present. Furthermore, B_2 is assumed

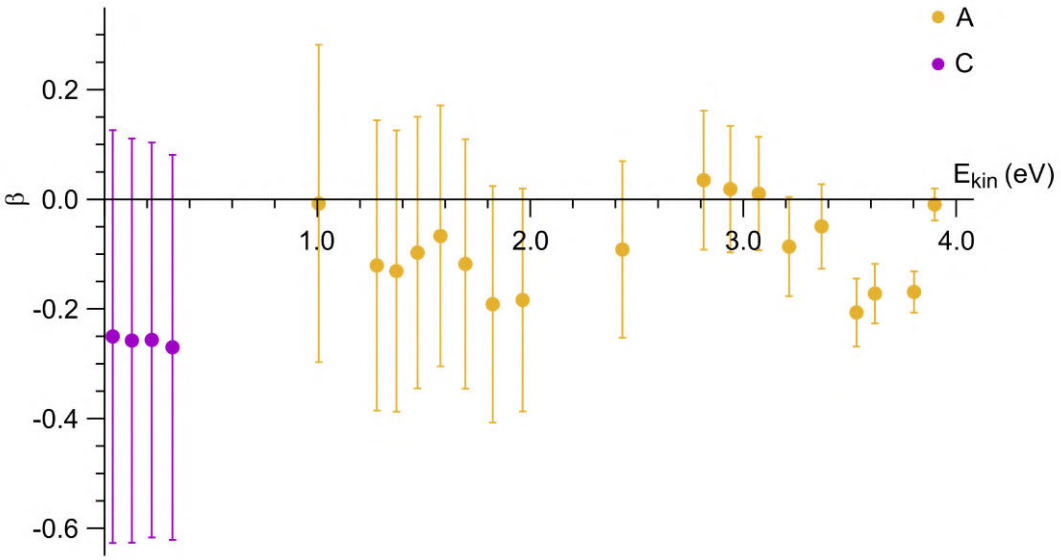

Fig. 5.3.6.: Anisotropy parameter for feature A (red) und C (blue) of $[\text{Ind(O)-H}]^-$. The error for β is based on the error function 3.2.20 determined from Au^- spectra. The error of E_{kin} is smaller than the dot size.

to be the, due to detachment out of, HOMO-1 and will be fitted with the corresponding values from the orbital composition analysis. For $[\text{Ind-H}]^-$ the data points are only fitted until 1 eV since the B peak is not resolved for higher kinetic energies and too many contributions would need to be considered to create an appropriate fit.

The fitting parameters can be obtained from the orbital composition analysis for $[\text{Ala-H}]^-$ (table 5.2.3) and $[\text{Ind-H}]^-$ (table 5.2.4). Some parameters like the Hanstrop parameter A and the evaluation of B/A are similar since the HOMOs (and HOMO-1) are localized at the oxygen atom for both molecules. If the orbital is dominated by the oxygen, the A parameter can be estimated to be 0.55 eV^{-1}, which is the same value as for an isolated oxygen anion [58]. Furthermore, all orbitals are of the type $1s$-$2p$ meaning that the ratio B/A can be calculated with $(1/768)(\zeta_{2p}/\zeta_{1s})^7$ (ζ's being the effective nuclear charges) [58]. First differences appear for the fractional p parameter f, which is 0.845 for $[\text{Ala(O)-H}]^-$, 0.860 for the HOMO and 0.913 for the HOMO-1 of eq. $[\text{Ind(O)-H}]^-$. The remaining parameter is the ratio $\zeta := \zeta_{2p}/\zeta_{1s}$, which is used here as a free parameter for fitting. The best fits are 3.43 for $[\text{Ala(O)-H}]^-$, 3.96 for the HOMO (blue) and 3.91 for HOMO-1 of $[\text{Ind(O)-H}]^-$ (red).

Further, the application of the s-p mixing model on the peak B_3 assigned to the C-O vibration is waged even if no orbital composition is at hand. However, the vibration is based on the HOMO and hence the same parameters as for the HOMO are used. A fit to these data points leads to $\zeta = 4.03$ (green).

Concerning the HOMO of [Ala(O)-H]$^-$, the *s*-*p*-mixing model from Sanov does not produce a satisfying match to the data points. The function might be within errors bars for most of the points but misses the last data point completely and is of different form than the points seem to have (figure 5.3.4). A little bit better, but still not satisfying, performs the fit for the HOMO of [Ind(O)-H]$^-$. The fit is within error bars for all data points and seems to follow the trend of the data points in the beginning but does not accompany the downtrend starting at around 0.2 eV. The best fits are obtained with B_2 and B_3 since the data points almost match the fitted curve but again the trend of the fit at higher kinetic energies seems not to be ideal.

The fits, especially the ones for the HOMOs, can probably be improved by adapting the assumptions. As for example, a better adapted A can be determined since the orbital might be dominated by oxygen but is certainly influenced by other contributions, which need consideration and will change the value for A. Furthermore, other conformers or different vibrational states (other than the C-O vibration) are not considered such that the superposition of the anisotropies is not described well. Even the B peak in the PES measured with vis-light for [Ind(O)-H]$^-$ could not be completely resolved and $B_{1\text{-}3}$ might still contain other contributions. The trend of the fit at the high kinetic energy end can be explained by the area of validity of the used model. The *s*-*p*-mixing model is in general valid for low kinetic energies and becomes more inaccurate with higher kinetic energy. This is especially important for [Ala-H]$^-$, where the fit does not catch the data point at $E_{\text{kin}} \approx 2.4$ eV at all. Furthermore, the PECD data of [Ind-H]$^-$ will show that the here used assumption of a negligible phase shift ($\cos(\delta_2 - \delta_0) = 1$) due to negligible interaction between electron and molecule can not be correct in photodetachment. A PECD signal presumes an interaction, which should also be considered for the anisotropy parameter in form of an adapted phase shift. As mentioned in section 2.2.2, several types of interactions could influence the phase shift. However, in the case of a (strong enough) dipole moment of the neutral radical an adapted model is recommended, which includes the influence of the dipole directly instead of changing the phase shift. Mabbs *et al.* [61] used such an adapted model for molecules with a (calculated) dipole moment of 2.03 D (and higher). The dipole moments calculated here for [Ala(O)-H]$^-$ is around 2.5 D and for [Ind(O)-H]$^-$ around 2.3 D, which would emphasize the use of this adapted model.

5.4. PECD

The PECD PADs are presented and the mean PECD values are calculated for certain binding energy ranges to investigate the influence of different PES contributions to the PECD signal. The standard error (SE) of mean is taken as error for the [Ala-H]$^-$ measurements and for [Ind-H]$^-$ the difference of PECD signals between forward and backward half (ΔPECD) is given as an error.

5.4.1. PECD of Deprotonated Alaninol

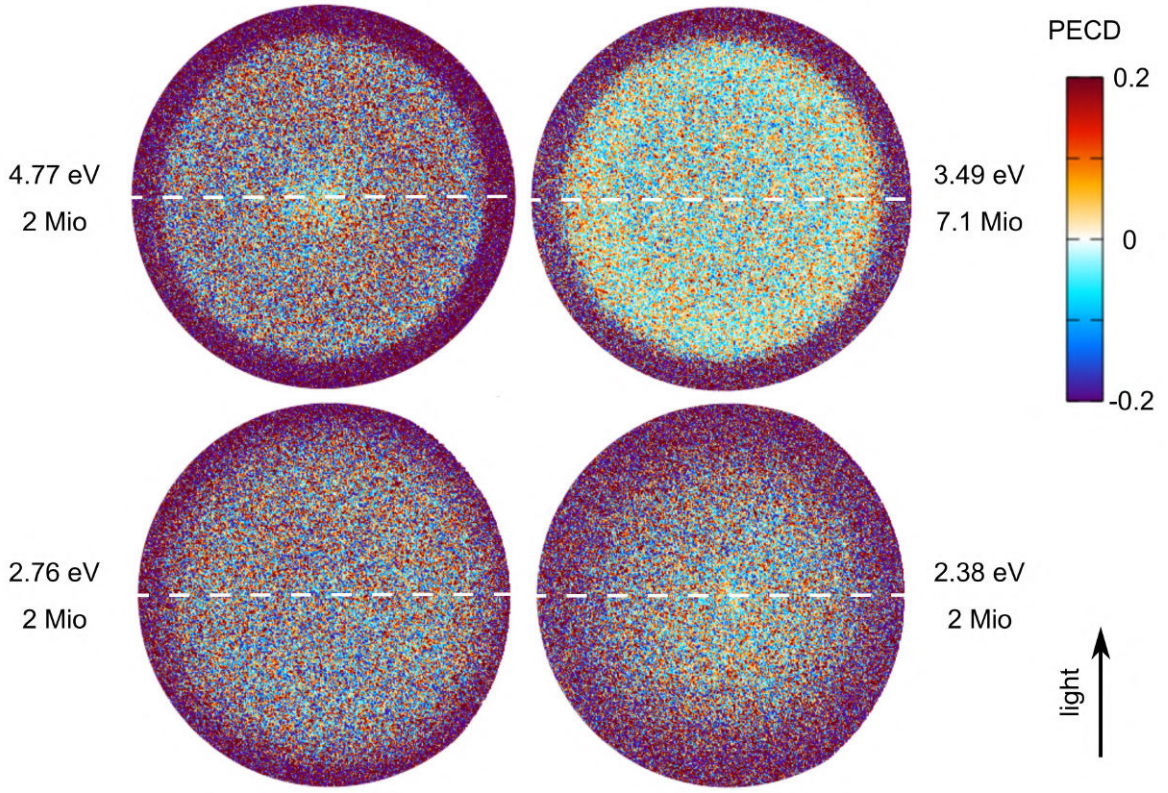

Fig. 5.4.1.: PECD PADs of $[Ala\text{-}H]^-$. Next to each PAD the photon energy and electron counts per polarization are given. The light propagates from down to up. The forward and backward half are separated by a dashed line.

The PECD PAD for $[Ala\text{-}H]^-$ are given in figure 5.4.1 and the corresponding mean PECD values are given in figures 5.4.2 and 5.4.3. In total six different binding energy regions are shown for each PECD PAD to reduce the average over different contributions, e.g. contributions from the tautomers deprotonated at the NH_2 group (A' at $E_B \approx 1.76$ eV) are considered separately from features originating from isomers deprotonated at the OH group (A at $E_B \approx 2.23$ eV) since both features might carry different PECD asymmetries.

Looking at the PECD PADs (figure 5.4.1), there is no PECD asymmetry recognizable for $E_{ph} = 3.49$ eV and 2.38 eV. However, there could be a faintly visible negative PECD asymmetry for $E_{ph} = 4.77$ eV in feature B (inner disk) and a positive PECD asymmetry for $E_{ph} = 2.76$ eV in the A feature. A PECD asymmetry for $E_{ph} = 4.77$ eV is not confirmed by an evaluation of the mean PECD value ($\overline{PECD}$) as seen in figure 5.4.3b. The PECD asymmetry has the same sign for forward and backward direction and hence is set to be zero. On the other hand, a PECD effect for $E_{ph} = 2.76$ eV seems possible since the mean PECD value is around 1% and has a small enough standard error (SE) (figure 5.4.2b). Considering that the standard error is only a statistical error and does

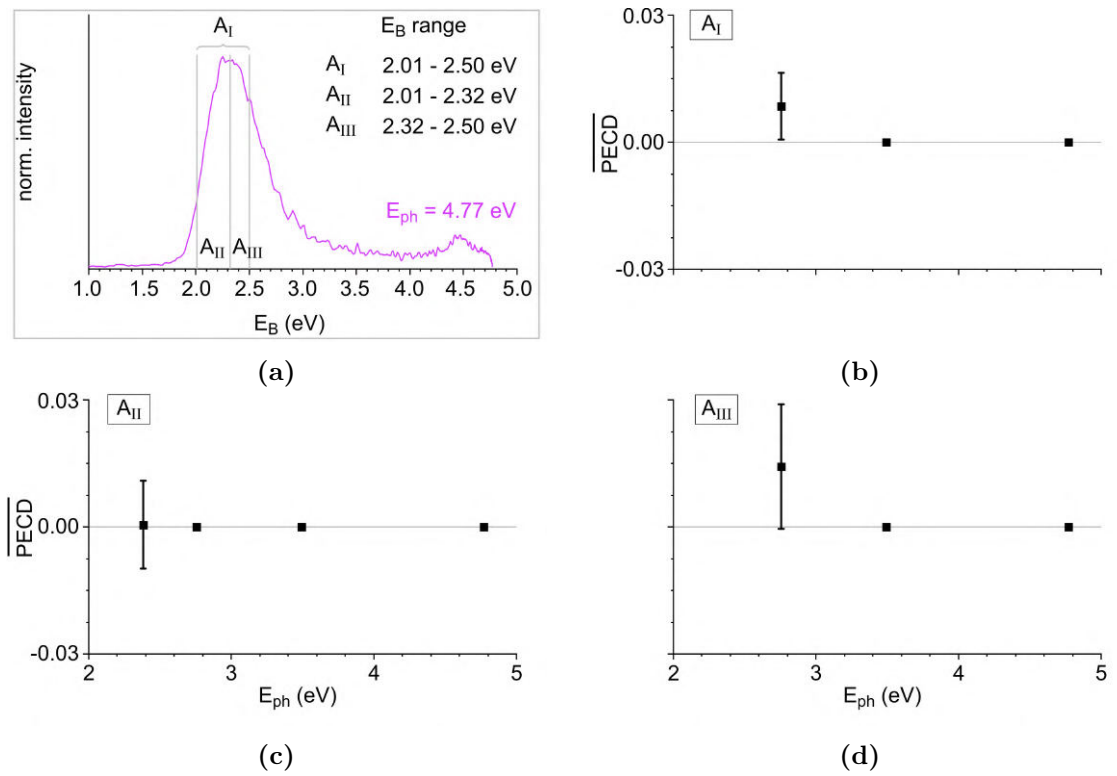

Fig. 5.4.2.: (a) PES at $E_{\mathrm{ph}} = 4.77$ eV with considered E_{B} regions for the analysis of PECD values of $[\mathrm{Ala\text{-}H}]^-$ in the A peak (b-d). The error is based on the standard error of the mean PECD value. (b) shows a PECD asymmetry of around 1%.

not reflect the complete error, e.g. polarization quality and substance purity are not considered here, it is possible that additional error contributions allow an inclusion of the zero value, too.

Despite the slight difference in structure between alaninol and $[\mathrm{Ala(O)\text{-}H}]^-$ a comparison between them can be ventured since the HOMO is in both cases dominated by the $2p$ orbital of the oxygen. Such comparisons to PECD studies on alaninol show how difficult the measurement of a PECD effect can be: Turchini *et al.* [30] calculated the PECD asymmetries of the HOMO (and more) for two isomers, which resemble the isomers A1.0 and A2.0 from figure 4.4.9 and most likely deprotonate to A-H1 and A-H2 (figure 5.2.2), respectively. The PECD asymmetries of both isomers seem to partly cancel each other out for the HOMO with the A1.0 having a stronger PECD asymmetry. The overlapping PECD strength is reduced by half, which is also confirmed by their experiments. This is just the interaction of two isomers and does not consider the other isomers for alaninol. The same could be happening for $[\mathrm{Ala(O)\text{-}H}]^-$ meaning that many isomers contributing to the PECD signal and resulting in an overall low PECD value, which might barely be in the order of the sensitivity of this experiment (1%).

In summary, the only potential candidate for a PECD asymmetry in $[\mathrm{Ala\text{-}H}]^-$ is measured with $E_{\mathrm{ph}} = 2.76$ eV. However, the asymmetry is around the same range as the experimental limit (around 1%).

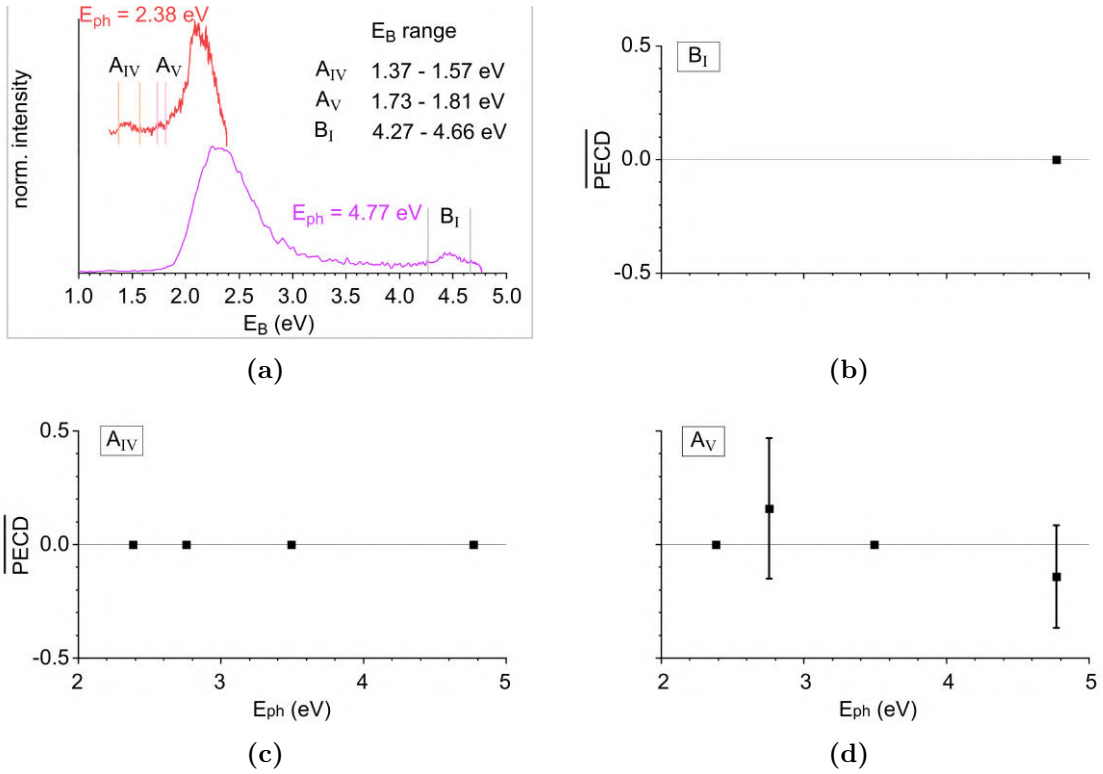

Fig. 5.4.3.: (a) PES at $E_{\mathrm{ph}} = 2.38$ and 4.77 eV with considered E_{B} regions for the analysis of PECD values of $[\mathrm{Ala\text{-}H}]^-$ in the B (b), A" (c) and A' (d) peak. The error is based on the standard error of the mean PECD value. No PECD asymmetry is observed.

5.4.2. PECD of Deprotonated 1-Indanol

5.4.2.1. PECD vs Photon Energy

For each PES measured with LIN light there is a PECD measurement. Hence, the same photon energies are used and the range is the same as for the LIN case with $E_{\mathrm{ph}} =$ 2.07 - 4.96 eV. Selected smoothed, raw PECD PADs and corresponding reconstructed images are presented in figure 5.4.4 alongside with the photon energy and electron counts per polarization. In contrary to the gold complexes and $[\mathrm{Ala\text{-}H}]^-$ a convincing PECD signal is visible for most measurements: The signal is stronger than the limit of the experimental setup (stronger than 1%). Furthermore, the PECD PADs show a relatively clean inversion of the asymmetry between forward and backward direction (separated by a white or gray dashed line in figure 5.4.4). Reconstructed images smooth out the PECD signals more than in the experimental PADs. However, the reconstructed images also seem to spill over into the other half of the image. Such imperfections can be caused by slight deformation of the circularity of the raw image or by non-uniform sensitivity across the detector. Hence they are only used for visualization purposes while other information is extracted from the experimental PECD PADs (left column of figure 5.4.4).

The corresponding mean PECD value ($\overline{\mathrm{PECD}}$) is evaluated for each peak individually over the binding energy range given in table 5.4.1 and is shown in figure 5.4.5 in the

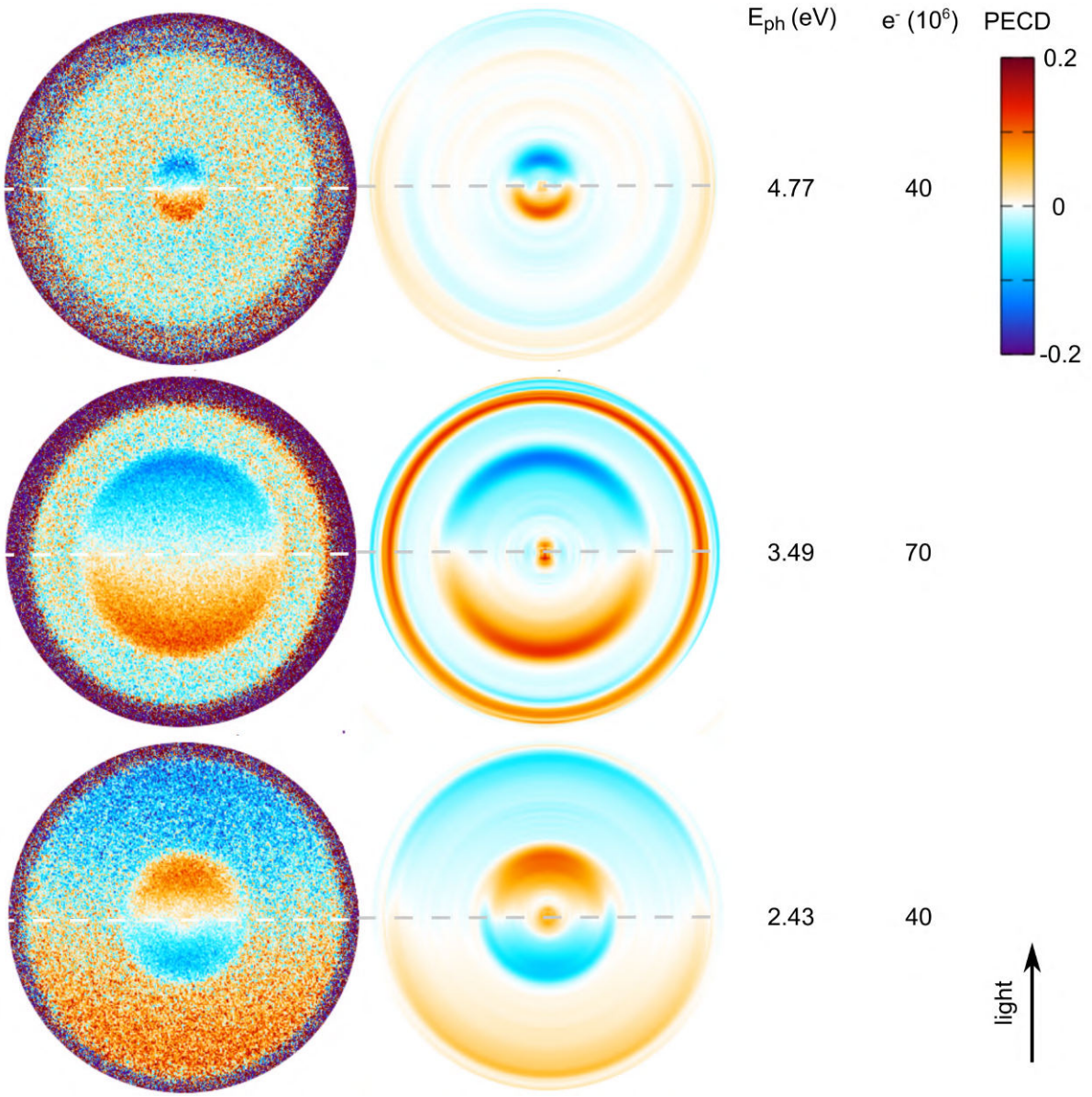

Fig. 5.4.4.: PECD asymmetries for $[\text{Ind-H}]^-$ exemplary shown for E_{ph} = 4.77, 3.49 and 2.43 eV as raw, smoothed (left) and reconstructed image (right). The light propagates from down to up. For- and backward half are separated by a dashed line.

combination with ΔPECD as error. This figure is published in a similar form in [48]. However, in contrast to [48] not the standard error (SE) is taken as error but ΔPECD is preferred here since it considers differences between Fw and Bw images halves (section 3.2.6).

The subfeatures $B_{1,2,3}$ can not be separated well by eye in the PADs for the visible photon energies but can be treated individually after image reconstruction (figure 5.4.6, with ΔPECD as error). In the UV region, peak B is not further resolved and the PECD asymmetry is evaluated over the E_{B} range covering $B_{1,2,3}$, thus resulting in an effective

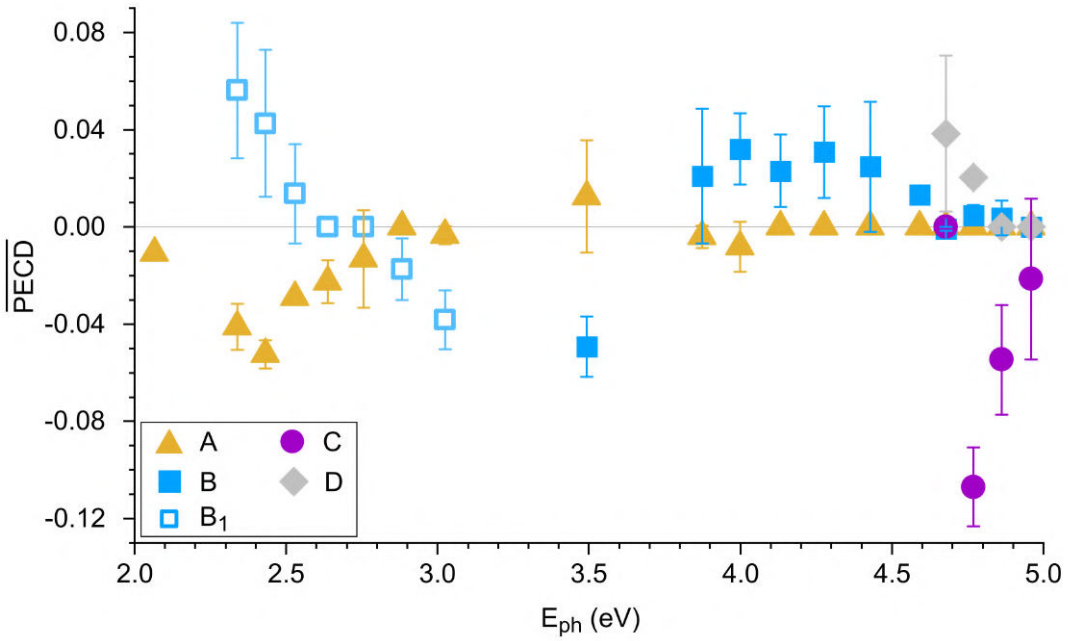

Fig. 5.4.5.: Mean PECD values for (R)-[Ind-H]$^-$ of the three main features plotted against the photon energy. B is represented by the subfeature B_1 for the region E_{ph} = 2.07 - 3.02 eV. The error is based on the difference between the PECD values in forward and backward half: error = $PECD_{FW}$ - $PECD_{BW}$.

PECD signal due to superposition of the three different PECD signals. In figure 5.4.5 feature B_1 represents B in the E_{ph} = 2.3 - 3.1 eV range. PECD values for the other subfeatures can be found in figure 5.4.6. They show the same PECD trend and do not cancel each other out (completely). If this trend continues in the UV region, then the PECD asymmetry from B is (more or less) the result of positive superposition of three different contributions.

A clear dependence on the photon energy and hence the kinetic energy is recognizable in each (sub)feature. Each transition seems to have its own, individual PECD trend, which also includes sign changes for features A and B. The strongest PECD asymmetry is measured for feature C with around -11% at E_{ph} = 4.77 eV or E_{kin} = 0.13 eV. Feature B has its maximum in B_2 with around 7% at E_{ph} = 2.43 eV or E_{kin} = 0.15 eV. A PECD signal which peaks with -5% at E_{ph} = 2.43 eV or E_{kin} = 1.37 eV is seen in the feature A. Also, feature D shows a PECD signal and peaks with 4% before it vanishes. These signals can only come from the chiral tautomer deprotonated at C3 seemingly dominating feature A and D. The exact contribution of the achiral tautomer deprotonated at C1 remains unknown. Magnitude and energy dependence of this anion PECD effect is generally consistent with the PECD experimentally seen in the photoionization of neutral molecules

In general, the PECD asymmetry seems to maximize for low kinetic energies, which speaks for the idea of increased interaction time between detached electron and chiral

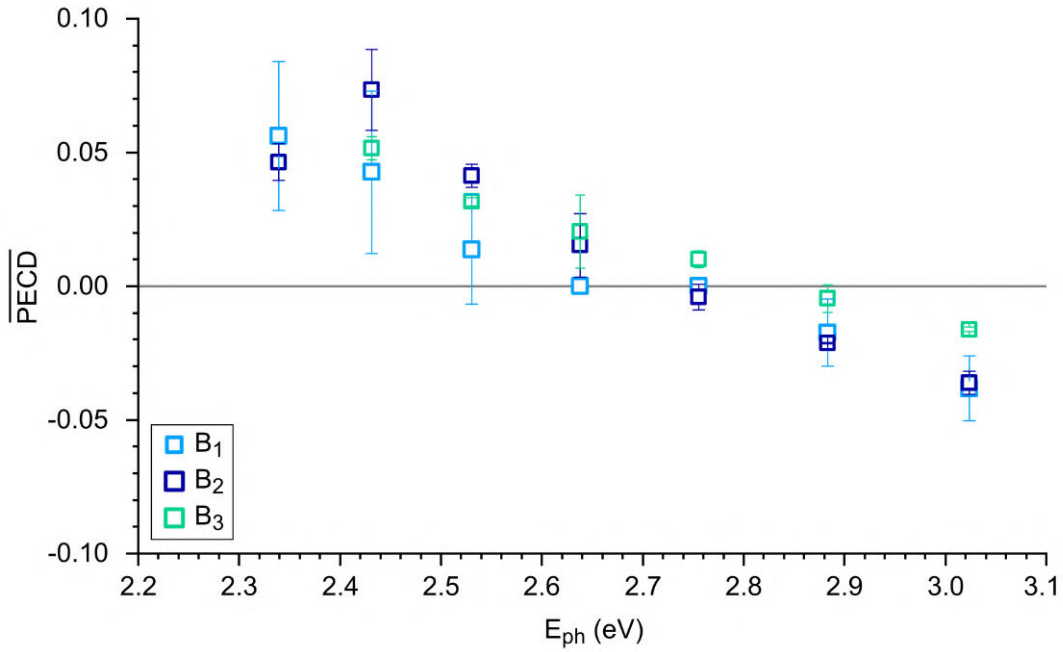

Fig. 5.4.6.: Mean PECD values for (R)-[Ind-H]$^-$ of the three subfeatures of B plotted against the photon energy. The error is based on the difference between the PECD values in forward and backward half: error = $PECD_{FW}$ - $PECD_{BW}$

environment. As for higher kinetic energies (over 1 eV), a departing electron (in general) is assumed to have no or a negligible interaction with the remaining neutral core in photodetachment. In such a case the electron can be described as a plane wave and hence the PECD signal has to vanish [49, 202]. However, here, recognizable PECD signals are shown for kinetic energies over 1 eV (A and B peak) and can be appear for kinetic energies as high as 2.2 eV. Observing a PECD asymmetry at such energies shows the failure of the plane wave ansatz for the PECD effect in photodetachment and the importance of short range interactions. If short-range interactions are not ignored in theory, PECD asymmetries could be observed for electrons with a kinetic energy of up to 12 eV [4].

5.4.2.2. Anion PECD vs Neutral PECD

These findings for the anion [Ind(O)-H]$^-$ can be compared to Dupont *et al.* [73], who investigated the PECD effect of (S)-(+)-1-indanol for HOMO, HOMO-1 and HOMO-2. Apart from having opposite enantiomers, the molecules also differ structurally, i.e. [Ind(O)-H]$^-$ has one less H. The PECD effect has shown to be quite sensitive to small structural changes and could be quite different (section 1.2).

Despite the differences, there are some similarities in the electronic structure of anion and neutral, which can be used to compare the PECD signals of the anion and neutral: HOMO and HOMO-1 of [Ind(O)-H]$^-$ (feature B) are mainly non-bonding, lone-pair and oxygen-centered orbitals (figure 5.2.5 and table 5.2.4), which are similar to HOMO-2

Table 5.4.1.: The mean PECD value is determined over these binding energy ranges for each peak. The (tentative) assignments for each peak are also given. The range given for $B_{1,2,3}$ is taken for the photon energies E_{ph} = 2.34 - 3.02 eV since the features can be separated here. Between E_{ph} = 3.49 - 4.96 eV, the subfeatures are not resolved and the ranges are condensed to one range, which is used for B. Other regions for B were also tested but did not change the PECD signal significantly.

Peak	assignment	E_B range (eV)
A	tautomers (C3, C1*)	0.85 - 1.30
B_1	HOMO of eq	2.19 - 2.24
B_2	HOMO-1 of eq	2.26 - 2.30
B_3	C-O stretch vibration	2.33 - 2.38
B	eq and ax?	2.19 - 2.38
C	HOMO-2	4.62 - 4.67
D	HOMO-1 of tautomers?	3.54 - 4.06

of neutral 1-indanol [73]. Dupont *et al.* [73] measured the PECD of HOMO-2 for a kinetic energy of 0.7 and 1.7 eV to be around -3% and (-7)-(-6)%, respectively. PECD measurements for $[Ind\text{-}H]^-$ are performed at similar kinetic energies, i.e 0.67 and 1.66 eV for HOMO as well as 0.74 and 1.72 eV for HOMO-1 (assuming HOMO-1 is indeed B_2). The PECD asymmetry of the HOMO is around -2% for E_{kin} = 0.67 eV (E_{ph} = 2.88 eV) and +2% for E_{kin} = 1.66 eV (E_{ph} = 3.87 eV). In the case of HOMO-1, a PECD signal of around -3% is measured for E_{kin} = 0.74 eV (E_{ph} = 3.02 eV) and +3% for E_{kin} = 1.72 eV (E_{ph} = 4.00 eV).

In the case of small kinetic energy (around 0.7 eV), the PECD signals for the HOMO-1 of the anion and the HOMO-2 of the neutral are the same (in sign and magnitude). The HOMO of the anion leads to a (slightly) smaller PECD signal than the HOMO-2 of the neutral. However, different enantiomers are taken and hence the PECD asymmetries are inverted for the same enantiomer. For higher kinetic energies (around 1.7 eV), the PECD signal of the HOMO-2 of the neutral is clearly stronger with (-7)-(-6)% in comparison to +2 or +3% of the HOMO or HOMO-1 of the anion, respectively. However, the direction of the PECD asymmetry is in this case the same for the same enantiomer.

Different for 1-indanol and $[Ind\text{-}H]^-$ are the magnitude of the PECD asymmetry at higher kinetic energies and the flip in sign between low and high kinetic energies for $[Ind\text{-}H]^-$ but not for 1-indanol. This could be attributed to the slight structural difference in the (existing or missing) H at the OH group, which turns out to be significant for the PECD signal. Another point is the localization of the HOMO-2 of 1-indanol in comparison to the HOMO of $[Ind(O)\text{-}H]^-$. It seems to be more delocalized if the orbital figure for HOMO-2 of 1-indanol from Dupont *et al.* [73] is compared to HOMO of $[Ind(O)\text{-}H]^-$ (figure 5.2.5a). Unfortunately, they do not provide an orbital composition analysis, which could be used for confirmation. Hence, eq. 1-indanol is calculated here

with B3LYP-D3/aug-cc-pVTZ. The HOMO-2 is compared to HOMO of eq. $[Ind(O)\text{-}H]^-$ via an own orbital composition analysis with Multiwfn. The orbital composition analysis confirms that the HOMO-2 of 1-indanol is indeed more delocalized: the main contribution for HOMO-2 of 1-indanol comes from the $2p$ shell of O (42%) as well as from the $2p$ of the chiral center C1 (14%) and its neighbors C2 (15%) and C5 (11%). In the case of HOMO of $[Ind(O)\text{-}H]^-$, the $2p$ shell of O also contributes the most but with around 64% while $2p$ of C1, C2, C5 barely contribute (in sum only around 6%) in comparison to the HOMO-2 of 1-indanol (table 5.2.4). These different orbital contributions and hence delocalization might be responsible for the different PECD behavior between anion and neutral.

Comparing the maximum PECD signal of $[Ind\text{-}H]^-$ (around -11%) to the maximum of neutral (1S,4R)-(+)-fenchone (around -10% for PECD experiments on valence orbitals [28]), the strength of the PECD asymmetry in anions can be as strong as in neutral molecules. Hence, the PECD effect of anions is in no way inferior to the PECD effect of neutrals strengthening the importance of short-range interactions.

5.4.2.3. PECD vs Counts

The evolution of PECD signal quality with the number of total electron counts is shown for three selected PADs in figure 5.4.7 and, in terms of mean PECD values for all measurements in figure 5.4.8. A comparison of the PECD signal measured with different total electrons shall give an estimation of the lower electron count limit to see a PECD asymmetry. These measurements are performed with a photon energy of 3.49 eV with the same laser pulse energy of 4 mJ measured before the light enters the VMI chamber and of 0.3 mJ after the VMI chamber. In contrary to the before presented PECD PADs, the space focus of the ion beam is not in the interaction zone with the detachment laser but at the ToF-MS detector. A PAD obtained with 70 Mio counts, measured with a laser pulse energy of 3 mJ before and 0.5 mJ after the VMI chamber, is recorded with the space focus in the interaction zone (middle row of figure 5.4.4).

In general, the error becomes smaller for more electron counts, which can be expected since the statistics become better and the error scales with $1/\sqrt{N}$ (N being the electron counts). This coincides also with better PAD image quality as can be seen in figure 5.4.7. All values agree within error bars or are within the gray stripe, which marks the reference area for the measurement with the most electron counts (figure 5.4.8).

Considering the mean PECD value, the lowest limit should be something around 0.5 Mio counts for $[Ind\text{-}H]^-$ measured at $E_{ph} = 3.49$ eV since the error is small enough to not include the zero value. The same limit holds for the case of the statistical error SE (not shown). If the PECD signal would be smaller, e.g. 1% more electrons of at least 4 Mio counts would be better. A smaller PECD asymmetry of 0.5% could be measured of 40 Mio electron counts per polarization. However, such high total electron counts require a stable and high ion signal, which is not easy to reproduce as can be seen for the (S)-enantiomer. Hence, the detection limit of PECD signals is based on the lower count number of 4 Mio and is estimated to be around 1%.

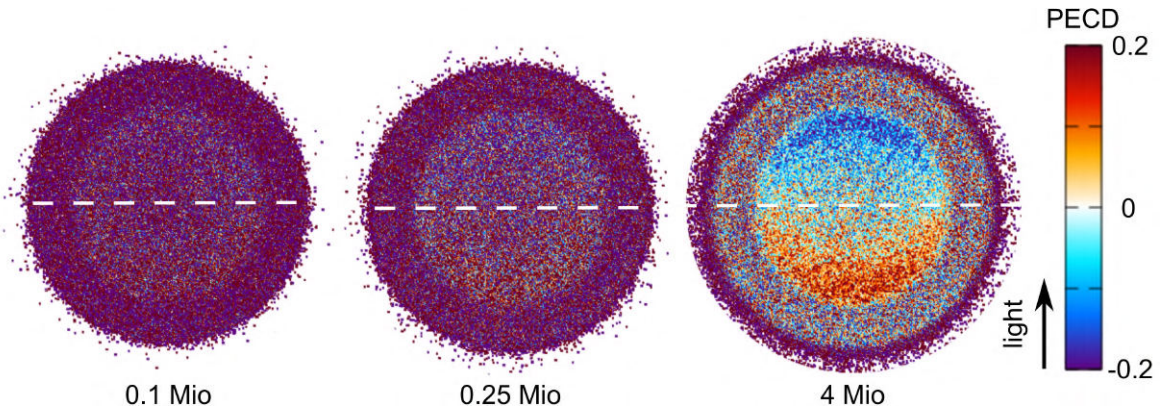

Fig. 5.4.7.: PECD PADs of $[\text{Ind-H}]^-$ at $E_{\text{ph}} = 3.49$ eV for three different electron counts. The PECD asymmetry becomes more visible for more electron counts.

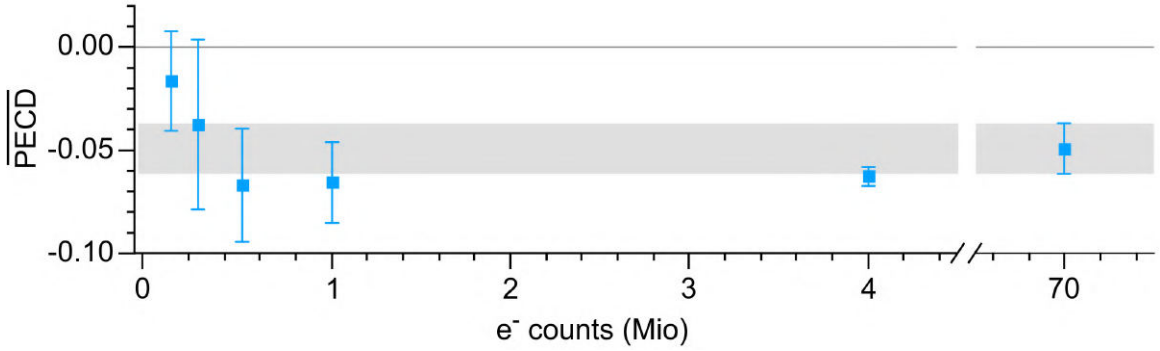

Fig. 5.4.8.: Mean PECD values of $[\text{Ind-H}]^-$ at $E_{\text{ph}} = 3.49$ eV plotted against electron counts per polarization. All points were measured with a laser pulse energy of 4 mJ/0.3 mJ (before/after the VMI chamber) except the point at 70 Mio counts. Here 3 mJ/0.5 mJ were recorded before/after the VMI chamber. The used E_{B} range for feature B is given in table 5.4.1. The error is based on ΔPECD. The gray bar marks a reference area of mean PECD value and error from the measurement with highest counts. Within errors, all PECD values are contained in the gray reference area.

In general, the exact electron count numbers are specific for $[\text{Ind-H}]^-$ since this also depend on the width and shape of the feature in the PES. However, the general concept of having smaller errors and better image quality after more electron counts does not change since this is more in the nature of statistic than of the specific system. The experimental limit of around 1% (or 0.5% after considerably more electron counts) will also stay valid for other molecular systems.

Historically, the dependence of the PECD signal on the laser pulse energy was investigated at $E_{\text{ph}} = 3.49$ eV to exclude that the measured PECD asymmetry arises from the neutral radical Ind-H before the experiment with the grid was done and before the kinetic energy dependence was known (section 3.2.5). PECD signal from the neutral radical could arise from a multiphoton process, which depends on the laser pulse energy. However, even with a laser pulse energy of 0.2 mJ measured before the VMI chamber still

produces a PECD signal agreeing with the previous results from section 3.2.5. The total count number scale linearly with the photon number and result in similar results than shown in this section for the PECD signal's dependence on the electron count number.

5.4.2.4. PECD vs Enantiomer

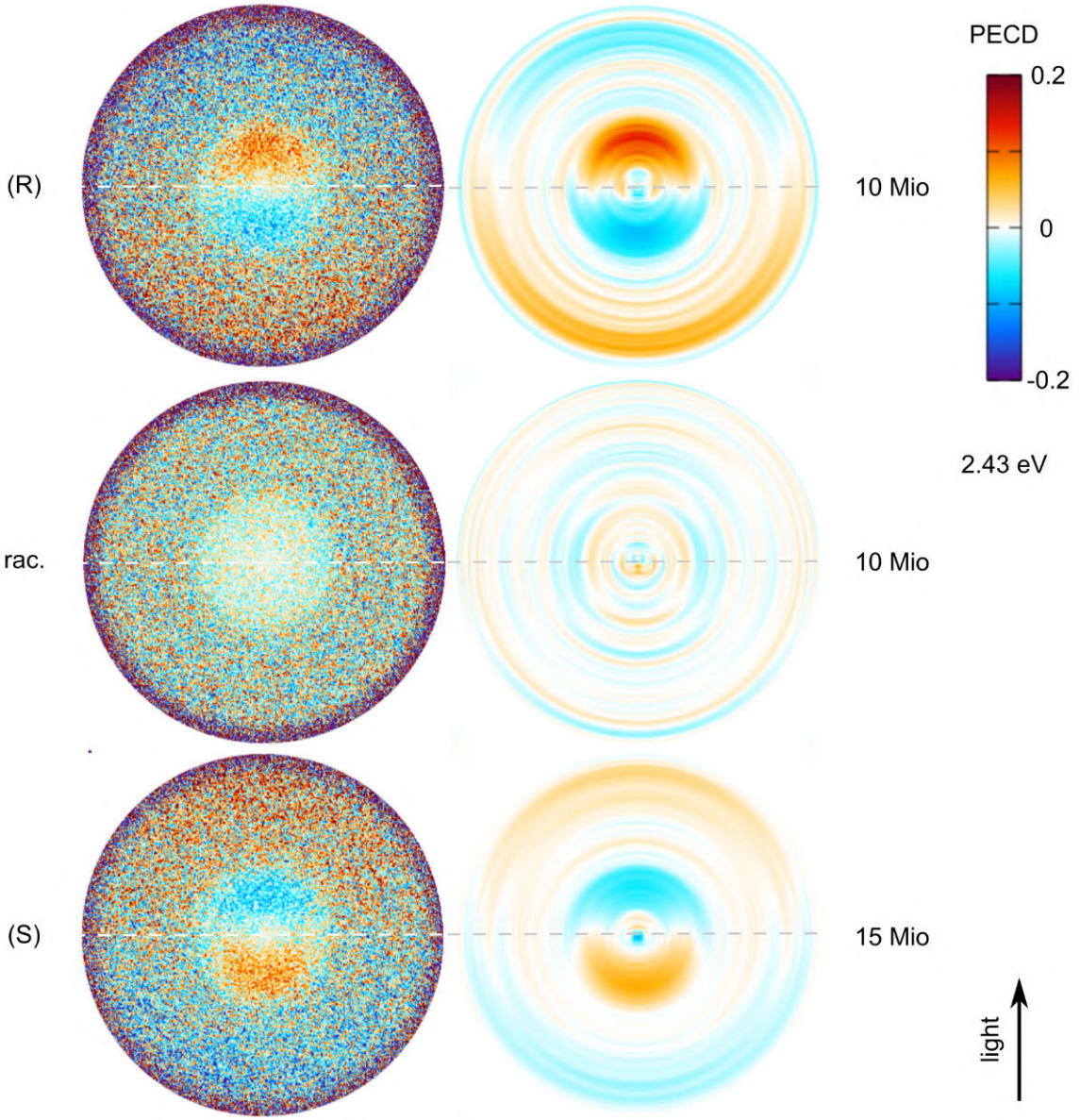

Fig. 5.4.9.: PECD PADs of (R)-, (S)- and racemate $[\text{Ind-H}]^-$ at $E_{\text{ph}} = 2.43$ eV. The counts per polarization are given next to the image. The racemic mixture shows no PECD signal while (R) and (S) show a clear inversed PECD signal for two transitions.

Basic symmetry considerations demand not only an inversion of the electron flux when the opposite circular light polarization is used but also when the other enantiomer

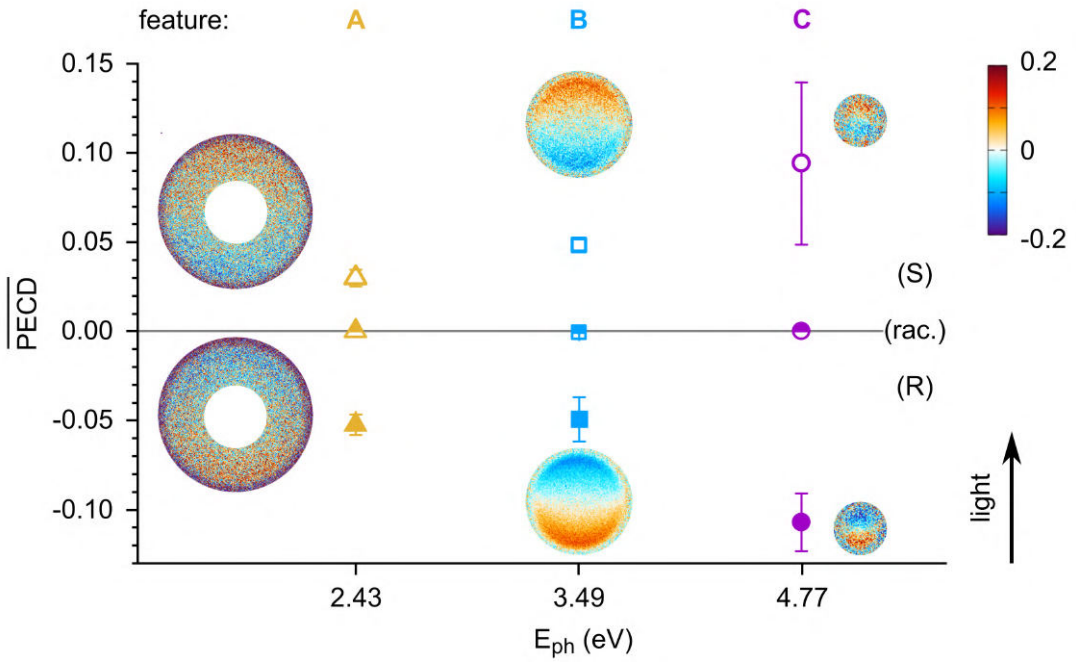

Fig. 5.4.10.: Mean PECD values of (R)-, (S)- and racemate $[Ind\text{-}H]^-$ for the three main features A (yellow), B (blue) and C (violet). Each photon energy (bottom) shows one feature (top). The raw angular distributions are partially masked to highlight the corresponding feature. Full raw images can be found in figure 5.4.9 (and in the figures B.1 and B.2 of the appendix). The error is based on the difference between the mean PECD values of forward and backward direction (ΔPECD).

is taken. Furthermore, the PECD signal has to vanish for the racemic mixture. In figure 5.4.9, the full PECD PADs are shown for the photon energy of 2.43 eV, in raw, smoothed and reconstructed form for both enantiomers and the racemic mixture. Also for photon energies of 3.49 and 4.77 eV, the two enantiomers and the racemate was measured (figures in the appendix B.1 and B.2). The PECD inversion upon enantiomer change is clearly visible and no PECD asymmetry for the racemic mixture can be seen.

The difference in quality of the PECD PADs between the enantiomers can be partly attributed to different electron counts. In the experiments, there was a more intense and more stable ion signal for the (R)-enantiomer than for the (S)-enantiomer or the racemate leading to a much better SNR for the (R)-enantiomer. Somehow, the ion intensity sensitively depends on source conditions (e.g., pressures, timings) but were difficult to reproduce after a change of sample.

Selected mean PECD values for the three samples with corresponding PECD PADs are shown in figure 5.4.10 with ΔPECD as error. For the photon energies 2.43, 3.49 and 4.77 eV the PECD values for the features A (yellow), B (blue) and C (violet) are shown, respectively. The PADs here are partly masked to emphasize the considered transition. $B_{1\text{-}3}$ could also be measured with the photon energy of 2.43 eV but are not shown in these figures.

Both enantiomers show for feature B and C the same but opposite PECD asymmetries within error bars (figure 5.4.10). Feature A, however, has a slightly smaller PECD signal for the (S)-enantiomer, which is catched neither by the SE (not shown) nor ΔPECD (figure 5.4.10). Two main reasons could be responsible for that: different source conditions leading to a changed tautomer distribution and a lower enantiomeric purity of the (S)-enantiomer.

The enantiomeric purity of (R)-(-)- and (S)-(+)-1-indanol from Sigma Aldrich was measured with chiral high-performance liquid chromatography (HPLC) by Synvenio. While the (R)-enantiomer has a good purity with an enantiomeric excess (e.e.) of around 99.1%, the e.e. of the (S)-enantiomer could vary around 70 and 90% within the same batch and even within the same bottle since the enantiomers seem not evenly distributed. This shows that manufacturer information about enantiomeric purity should be looked at critically, even if the here used (S)-enantiomer stems from another company.

Furthermore, deviations between the PECD values for the (R)- and (S)-enantiomer might be attributed to the enantiomeric purity but the stronger deviation for feature A in comparison to B and C can not be solely described by this. A more likely theory is different source conditions for the three samples leading to different tautomer distributions and PADs of different qualities as described earlier.

5.5. Summary

Anions of deprotonated alaninol and 1-indanol are investigated for their anion PES and PECD effect via a VMI spectrometer, which not only allows energy resolved measuremens but also PECD PADs as seen in figure 5.4.4. DFT calculation of these anions revealed several isomers even if only the hydroxy group is considered for deprotonation. In the case of $[Ind(O)\text{-}H]^-$, the isomers are eq. and ax. $[Ind\text{-}H]^-$. More isomers can be expected for $[Ala(O)\text{-}H]^-$ since alaninol is a relatively flexible molecule.

All calculated energies could be assigned in the PES of both anions: HOMO and HOMO-1 of $[Ala(O)\text{-}H]^-$ are contained in the A peak and HOMO-2 could be assigned to feature B in the PES of $[Ala\text{-}H]^-$. Further resolving peak A even revealed a transition matching well with the calculated tautomers $[Ala(N)\text{-}H]^-$ but HOMO and HOMO-1 of $[Ala(O)\text{-}H]^-$ could not be resolved. Probably many isomers of $[Ala(O)\text{-}H]^-$ are overlapping in A leading to the relatively broad feature. Only one peak in this PES could not be assigned.

For $[Ind\text{-}H]^-$, HOMO and HOMO-1 are contained in feature B, which could be resolved for smaller photon energies (B_1, B_2). A third feature (B_3) is assigned to a C-O stretch vibration of $[Ind(O)\text{-}H]^-$ after a FC simulation. HOMO-2 is assigned to feature C. The contribution of ax. $[Ind(O)\text{-}H]^-$ to the PES is not clear but the experimental PES resembles more the simulated spectrum of eq. $[Ind(O)\text{-}H]^-$ or the combination of eq. and ax. $[Ind(O)\text{-}H]^-$. The tautomers $[Ind(C3)\text{-}H]^-$ and $[Ind(C1)\text{-}H]^-$ match with the transitions A (HOMO) and D (HOMO-1) but could not be resolved further.

For $[Ala(O)\text{-}H]^-$ and $[Ind(O)\text{-}H]^-$, HOMO and HOMO-1 are energetically close since, in both cases, these orbitals are dominated by the $2p$ shell of the oxygen, hence, detach-

ment happens in states, which are nearly degenerate. Only HOMO-2 is dominated from other parts of the molecule, which is the nitrogen for $[Ala(O)\text{-}H]^-$ and $2p$ shells of some members of the benzene ring for $[Ind(O)\text{-}H]^-$. This is reflected more or less in the measured anisotropy parameters which follow more or less a trend known for a p dominated orbital in the s-p mixing model from Sanov (figure 2.2.2 in section 2.2.2). Unfortunately, the attempted fits do not agree well with the data but effects like the influence of the neutral radical on the departing electron, e.g. the dipole moment, were neglected, which could account for some of the disagreement. Furthermore, lots of not resolved isomer contributions and vibrations could overlapping, hence give a superimposed anisotropy parameter. In the case of $[Ind\text{-}H]^-$, the anisotropy parameter could agree with other studies if certain symmetries of vibrational states dominate [201].

The first successful PECD signal was measured for $[Ind\text{-}H]^-$. Even $[Ala\text{-}H]^-$ seems to show a PECD asymmetry in feature B but it is relatively small and almost at the detection limit of the experiment, which was determined with the help of total electron counts measurements of $[Ind\text{-}H]^-$ and is around 1%. $[Ind\text{-}H]^-$ shows a more convincing PECD signal in all features and changes sign upon switching the light polarization and enantiomer without giving a PECD signal for the racemic mixture. The dependency of the PECD signal on the photon energy (or kinetic energy) shows an individual trend for all features, e.g. feature A (HOMO of the tautomers, especially $[Ind(C3)\text{-}H]^-$) has always a PECD signal with opposite sign than feature B (HOMO and HOMO-1 of $[Ind(O)\text{-}H]^-$). The strongest PECD signal of around -11% is measured for feature C. In comparison to other experimental PECD studies on anions by Krüger *et al.* [2], the strongest PECD signal reported so far was around 4.6% for glutamic acid. Feature B peaks at -6-(-5)%. Even feature A and D, which are assigned to the tautomers, shows a quite strong PECD signal hinting to a contribution of the $[Ind(C3)\text{-}H]^-$ tautomer. They peak at around -5% and 4%, respectively. Furthermore, the PECD signal of feature A and B always have the opposite sign, which emphasizes the importance of energy resolved measurements, since else the total PECD signal is a result of the superimposed PECD signals of A and B making the total PECD signal appears weaker.

In comparison to PECD asymmetries on neutral molecules, e.g. 1-indanol [73] and fenchone [28], the signal strength in anion PECD is in no way inferior. HOMO/HOMO-1 of $[Ind\text{-}H]^-$ and HOMO-2 of 1-indanol, which can be quite similar, e.g. $2p$ of oxygen dominates these orbitals, but also different, e.g. weaker localization of HOMO-2 of 1-indanol, can have similar PECD strengths but also have to opposite PECD asymmetries for low kinetic energies.

PECD signals are measured for kinetic energies between 0.04 eV up to 3.90 eV. The highest kinetic energy with a PECD signal is around 2.2 eV for feature B ($E_{\mathrm{ph}} = 4.59$ eV). Measuring a PECD signal at such high kinetic energies is in contrast to the idea of treating the departing electron as a plane wave and neglecting short-range interactions with the neutral core. The electron is neither a plane wave nor is the influence of short-range interactions unimportant.

6. Summary and Outlook

The aim of this work was to measure PECD signals on anions. Next to experimental advantages like mass spectrometry before photodeteachment and the use of table-top laser instead of e.g synchrotron facilities, the role of short-range interactions regarding the creation of a PECD asymmetry can be studied since long-range monopole interactions are missing. The departing electron is then only influenced by short-range interactions occurring, e.g., due to the presence of bond dipols or scattering potentials. In the beginning, PECD effects on anions were predicted to be non-existent, since photodetached electrons are considered to be a plane wave [49], which can not carry any asymmetry. The lack of PECD experiments on anions seemed to support such assumptions. Initially, only the study of Dreiling *et al.* [50] gave hope on a working PECD experiment on anions. They used quasi-elastic electron-bromocamphor scattering to show that transmission asymmetries of spin-polarized electrons through neutral chiral molecules are non-zero. However, new studies reporting theoretically and experimentally on a non vanishing PECD signal emerged recently and gave new hope in the direction of detecting anion PECD asymmetries [2–4]. Not long after these studies, $[\text{Ind-H}]^-$ also showed the wanted PECD signal. In addition, not only PECD values could be extracted but also PECD images containing the full spatial and energy information are obtained.

The PECD effect for anions was studied on gold-metal complexes and deprotonated molecules. Gold-metal complexes consists of Au^-, which acts as electron source, and a neutral chiral molecule. Deprotonated molecules, on the other hand, carry the charge directly at the molecule itself and have no achiral part, where the electron can be (strongly) localized.

Gold complexes are produced in a laser ablation source, while deprotonated molecules are created in a plasma entrainment souce. Subsequent mass spectrometry separates the desired system from other source products in time. A tunable pulsed laser is synchronized with the time of flight of the desired system and detaches the electrons, which are imaged by a VMI spectrometer on a position sensitive detector. Depending on the polarization of the light, photoelectron spectra can be used to extract binding energies, anisotropy parameters and PECD images. DFT calculations support the experimental findings and reveal the presence and nature of isomers.

While gold complexes do not show a PECD effect, photoelectron spectra recorded with linear polarized light and DFT calculations reveal the bond nature of these complexes. Hydrogen bonds occur between a nonconventional hydrogen acceptor (Au^-), conventional hydrogen donor (O and N) and the hydrogen. However, this was already seen in other studies [127, 176] and could be shown as well for Au^--3HTHF and Au^--Ala. A more interesting focus is directed towards nonconventional acceptors and donors (C), forming $Au^- \cdots$ H-C and if they can be called a hydrogen bond as well. Indeed, all

considered properties of this bond type, e.g. electron donation character, show hydrogen bond characteristics and also fulfill the definition from IUPAC. In comparison to other studies, $Au^- \cdots$ H-C can in fact be called a hydrogen bond of weak strength. This hydrogen bond shows that the Au^- has an effect on the molecule and that the electron indeed interacts with the chiral molecule. Hence, a PECD asymmetry is not excluded but the interaction might be too weak for measuring one.

Fortunately, the deprotonated molecules $[Ala\text{-}H]^-$ and $[Ind\text{-}H]^-$ show a PECD signal in the photodetachment. However, the $[Ala\text{-}H]^-$ anion showed a weak PECD asymmetry for one photon energy, which is (almost) at the detection limit of the experiment (around 1%). Only for the $[Ind\text{-}H]^-$ anion a recognizable PECD signal could be observed. The measured PECD signal depends on the photon energy (or the kinetic energy), reverses its sign upon change of the enantiomer and vanishes for the racemate, just like for the PECD effect on neutrals. For each transition, even for certain subfeatures, an individual PECD signal could be recorded. The strongest PECD signal was around -11 %. For comparison, the strongest PECD signal reported before for electron detachment is 4.6% for deprotonated glutamic acid [2]. Other features for $[Ind\text{-}H]^-$ are similar strong with around -6%. These values are comparable to PECD asymmetries on neutral molecules like 1-indanol [73] and fenchone [28], indicating that, in general, the PECD effect in anions is not inherently weaker than in anions and that short-range effect play an important role regarding PECD signals.

Outlook

$[Ind\text{-}H]^-$ revealed already a nice set of results but some open question remain for the moment: Peak A, assigned to an achiral and a chiral tautormer, could be resolved further to separate the different contributions, which are probably making up this feature. The contribution of the ax. $[Ind\text{-}H]^-$ to the overall spectrum are not completely clear at the moment and require separation from the eq. $[Ind\text{-}H]^-$ before or a better resolution of the VMI spectrometer. Furthermore, the question of the correct sign of PECD values is still unsolved since measurements with PEM and quarter waveplate (QWP) give different signs probably due to a wrong or mislabeled fast axis. However, the absolute values and zero-crossings will still be correct maintaining the non-zero PECD asymmetry for $[Ind\text{-}H]^-$ in photodetachment.

Other potential candidates are $[Ala\text{-}H]^-$, deprotonated 3HTHF or even Au^--1-indanol. $[Ala\text{-}H]^-$ already showed a potentially weak PECD signal and repeating this experiment will probably be successful. 3HTHF has less conformers than alaninol and the deprotonated form could also be a good candidate with an easier PES than $[Ala\text{-}H]^-$. Going back to the gold complexes could also be considered since now, after a successfully measured PECD signal, null-PECD values can be excluded to be from the experimental method. Au^--1-indanol could work due to the success with $[Ind\text{-}H]^-$.

More general questions regarding the anion PECD effect itself could be a comparison in the capabilities between neutral and anion PECD effects. Here, $[Ind\text{-}H]^-$ already shows that anion PECD experiments produce PECD signals in comparable strength to

neutral PECD methods but how does the PECD asymmetry look for the neutral radical Ind-H in comparison? What else is similar/different? Neutral PECD signals vanish if the electrons have a too high kinetic energy supporting the theory of electron having not enough time to scatter properly with the chiral potential. Is there a cutoff energy? And if yes, where is this cutoff energy for anion PECD asymmetries? Artemyev [4] calculated a cutoff energy of around 12 eV for a model chiral system but this was not experimentally confirmed so far and might be vary for different models/chiral systems. Do the PECD signals of vibrational excitations in anion PECD experiments behave in a similar manner than the neutral PECD experiments? Other experiments on neutral PECD asymmetries involved lasers with quite short pulses to follow the evolution of PECD signals. Can there be differences in the evolution of anion and neutral PECD signals?

Anion PECD methods also seemed to be a difficult topic among experimentalists since some groups seemed to have tried such kind of experiments but could not successfully report on it as was indicated by Lai-Sheng Wang and Manfred Kappes in private correspondence. This study also showed problems in the beginning especially with the gold complexes, which do not reveal any detectable PECD asymmetry. For this project, $[\text{Ind-H}]^-$ is – so far – the only successful candidate. What unifies the (un)successful chiral systems regarding anion PECD measurements? Can anion PECD experiments work if an achiral anion, like Au^-, dominates the system or if the charge is too strongly localized at such places? Apart from gold complexes, does the dipole moment of the neutral radical play an important role?

First steps towards anion PECD experiments are done with $[\text{Ind-H}]^-$. However, more work needs to be done in this only a few years old technique to reveal further the nature of the PECD effect.

7. Appendix

A. Gold Complexes

A.1. Structures

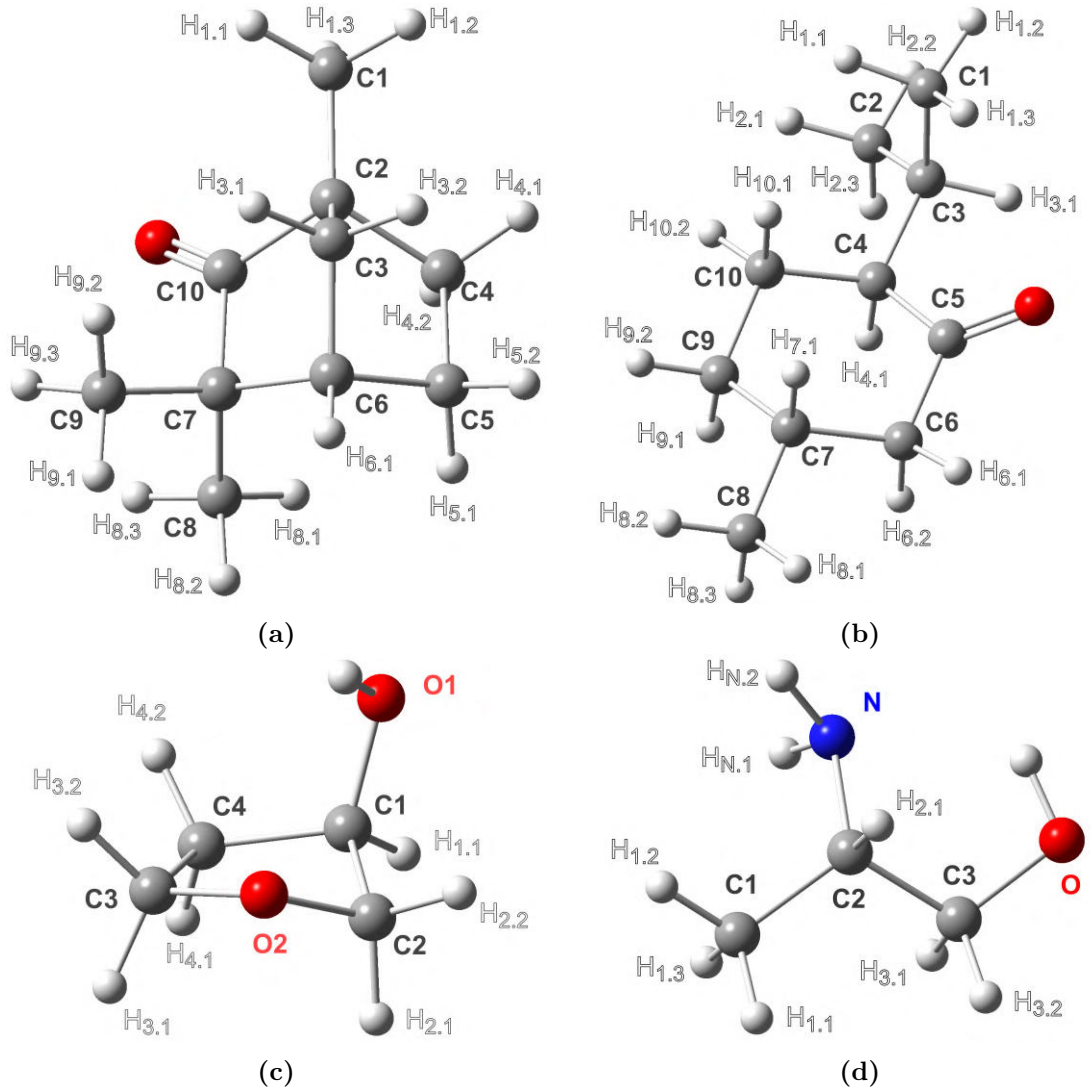

Fig. A.1.: Labeled molecules for Au^--Fen (a), Au^--Men (b), Au^--3HTHF (c) and Au^--Ala (d) for tables A.1 - A.4.

Table A.1.: Structure of F1. Labels according to figure A.1a.

Label	Tag	Symbol	NA	NB	NC	Bond	Angle	Dihedral
O	1	O						
C_2	2	C	1			2.4540083		
C_6	3	C	2	1		2.2845373	97.7357356	
C_7	4	C	3	2	1	1.5565402	77.3292524	-1.2497460
C_3	5	C	3	2	1	1.5422892	42.3444709	-125.9357763
C_4	6	C	2	1	4	1.5671834	110.4757214	77.7575505
C_5	7	C	3	2	1	1.5405022	77.4632584	113.7942513
C_{10}	8	C	1	4	3	1.2117133	31.2401638	-1.8694603
C_1	9	C	2	1	8	1.5106483	94.2016902	-163.5625129
C_2	10	C	4	3	2	1.5313436	116.2591866	119.8785848
C_9	11	C	4	3	2	1.5377218	111.6051247	-115.0549714
$H_{6.1}$	12	H	3	2	1	1.0904550	158.1213584	-121.6102703
$H_{3.1}$	13	H	5	3	2	1.0913231	114.6665852	118.1950140
$H_{3.2}$	14	H	5	3	2	1.0912130	112.9333190	-115.7649346
$H_{4.1}$	15	H	6	2	1	1.0917505	107.9124007	145.4285549
$H_{4.2}$	16	H	6	2	1	1.0918161	111.6602544	25.8415521
$H_{5.1}$	17	H	7	3	2	1.0892052	113.6796597	-127.7261680
$H_{5.2}$	18	H	7	3	2	1.0909839	109.5212046	111.2133377
$H_{1.1}$	19	H	9	2	1	1.0920401	111.0515224	66.9201612
$H_{1.2}$	20	H	9	2	1	1.0904893	109.4841608	-172.8227618
$H_{1.3}$	21	H	9	2	1	1.0914928	110.7590731	-52.5790028
$H_{8.1}$	22	H	10	4	3	1.0884149	112.2384176	-59.0090586
$H_{8.2}$	23	H	10	4	3	1.0927883	110.4227209	61.7200571
$H_{8.3}$	24	H	10	4	3	1.0906825	109.8060299	-178.6528451
$H_{9.1}$	25	H	11	4	3	1.0926329	109.7334536	-71.5400713
$H_{9.2}$	26	H	11	4	3	1.0889911	112.3544114	48.5349805
$H_{9.3}$	27	H	11	4	3	1.0908195	110.1634671	169.0058786
Au	28	Au	6	2	1	3.7769983	95.9107105	177.2728170

Table A.2.: Structure of M1.1. Labels according to figure A.1b.

Label	Tag	Symbol	NA	NB	NC	Bond	Angle	Dihedral
O	1	O						
C_{14}	2	C	1			2.4140363		
C_{10}	3	C	2	1		1.5447253	123.1071723	
C_{7}	4	C	3	2	1	2.5395873	91.2160675	50.2242824
C_{9}	5	C	3	2	1	1.5281514	111.6406693	78.0240867
C_{3}	6	C	2	1	3	1.5371931	88.9942738	-120.1910955
C_{6}	7	C	4	3	2	1.5410125	88.5678868	-1.4958669
C_{5}	8	C	1	7	4	1.2198943	32.2404149	64.3197472
C_{8}	9	C	4	3	2	1.5282351	145.2187833	123.9794530
C_{1}	10	C	6	2	1	1.5325717	113.6916911	72.2923401
C_{2}	11	C	6	2	1	1.5321520	111.0896292	-161.5457525
$H_{4.1}$	12	H	2	1	8	1.1074416	114.6376694	68.0446834
$H_{10.1}$	13	H	3	2	1	1.0952574	109.8959839	-44.1108012
$H_{10.2}$	14	H	3	2	1	1.0915957	108.9768666	-160.9598349
$H_{7.1}$	15	H	4	3	2	1.0985412	91.6302650	-109.3332617
$H_{9.1}$	16	H	5	3	2	1.0944170	108.6637261	63.4090614
$H_{9.2}$	17	H	5	3	2	1.0948197	110.0205011	-179.0212575
$H_{3.1}$	18	H	6	2	1	1.0928394	105.7718341	-44.9155568
$H_{6.1}$	19	H	7	4	3	1.0906992	111.6021446	-148.2601537
$H_{6.2}$	20	H	7	4	3	1.1007487	107.8565432	91.8925217
$H_{8.2}$	21	H	9	4	3	1.0929895	111.1010915	61.9266304
$H_{8.1}$	22	H	9	4	3	1.0927095	111.3393461	-177.5835445
$H_{8.3}$	23	H	9	4	3	1.0916869	109.9510677	-57.7504803
$H_{1.1}$	24	H	10	6	2	1.0926838	111.3201841	67.3139590
$H_{1.2}$	25	H	10	6	2	1.0930013	110.4223530	-173.5890399
$H_{1.3}$	26	H	10	6	2	1.0892833	110.9196637	-53.7332813
$H_{2.1}$	27	H	11	6	2	1.0927194	111.4303273	-67.1521861
$H_{2.2}$	28	H	11	6	2	1.0932073	110.6758274	173.4577332
$H_{2.3}$	29	H	11	6	2	1.0906785	111.0370105	52.8026138
Au	30	Au	2	1	8	3.7261243	113.0613903	53.4576132

Table A.3.: Structure of H1.1. Labels according to figure A.1c.

Label	Tag	Symbol	NA	NB	NC	Bond	Angle	Dihedral
O_2	1	O						
O_1	2	O	1			3.1640680		
C_1	3	C	2	1		1.4143126	45.6982440	
C_4	4	C	3	2	1	1.5368473	111.8472878	74.8198879
C_2	5	C	1	4	3	1.4406270	73.5968189	-13.5954730
C_3	6	C	1	5	3	1.4374186	108.4829591	-3.2045412
$H_{1.1}$	7	H	3	2	1	1.0937392	110.4895257	-160.4060944
$H_{4.1}$	8	H	4	3	2	1.0934770	110.1874688	162.3526680
$H_{4.1}$	9	H	4	3	2	1.0879639	110.5013891	41.7861427
$H_{2.1}$	10	H	5	1	6	1.0943230	107.9898825	-124.1269828
$H_{2.2}$	11	H	5	1	6	1.0917764	109.8969631	116.7129245
$H_{3.2}$	12	H	6	1	5	1.0952583	109.9500930	-92.5693274
$H_{3.1}$	13	H	6	1	5	1.0912121	107.5667887	148.7526284
$H_{O.1}$	14	H	2	1	6	0.9918573	141.0091808	-33.3103656
Au	15	Au	2	1	6	3.2814733	131.9377092	-41.8874732

Table A.4.: Structure of A1.1. Labels according to figure A.1d.

Label	Tag	Symbol	NA	NB	NC	Bond	Angle	Dihedral
O	1	O						
N	2	N	1			2.9372079		
C_2	3	C	2	1		1.4659447	56.5534170	
C_3	4	C	1	3	2	1.4134254	35.3449397	-130.7738724
C_1	5	C	3	2	1	1.5265772	109.7600290	-150.2010976
$H_{2.1}$	6	H	3	2	1	1.0959128	106.8197215	92.0427850
$H_{3.1}$	7	H	4	1	3	1.0973328	110.1894885	121.5766587
$H_{3.2}$	8	H	4	1	3	1.0970525	107.7650208	-120.6406687
$H_{1.1}$	9	H	5	3	2	1.0928596	111.4044613	-178.4143879
$H_{1.3}$	10	H	5	3	2	1.0932861	110.2475562	61.8775801
$H_{1.2}$	11	H	5	3	2	1.0904932	110.5688384	-57.3344337
$H_{N.2}$	12	H	2	1	4	1.0189387	93.2743968	-80.0425928
$H_{N.1}$	13	H	2	1	4	1.0156141	59.2689268	177.1633113
H_O	14	H	1	4	3	0.9889543	107.0913182	-91.8358229
Au	15	Au	1	4	3	3.2931470	95.5017829	-90.7586859

A.2. Calculations

Table A.5.: Comparison of D_0 for B3LYP-D3/aug-cc-pVTZ(-PP), B3LYP-D3(BJ)/def2-tzvp and B3LYP-D3(BJ)/ma-tzvp given in eV. ma-tzvp is the def2-tzvp with the *s* and *p* diffuse basis functions on non-hydrogenic atoms. Hence, def2-tzvp is taken for a reference calculation. ma-tzvp does not contain a basis set for Au. Therefore F^- is taken as substitute for a closed-shell (anionic) system. B3LYP-D3/aug-cc-pVTZ(-PP) and B3LYP-D3(BJ)/ma-tzvp lead to similar results and are closest to the literature values in the case of F^--H_2O.

D_0 (eV)	F^--H_2O	Au^--H_2O
literature	1.136 [203]	0.45 eV [146]
B3LYP-D3 aug-cc-pVTZ(-PP)	1.172	0.515
B3LYP-D3(BJ) def2-tzvp	1.478	0.567
B3LYP-D3(BJ) ma-tzvp	1.186	-

A.3. Bond Lengths and Angles of Au^--M

Table A.6.: Bond lengths and angles for Au^--Fen. The undisturbed C-H bond length is in all cases 0.109 nm.

Complex	H-bond	length (nm) C-H	length (nm) H$\cdots$Au$^-$	angle(°)
F1	C3-H$\cdots$Au	0.109	0.288	151.2
	C4-H$\cdots$Au	0.109	0.293	134.9
	C5-H$\cdots$Au	0.109	0.316	128.4
F2	C6-H$\cdots$Au	0.109	0.292	141.1
	C8-H$\cdots$Au	0.109	0.304	145.8
	C9-H$\cdots$Au	0.109	0.306	144.4
F3	C1-H$\cdots$Au	0.109	0.321	144.0
	C3-H$\cdots$Au	0.109	0.273	158.5
	C9-H$\cdots$Au	0.109	0.297	166.4
F4	C4-H$\cdots$Au	0.109	0.309	129.0
	C5-H$\cdots$Au	0.109	0.294	136.7
	C8-H$\cdots$Au	0.109	0.294	168.4

Table A.7.: Bond lengths and angles for Au^--Men. If the C-H bond length changed due to the disturbance of Au^- the undisturbed bond length is given in brackets else the brackets are omitted.

Complex	H-bond	length (nm) C-H	length (nm) H$\cdots$Au$^-$	angle(°)
M1.1	C4-H$\cdots$Au	0.111(0.110)	0.226	161.0
	C6-H$\cdots$Au	0.110	0.295	144.3
	C9-H$\cdots$Au	0.109(0.110)	0.291	144.8
M2.1	C4-H$\cdots$Au	0.110	0.274	158.2
	C6-H$\cdots$Au	0.110	0.292	147.0
	C9-H$\cdots$Au	0.109(0.110)	0.290	145.7
M3.1	C4-H$\cdots$Au	0.111(0.110)	0.266	162.0
	C6-H$\cdots$Au	0.110	0.293	145.1
	C9-H$\cdots$Au	0.109(0.110)	0.292	144.4
M4.1	C3-H$\cdots$Au	0.109	0.281	173.1
	C6-H$\cdots$Au	0.110(0.109)	0.278	147.5
	C9-H$\cdots$Au	0.109	0.293	142.1

Table A.8.: Bond lengths and angles for Au^--Men. The C-H bond lengths remain unchanged despite disturbance of Au^-

Complex	H-bond	length (nm) C-H	length (nm) H$\cdots$Au$^-$	angle(°)
M1.2	C7-H$\cdots$Au	0.110	0.298	130.7
	C9-H$\cdots$Au	0.109	0.308	117.7
	C10-H$\cdots$Au	0.109	0.307	130.1
M3.2	C7-H$\cdots$Au	0.110	0.298	130.9
	C9-H$\cdots$Au	0.109	0.308	117.7
	C10-H$\cdots$Au	0.109	0.307	130.3
M2.2	C7-H$\cdots$Au	0.110	0.303	126.9
	C9-H$\cdots$Au	0.109	0.298	122.4
	C10-H$\cdots$Au	0.109	0.322	124.3
M4.2	C7-H$\cdots$Au	0.109	0.305	121.3
	C8-H$\cdots$Au	0.109	0.319	125.9
	C9-H$\cdots$Au	0.109	0.308	123.1

Table A.9.: Bond lengths and angles for Au^--Men. The undisturbed C-H bond length is 0.109 nm.

Complex	H-bond	length (nm) C-H	length (nm) H$\cdots$Au$^-$	angle(°)
M4.3	C2-H$\cdots$Au	0.109	0.293	149.3
	C4-H$\cdots$Au	0.109	0.315	125.3
	C10-H$\cdots$Au	0.109	0.312	119.3
M1.3	C1-H$\cdots$Au	0.109	0.306	151.6
	C2-H$\cdots$Au	0.109	0.289	159.5
	C3-H$\cdots$Au	0.109	0.427	87.9
M2.3	C1-H$\cdots$Au	0.109	0.288	164.5
	C2-H$\cdots$Au	0.109	0.308	153.1
	C3-H$\cdots$Au	0.109	0.442	83.9

Table A.10.: Bond lengths and angles for Au^--3HTHF. If the C-H or O-H bond length changed due to the disturbance of Au^- the undisturbed bond length is given in brackets else the brackets are omitted. A clear change is visible for the O-H bond length.

Complex	H-bond	length (nm) C,O-H	length (nm) H$\cdots$Au$^-$	angle(°)
H1.1	C1-H$\cdots$Au	0.109	0.231	92.2
	C4-H$\cdots$Au	0.109	0.318	124.8
	O-H$\cdots$Au	0.099(0.096)	0.231	164.6
H1.2	C1-H$\cdots$Au	0.109	0.337	96.3
	C2-H$\cdots$Au	0.109	0.339	111.2
	O-H$\cdots$Au	0.099(0.096)	0.231	162.1
H1.3	C2-H$\cdots$Au	0.110	0.321	127.2
	C3-H$\cdots$Au	0.110(0.109)	0.312	128.6
	C4-H$\cdots$Au	0.109	0.319	115.5
	O-H$\cdots$Au	0.099(0.096)	0.234	169.0

Table A.11.: Bond lengths and angles for Au^--3HTHF. If the C-H bond length changed due to the disturbance of Au^- the undisturbed bond length is given in brackets else the brackets are omitted.

Complex	H-bond	length (nm) C-H	length (nm) H$\cdots$Au$^-$	angle(°)
H1.4	C2-H$\cdots$Au	0.110	0.299	139.5
	C3-H$\cdots$Au	0.109	0.325	121.9
	C4-H$\cdots$Au	0.109	0.292	131.1
H2.1	C1-H$\cdots$Au	0.109	0.298	124.5
	C2-H$\cdots$Au	0.109	0.309	130.5
	C4-H$\cdots$Au	0.109	0.313	130.7
H2.2	C1-H$\cdots$Au	0.109	0.304	119.4
	C2-H$\cdots$Au	0.110(0.109)	0.316	125.9
	C3-H$\cdots$Au	0.110(0.109)	0.327	123.3
	C4-H$\cdots$Au	0.109	0.319	113.8

Table A.12.: Bond lengths and angles for Au^--Ala. If the C-H, N-H or O-H bond length changed due to the disturbance of Au^- the undisturbed bond length is given in brackets else the brackets are omitted. A clear change is visible for the O-H bond length. The N-H bond length changes like C-H.

Complex	H-bond	length (nm) C,O,N-H	length (nm) H$\cdots$Au$^-$	angle(°)
A1.1	C3-H$\cdots$Au	0.110	0.323	107.1
	N-$H_{N.1}\cdots$Au	0.102(0.101)	0.331	102.0
	N-$H_{N.2}\cdots$Au	0.102(0.101)	0.301	122.4
	O-H$\cdots$Au	0.099(0.097)	0.233	163.5
A2.1	C3-H$\cdots$Au	0.110	0.324	107.0
	N-$H_{N.1}\cdots$Au	0.102(0.101)	0.300	122.6
	O-H$\cdots$Au	0.099(0.097)	0.233	164.0
A3.1	C2-H$\cdots$Au	0.110	0.307	133.6
	C3-H$\cdots$Au	0.110(0.109)	0.350	93.1
	O-H$\cdots$Au	0.099(0.096)	0.232	165.1
A4.1	C2-H$\cdots$Au	0.109(0.110)	0.322	127.6
	C3-H$\cdots$Au	0.110	0.330	100.0
	O-H$\cdots$Au	0.099(0.096)	0.232	162.2

Table A.13.: Bond lengths and angles for Au^--Ala.If the C-H, N-H or O-H bond length changed due to the disturbance of Au^- the undisturbed bond length is given in brackets else the brackets are omitted. A clear change is visible for the O-H bond length. The N-H bond length changes like C-H but for A2.2 where N-H is elongated more.

Complex	H-bond	length (nm) C,O,N-H	length (nm) H$\cdots$Au$^-$	angle(°)
A4.2	C2-H$\cdots$Au	0.109(0.110)	0.305	121.1
	N-$H_{N.1}\cdots$Au	0.102(0.101)	0.297	138.5
	O-H$\cdots$Au	0.099(0.096)	0.232	170.0
A3.2	C3-H$\cdots$Au	0.110	0.390	85.9
	N-$H_{N.2}\cdots$Au	0.102(0.101)	0.254	174.7
	O-H$\cdots$Au	0.099(0.096)	0.232	175.3
A2.2	C1-H$\cdots$Au	0.109	0.373	126.8
	N-$H_{N.1}\cdots$Au	0.103(0.101)	0.253	171.6
	O-H$\cdots$Au	0.099(0.097)	0.232	173.5
A5.1	C2-H$\cdots$Au	0.109(0.110)	0.317	127.5
	C3-H$\cdots$Au	0.110(0.109)	0.324	101.6
	O-H$\cdots$Au	0.099(0.096)	0.236	159.4

Table A.14.: Bond lengths and angles for Au^--Ala. If the C-H or N-H bond length changed due to the disturbance of Au^- the undisturbed bond length is given in brackets else the brackets are omitted. The N-H bond length is clearly changed and is (almost) always longer than in the first two groups of Au^--Ala (with $Au^- \cdots$ H-O).

Complex	H-bond	length (nm) C,N-H	length (nm) H$\cdots$Au$^-$	angle(°)
A1.2	C1-H$\cdots$Au	0.109	0.309	136.2
	C2-H$\cdots$Au	0.109	0.366	94.9
	N-$H_{N.2}\cdots$Au	0.103(0.101)	0.251	157.9
A1.3	C1-H$\cdots$Au	0.109	0.301	140.3
	C3-H$\cdots$Au	0.110	0.343	131.6
	N-$H_{N.1}\cdots$Au	0.103(0.101)	0.252	167.3
A2.3	C1-H$\cdots$Au	0.109	0.314	134.5
	C2-H$\cdots$Au	0.110	0.363	95.2
	N-$H_{N.1}\cdots$Au	0.103(0.101)	0.253	150.8
A2.4	C2-H$\cdots$Au	0.110	0.320	112.7
	C3-H$\cdots$Au	0.110	0.350	122.3
	N-$H_{N.2}\cdots$Au	0.103(0.101)	0.252	151.5

Table A.15.: Bond lengths and angles for Au^--Ala. If the C-H or N-H bond length changed due to the disturbance of Au^- the undisturbed bond length is given in brackets else the brackets are omitted. Only A5.2 shows a clear elongation for N-H. The rest changes like the C-H bond.

Complex	H-bond	length (nm) C,N-H	length (nm) H$\cdots$Au$^-$	angle(°)
A5.2	C1-H$\cdots$Au	0.109	0.318	128.7
	C2-H$\cdots$Au	0.110	0.320	111.5
	N-$H_{N.2}\cdots$Au	0.102(0.101)	0.263	149.6
A5.3	C1-H$\cdots$Au	0.109	0.321	137.1
	C3-H$\cdots$Au	0.109(0.110)	0.310	134.0
	N-$H_{N.2}\cdots$Au	0.103(0.101)	0.255	161.4
A4.3	C1-H$\cdots$Au	0.109	0.298	143.4
	C3-H$\cdots$Au	0.109	0.308	141.8
	N-$H_{N.2}\cdots$Au	0.102(0.101)	0.273	156.6

A.4. Scaling Factors for PECD measurements with Au^--M

Table A.16.: Scaling factors for the PES of Au^--M for the PECD measurements. Maximum of fully peeled LCP spectrum divided by the maximum of the RCP spectrum gives the scaling factor. Au^--Ala produces more spectra with scaling factors being closer to 1 than for the other Au^-M. In the case for the quarter waveplate (QWP) this can be attributed to signal stability while the measurements with PEM benefit from the shot-to-shot measurement. U_R is the used repeller voltage of the VMI spectrometer.

System	E_{ph} (eV)	scaling factor (LCP/RCP)	comments
Au^-Fen	4.13	1.5468	
	3.02	0.9953	
	2.79	0.9138	
Au^-Men	4.35	0.8466	
	4.13	7.6512	
	2.85	0.9429	
Au^-3HTHF	4.40	1.0179	
	3.49	0.8291	
Au^-Ala (QWP)	4.13	0.9932	
	3.49	1.0184	
	3.02	0.9522	$U_R = 800$ V
	3.02	1.0349	$U_R = 100$ V
Au^-Ala (PEM)	4.35	1.0392	$U_R = 1900$ V
	4.35	0.9502	$U_R = 700$ V
	3.49	0.9588	
	3.02	0.9657	

B. Deprotonated Molecules

B.1. Structures

Table B.1.: Structure of A-H1.

Label	Tag	Symbol	NA	NB	NC	Bond	Angle	Dihedral
	1	O						
	2	N	1			2.8175384		
C_2	3	C	2	1		1.4762404	59.3828344	
C_3	4	C	1	3	2	1.3375980	36.3555748	-135.2480684
C_1	5	C	3	2	1	1.5209991	110.8617700	-148.8439681
$H_{2.1}$	6	H	3	2	1	1.0970319	106.4452257	92.5459148
$H_{3.1}$	7	H	4	1	3	1.1386138	114.2278594	119.1573187
$H_{3.2}$	8	H	4	1	3	1.1318903	115.0989910	-121.1436237
$H_{1.1}$	9	H	5	3	2	1.0937463	110.4355486	-179.7182482
$H_{1.3}$	10	H	5	3	2	1.0955159	110.4282384	61.5853330
$H_{1.2}$	11	H	5	3	2	1.0937035	111.9132687	-58.6503937
$H_{N.2}$	12	H	2	1	4	1.0196691	101.5298644	-74.9414458
$H_{N.1}$	13	H	2	1	4	1.0252842	45.4189881	-173.0212732

Table B.2.: Structure of eq. Ind-H.

Label	Tag	Symbol	NA	NB	NC	Bond	Angle	Dihedral
C_5	1	C						
C_4	2	C	1			1.3950314		
C_9	3	C	2	1		1.3883794	120.6957794	
C_8	4	C	3	2	1	1.3974118	119.1805217	-0.0462083
C_7	5	C	4	3	2	1.3954994	120.0670447	0.6644738
C_6	6	C	1	2	3	1.3859441	120.2349155	-1.0686706
C_3	7	C	2	1	6	1.5137947	109.9439474	177.6432044
	8	H	3	2	1	1.0858467	120.7096044	178.8841178
	9	H	4	3	2	1.0839052	119.9856304	179.4298517
	10	H	5	4	3	1.0847592	119.4492265	178.8593845
	11	H	6	1	2	1.0836841	118.5454010	-176.9699089
C_1	12	C	1	6	5	1.5420134	127.4411389	179.5791170
C_2	13	C	7	2	1	1.5421002	102.5681207	-19.0449251
	14	H	7	2	1	1.0972242	110.0128174	98.4225519
	15	H	7	2	1	1.0943030	112.5097288	-142.6873616
	16	H	13	7	2	1.0940651	110.6040823	-83.7828960
	17	H	13	7	2	1.0914588	113.8142979	153.7879706
	18	O	12	1	6	1.3228990	117.8870667	-30.8248088
	19	H	12	1	6	1.1417610	102.5214933	95.3487313

B.2. PECD

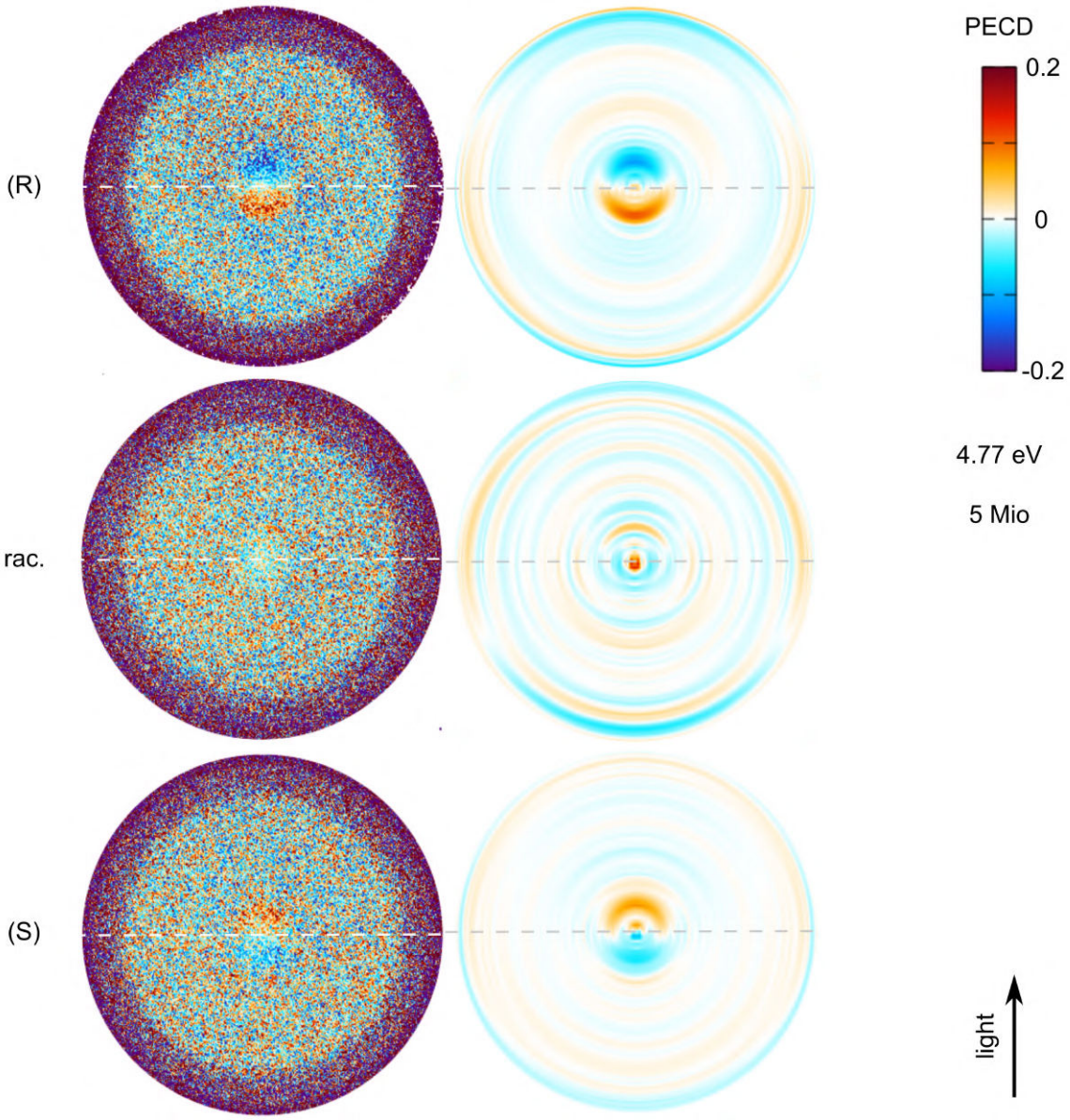

Fig. B.1.: PECD PADs of (R)-, (S)- and racemate [Ind-H]$^-$ at $E_{\mathrm{ph}} = 4.77$ eV. All images have the same counts of 5 Mio electrons. Despite the same counts, the (S)-[Ind-H]$^-$ measurement shows a less pronounced PECD signal than the (R)-[Ind-H]$^-$. This can be explained by the worse signal-to-noise ratio. The racemic mixture shows no PECD signal.

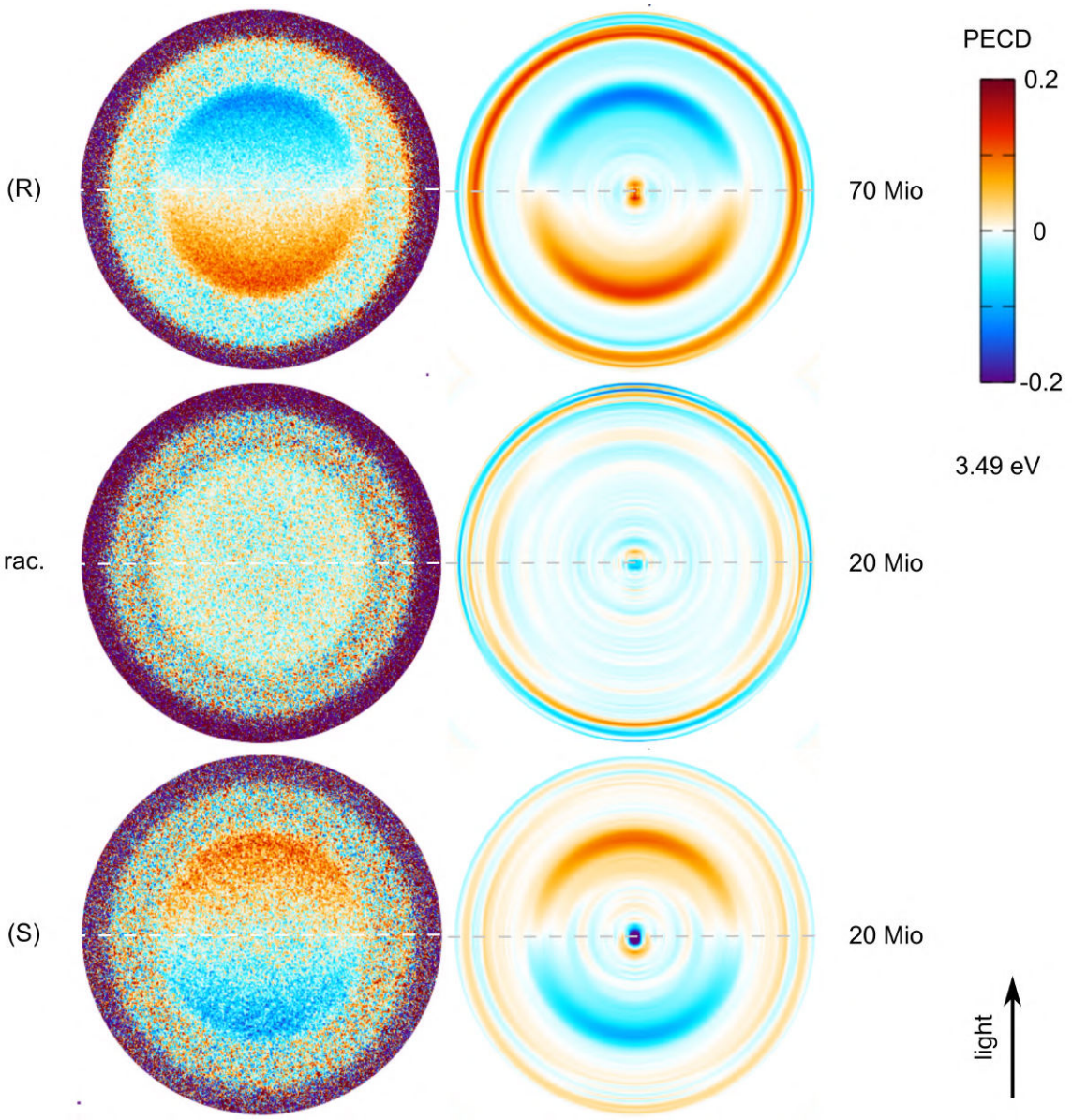

Fig. B.2.: PECD PADs of (R)-, (S)- and racemate $[\text{Ind-H}]^-$ at $E_{\text{ph}} = 3.49$ eV. The counts per polarization are given next to the image. The racemic mixture shows no PECD signal while (R) and (S) show a clear inversed PECD signal.

Bibliography

[1] V. Ulrich, S. Barth, S. Joshi, U. Hergenhahn, E. Mikajlo, C. J. Harding, I. Powis, *The Journal of Physical Chemistry A* **2008**, *112*, 3544–3549.

[2] P. Krüger, K.-M. Weitzel, *Angewandte Chemie* **2021**, DOI 10.1002/anie.202107150.

[3] P. Krüger, J. H. Both, U. Linne, F. Chirot, K.-M. Weitzel, *The Journal of Physical Chemistry Letters* **2022**, *13*, 6110–6116.

[4] A. N. Artemyev, E. Kutscher, P. V. Demekhin, *The Journal of Chemical Physics* **2022**, *156*, 031101.

[5] G. Nagendrappa, *Resonance* **2007**, *12*, 38–48.

[6] I. Ilisz, R. Berkecz, A. Péter, *Journal of pharmaceutical and biomedical analysis* **2008**, *47*, 1–15.

[7] X. Yu, Z.-P. Yao, *Analytica Chimica Acta* **2017**, *968*, 1–20.

[8] A. V. Orlova, R. R. Andrade, C. O. da Silva, A. I. Zinin, L. O. Kononov, *ChemPhysChem* **2014**, *15*, 195–207.

[9] V. Parchaňskỳ, J. Kapitán, P. Bouř, *RSC Advances* **2014**, *4*, 57125–57136.

[10] B. Ranjbar, P. Gill, *Chemical biology & drug design* **2009**, *74*, 101–120.

[11] V. A. Shubert, D. Schmitz, M. Schnell, *Journal of Molecular Spectroscopy* **2014**, *300*, 31–36.

[12] S. Eibenberger, J. Doyle, D. Patterson, *Physical review letters* **2017**, *118*, 123002.

[13] M. Pitzer, M. Kunitski, A. S. Johnson, T. Jahnke, H. Sann, F. Sturm, L. P. H. Schmidt, H. Schmidt-Böcking, R. Dörner, J. Stohner, et al., *Science* **2013**, *341*, 1096–1100.

[14] K. Fehre, S. Eckart, M. Kunitski, M. Pitzer, S. Zeller, C. Janke, D. Trabert, J. Rist, M. Weller, A. Hartung, et al., *Science advances* **2019**, *5*, eaau7923.

[15] L. Nahon, G. A. Garcia, I. Powis, *Journal of Electron Spectroscopy and Related Phenomena* **2015**, *204*, 322–334.

[16] B. Ritchie, *Physical Review A* **1976**, *13*, 1411.

[17] N. Böwering, T. Lischke, B. Schmidtke, N. Müller, T. Khalil, U. Heinzmann, *Physical review letters* **2001**, *86*, 1187.

[18] T. Jahnke, T. Weber, A. Landers, A. Knapp, S. Schössler, J. Nickles, S. Kammer, O. Jagutzki, L. Schmidt, A. Czasch, et al., *Physical review letters* **2002**, *88*, 073002.

[19] J. Viefhaus, L. Avaldi, G. Snell, M. Wiedenhöft, R. Hentges, A. Rüdel, F. Schäfers, D. Menke, U. Heinzmann, A. Engelns, et al., *Physical review letters* **1996**, *77*, 3975.

[20] M. Tia, M. Pitzer, G. Kastirke, J. Gatzke, H.-K. Kim, F. Trinter, J. Rist, A. Hartung, D. Trabert, J. Siebert, et al., *The journal of physical chemistry letters* **2017**, *8*, 2780–2786.

[21] S. Beaulieu, A. Ferré, R. Géneaux, R. Canonge, D. Descamps, B. Fabre, N. Fedorov, F. Légaré, S. Petit, T. Ruchon, et al., *New Journal of Physics* **2016**, *18*, 102002.

[22] M. Wollenhaupt, *New Journal of Physics* **2016**, *18*, 121001.

[23] T. Lischke, N. Böwering, B. Schmidtke, N. Müller, T. Khalil, U. Heinzmann, *Physical Review A* **2004**, *70*, 022507.

[24] U. Hergenhahn, E. E. Rennie, O. Kugeler, S. Marburger, T. Lischke, I. Powis, G. Garcia, *The Journal of chemical physics* **2004**, *120*, 4553–4556.

[25] I. Powis, *The Journal of Chemical Physics* **2000**, *112*, 301–310.

[26] D. Di Tommaso, M. Stener, G. Fronzoni, P. Decleva, *Chemphyschem: a European journal of chemical physics and physical chemistry* **2006**, *7*, 924–934.

[27] G. A. Garcia, H. Dossmann, L. Nahon, S. Daly, I. Powis, *Physical Chemistry Chemical Physics* **2014**, *16*, 16214–16224.

[28] I. Powis, C. J. Harding, G. A. Garcia, L. Nahon, *ChemPhysChem* **2008**, *9*, 475–483.

[29] L. Nahon, L. Nag, G. A. Garcia, I. Myrgorodska, U. Meierhenrich, S. Beaulieu, V. Wanie, V. Blanchet, R. Géneaux, I. Powis, *Physical Chemistry Chemical Physics* **2016**, *18*, 12696–12706.

[30] S. Turchini, D. Catone, G. Contini, N. Zema, S. Irrera, M. Stener, D. Di Tommaso, P. Decleva, T. Prosperi, *ChemPhysChem* **2009**, *10*, 1839–1846.

[31] D. Catone, S. Turchini, G. Contini, T. Prosperi, M. Stener, P. Decleva, N. Zema, *Chemical Physics* **2017**, *482*, 294–302.

[32] D. Loru, M. A. Bermúdez, M. E. Sanz, *The Journal of chemical physics* **2016**, *145*, 074311.

[33] M. Tia, B. Cunha de Miranda, S. Daly, F. Gaie-Levrel, G. A. Garcia, L. Nahon, I. Powis, *The Journal of Physical Chemistry A* **2014**, *118*, 2765–2779.

[34] G. A. Garcia, L. Nahon, S. Daly, I. Powis, *Nature Communications* **2013**, *4*, 2132.

[35] S. Turchini, N. Zema, G. Contini, G. Alberti, M. Alagia, S. Stranges, G. Fronzoni, M. Stener, P. Decleva, T. Prosperi, *Physical Review A* **2004**, *70*, 014502.

[36] S. Malerz, H. Haak, F. Trinter, A. B. Stephansen, C. Kolbeck, M. Pohl, U. Hergenhahn, G. Meijer, B. Winter, *Review of Scientific Instruments* **2022**, *93*, 015101.

[37] M. N. Pohl, S. Malerz, F. Trinter, C. Lee, C. Kolbeck, I. Wilkinson, S. Thürmer, D. M. Neumark, L. Nahon, I. Powis, et al., *Physical Chemistry Chemical Physics* **2022**, *24*, 8081–8092.

[38] M. Tia, B. Cunha de Miranda, S. Daly, F. Gaie-Levrel, G. A. Garcia, I. Powis, L. Nahon, *The Journal of Physical Chemistry Letters* **2013**, *4*, 2698–2704.

[39] A. Kastner, G. Koumarianou, P. Glodic, P. C. Samartzis, N. Ladda, S. T. Ranecky, T. Ring, S. Vasudevan, C. Witte, H. Braun, et al., *Physical Chemistry Chemical Physics* **2020**, *22*, 7404–7411.

[40] A. Kastner, T. Ring, H. Braun, A. Senftleben, T. Baumert, *ChemPhysChem* **2019**, *20*, 1416–1419.

[41] R. E. Goetz, C. P. Koch, L. Greenman, *Physical review letters* **2019**, *122*, 013204.

[42] M. M. R. Fanood, N. B. Ram, C. S. Lehmann, I. Powis, M. H. Janssen, *Nature communications* **2015**, *6*, 1–8.

[43] C. S. Lehmann, N. B. Ram, I. Powis, M. H. Janssen, *The Journal of Chemical Physics* **2013**, *139*, 234307.

[44] C. S. Lehmann, K.-M. Weitzel, *Physical Chemistry Chemical Physics* **2020**, *22*, 13707–13712.

[45] J. Miles, D. Fernandes, A. Young, C. Bond, S. Crane, O. Ghafur, D. Townsend, J. Sá, J. Greenwood, *Analytica chimica acta* **2017**, *984*, 134–139.

[46] A. Comby, C. M. Bond, E. Bloch, D. Descamps, B. Fabre, S. Petit, Y. Mairesse, J. B. Greenwood, V. Blanchet, *Chirality* **2020**, *32*, 1225–1233.

[47] I. Powis, S. Daly, M. Tia, B. C. de Miranda, G. A. Garcia, L. Nahon, *Physical Chemistry Chemical Physics* **2014**, *16*, 467–476.

[48] J. Triptow, A. Fielicke, G. Meijer, M. Green, *Angewandte Chemie International Edition* **2022**, DOI 10.1002/anie.202212020.

[49] S. Gozem, A. O. Gunina, T. Ichino, D. L. Osborn, J. F. Stanton, A. I. Krylov, *The journal of physical chemistry letters* **2015**, *6*, 4532–4540.

[50] J. Dreiling, T. J. Gay in Journal of Physics: Conference Series, *Vol. 635*, IOP Publishing, **2015**, p. 012015.

[51] J. Triptow, G. Meijer, A. Fielicke, O. Dopfer, M. Green, *The Journal of Physical Chemistry A* **2022**, DOI 10.1021/acs.jpca.2c02725.

[52] J. Franck, E. Dymond, *Transactions of the Faraday Society* **1926**, *21*, 536–542.

[53] E. Condon, *Physical Review* **1926**, *28*, 1182.

[54] J. Cooper, R. N. Zare, *The Journal of chemical physics* **1968**, *48*, 942–943.

[55] C. Melania Oana, A. I. Krylov, *The Journal of chemical physics* **2007**, *127*, 234106.

[56] J. A. DeVine, M. C. Babin, K. Blackford, D. M. Neumark, *The Journal of Chemical Physics* **2019**, *151*, 064302.

[57] D. Hanstorp, C. Bengtsson, D. Larson, *Physical Review A* **1989**, *40*, 670.

[58] A. Sanov, *Annual review of physical chemistry* **2014**, *65*, 341–363.

[59] A. Sanov, E. R. Grumbling, D. J. Goebbert, L. M. Culberson, *The Journal of chemical physics* **2013**, *138*, 054311.

[60] E. Surber, R. Mabbs, A. Sanov, *The Journal of Physical Chemistry A* **2003**, *107*, 8215–8224.

[61] R. Mabbs, E. Surber, A. Sanov, *The Journal of chemical physics* **2005**, *122*, 054308.

[62] M. H. Janssen, I. Powis, *Physical Chemistry Chemical Physics* **2014**, *16*, 856–871.

[63] K.-N. Huang, *Physical Review A* **1980**, *22*, 223.

[64] H. A. Bethe, E. E. Salpeter, *Quantum mechanics of one-and two-electron atoms*, Springer Science & Business Media, **2012**.

[65] E. P. Wigner, *Physical Review* **1948**, *73*, 1002.

[66] R. Mabbs, F. Mbaiwa, J. Wei, M. Van Duzor, S. T. Gibson, S. J. Cavanagh, B. R. Lewis, *Physical Review A* **2010**, *82*, 011401.

[67] V. Ivanov, *Radiation Physics and Chemistry* **2004**, *70*, 345–370.

[68] D. Y. Valdivielso, PhD thesis, Technische Universität Berlin, **2022**.

[69] T. Schirmeister, C. Schmuck, P. R. Wich, *Beyer/Walter— Organische Chemie*, Hirzel Verlag, **2015**.

[70] G. P. Moss, *Pure and applied chemistry* **1996**, *68*, 2193–2222.

[71] M. Born, E. Wolf, *Principles of optics: electromagnetic theory of propagation, interference and diffraction of light*, Elsevier, **2013**.

[72] V. Svoboda, M. D. Waters, D. Zindel, H. J. Wörner, *Optics Express* **2022**, *30*, 14358–14367.

[73] J. Dupont, V. Lepère, A. Zehnacker, S. Hartweg, G. A. Garcia, L. Nahon, *The Journal of Physical Chemistry Letters* **2022**, *13*, 2313–2320.

[74] A. Giardini, D. Catone, S. Stranges, M. Satta, M. Tacconi, S. Piccirillo, S. Turchini, N. Zema, G. Contini, T. Prosperi, et al., *ChemPhysChem* **2005**, *6*, 1164–1168.

[75] R. Fausto, C. Cacela, M. Duarte, *Journal of Molecular Structure* **2000**, 365–388.

[76] J. Schiller, J. Hormes, *Nuclear Instruments and Methods in Physics Research Section A: Accelerators Spectrometers Detectors and Associated Equipment* **1986**, *246*, 772–775.

[77] T. Andersen, H. Haugen, H. Hotop, *Journal of Physical and Chemical Reference Data* **1999**, *28*, 1511–1533.

[78] P. Linstrom, E. W.G. Mallard, *NIST Chemistry WebBook, NIST Standard Reference Database Number 69*, National Institute of Standards and Technology, Gaithersburg MD, 20899, **2023**.

[79] P. Grüne, PhD thesis, Technische Universität Berlin, **2009**.

[80] M. Härtelt, PhD thesis, Technische Universität Berlin, **2012**.

[81] Y.-J. Lu, J. H. Lehman, W. C. Lineberger, *The Journal of chemical physics* **2015**, *142*, 044201.

[82] T. G. Dietz, M. A. Duncan, D. E. Powers, R. E. Smalley, *The Journal of Chemical Physics* **1981**, *74*, 6511–6512.

[83] D. E. Powers, S. G. Hansen, M. Geusic, A. Puiu, J. Hopkins, T. Dietz, M. Duncan, P. Langridge-Smith, R. Smalley, *The Journal of Physical Chemistry* **1982**, *86*, 2556–2560.

[84] V. Bondybey, J. English, *The Journal of Chemical Physics* **1981**, *74*, 6978–6979.

[85] M. A. Duncan, *Review of Scientific Instruments* **2012**, *83*, 041101.

[86] A. Fielicke, G. Von Helden, G. Meijer, *The European Physical Journal D-Atomic Molecular Optical and Plasma Physics* **2005**, *34*, 83–88.

[87] H. Conrads, M. Schmidt, *Plasma Sources Science and Technology* **2000**, *9*, 441.

[88] A. Bogaerts in *Encyclopedia of spectroscopy and spectrometry/Lindon, JC [edit.]* **2000**, pp. 669–676.

[89] C. Budtz-Jørgensen, J. Bøttiger, P. Kringhøj, *Surface and Coatings Technology* **2001**, *137*, 104–110.

[90] P. Hartmann, R. Haubner, B. Lux, *Diamond and related materials* **1996**, *5*, 850–856.

[91] D. L. Osborn, D. J. Leahy, D. R. Cyr, D. M. Neumark, *The Journal of chemical physics* **1996**, *104*, 5026–5039.

[92] D. W. Boo, Y. Ozaki, L. H. Andersen, W. Lineberger, *The Journal of Physical Chemistry A* **1997**, *101*, 6688–6696.

[93] M. Jiménez-Redondo, E. Carrasco, V. J. Herrero, I. Tanarro, *Plasma Sources Science and Technology* **2015**, *24*, 015029.

[94] P. Brix, G. Herzberg, *The Journal of Chemical Physics* **1953**, *21*, 2240–2240.

[95] S. T. Arnold, J. H. Hendricks, K. H. Bowen, *The Journal of chemical physics* **1995**, *102*, 39–47.

[96] W. Wiley, I. H. McLaren, *Review of scientific instruments* **1955**, *26*, 1150–1157.

[97] A. T. Eppink, D. H. Parker, *Review of Scientific Instruments* **1997**, *68*, 3477–3484.

[98] D. A. Horke, G. M. Roberts, J. Lecointre, J. R. Verlet, *Review of Scientific Instruments* **2012**, *83*, 063101.

[99] I. León, Z. Yang, H.-T. Liu, L.-S. Wang, *Review of Scientific Instruments* **2014**, *85*, 083106.

[100] A. Osterwalder, M. J. Nee, J. Zhou, D. M. Neumark, *The Journal of chemical physics* **2004**, *121*, 6317–6322.

[101] C. Hock, J. B. Kim, M. L. Weichman, T. I. Yacovitch, D. M. Neumark, *The Journal of chemical physics* **2012**, *137*, 244201.

[102] D. R. Herschbach, *Discussions of the Faraday Society* **1962**, *33*, 149–161.

[103] M. N. Ashfold, N. H. Nahler, A. J. Orr-Ewing, O. P. Vieuxmaire, R. L. Toomes, T. N. Kitsopoulos, I. A. Garcia, D. A. Chestakov, S.-M. Wu, D. H. Parker, *Physical Chemistry Chemical Physics* **2006**, *8*, 26–53.

[104] A. Bodi, P. Hemberger, R. P. Tuckett, *Physical Chemistry Chemical Physics* **2017**, *19*, 30173–30180.

[105] M. Génévriez, K. M. Dunseath, M. Terao-Dunseath, A. Hibbert, A. Dochain, R. Marion, X. Urbain, *Physical Review A* **2018**, *98*, 033410.

[106] N. H. Abel, **1826**, DOI 10.1515/crll.1826.1.153.

[107] B. Whitaker, *Imaging in Molecular Dynamics, Technology and Application*, Cambridge University Press, **2003**.

[108] K. Zhao, T. Colvin, W. T. Hill, G. Zhang, *Review of Scientific Instruments* **2002**, *73*, 3044–3050.

[109] V. Dribinski, A. Ossadtchi, V. A. Mandelshtam, H. Reisler, *Review of Scientific Instruments* **2002**, *73*, 2634–2642.

[110] G. A. Garcia, L. Nahon, I. Powis, *Review of Scientific Instruments* **2004**, *75*, 4989–4996.

[111] G. M. Roberts, J. L. Nixon, J. Lecointre, E. Wrede, J. R. R. Verlet, *Review of Scientific Instruments* **2009**, *80*, 053104.

[112] S. T. Gibson, D. D. Hickstein, R. Yurchak, M. Ryazanov, D. D. Das, G. Shih, **2022**, DOI 10.5281/zenodo.5888391.

[113] B. Dick, *Physical Chemistry Chemical Physics* **2014**, *16*, 570–580.

[114] D. D. Hickstein, S. T. Gibson, R. Yurchak, D. D. Das, M. Ryazanov, *Review of Scientific Instruments* **2019**, *90*, 065115.

[115] M. Ryazanov, PhD thesis, University of Southern California, USA, **2012**.

[116] B. Dick, *Physical Chemistry Chemical Physics* **2019**, *21*, 19499–19512.

[117] J. E. Sansonetti, W. C. Martin, *Journal of physical and chemical reference data* **2005**, *34*, 1559–2259.

[118] P. Johnsson, A. Rouzée, W. Siu, Y. Huismans, F. Lépine, T. Marchenko, S. Düsterer, F. Tavella, N. Stojanovic, H. Redlin, et al., *Optics letters* **2010**, *35*, 4163–4165.

[119] B. Schaefer, E. Collett, R. Smyth, D. Barrett, B. Fraher, *American Journal of Physics* **2007**, *75*, 163–168.

[120] A. Hong, C. M. Choi, H. J. Eun, C. Jeong, J. Heo, N. J. Kim, *Angewandte Chemie International Edition* **2014**, *53*, 7805–7808.

[121] J. C. Kemp, *J. Opt. Soc. Am.* **1969**, *59*, 950–954.

[122] D. Yang, J. Canit, E. Gaignebet, *Journal of optics* **1995**, *26*, 151.

[123] M. Bonmarin, J. Helbing, *Chirality: the pharmacological biological and chemical consequences of molecular asymmetry* **2009**, *21*, E298–E306.

[124] S. Hosokawa, N. Takahashi, M. Saito, Y. Haruyama, *Review of Scientific Instruments* **2010**, *81*, 063301.

[125] K. Tobita, H. Takeuchi, H. Kimura, Y. Kusama, M. Nemoto, *Japanese journal of applied physics* **1987**, *26*, 509.

[126] S. Gopalakrishnan, PhD thesis, School of The Ohio State University, USA, **2003**.

[127] Y. Wang, C. Han, Z. Fei, C. Dong, H. Liu, *The Journal of Physical Chemistry A* **2020**, *124*, 5590–5598.

[128] M. L. Green, PhD thesis, Emory University, Atlanta, **2020**.

[129] R. Wilson, *Journal of Applied Physics* **1966**, *37*, 2261–2267.

[130] T. Maeda, S. Saito, *Japanese journal of applied physics* **1986**, *25*, 1623.

[131] R. Ishii, K. Matsumura, A. Sakai, T. Sakata, *Applied surface science* **2001**, *169*, 658–661.

[132] A. Savitzky, M. J. Golay, *Analytical chemistry* **1964**, *36*, 1627–1639.

[133] K. Burke, *The Journal of chemical physics* **2012**, *136*, 150901.

[134] W. Koch, M. C. Holthausen, *A Chemist's Guide to Density Functional Theory*, Wiley-VCH Verlag GmbH, **2001**.

[135] N. Argaman, G. Makov, *American Journal of Physics* **2000**, *68*, 69–79.

[136] N. Harrison, *Nato Science Series Sub Series III Computer and Systems Sciences* **2003**, *187*, 45–70.

[137] R. Coquet, K. L. Howard, D. J. Willock, *Chemical Society Reviews* **2008**, *37*, 2046–2076.

[138] L. H. Thomas in Mathematical proceedings of the Cambridge philosophical society, *Vol. 23*, Cambridge University Press, **1927**, pp. 542–548.

[139] W. Kohn, L. J. Sham, *Physical review* **1965**, *140*, A1133.

[140] P. Hohenberg, W. Kohn, *Physical review* **1964**, *136*, B864.

[141] C. Lee, W. Yang, R. G. Parr, *Physical review B* **1988**, *37*, 785.

[142] S. Grimme, J. Antony, S. Ehrlich, H. Krieg, *The Journal of chemical physics* **2010**, *132*, 154104.

[143] S. Grimme, *Journal of computational chemistry* **2004**, *25*, 1463–1473.

[144] S. Grimme, *Journal of computational chemistry* **2006**, *27*, 1787–1799.

[145] M. J. Frisch, G. W. Trucks, H. B. Schlegel, G. E. Scuseria, M. A. Robb, J. R. Cheeseman, G. Scalmani, V. Barone, G. A. Petersson, H. Nakatsuji, X. Li, M. Caricato, A. V. Marenich, J. Bloino, B. G. Janesko, R. Gomperts, B. Mennucci, H. P. Hratchian, J. V. Ortiz, A. F. Izmaylov, J. L. Sonnenberg, D. Williams-Young, F. Ding, F. Lipparini, F. Egidi, J. Goings, B. Peng, A. Petrone, T. Henderson, D. Ranasinghe, V. G. Zakrzewski, J. Gao, N. Rega, G. Zheng, W. Liang, M. Hada, M. Ehara, K. Toyota, R. Fukuda, J. Hasegawa, M. Ishida, T. Nakajima, Y. Honda, O. Kitao, H. Nakai, T. Vreven, K. Throssell, J. A. Montgomery, Jr., J. E. Peralta, F. Ogliaro, M. J. Bearpark, J. J. Heyd, E. N. Brothers, K. N. Kudin, V. N. Staroverov, T. A. Keith, R. Kobayashi, J. Normand, K. Raghavachari, A. P. Rendell, J. C. Burant, S. S. Iyengar, J. Tomasi, M. Cossi, J. M. Millam, M. Klene, C. Adamo, R. Cammi, J. W. Ochterski, R. L. Martin, K. Morokuma, O. Farkas, J. B. Foresman, D. J. Fox, Gaussian˜16 Revision A.03, Gaussian Inc. Wallingford CT, **2016**.

[146] W. Zheng, X. Li, S. Eustis, A. Grubisic, O. Thomas, H. de Clercq, K. Bowen, *Chemical Physics Letters* **2007**, *444*, 232–236.

[147] T. Lu, F. Chen, *Journal of computational chemistry* **2012**, *33*, 580–592.

[148] I. Alkorta, I. Rozas, J. Elguero, *Chemical Society Reviews* **1998**, *27*, 163–170.

[149] L. Brammer, *Dalton Transactions* **2003**, 3145–3157.

[150] R. H. Crabtree, *Science* **1998**, *282*, 2000–2001.

[151] R. H. Crabtree, P. E. Siegbahn, O. Eisenstein, A. L. Rheingold, T. F. Koetzle, *Accounts of chemical research* **1996**, *29*, 348–354.

[152] Y. Gao, W. Huang, J. Woodford, L.-S. Wang, X. C. Zeng, *Journal of the American Chemical Society* **2009**, *131*, 9484–9485.

[153] S. J. Grabowski, *The Journal of Physical Chemistry A* **2001**, *105*, 10739–10746.

[154] L. Jiang, L. Lai, *Journal of Biological Chemistry* **2002**, *277*, 37732–37740.

[155] E. Kryachko, S. Scheiner, *The Journal of Physical Chemistry A* **2004**, *108*, 2527–2535.

[156] S. Tsuzuki, A. Fujii, *Physical Chemistry Chemical Physics* **2008**, *10*, 2584–2594.

[157] L. Epstein, E. Shubina, *Coordination chemistry reviews* **2002**, *231*, 165–181.

[158] E. Arunan, G. R. Desiraju, R. A. Klein, J. Sadlej, S. Scheiner, I. Alkorta, D. C. Clary, R. H. Crabtree, J. J. Dannenberg, P. Hobza, et al., *Pure and applied chemistry* **2011**, *83*, 1637–1641.

[159] E. S. Kryachko, *Journal of Molecular Structure* **2008**, *880*, 23–30.

[160] H. Schmidbaur, *Angewandte Chemie International Edition* **2019**, *58*, 5806–5809.

[161] S. Emamian, T. Lu, H. Kruse, H. Emamian, *Journal of computational chemistry* **2019**, *40*, 2868–2881.

[162] A. Albinati, F. Lianza, P. S. Pregosin, B. Mueller, *Inorganic Chemistry* **1994**, *33*, 2522–2526.

[163] A. Albinati, P. Pregosin, F. Wombacher, *Inorganic chemistry (Print)* **1990**, *29*, 1812–1817.

[164] J. L. Atwood, F. Hamada, K. D. Robinson, G. W. Orr, R. L. Vincent, *Nature* **1991**, *349*, 683–684.

[165] D. Braga, F. Grepioni, E. Tedesco, K. Biradha, G. Desiraju, *Organometallics* **1997**, *16*, 1846–1856.

[166] L. Brammer, J. M. Charnock, P. L. Goggin, R. J. Goodfellow, A. G. Orpen, T. F. Koetzle, *Journal of the Chemical Society Dalton Transactions* **1991**, 1789–1798.

[167] G. Park, F. P. Gabbai, *Journal of the American Chemical Society* **2021**, *143*, 12494–12498.

[168] B. Bankiewicz, P. Matczak, M. Palusiak, *The Journal of Physical Chemistry A* **2012**, *116*, 452–459.

[169] M. Jansen, *Chemical Society Reviews* **2008**, *37*, 1826–1835.

[170] A. L. Jesus, J. Redinha, *The Journal of Physical Chemistry A* **2011**, *115*, 14069–14077.

[171] H. Schneider, A. D. Boese, J. M. Weber, *The Journal of chemical physics* **2005**, *123*, 084307.

[172] D.-Y. Wu, S. Duan, X.-M. Liu, Y.-C. Xu, Y.-X. Jiang, B. Ren, X. Xu, S. Lin, Z.-Q. Tian, *The Journal of Physical Chemistry A* **2008**, *112*, 1313–1321.

[173] E. Kryachko, F. Remacle, *The Journal of chemical physics* **2007**, *127*, 194305.

[174] E. S. Kryachko, F. Remacle in *Topics in the Theory of Chemical and Physical Systems*, Springer, **2007**, pp. 161–191.

[175] E. Kryachko, A. Karpfen, F. Remacle, *The Journal of Physical Chemistry A* **2005**, *109*, 7309–7318.

[176] X. Wu, K. Tan, Z. Tang, X. Lu, *Physical Chemistry Chemical Physics* **2014**, *16*, 4771–4777.

[177] G.-J. Cao, H.-G. Xu, R.-Z. Li, W. Zheng, *The Journal of chemical physics* **2012**, *136*, 014305.

[178] A. Z. Msezane, Z. Felfli, K. Suggs, A. Tesfamichael, X.-Q. Wang, *Gold Bulletin* **2012**, *45*, 127–135.

[179] H. Darmandeh, J. Löffler, N. V. Tzouras, B. Dereli, T. Scherpf, K.-S. Feichtner, S. Vanden Broeck, K. Van Hecke, M. Saab, C. S. Cazin, et al., *Angewandte Chemie* **2021**, *133*, 21182–21192.

[180] S. P. Dubey, M. Lahtinen, M. Sillanpää, *Process Biochemistry* **2010**, *45*, 1065–1071.

[181] A. Jafarizad, K. Safaee, S. Gharibian, Y. Omidi, D. Ekinci, *Procedia Materials Science* **2015**, *11*, 224–230.

[182] A. K. Mittal, Y. Chisti, U. C. Banerjee, *Biotechnology advances* **2013**, *31*, 346–356.

[183] Y. Luo, H. Ma, S. Zhang, D. Zheng, P. Che, X. Liu, M. Zhang, J. Gao, J. Xu, *Journal of the American Chemical Society* **2020**, *142*, 6085–6092.

[184] Y. Luo, H. Ma, Y. Sun, P. Che, X. Nie, T. Wang, J. Xu, *The Journal of Physical Chemistry A* **2018**, *122*, 843–848.

[185] X. Wu, L. Senapati, S. Nayak, A. Selloni, M. Hajaligol, *The Journal of chemical physics* **2002**, *117*, 4010–4015.

[186] L. C. Allen, *Journal of the American Chemical Society* **1989**, *111*, 9003–9014.

[187] Z. Qin, R. Cong, X. Wu, Z. Liu, H. Xie, Z. Tang, L. Jiang, H. Fan, *The Journal of Chemical Physics* **2013**, *139*, 034315.

[188] D. Schmitz, V. A. Shubert, T. Betz, M. Schnell, *Frontiers in chemistry* **2015**, *3*, 15.

[189] R. J. Lavrich, R. L. Rhea, J. W. McCargar, M. J. Tubergen, *Journal of molecular spectroscopy* **2000**, *199*, 138–143.

[190] S. S. Batsanov, *Inorganic materials* **2001**, *37*, 871–885.

[191] J. P. Lommerse, S. L. Price, R. Taylor, *Journal of computational chemistry* **1997**, *18*, 757–774.

[192] J. Demaison, M. Herman, J. Liévin, *International Reviews in Physical Chemistry* **2007**, *26*, 391–420.

[193] R. F. Bader, T. Nguyen-Dang in *Advances in Quantum Chemistry*, *Vol. 14*, Elsevier, **1981**, pp. 63–124.

[194] S. Shahbazian, *Chemistry–A European Journal* **2018**, *24*, 5401–5405.

[195] T. Shimanouchi, H. Matsuura, Y. Ogawa, I. Harada, *Journal of physical and chemical reference data* **1978**, *7*, 1323–1444.

[196] T. Tsuneda, J.-W. Song, S. Suzuki, K. Hirao, *The Journal of chemical physics* **2010**, *133*, 174101.

[197] W. Richards, *International Journal of Mass Spectrometry and Ion Physics* **1969**, *2*, 419–424.

[198] A. O. Hernandez-Castillo, J. Bischoff, J. H. Lee, J. Langenhan, M. Karra, G. Meijer, S. Eibenberger-Arias, *Physical Chemistry Chemical Physics* **2021**, *23*, 7048–7056.

[199] A. Bouchet, J. Altnöder, M. Broquier, A. Zehnacker, *Journal of Molecular Structure* **2014**, *1076*, 344–351.

[200] J. P. Merrick, D. Moran, L. Radom, *The Journal of Physical Chemistry A* **2007**, *111*, 11683–11700.

[201] T. M. Ramond, G. E. Davico, R. L. Schwartz, W. C. Lineberger, *The Journal of Chemical Physics* **2000**, *112*, 1158–1169.

[202] A. F. Ordonez, O. Smirnova, *Physical Review A* **2018**, *98*, 063428.

[203] P. Weis, P. R. Kemper, M. T. Bowers, S. S. Xantheas, *Journal of the American Chemical Society* **1999**, *121*, DOI 10.1021/ja9842161.

Acknowledgements

I express my gratitude to my colleagues, friends, and family without whom this thesis and the accompanying research would not have been possible.

First and foremost, I thank my group leader, André Fielicke, who not only proposed this research topic but also provided guidance throughout my entire journey as a Ph.D. student. I extend my appreciation to Otto Dopfer and Gerard Meijer, who enabled my scientific career at the TU Berlin and FHI and also were there for help and advise.

Special recognition is due to fellow group members David Yubero Valdivielso, Sascha Schaller, Mallory Green, and Viktoria Brandt. Besides research our discussion topics also extended to the simple pleasures in life, such as dogs and cats.

I am grateful to Wolfgang Erlebach, Henrik Haak, Uwe Hoppe, Sebastian Kray, Klaus Peter Vogelgesang (KPV), the workshop and the E-Lab of the FHI, whose invaluable contributions were indispensable for the essential designs and updates to the experiment.

My thanks is extended to Jesús Ríos and Xiangyue Liu, who got me started on DFT calculations, which played an important role for this thesis.

I also thank my (former) coworkers from the FHI and TU: Johannes Bischoff, Bruno Credidio, Sandra Eibenberger-Arias, Marko Förstel, Sandy Gewinner, Nadia Gonzalez Rodriguez, Karin Grassow, Alan Günther, Uwe Hergenhahn, Manuela Misch, Pablo Nieto, Evely Prohn, Christian Schewe, Stefan Schlichting, Wieland Schöllkopf, Johannes Seifert, Russel Thomas, America Torres, Florian Trinter, Bernd Winter, Sidney Wright and many more for interesting discussions and fun activities.

Appreciation is extended to our external collaborators, including Christiane Koch and Vít Svoboda, who initiated first calculations in the realm of anion PECD. I also have to mention C. William McCurdy, whom I had the privilege of meeting at the Gordon Research Conference 2018. He recommended a paper, which infused renewed hope during a time when doubts first emerged about the feasibility of our anion PECD experiment.

Last but certainly not least, I express my gratitude to my friends for countless adventures in board games, quizzes and bouldering. I reserve special thanks for my boyfriend, Max Heimel, and my parents, Sabine and Klemens Triptow, whose unwavering support took many forms.

To each and every one of you, whether explicitly mentioned or not, I extend a sincere thank you for contributing to a period of my life that was both enriching and enlightening.